Developing Experimental Models of Non-traumatic Spinal Cord Injury

Katherine Victoria Timms

Submitted in accordance with the requirements for the degree of Doctor of Philosophy in Tissue Engineering and Regenerative Medicine (Innovation in Medical and Biological Engineering)

The University of Leeds

School of Mechanical Engineering

Faculty of Engineering

March, 2020

The candidate confirms that the work submitted is her own and that appropriate credit has been given where reference has been made to the work of others.

This copy has been supplied on the understanding that it is copyright material and that no quotation from the thesis may be published without proper acknowledgement.

Abstract

Over 50% of non-traumatic spinal cord injuries (NTSCI) are caused by mechanical compression either due to osteophytes in degenerative disease, or tumours (New et al., 2014). The pathophysiology of NTSCI is poorly understood, with no distinct injury cascade (Karadimas et al., 2013). The aim of this project was to evaluate cellular responses to mechanical insults in the context of NTSCI.

In-vitro, a model was developed to apply high and low velocity compression to astrocyte-seeded collagen hydrogels. Outcomes included hydrogel contraction, GFAP expression, cellular shape, and cytokine release. In-vivo a balloon lesion model was modified to induce a non-traumatic ventral lesion, by developing an injection port and inflating over 3 days. Functional deficits and histological outcomes were assessed.

In-vitro, 100 mm.s^{-1} compression elicited an astrogliotic and inflammatory response from day 11, indicative of TSCI. This comprised a significant increase in GFAP area per cell, astrocyte ramification, and IL-6 expression. Conversely, at <100 mm.s^{-1}, no differences were observed. The findings of this study suggest slow compression of astrocytes alone does not induce NTSCI.

In-vivo, surgery was undertaken on 10 animals (including 3 shams). In injury groups, functional deficits were observed , which increased with each inflation. Animals were grouped into mild and severe based on their motor function (severe animals exhibited paraplegia). Minimum motor function correlated with minimum cross-sectional area, and greater parenchyma disruption. In the severe group only, there was a trend of mild astrogliosis, demyelination and vasculature narrowing at the epicentre. This corresponds with the wider literature, where demyelination and disruption to the vasculature are hypothesised to be involved in NTSCI pathology.

Overall, in-vitro and in-vivo models of NTSCI have been successfully developed. Physiological changes were observed in both models, with differences to TSCI. Further investigations can be undertaken to understand the pathology of NTSCI.

Acknowledgements

I have gone through some difficult times in the process of doing this research, and I could not be more grateful and relieved that it is finally at an end.

Firstly, thanks have to go to my supervisors- Richard, Jessica, Ronaldo, Joanne, James, and Lucia in Prague; your individual expertise have helped me in each aspect of my work at various points during the last four years. In particular Richard, for the rapid turnaround of my thesis every single time I sent you yet more writing, and the meetings that always gave me something to work towards. A special thank you to Jessica. As well as your guidance with the experiments and thesis, your positivity and understanding helped me through my darkest times. I truly would not have been able to get through my PhD without you.

I would also like to thank the Kwok group, FBS lab group, and the rest of my CDT cohort. In particular Sian and Trang, whose help with developing the in vivo and in vitro work respectively was instrumental.

Thank you to my amazing friends and family, for putting up with me always. Tom, Tanya, Miles, and Sarah: you really do make it the magnificent six. Mum and Dad, thank you for your own determination in all that you do, helping me endlessly, and making me feel like this was possible. Andy and Becky, look at what proper adults we have become! I am so lucky and thankful to have you all.

And finally, the biggest thank you to Tom. In my lowest moments you have kept me going. You have helped me carry this burden whilst simultaneously carrying your own. I am beyond proud of you and us. To have you by my side has given me a huge advantage in everything I have done. **Let's get married.**

Contents

List of figures

List of tables

List of Abbreviations

Abbreviated form	Full term
2D	Two dimensional
3D	Three dimensional
3R	3R principles: reduction, replacement, refinement
ANOVA	Analysis of variance
BBB	Basso, Beattie and Bresnahan
BSA	Bovine serum albumin
CNS	Central nervous system
CSPG	Chondroitin sulphate proteoglycan
CT	Computed tomography
DNA	Deoxyribonucleic acid
DMEM	Dulbecco's Modified Eagle's Medium
ELISA	Enzyme-linked immunosorbent assay
FBS	Foetal bovine serum
GFAP	Glial fibrillary acidic protein
H&E	Haematoxylin and eosin
HBSS	Hank's buffered salt solution
HCl	Hydrochloric acid
HEPA	High-efficiency particulate air
IHC	Immunohistochemistry
MBP	Myelin basic protein
MEM	Modified Eagle's Medium
NTSCI	Non-traumatic spinal cord injury
OCT	Optimum cutting temperature
PBS	Phosphate buffered saline
PFA	Paraformaldehyde
P.I.D.	Proportional, integral, derivative
PDL	Poly-D-lysine
NaCl	Sodium chloride
NaOH	Sodium hydroxide
SEM	Standard error of the mean
TSCI	Traumatic spinal cord injury
TBS	Tris buffered saline
TNS	Tris no saline
TGF-beta	Transforming growth factor beta

Chapter 1

Introduction

1.1 Preface

1.1.1 Spinal Cord Injury

The spinal cord connects the brain and peripheral nervous systems, processing and transmitting motor and sensory information, and modulating reflex responses. Spinal cord damage through compression or other mechanisms causes dysfunction in the form of pain, limb weakness, numbness, bladder/bowel dysfunction, and irregular gait (NICE, 2016). Clinical outcomes vary with magnitude, type of injury, severity, location and biomechanical origin. Spinal cord injuries can be classified by velocity. High velocity insults, up to 4.5 $m.s^{-1}$ (Wilcox et al., 2003), cause traumatic spinal cord injuries (TSCI). Conversely, slow velocity insults where trauma is not involved, with development over a timescale between months to years, can be classified as non-traumatic spinal cord injuries.

NTSCI are predominantly caused by chronic illness and disease, with 50% caused by degenerative diseases and cancers (New et al., 2014). The key features which distinguish NTSCI from TSCI, as determined by Karadimas et al. (2015) are:

1. No acute mechanical insult, slow velocity compression

2. Absence of gross haemorrhagic necrosis

3. Chronic and progressive nature (likely induces compensatory mechanisms)

There is a lack of data describing the epidemiology and aetiology of NTSCI. This is likely to be due to the wide range of causes, the lack of national registries, and the secondary nature of NTSCI leading to patients not always being admitted to specialist spinal cord injury units (New et al., 2014). The prevalence of NTSCI has been estimated to be 1120 per million and 2310 per million in the only two studies undertaken (Razdan et al., 1994; Noonan et al., 2012). Annual incidence is estimated to be between 6 and 76 cases per million (New et al., 2014). Since the incidence of traumatic injury is estimated to be between 10 and 40 cases per million per year, NTSCI affects the same number or more people annually than traumatic injury (Lee et al., 2014). Demographic studies have identified that NTSCI patients have median ages of 62 to 67 years old; with an even gender divide (Gupta et al., 2009; Guilcher et al., 2010; New et al., 2011). In TSCI, approximately 80% of patients are males and the mean age is between 38 and 52 years old (Cosar et al., 2010; New et al., 2011; World Health Organisation, 2016).

Spinal cord injuries are a complex clinical problem, affecting quality of life and lifespan. Alongside the damage caused by injury, complications and secondary illnesses occur frequently in spinal cord injury, and vary based on type of injury. Urinary tract infections, spasticity and pressure ulcers affect at least 20% of NTSCI patients (Gupta et al., 2009). Mortality in all patients with spinal cord injury is up to three times greater than the general population, with significantly higher levels of mortality in NTSCI patients than TSCI patients (van den Berg et al., 2010). This difference in patients with NTSCI may be due to the increased age of NTSCI patients, as well as increased rate of co-morbidities in such populations.

New and Jackson (2010) carried out a study evaluating the costs associated with SCI patients. In TSCI, the first admission to hospital is longer and more costly for traumatic injury ($54,000, 51.3 days) than NTSCI ($18,000, 16.5 days). Patients with NTSCI had an increased rate of subsequent readmission with disease progression, whereas this was

not the case for TSCI patients. Therefore, comparing NTSCI and TSCI, case-by-case costs are estimated to be similar overall (New and Jackson, 2010). However, NTSCI has an increased prevalence than TSCI and therefore, may be a greater direct cost to society. Indirect socio-economic losses to society also occur in spinal cord injuries. These are linked to insufficient or inappropriate transport services and accessibility, chronic pain and high rates of depression; all causing reduced societal participation (Goossens et al., 2009; Ataoglu et al., 2013).

In patients with NTSCI, treatment is limited and predominantly involves surgical decompression and fixation (NHS, 2010; NICE, 2015, 2016). These interventions may arrest injury progression, but neurological deficits remain and one in twenty patients are at risk of severe neurological complications (Alafifi et al., 2007).

With prevalence predicted to increase with the ageing population, a deeper understanding and characterisation of NTSCI is needed to guide management and improve outcomes of such injuries. Experimental models may be used to develop understanding of the pathology of spinal cord injuries.

Both *in-vitro* and *in-vivo* models of spinal cord injury allow evaluation of cellular and tissue morphology at various timepoints both before and after the injury. They also allow greater control of the injury parameters themselves, minimising the variation seen clinically. Together, this means greater understanding of how injury mechanics affect injury outcomes can be established. *In-vivo* models allow assessment in a whole system approach, and understanding of how systems interact in the injury cascade. However, this can mean factors associated with other biological systems (e.g. an immune response, damage to musculoskeletal tissues instead of the spinal cord) confound results and the exact cause and response of a particular insult on a particular cell population cannot be elucidated. Further, there are ethical implications of using animals for research. The 3R principles (refinement, reduction and replacement) guide researchers towards alternatives to *in-vivo* models. In the case of spinal cord injury and other neural injuries, there have been studies using isolated primary cell populations in matrices to elucidate injury

mechanisms. The advantages of *in-vitro* modelling are that the effects of a single input on a single output can be studied in isolation, however the relevance to clinical physiology must be validated. Once experimental models of injuries have been established, they provide a platform for developing and testing new treatments.

1.1.2 Research Purpose

Non-traumatic spinal cord injury (NTSCI) has a poorly established pathophysiology in spite of its increasing prevalence. Slow velocity lesions over an extended time frame are rarely evaluated in spinal cord injury studies *in-vitro* and *in-vivo*. Therefore, neural cell responses to such mechanical insults are not known. Other studies have shown that injury mechanics directly affect outcomes in clinical circumstances, preclinical, and cellular models. This research aims to establish how changing mechanical insults affect neural cell responses in the context of NTSCI, through development of experimental models (Figure 1.1). The first chapter will entail a literature review, describing the anatomy and physiology of the spinal cord, pathology in spinal cord injuries, and methods to model spinal cord injury experimentally.
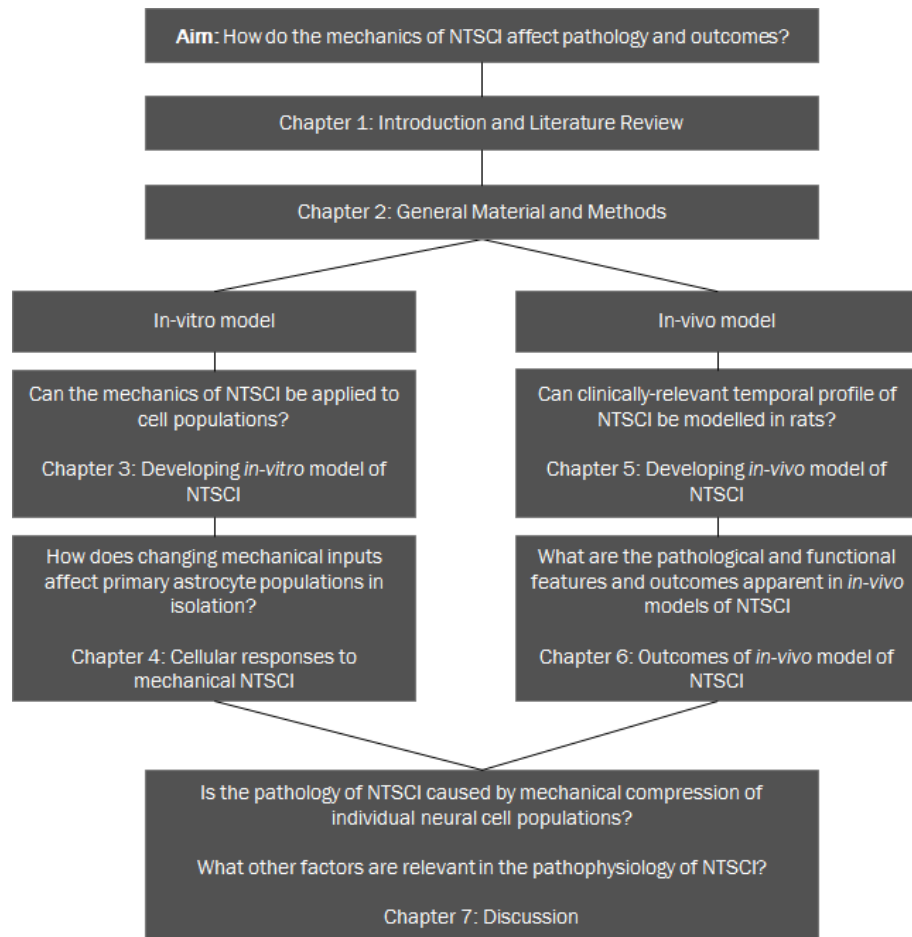
Figure 1.1: ***Overview of the core aims, research questions posed, and chapters in this thesis.*** *The document is split into seven chapters, incorporating literature review; general methods; development and results from in-vitro and in-vivo studies; and a discussion.*

1.2 Spinal Anatomy and Physiology

1.2.1 Gross Anatomical Structure

The spine provides skeletal stability and mobility from the skull to the pelvis (Harms and Tabasso, 1999). In human adults, the spine is a column of 24 individual vertebrae plus the fused sacrum and coccyx (comprising of and 4 vertebrae, respectively). Articulating (i.e. non-fused) vertebrae are divided into anatomical regions, comprising 7 cervical (C1-7), 12 thoracic (T1-12), and 5 lumbar (L1-5) vertebrae. Vertebrae are connected with ligaments, muscles and intervertebral discs (White and Panjabi, 1990). Each individual vertebra has a central vertebral foramen which forms the vertebral canal running the length of the spinal column (Figure 1.2). This encloses and protects the spinal cord; part of the central nervous system. When the spinal cord is damaged, neurological deficits occur.
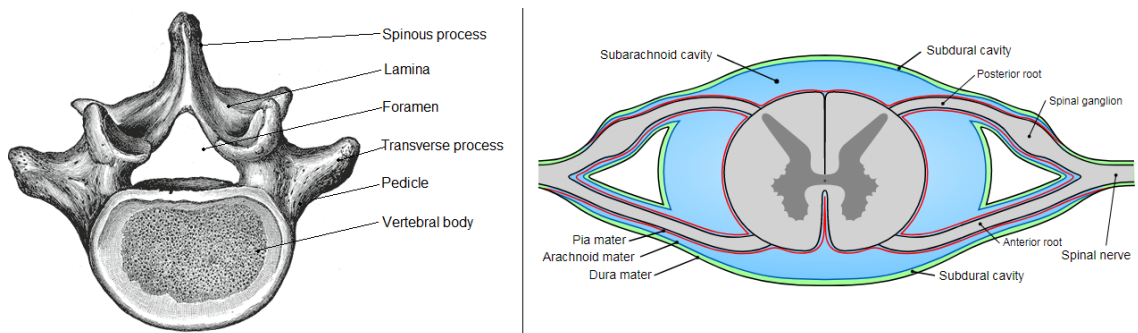
Figure 1.2: **Anatomy of a single vertebra (left) and diagram of the gross structure and meninges of the spinal cord (right).** *The vertebra shown is a superior view of L5. The spinal cord sits within the central vertebral foramen, and runs from the base of the skull to the lumbar region. The meninges protect the spinal cord. Image adapted from Gray (1918)*

The spinal cord runs from the brain cranially to the cauda equina after approximately the first lumbar vertebra (Martini et al., 2011). It is surrounded by meninges (the dura, arachnoid and pia mater, Figure 1.2), which create a barrier to prevent entry of foreign entities, and provide both form and physical protection for the cord (Russi and Brown, 2015). The spinal cord is 42 to 45 cm long, with a cylindrical shape 10 to 15 mm in

diameter (Gray, 1918; Fratini et al., 2014). The diameter is largest at the cervical and lumbar enlargements, where nerves from the limbs enter the spine (Panjabi et al., 1991, 1992). A total of 31 pairs of nerve roots split laterally from the spinal cord through the interpedicular spaces, with one pair at each vertebral level (Martini et al., 2011). Each nerve root innervates or is innervated by a distinct area of the body. These regions can be roughly mapped on the skin as dermatomes (Greenberg, 2003; Lee et al., 2008).

1.2.2 Spinal Cord Cell Types

Neural tissue, including the spinal cord, comprises cellular components (80% of total volume) in an extracellular matrix (20% of total volume) of proteoglycans and glycosaminoglycans; which form basement membranes around vasculature, interstitial matrix between cells, and organised perineuronal nets surrounding neurons (Nicholson and Sykova, 1998; Sobel, 1998; Kwok et al., 2011; Burnside and Bradbury, 2014; Haggerty et al., 2017). Cells interact with the matrix via trans-membrane integrins and their receptors; which modulate behaviours such as plasticity, synapse formation, and axon sprouting (Crapo et al., 2012). Neurons and glia are the two major cell types in the spinal cord, and they have distinct roles (see Table 1.1). Neurons are oriented cells which are responsible for the electrical signalling. They have a central cell body and processes called neurites which either receive or transmit information (dendrites and axons, respectively). Glial cells play a supporting role, and the two types of glia core to spinal cord injury responses are astrocytes and microglia.

Astrocytes are the most abundant cell type in the CNS, constituting up to 30% of all cells (Liddelow and Barres, 2017). They form connections with nodes of Ranvier, modulating neuronal electrical transmission; synapses, regulating chemical neurotransmission; vasculature and other astrocytes (Sofroniew, 2005). In the CNS, only astrocytes express glial fibrillary acidic protein (GFAP). The amount of GFAP expressed by astrocytes varies under physiological conditions in different brain regions (Schitine

Table 1.1: **Cell types in the central nervous system.** *The spinal cord contains neurons and glial cells. The axons of cells in the white matter are coated with myelin, an insulating substance increasing the speed of electrical propagation. The information in this table is simplified for the scope of this project. (Gray, 1918; Sofroniew and Vinters, 2010; Burke et al., 2016)*

Cell type	Spinal cord location	Function
Inter-neurons	Within the grey matter. Their axons are short and predominantly unmyelinated.	Modulate (activate or inhibit) local neurons in the grey matter
Motor-neurons (efferent neurons)	Cell soma in the ventral grey matter. Axons leave the spinal cord via the ventral horn.	Receive electrochemical information from interneurons and descending tracts and transmit information to effectors.
Sensory neurons (entering cord)	Cell soma in dorsal root ganglia, axons project onto neurons in grey matter	Afferent myelinated neurons transmit sensory information from the peripheral to central nervous systems.
Astrocytes	The most common glial cell type, found through the spinal cord. They have a stellate shape.	Maintaining electrochemical gradients, contributing to electrical behaviour, controlling blood flow, and metabolite storage/transport
Microglia	Throughout the spinal cord	Specialised macrophages with a role in protection and repair of the spinal cord
Oligo-dendro-cytes	Higher density within the white matter	Myelinating cells, ensheathing axons and creating the myelin sheath.

et al., 2015). Morphological differences in astrocytes were identified even in Cajal's early drawings from the late 19th century (Garcia-Lopez et al., 2010). Two well established populations from these drawings are fibrous and protoplasmic astrocytes (Garcia-Marin et al., 2007). Fibrous astrocytes have longer but fewer processes, and are found in the white matter; whereas protoplasmic astrocytes have a greater number of shorter projections and are located in the grey matter (Khakh and Sofroniew, 2015). The latest methods in molecular biology have shown that heterogeneity in astrocyte populations extends to differences in gene expression, electrophysiological properties, and functional differences. These have been reviewed extensively in the literature, yet clear consensus on further sub-populations and their specific functions remains to be established (Zhang

and Barres, 2010; Schitine et al., 2015; Yoon et al., 2017).

1.2.3   Spinal Cord Tissue Regions: Grey and White Matter

Further, the cord can be compartmentalised into grey and white matter (Gray, 1918; Silva et al., 2014). The grey matter is central, and contains multipolar neurons. Neurons in dorsal regions are innervated by sensory afferents, and those in ventral regions innervate peripheral effectors. The white matter is made up of axons sheathed in myelin, an insulating substance with a high fat content which improves conduction of electrical impulses. These axons run along the length of the cord, and are grouped into tracts which either ascend and transmit information to the brain, or descend and transmit information to effectors (Figure 1.3). Ascending tracts have cell soma in the grey matter, with myelinated axons which project into the white matter and transmit information up to the brain. Conversely, descending tracts originate from cell soma in the brain, where myelinated axons form tracts in the white matter that allow descending control of motor outputs by modulating motorneurons. Damage to any of these tracts can cause functional deficits that are apparent in spinal cord injury. The ventral spinal artery runs along the length of the spinal cord within the ventral median fissure.

In man, the largest sensory tract is the dorsal column medical lemniscus pathway. Found in the medio-dorsal area of the spinal cord white matter, this tract transmits fine touch and conscious proprioception (Navarro-Orozco and Bollu, 2018). The spinothalamic tract transmits nociception, thermoception and crude touch (Devlin, 2012).

The corticospinal tract is the major motor pathway, controlling voluntary distal movements, including skilled movements such as walking (Welniarz et al., 2017). Damage to the tract has profound effects on walking (Nathan, 1994; Petersen et al., 2012). The corticospinal tract has has two components, dorsal and ventral. The lateral fibres are lateral to the grey matter dorsal horn, whereas the ventral fibres are in the ventral white matter, adjacent to the ventral median fissure. The ventral bundle innervates trunk muscles, and as such ends at the mid-thoracic level (Lingford-Hughes and Kalk, 2012).

In the dorsal column medial lemniscus tract and lateral corticospinal tract, the lateral most axons transmit information from and to the legs. Medial to these axons are areas associated with the trunk, and medial to the trunk axons are areas associated with the arms (Raiszadeh and Spivak, 1999).

Ascending (sensory) tracts
- Dorsal column medial lemniscus
- Spinothalamic
- Spinocereballar

Descending (motor) tracts
- Raphespinal
- Corticospinal
- Rubrospinal
- Reticulospinal
- Vestibulospinal
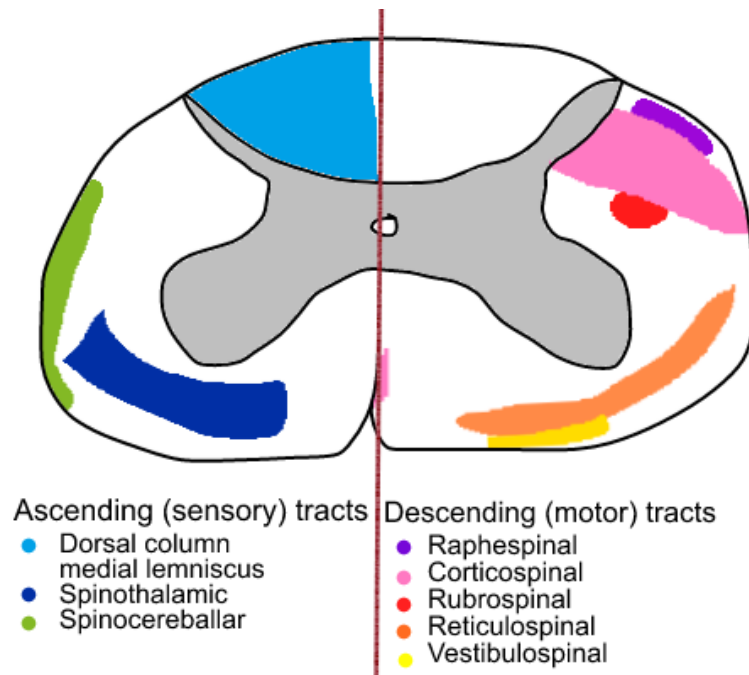
Figure 1.3: **Human spinal cord cross-section showing grey and white matter, with position of ascending and descending tracts** *Grey matter forms a central butterfly-like shape; white matter surrounds this and contains tracts. Ascending tracts (on the left of the diagram) transmit sensory information from effectors to other parts of the central nervous system. Motor tracts (right of the diagram) transmit motor information from the brain to caudal parts of the nervous system. Image adapted from (Watson et al., 2009)*

1.2.4 Mechanical Properties of the Spinal Cord

Understanding the mechanical properties of the spinal cord can help predict responses to loading, deformation, and injury (Clarke, 2011). There is no consensus on the properties of the spinal cord; with elastic modulus *ex-vivo* being reported between 40.12 kPa to 1.37 MPa for post-mortem human tissue (Bilston and Thibault, 1996; Mazuchowski and Thibault, 2003; Karimi et al., 2017), and 6.63 to 40 kPa for other mammals (Chang

et al., 1981, 1988; Ichihara et al., 2001; Fiford and Bilston, 2005). It is worth noting that these studies all use post-mortem tissue, and not tissue *in-situ*, which could affect results. Variations in values are likely to be due to differing experimental procedures and apparatus. A recent review describes the advantages, disadvantages and confounding potential of several methods for testing the mechanical properties of the spinal cord (Bartlett et al., 2016a). For instance, the tissue source (species, age) and preparation can affect reported material properties of the spinal cord. This was demonstrated in a study which conducted tensile mechanical testing of porcine spinal cords *in-vivo* and *ex-vivo* showed significantly greater peak stress and relaxation in *ex-vivo* specimens (Ramo et al., 2018).

Further, the spinal cord is anisotropic and viscoelastic, which may also lead to differences in measured mechanical properties (Feng et al., 2013). The stiffness of viscoelastic materials therefore depends on the strain rate (Dogliotti and Yelland, 1964; Hussein, 2018). These properties are seen widely across organised soft tissues (Fung, 1993; Taylor et al., 2009). They also add complexity to mechanical testing where factors such as pre-conditioning, strain rate, and amount of strain must be controlled during each test (Bilston and Thibault, 1996; Ichihara et al., 2003). As an example, increasing the strain rate from 0.5 s^{-1} to 50 s^{-1} in transverse compression increased the compound elastic modulus of the porcine spinal cord by 170% (Fradet et al., 2016). *In-vivo* the cord is subject to perfusion pressure of between 60 and 90 mmHg (Werndle et al., 2014), temperature of 36.6°C $\pm$ 1°C (Khan et al., 2007), and a pH of 7.32 (Langer et al., 2016). These environmental factors are often unreported, yet inadequate replication of these conditions during mechanical testing could contribute to variation.

Overall, the spinal cord is a complex anisotropic structure with non-linear viscoelastic properties and a low elastic modulus (Clarke, 2011). The reproducibility of previous data, its relevance to human tissue *in-vivo* and how these mechanical properties influence injury are not fully understood. The low elastic modulus of the spinal cord means that it is easily deformed which has the potential to damage cells. It is important

to understand the extent physiological deformation of the spinal cord before the impact of spinal cord injury can be established.

1.2.5 Physiological Deformations on the Spinal Cord

The greatest physiological deformation of the spinal cord occurs during flexion-extension movements, and at rest due to rhythmic movements associated with breathing and circulation. Flexion causes an increase in cervical cord length of 7% for the ventral region, and 11% for the dorsal region (Koschorek et al., 1986; Yuan et al., 1998; Kuwazawa et al., 2006). The thoracic spinal cord has less mobility due to attachment of the ribcage (Harrison et al., 1999a; Lee, 2015). By contrast, there is substantial elongation (3.6%) of the lumbosacral cord (Tani et al., 1991; Harrison et al., 1999b). At the conus medullaris, which is tethered to the coccyx, movement is minimal in flexion (Fettes et al., 2006). This reduced vertebral canal diameter means impingement onto the spinal cord is increasingly likely; in particular during extension where in healthy populations the vertebral canal decreases in diameter by 3 to 5% (0.5 mm) (Sayıt et al., 2015). Spinal cord deformation from 0.60 to 1.32 mm has been identified during the cardiac cycle and forced breathing (Cai et al., 2007; Figley and Stroman, 2007; Winklhofer et al., 2014). Although these values are minimal and not an issue for the healthy population, in patients with spinal canal stenosis and vasculature remodelling they may be different and become problematic, resulting in spinal cord impingement.

The spinal cord is deformable, and deformations during physiological movement do not lead to functional deficits. When a mechanical insult results in supra-physiological loading or displacement of the cord, cells in the spinal cord either directly become damaged, respond to the change through direct connections to the extracellular matrix, or respond indirectly through signalling mechanisms or ischaemia. The close interactions between neural cells and the spinal cord extracellular matrix mean mechanical insults to the cord have the capacity to cause changes in cellular phenotype and function.

1.3 Spinal Cord Injury Pathophysiology and Biomechanics

International standards have been developed to categorise injury (International Standards for Neurological Classification of Spinal Cord Injury, published by the American Spinal Injury Association (ASIA)). (Kirshblum et al., 2011). Injury level describes where along the length of the spinal cord it has been damaged. Absence of sensation or motor output in one dermatome means the injury is above that associated vertebra. The lowest dermatome where function is normal is defined as the level of injury. Further, injury severity is based on which tracts or cells are damaged. 'Complete' injuries occur when the entire cord is damaged, and no motor or sensory function is maintained. If there is any motor or sensory function below the injured level, the injury is 'incomplete'. Across all global regions, 71% of patients with NTSCI experience paraplegia, the remaining 29% are tetraplegic (New et al., 2014). Further, incomplete injuries are 20 to 40% more common than complete injuries (McKinley et al., 1999; Cosar et al., 2010; Marinho et al., 2012). This indicates that NTSCI predominantly affect areas below the lower cervical region and do not damage all tracts i.e. are incomplete and cause paraplegia. These facts are important considerations in experimental modelling of NTSCI.

1.3.1 Pathological Cascade in Spinal Cord Injury

Categorisation of NTSCI based on aetiology has only recently been attempted; and divides injuries into congenital-genetic or acquired disorders (New and Marshall, 2014). Acquired disorders such as degeneration and neoplasms are biomechanical in origin (i.e. caused by direct compression of the spinal cord) and will be the focus of this study. The biological consequences of chronic compression-induced spinal cord injury have similarities and differences to that of traumatic injury (Table 1.2). Many of the pathological features found in NTSCI have not been extensively assessed or reliably established, and further study is required. Conversely, in traumatic spinal cord injury,

a primary and secondary injury cascade have been identified and well-established (Anwar et al., 2016; Morin, 2018). Primary injury comprises the discrete mechanical insult itself and associated cell death, whereas secondary injury entails ischaemia, necrosis, Wallerian degeneration, and glial scar formation (Table 1.2). The glial scar and astrogliosis are major parts of the secondary injury cascade in traumatic spinal cord injury, and are initiated by glial cells in the spinal cord. This separation of injury into primary and secondary events is clear in traumatic injuries since the injury itself is a one-off, singular event. In NTSCI, there is no clear pathological distinction between primary and secondary events due to the continuous nature of the insult. In NTSCI with a biomechanical sequence, the canal is slowly and progressively occluded.

There have been several attempts to identify the change in cross-sectional area required to elicit symptomatic spinal cord compression at the cervical level. Differences in cross-sectional area reduction observed in symptomatic and asymptomatic populations have ranged from 15 to 30% (Penning et al., 1986; Kadanka et al., 2017). One study using a cut off of 60%, found that after 5 years, 100% of subjects with over 60% reduction in spinal cord cross-sectional area developed myelopathy (Matsunaga et al., 2008). This study did not define how they determined if myelopathy was present. Other studies have tried to identify asymptomatic cervical cord compression in healthy subjects, but findings have indicated a change in shape (i.e. one dimension of the cord such as anterio-posterior diameter due to disc protrusion), and no reported significantly different changes in cross-sectional area (Boden et al., 1990b; Matsumoto et al., 1998, 2013; Nakashima et al., 2016; Martin et al., 2018). A discordance exists between imaging outcomes and spinal cord compression (Witiw et al., 2018).

Similar trends have been identified in lumbar stenosis. Asymptomatic patients often have degenerative changes and disc herniation (Boden et al., 1990a). A multi-centre analysis found radiological severity was not associated with clinical outcomes before or after decompressive surgery in lumbar stenosis (Weber et al., 2016). Another study found that a 25% reduction in spinal cord (dural sac) cross-sectional area was associated

with low back pain, but only used participants from one area of Japan (Iwahashi et al., 2016). A retrospective study identified a reduction in vertebral canal cross-sectional area of 41% and a reduction in dural sac cross-sectional area of 47% between control and symptomatic patients (Lim et al., 2017). These studies do not indicate the minimum value of compression at which symptoms occur, but this must be below the range of 25 to 50%. Overall, the picture for lumbar stenosis is no more clear than that of cervical myelopathy, and the radiological criteria currently are not well established (Steurer et al., 2011).

Overall, the effect of compression extent and reduction of cross-sectional area on symptoms is not clear. Studies are contradictory, but suggest that a reduction in area of 15 to 50% is apparent in symptomatic populations. Compression of the spinal cord above the threshold level damages nerve fibres (Table 1.2). Increasing compression corresponds with onset of symptoms, which then progressively deteriorate as occlusion continues to increase (Kim et al., 2004; Kubota et al., 2011). The latent period, followed by insidious onset of symptoms and progressive deterioration are key features of NTSCI.

The picture is further complicated since stenosis identified on MRI or CT scans does not correlate with functional deficits, due to viscoelasticity, remodelling and plasticity of neural circuits in the spinal cord. Instead, NTSCI is associated with a 33% reduction in the number of local blood vessels (Karadimas et al., 2013; Long et al., 2014). Microvascular remodelling has traditionally been measured with ex-vivo extraction and preparation of the tissue for antibody-labelling. This has disadvantages and results in poor understanding of disease progression due to the limited availability of samples over time. However, future improvement in microCT scanning may provide a method for assessing vascular changes *in-vivo*. This may give a more accurate representation of changes associated with injury (Long et al., 2014). Improved understanding of the mechanisms of NTSCI is required, particularly how the extended time frame and slow velocity of the primary insult influences the pathological cascade.

Table 1.2: **Pathophysiology of spinal cord injuries.** *Symptoms are similar between traumatic and non-traumatic injury, but pathophysiologies are distinct. Abbreviations: CNS = central nervous system; IHC = immunohistochemistry; NTSCI = non-traumatic spinal cord injury; TSCI = traumatic spinal cord injury.*

Feature	Traumatic spinal cord injury	Non-traumatic spinal cord injury	References
Timescale/ velocity	High velocity acute injuries – dynamic loading at 4.5 m/s	No quantitative detail of velocity	NTSCI: no studies available. TSCI (Wilcox et al., 2003)
Immediate (primary) changes	Gross damage causing non-specific cell death, haematoma, microglial activation and ischaemia	No changes occur immediately due to the long term nature of this type of injury	TSCI: (Donnelly and Popovich, 2008; Rowland et al., 2008)
Vascular changes	Gross immediate ischaemia due to damage to vasculature from insult itself.	Gradual compression of the cord in confined environment reduces local vascular supply (ischaemia). Endothelium is disrupted, unknown mechanisms.	NTSCI: (Karadimas et al., 2013; Long et al., 2014).TSCI: (Anwar et al., 2016)
Vascular remodelling	No opportunity for remodelling during the injury process as insult is immediate.	Vascular remodelling seen in humans and animal studies. Chronic compression leads to local hypoxia, and compensatory changes.	NTSCI: (Doppman, 1990; Kurokawa et al., 2011; Karadimas et al., 2012)
Blood-spinal cord barrier	Dramatically disrupted in injury event and subsequent cytokine release, but permeability recovers after several weeks	Increased permeability due to endothelial cell damage – allow white blood cells to enter. This is maintained to chronic stages	NTSCI: (Karadimas et al., 2013). TSCI: (Strbian et al., 2008; Cohen et al., 2009)
Cell death	Necrosis. Cell contents are released from neurons and endothelial cells which are damaged during the insult. This causes necrosis.	Apoptosis, as determined in several human tissue and animal experiments. Predominantly oligodendrocyte apoptosis with some neuronal cell loss (see 'Myelin')	NTSCI: (Newcombe et al., 2015). TSCI:(Macaya and Spector, 2012)

Pathophysiology of spinal cord injuries continued

Feature	Traumatic spinal cord injury	Non-traumatic spinal cord injury	References
Neuronal (Wallerian) degeneration	Expansive number of secondary consequences causes injury site to expand, and nearby axons to further degenerate, forming neuronal end bulbs	Wallerian degeneration has been seen in mouse models, proportional to compression. This occurs mainly in ventral horn neurons (motor neurons in grey matter)	NTSCI: (Uchida et al., 2002). TSCI:(Dong et al., 2003; Bradke et al., 2012)
Immune cell invasion	Injury immediately activates microglia. Neutrophils invade after 3 hrs, but M1 macrophages infiltrate at day 7 and 60	Microglia activate, recruit peripheral immune cells (predominantly macrophages, less lymphocytes and neutrophils)	NTSCI: (Yu et al., 2011). TSCI: (Anwar et al., 2016; Kjell and Olson, 2016)
Effect of immune response	Inflammatory response up to day 7 (M1 macrophages), followed by anti-inflammatory M2 macrophages stabilisation of scar	M1 macrophage activation, leading to synapse degeneration proportional to compression	NTSCI: (Takano et al., 2014). TSCI: (Zhou et al., 2014)
Myelin	Oligodendrocyte necrosis within an hour of injury due to enzyme release from nearby cells, chronic apoptosis due to Wallerian degeneration.	Demyelination occurs due to oligodendrocyte apoptosis. Some evidence myelin is susceptible to mechanical pressure.	NTSCI: (Karadimas et al., 2013). TSCI: (Dong et al., 2003; Almad et al., 2011)
Glial scar formation	Astrocytes at periphery of lesion are activated, and express glial fibrillary acidic protein. Forming a scar	No reports of in-vivo glial scar formation in the literature. Human MRI studies show lightened areas which may be gliosis	NTSCI: (Coronado et al., 2009). TSCI: (Wanner et al., 2013)
Lesion expansion	Oligodendrocyte apoptosis away from initial site causes expansion	Not established	TSCI: (Almad et al., 2011; Aarabi et al., 2012)
Plasticity	Short timescale of acute injury – no plasticity	Long timescale permits CNS plasticity	NTSCI: (Zhou et al., 2015)

1.3.2 Biomechanical Events in Spinal Cord Injury

The mechanics of traumatic spinal cord injuries vary with injury type. Dislocation, flexion-distraction and burst fracture account for 75% of all traumatic injuries; these are associated with lateral translation, tension and compression respectively (Sekhon and Fehlings, 2001; LaPlaca et al., 2007). In burst fractures, vertebral bone fragments are displaced into the vertebral canal at velocities of between 1 and 4.5 m.s^{-1} (Wilcox et al., 2003). Clinically, the severity of traumatic injuries, in particular car crashes, depends on the velocity and energy transferred to the spinal cord (Smith et al., 2005). For instance, people in vehicles colliding with fixed objects had a greater risk of severe spinal cord injury (Bilston et al., 2011); as did those not wearing a seatbelt (Funk et al., 2012). This highlights the importance of and interaction between velocity, force and energy in outcomes of spinal cord injury.

NTSCI involves increasing compression of the spinal cord over an extended period of time. The two major causes, degenerative disease and neoplasms, will be discussed further. It is worth noting that neoplasms also have the potential to cause a burst tissue fracture (Whyne et al., 2003; Tschirhart et al., 2004). Degenerative disease, known as spondylosis, stenosis or myelopathy, can occur at any level but cervical spondylotic myelopathy and lumbar stenosis are major causes of NTSCI (Kalsi-Ryan et al., 2013). The diseases begin in the spinal discs, with the central gel-like nucleus pulposus losing its water drawing capacity and becoming increasingly stiff (Roughley et al., 2006; Ferrara, 2012). This means intradiscal pressure and disc height are reduced, and the disc begins to herniate dorsally into the vertebral canal. Further, the reduced load-bearing capacity of the disc causes impairment of the dorsal ligamentous complex which, in turn, increases load on vertebral endplates (Baptiste and Fehlings, 2006; Ferrara, 2012; Tetreault et al., 2015). In response to this, osteophytes can grow from the ventral vertebral body into the vertebral canal which further impinge the cord. These changes are exacerbated over time and compression of the cord continues. As an example, one study found that cervical

spondylotic myelopathy can cause a reduction in cervical canal diameter of 3.03 ± 0.99 mm (Jiang et al., 2016). It is worth noting that these causes of injury (osteophytes and disc degeneration) compress the cord from the ventral aspect, and predominantly cause flattening and indentation; both direct compression without shear components (Martin et al., 2018). The time frame or velocity, and pressure or load, exerted onto the spinal cord in these injuries had not been quantified in the literature. If the timeframe were to be estimated, this would be between weeks for an infection, up to months for a cancer, and years for bone spurs.

A total of 70% of neoplasms in the spine affect the thoracic region, with metastases arising from the ventral vertebral body (Klimo and Schmidt, 2004). In these tumours, cancer cells multiply and form a tumour which can grow into the foramen and thus compress the spinal cord. Similarly to spondylosis or myelopathy, these tumours compress the cord from the ventral aspect. Alternatively, metastases can cause fractures to the vertebral body, resulting in TSCI, although the frequency of this is not fully understood (Hamimi et al., 2015). Biomechanical-induced NTSCI causes increasing displacement of the spinal cord, which in turn causes symptomatic onset. Further research is required to establish the importance of factors such as velocity and displacement in non-traumatic spinal cord injury; and the response of neuronal or glial cells in isolation compared with a whole-system.

1.4 Experimental Modelling of Spinal Cord Injury

Experimental models can be used to investigate spinal cord injury; including improving understanding of pathophysiology. Spinal cord injury models have been developed using both *in-vivo* and *in-vitro* methods; the utilities and drawbacks of each of these will be further discussed.

1.4.1   Modelling Spinal Cord Injury *in-vivo*

In-vivo models recapitulate the complex architecture of the spinal cord and allow it to be evaluated in the context of other biological tissues and systems, and with greater detail than would be possible in human studies. Animal experiments allow recordings before, during and after the injury process by terminating animal at various timepoints. This detail of baseline, injury pathology, and recovery is not feasible clinically. Further, the injury process can be controlled and measured in order to minimise variation.

Rats are widely used in spinal cord injury studies. They have reduced ethical constraints, are well understood, easy to handle, relatively low cost, small enough to house in substantial numbers, and of sufficient size to undertake spinal cord surgery without specialist equipment (Talac et al., 2004; Zhang et al., 2014). Rat models of traumatic spinal cord injury have shown a pathological cascade involving initial haemorrhage and subsequent scar formation, similar to that of humans (Kjell and Olson, 2016). All animal models come with limitations and restrictions. Across animal research, adherence to the '3R' principles motivates researchers to use fewer animals wherever possible (Russell and Burch, 1992). Nevertheless, *in-vivo* rat models remain essential in studying complex pathologies using a whole system approach.

There are anatomical differences between humans and rats which have the capacity to alter outcomes of spinal cord injury. The rat spinal cord is approximately 3.5 mm in diameter; compared with 12.5 mm for a human spinal cord (Watson et al., 2009). This means functional recovery following injury is more likely in rats since axons have a reduced distance to grow and therefore neural networks can be more easily re-established (Kjell and Olson, 2016). Furthermore, the locations, size, and relative importance of ascending and descending tracts are different in humans and rats (Figure 1.4 compared with Figure 1.3 in section 1.2). In humans, the major corticospinal bundle is in the lateral column while in rodents it is in the ventral part of the dorsal funiculus. The corticospinal tract is responsible for voluntary skilled movements (Silva et al., 2014).

In man, the corticospinal tract has evolved for extensive fine control of distal muscles; and some fibres synapse directly onto motor neurons. Rats do not have such sensitive digital control, and the corticospinal tract projects onto interneurons in the grey matter (Watson et al., 2009). In rats the reticulospinal tract and spinothalamic tract are closest to the ventral median fissure. The reticulospinal tract has large numbers of connections to interneurons and propriospinal neurons in rats (Mitchell et al., 2016). The tract initiates motion and is responsible for postural control and left right motor activity in rats. In rats, the spinothalamic tract, in the ventral funiculus, transmits crude touch and pressure (Sengul and Watson, 2015).

Ascending (sensory) tracts | **Descending (motor) tracts**

Ascending (sensory) tracts
- Dorsal column medial lemniscus
- Spinothalamic
- Spinocereballar

Descending (motor) tracts
- Raphespinal
- Corticospinal
- Rubrospinal
- Reticulospinal
- Vestibulospinal
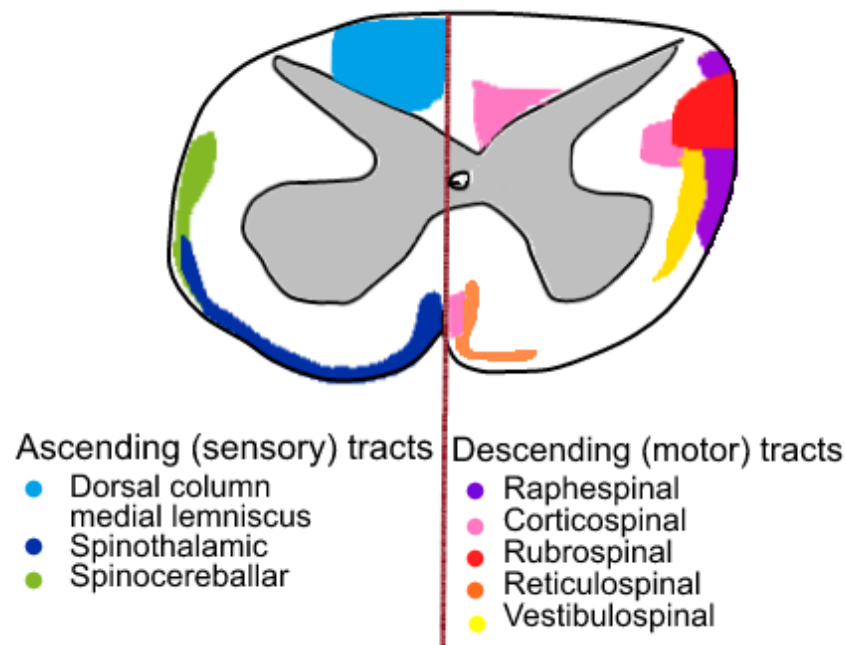
Figure 1.4: **Rat spinal cord cross-section showing grey and white matter, with position of ascending and descending tracts** *Grey matter forms a central butterfly-like shape; white matter surrounds this and contains tracts. Ascending tracts (on the left of the diagram) transmit sensory information from effectors to other parts of the central nervous system. Motor tracts (right of the diagram) transmit motor information from the brain to caudal parts of the nervous system. Image adapted from (Watson et al., 2009)*

1.4.1.1 Inducing Non-Traumatic Spinal Cord Injury *In-vivo*

To accurately recapitulate the types of injuries experienced by humans in animal models is challenging for several reasons; summarised in Table 1.3. Clinical injuries are caused by a series of internal pathological events; whereas the injury in animal models is induced by external mediators. Furthermore, the clinical time frame of NTSCI is in the range of months to years, and extended beyond the lifespan of a rat. Therefore, time frames must be scaled down to suit the model. Across models of NTSCI, the temporal profile is a key factor which should be represented. The three stages of injury progression are initial stenosis of the canal with no symptoms (a latent period), followed by increased stenosis and symptom onset, followed an increase in symptom severity (functional degeneration) (Kim et al., 2004). The parameters most pertinent to this study are the biomechanics to induce injury, and methods to measure outcomes.

Factors which must be considered in developing an *in-vivo* model of NTSCI include:

- Capacity to control the insult i.e. control the degree of stenosis during the study

- Capacity to measure the insult i.e. measure the degree of stenosis either during or after the study

- As minimally invasive as possible to prevent disruption to spinal stability

- In keeping with time scale of the project

- From the ventral aspect to mimic clinical NTSCI injuries

- Allow decompression

- Replicate temporal profile (i.e. not in the range of milliseconds).

This last factor of timescale is core to modelling NTSCI as opposed to TSCI. All the other factors would be relevant for both NTSCI and TSCI.

Table 1.3: **The ideal animal model of non-traumatic spinal cord injury.** *In-vivo modelling of spinal cord injury of traumatic origin is well established. However to accurately model non-traumatic injuries, and their subsequent stabilisation, further considerations must be taken into account and measured.*

Factor	Details	Confounding potential	Control or measurement	Reference(s)
Injury level	Clinically, most NTSCI occurs at thoracic or lumbar levels. Surgically, consider surrounding tissues	Injury level in-vivo directly affects outcome measures. High risk at cervical and lumbar levels due to increased vascular density	Injure at the lower thoracic level on all animals to be clinically relevant, aid outcome measure and preclude risk	(Tveten, 1976; McKinley et al., 1999)
Surgical approach for inducing pathology	Clinically, surgery does not cause NTSCI and most lesions are from ventral vertebral body. Surgically, minimise surrounding tissue damage.	Different approach will cause different symptoms due to anatomical asymmetry of the spinal cord. A dorsal approach and laminectomy is technically easier in surgery and minimises tissue damage.	Ideally injure using a ventral method, but accessing the injury site dorsally. Use sham procedure and healthy control groups to ensure the surgery itself is not confounding results.	See text in this section for further details.
Extent of injury	Clinically, injuries are incomplete, and symptoms occur with stenosis greater than 22 to 25% vertebral canal cross-sectional area.	Differing extent of injury will directly affect symptoms and outcomes of animal model	Vertebral canal stenosis should be the same extent in all animals. Maximum canal stenosis should be less than 100%. Measure where possible (MRI/CT imaging)	(Teresi et al., 1987; Dimar et al., 1999; Nakashima et al., 2016; Sun et al., 2016)
Injury timescale	Clinically, NTSCI take place over months to years. Surgically, must consider the time/cost requirements in relation to the research project.	A fast injury would induce traumatic spinal cord injury; which has a different pathological cascade to non-traumatic injuries.	10 years in a human is approximately equivalent to 2 weeks, 1 year in a human is equivalent to 1.5 days. Therefore, the timescale of the injury should be greater than 1.5 days in a rat.	(Quinn, 2005; ?)

The ideal animal model of non-traumatic spinal cord injury continued.

Factor	Details	Confounding potential	Control or measurement	Reference(s)
Method for inducing injury	Should recapitulate clinical temporal profile of injury, and symptoms. Surgically, lesion should be closed (i.e. no laminectomy at lesion site itself)	Non clinically-relevant paradigm will not cause a relevant NTSCI; so subsequent investigations will not be valid	Develop a method using a closed lesion site. Ex-vivo characterisation of method prior to use in animals. Then, able to correlate compression with functional deficits.	See text in this section and Table 1.4
Decomp-ression	Clinically, decompression is the main treatment for NTSCI. Surgically, must be able to remove the cause of compression without causing further damage	Must be able to remove cause of compression easily and prevent further damage to surrounding tissues	Develop a method where decompression is facilitated. Compare injured and sham operated/control groups	None found. No studies have undertaken decompression.
Physiological outcomes	Outcomes must be relevant to clinical non-traumatic injury	Poor measurement of outcomes will prevent valid conclusions being drawn about effects of injury/intervention	Behavioural methods (BBB/locomotor analysis), electrophysiology, imaging, ex-vivo outcomes	(Kwon et al., 2002; Sharif-Alhoseini and Rahimi-Movaghar, 2014)

Several methods have been developed for inducing NTSCI *in-vivo*. The most basic involves implanting a material into the vertebral canal; however this does not replicate the unique temporal profile of NTSCI (Sekiguchi et al., 2004; Ito et al., 2007; Karadimas et al., 2013). One method which replicates the temporal profile is a screw-tightening model, wherein a device is implanted that can manually compress the cord with each screw turn; but this method is highly invasive (Xu et al., 2008; Lee et al., 2012; Sun et al., 2016). A further, less invasive model involves using a wire to surround the spinal cord of a juvenile rat. As the rat grows, the cord compresses (Iwamoto et al., 1995; Kubota et al., 2011). The cord is compressed in all directions, whereas clinically in NTSCI compression is from the ventral aspect alone. Further, this method has a time frame of 9 months for each rat, so is not suitable for use in the present study. Finally, the model of injury must allow decompression for future research into interventions. Injection of cancer cells to form metastatic lesions has been used to induce NTSCI in previous *in-vivo* models; but this method has a lack of control of stenosis, and the process of decompression is highly complex (Hojjat et al., 2012; Zibly et al., 2012). The remaining two methods in the literature have the potential to be minimally invasive, with increasing compression, a relevant temporal timescale, and allow decompression. These are an expanding material; or an implanted balloon catheter (Table 1.4).

It is worth noting that the balloon catheter method has only been used to induce traumatic injuries (i.e. expand fully immediately upon insertion, followed by removal before suturing). This method could be adapted by implanting the balloon catheter in the vertebral canal, and inflating it slowly over an extended time period relevant to NTSCI. Clinically, NTSCI occurs ventrally (see section 1.3.2), whereas all models used for NTSCI have introduced the injury from the dorsal aspect or by compression the entire cord.

Table 1.4: ***Previous balloon catheter or expanding material in-vivo models of spinal cord injury.*** *Expanding material models induced NTSCI (increase in area over an extended duration); whereas balloon catheter models caused TSCI (increase in area during surgery, and immediately decompress). All of these models used a dorsal approach. CSA: cross-sectional area.*

Reference	Method	Model	Size/volume changes	Timeframe
(Kim et al., 2004)	Aquaprene material	Rat C5-6	Initially 3 x 5 x 0.7 mm.	Volume increased by 24% in 24 hours
(Kurokawa et al., 2011)		Rat, C5-6	Initially 3 x 5 x 0.7 mm.	Not described
(Hu et al., 2011)	Agarose gel polymer, dried and coated with polyurethane membrane with laser-cut microholes	Rat, Cervical	Size described as 'thin'.	Maximum expansion in 24 hrs
(Long et al., 2013)		Rat, C5-6	1 x 3 x 1 mm; max. expansion (7x) volume in 2 or 24 hr	Changes not reported
(Xu et al., 2017)		Rat, C5-6	Not described	Not described
(Yang et al., 2015)	Polymer network 1:1 polyvinyl alcohol and polyacrylamide	Rat T8-9	Initially 2.5 x 2.0 x 0.8mm to 3.5 x 3.0 x 2.4mm	Not described
(Fonseca et al., 2016)	Expanding balloon (4F fogarty catheter)	Rabbit	Inflated with 1000 μL air	Inflated rapidly, left for ten minutes, then removed
(Vanicky et al., 2001)	Expanding balloon (2F fogarty catheter)	Rat, T8-9	Inflated with 10 to 20 μL of saline	Inflated rapidly, left for five minutes, then removed
(Lonjon et al., 2010)		Rat, T8-9	Inflated with 10 or 15 μL of water	Inflated rapidly, then removed
(Pedram et al., 2010)		Rat, T8-9	Inflated with 20 μL of water	Inflated rapidly, left for five minutes, then removed
(Chung et al., 2013)		Rat, T9	Inflated with 20 to 50 μL of saline	Inflated rapidly, left for ten minutes, then removed
(Su et al., 2015)		Rat, T7	Inflated with 200 μL air	Inflated rapidly, left for ten minutes, then removed

The direction of injury (ventral or dorsal) is important, since the spatial distribution and relative importance of white matter tracts varies in humans and rats (Figure 1.4 in section 1.4.1 compared with Figure 1.3 in section 1.2). In humans, bilateral corticospinal tract lesions greatly impact walking, and cortical activity via the corticospinal tract is

vital for walking in humans. This has been determined by studying patients undergoing cordotomies for pain relief in cancer, and using electroencephalogy in healthy humans (Nathan, 1994; Petersen et al., 2012). In rats, the dorso-lateral rubrospinal tract and corticospinal tract are both important for gait, spinal cord function, and injury modelling (Morris and Whishaw, 2016) (Figure 1.5). Grill et al. (1997) compared the effects of damaging the dorsal corticospinal tract in rats versus dorsal hemisection (damaging corticospinal and rubrospinal tracts). Animals with a dorsal hemisection had persistent deficits in sensorimotor skills, whereas those with corticospinal tract damage alone did not.

Dorsal hemisection
Damages corticospinal and rubrospinal tracts

Right sided hemisection
Damages one side corticospinal, rubrospinal and reticulospinal tracts

Ventral hemisection
Damages reticulospinal tracts

Ventro-lateral funiculus damage
Reticulospinal tracts

Dorso-lateral funiculus damage
Damages rubrospinal tracts

Dorsal corticospinal tract
Damages corticospinal tract only

*Figure 1.5: **Tracts injured in various rat spinal cord injury models.***

Control of gait and locomotion in rats is further complicated since dorsal hemisection injuries (which would damage both dorsal corticospinal and rubrospinal tracts) produce

different outcomes to injuries where ventral tracts are also damaged (Agrawal et al., 2010). A study by Metz et al. (2000) compared a dorsal hemisection to a contusion model using the New York University impactor in rats. Animals with a contusion had histological damage to the ventral and dorsal tracts, and had a reduced open field locomotor score for two weeks post-injury compared with dorsal hemisection alone. Where lesions to the lateral and ventral spinal tract were performed and compared in rats, the strongest correlations to locomotor score were in lesion depth and spared white tissue matter in the ventral reticulospinal tract (Schucht et al., 2002). Further, reticulospinal tract neurons showed an increased propensity to sprout fibres in a cervical hemisection injury, and are involved in propriospinal plasticity following injury (Filli et al., 2014). In another study, at T10, lesions to the ventral funiculus were produced in isolation and in combination with dorsal funiculus lesions, both at T10 (Loy et al., 2002). At 4 weeks post-lesion, animals with lesions to both dorsal and ventral components had significantly reduced open field locomotor scores compared with either dorsal or ventral lesions. This indicates locomotion in rats has dorsal and ventral white matter components. The role of white matter tracts in locomotion are complex, and tracts in both the dorsal and ventral spinal cord have a role. All of the studies described evaluating tract contribution to locomotion in spinal cord injury have used TSCI methods (transection or contusion), none have used NTSCI models.

The expanding materials used in NTSCI studies are either not commercially available in the UK (Aquaprene) or have a complex manufacturing process which are not suitable for this study. However, other commercially available materials which absorb water may be used (Figure 1.6).

Cellulose sponges absorb up to 50% of their volume in water at equilibrium, but absorb water rapidly (Goodfellow, 2017). Conversely, nylon 6 absorbs 2.7% water isotropically over 24 hours; with equilibrium being reached at 8 to 10% (Baschek et al., 1999; Gerbig, 2014; Goodfellow, 2017). Nylon 6 is sold in membranes; so one approach may be to encase a cellulose sponge in nylon film. The outer membrane will allow slow

Cellulose sponge surrounded by Nylon 6,6 membrane	Freeze dried rat type I collagen hydrogel sponge	Balloon catheter attached to pump or port
+ Overcome issues with water absorption in materials separately + Commercially available components - Difficult to manufacture - Uncontrollable expansion - Unknown timescale	+ No immune response (biologic, same species) - Uncontrollable expansion - Unknown timescale, likely to be up to 24 hours - Not directly commercially available - Collagen could cause cellular infiltration	+ Controlled filling volume + Balloon component used frequently in TSCI + Commercially available components + Adaptable timescale based on pump or port - Not previously attempted for NTSCI with pump/port

*Figure 1.6: **Potential methods for inducing non-traumatic spinal cord injury in-vivo.** These include water-absorbing materials which swell in volume over time, or using a balloon catheter with osmotic mini-pump. All three methods can be easily sterilised, or are supplied sterile. All will require characterisation ex-vivo prior to the use in animal experiments. Research collaborations exist between the research group at the University of Leeds where the model of NTSCI was being developed, and the relevant research group who have developed the balloon catheter model for TSCI.*

water penetration; and the cellulose sponge will increase in volume. Collagen hydrogels also absorb water. This occurs upon their initial creation (Ahmed, 2015). They can also be freeze dried to form sponges which can then be implanted and absorb water *in-vivo*. This sponge can be made of rat type I collagen, meaning it would be biocompatible *in-vivo*; this is important to prevent a host immune response. However, its absorption mechanics require further evaluation.

A third method is to use a 2F balloon catheter which expands slowly over time. This could be achieved through attachment to an osmotic mini pump or port for repeat injections (Figure 1.6). Balloon catheters have been used to induce traumatic spinal cord injuries (Vanicky et al., 2001; Lonjon et al., 2010; Pedram et al., 2010; Chung et al., 2013; Su et al., 2015); and osmotic mini pumps have been used to apply drugs within the spinal cord (Maier et al., 2009); the two components have not been used for filling a balloon

catheter to induce spinal cord injury. Using either the osmotic pump or injection port has advantages since the volume filling the balloon can be controlled, and balloon expansion can be characterised ex-vivo initially. When implanted *in-vivo*, the measurements of the balloon would be understood, and functional deficits could be measured. This would facilitate correlation between balloon expansion (i.e. cord compression) and functional deficits. Balloon catheter insertion into the vertebral canal can be undertaken using a laminotomy or partial laminectomy at just one spinal level (Vanicky et al., 2001). One research group have developed a method to insert the balloon catheter to form a ventral lesion, although this is yet to be published (Urdzikova and Kwok, 2019). This is noteworthy since all previous studies have only used dorsal lesions.

1.4.1.2 The Effects of Injury Mechanics in Spinal Cord Injury *in-vivo*

Various *in-vivo* spinal cord injury studies have been carried out with control of either displacement, force or speed. In rats, two studies have carried out compression at T10 (Scheff et al., 2003; Sparrey et al., 2008). In the study undertaken by Sparrey et al. (2008), the speed of the injury was either 3 or 3000 mm.s^{-1}; with a displacement of 1mm in both cases. At two minutes after injury, the fast lesion model had a greater haemorrhage volume in the white matter, and greater axonal damage ($p<0.05$). It is worth noting that the recorded force also varied between groups; with 0.54N being applied at 3 mm.s^{-1}, and 2.37 N at 3000 mm.s^{-1}. Another study applied force-controlled injuries at 1, 1.5 and 2 N with a controlled speed of 130 mm.s $^{-1}$ (Scheff et al., 2003). Increasing force correlated with reduced locomotor activity and loss of grey and white matter at 7 and 42 days post-injury. However, the displacement extent also varied with force; from between 0.8 mm to 1.2 mm.

A further rat contusion study, with injury at C6, evaluated the effects of both speeds and displacement (Lam et al., 2014). Comparing impact speeds of 8, 80 and 800 mm.s^{-1} and displacements of 0.9 and 1.5 mm; the greater displacement caused greater functional deficits and nerve fibre damage across all speeds. This could indicate that displacement

extent is more important than speed in determining injury outcome; however force also differed across groups.

In a non-human primate contusion model using a speed of 1000 mm.s^{-1} and two displacement parameters, displacement and force correlated with paralysis and lesion volume (Salegio et al., 2016).

Some studies describe displacement extent as the predominant factor determining injury severity (Anderson, 1982; Bresnahan et al., 1991; Behrmann et al., 1992; Pearse et al., 2005; Maikos et al., 2008), and report no effect of changing velocity (Kearney et al., 1988; Kwo et al., 1989; Kim et al., 2009). Whereas others state velocity is the most important (Anderson, 1985). It is likely that a combination of these factors is important (Dohrmann and Panjabi, 1976; Noyes, 1987; Black et al., 1988; Basso et al., 1996; Jakeman et al., 2000; Seki et al., 2002; Lam, 2013; Lam et al., 2014). Work done is not frequently reported in these studies; but should be considered as it incorporates both displacement and load, and reflects the energy imparted onto the system. There is a need to characterise the effect of mechanical parameters in isolation, which is nigh on impossible *in-vivo*. Further, all of these studies have used traumatic spinal cord injuries and no studies have carried out experiments at speeds under 1 mm.s^{-1}.

1.4.2 Modelling Spinal Cord Injury *in-vitro*

In-vitro models allow evaluation of cellular responses in a controlled environment. Using these models also helps implement the 3Rs (replacement, reduction, refinement), by reducing animal numbers (Fenwick et al., 2009). *In-vitro* models allow greater control of isolated parameters and assessment of their individual effects which would not be possible *in-vivo*. For example, the effects of varying strain rate on individual cell populations can be established. *In-vitro* cell culture systems can either be 2D or 3D, and comprise varying matrices (Table 1.5). Systems which are 3D are more physiologically relevant; since the presence of a 3D matrix influences cellular behaviour, cell-cell and cell-matrix interactions in keeping with physiological conditions (Abu-Rub et al., 2010).

Table 1.5: **In-vitro models of the spinal cord using 2D and 3D methods.** *Cells previously used in such models include astrocytes, dorsal root ganglion cells, neural crest stem cells and mesenchymal stem cells (East et al., 2010, 2012, 2013)*

	2D cellular model	**3D organotypic slice culture**	**3D hydrogel model**	**3D synthetic model**
Diagram				
Type of model	• Monolayer of cells on a functionalised surface	• Approx. 350 μm thick slices of animal spinal cord	• Natural peptide hydrogel (e.g. collagen) seeded with cells	• Synthetic material (e.g. polycapro-lactone) seeded with cells
Pros	• Simple • Low cost	• Cells within 3D environment • Have been used to mimic lesion injury	• Cell adhesion motifs retained • Cells within 3D environment • Have been used to mimic injury and gliosis	• Modification of chemical/ physical properties
Cons	• No mechanical cues from matrix, or cell-matrix interactions • Cannot induce mechanical insult	• Must be <500 μm thick • No control of cells or matrix • Needs animals • Inherent damage during preparation	• Cannot easily tailor mechanical properties • Does not replicate all areas of the cord (grey/white matter)	• Increased complexity/cost • Cell adhesion motifs not inherent • Does not replicate all areas of the cord
References	(Hopkins et al., 2015)	(Abu-Rub et al., 2010)	(East et al., 2010; Phillips, 2014b; Caliari and Burdick, 2016)	(Schaub et al., 2016)

A 3D organotypic slice model is the most physiologically relevant 3D milieu, since it contains adhesion motifs and represents the tissue-level architecture of the spinal cord. Rat and mouse spinal cord slices 350 μm in thickness have been used

to study spinal cord injury responses, by transecting the slices directly using a scalpel (Bonnici and Kapfhammer, 2008; Weightman et al., 2014). In these studies, astrocytes became increasingly reactive at lesion margins, microglia infiltrated the lesion site, and neuronal axon regeneration across the lesion site could be measured. A further study using transection of rat spinal cord slices used electrophysiology readings to investigate functional regeneration (Heidemann et al., 2015). Similarly, weight drop devices have been used in rat spinal cord slices to simulate spinal cord injury, resulting in cell death and TNF-alpha expression (Pandamooz et al., 2019). Lesioned slices have been used to evaluate the efficacy and regenerative capacity of synthetic scaffold bridges, valproic acid, and a novel peroxisome proliferator-activated receptor agonist (Esposito et al., 2012; Weightman et al., 2014; Pandamooz et al., 2019).

There are difficulties in preparation and maintenance of organotypic spinal cord slice cultures, such as damage induced during slicing and death of slices after a week in culture (Sypecka et al., 2015). It is difficult to evaluate the effects of spinal cord injury on a single cell population in isolation using spinal cord slices. For instance, slices contain a heterogenous distribution of neurones and glia. Further, the matrix is also heterogenous, containing white and grey matter, the proportions of which differ based on spinal level. To fully understand the impact of an injury on one cell type, all cell types and matrix components should be controlled, and the same for every test undertaken.

In terms of materials, a 3D collagen hydrogel model has been shown to be compatible with various cell types, with primary neural cells able to retain their phenotype through the inherent presence of adhesion motifs (East et al., 2010, 2012, 2013). Such motifs are not present in synthetic materials. Mechanical compression has been applied to simple geometry, disc shaped collagen hydrogels *in-vitro* with neural cells to model traumatic brain injury (Bar-Kochba et al., 2016). Tethered collagen hydrogels models have also previously been used in spinal cord injury studies (East et al., 2010; Phillips, 2014a; Smith, 2016). Collagen hydrogels have further advantages in evaluating matrix remodelling; their composition of a single material means deposition of new matrix and

other proteins can be easily studied.

1.4.2.1   Inducing Spinal Cord Injury *in-vitro*

Methods used to induce cellular phenotypic changes observed in spinal cord injury *in-vitro* include changing the chemical environment; such as hypoxic conditions and adding moieties, or through causing a mechanical insult (Table 1.6). The biochemical pathways and cytokines involved in NTSCI are not established in the literature. As such, chemical induction of NTSCI is not possible based on current knowledge and understanding.

Of the methods used for inducing a mechanical injury to the spinal cord *in-vitro*, only three are appropriate for applying a controlled mechanical insult to a 3D hydrogel model to simulate spinal cord injury: using increasing pressure in pulsatile flow system, using a microfluidic platform, and using a mechanical device such as the Infinite Horizon impactor or BOSE 5110 Electroforce bioreactor. There are three factors which further determine the suitability of each of these methods for the study of NTSCI. The first is availability of the apparatus, materials testing machines have the capacity to be adapted for applying mechanical insults *in-vitro*, BOSE manufactured devices have been used in spinal cord injury studies (Busby et al., 2013; Koivisto et al., 2017; Kirk, 2018). The second factor is the mechanics and relevance to clinical injuries: one key feature distinguishing TSCI and NTSCI are velocity, with TSCI being in the range of metres per second (Wilcox et al., 2003), whereas NTSCI taking between months to years. So, any device needs to apply both high and low velocities. *In-vivo* impactors have a maximum velocity of 0.333 mm.s^{-1}, whereas materials testing machines use a range of velocities (Stokes, 1992; Scheff et al., 2003; TAInstruments, 2016). The third factor is the capacity to perform long-term studies simulating NTSCI under sterile conditions. The BOSE 5110 Electroforce fits this purpose as it has a bioreactor system, which can be sterilised (TAInstruments, 2016; Kirk, 2018).

Table 1.6: **Methods used to induce spinal cord injury in-vitro.** *Several methods have been used to simulate spinal cord injury in-vitro. Each of those detailed in the table have associated advantages and disadvantages. It is worth noting that none have specifically used a biomechanical insult to induce non-traumatic spinal cord injury (NTSCI)*

Injury induction	Advantages	Disadvantages	Reference(s)
Chemical moieties (kainite, transforming growth factor β)	• Induce glutamatergic excitotoxicity • Scar-like cascade in astrocytes	• Does not recapitulate mechanics • Excitotoxicity not established in NTSCI	(East et al., 2009; Shabbir et al., 2015a,b; Vogelaar et al., 2015; Kaur et al., 2016; Samano et al., 2016)
Ischaemia: reducing amount of O_2 in media or environment	• Better replicates ischaemia of NTSCI	• Does not recapitulate mechanics • Ischaemia in NTSCI not fully understood	(Oliveira et al., 2014; Samano et al., 2016)
Ex-vivo injury induction (via scalpel blades or weight drop device) on healthy spinal cord slices	• Use mechanical insult	• Not used in NTSCI • Requires use of whole animals • Disadvantages of slice model method	(Bonnici and Kapfhammer, 2008; Esposito et al., 2012; Weightman et al., 2014; Sypecka et al., 2015; Pandamooz et al., 2019)
Polymer (mimicking spinal cord) in a fluid under pulsatile flow and increasing pressure	• Does not require animals • Increasing fluid pressure could mimic stenosis	• Complex systems. • Have not been used in long-term experiments	(Frieboes and Gupta, 2009)
Dual layer system: microfliuidic channels atop cell-seeded platform	• Single axon studies (20μm diameter) can be carried out	• Complex set up • Have not been used in NTSCI	(Hosmane et al., 2011; Fournier et al., 2015)

Methods used to induce spinal cord injury in-vitro continued.

Injury induction	Advantages	Disadvantages	Reference(s)
Compression of model using impaction system	• Long term compression • Control conditions (mechanics and environment)	• Require characterisation of force and loads • Not established in current literature	(Butler et al., 2009; TAInstruments, 2016)

1.4.2.2   The Effects of Injury Mechanics in Spinal Cord Injury *in-vitro*

In-vitro studies evaluating neural cell responses to varying mechanical parameters focus on traumatic brain injuries. These have key differences to NTSCI in terms of the type of strain (shear strain as opposed to compression in NTSCI); and strain rates (up to $30.s^{-1}$ compared with quasi-static in NTSCI). However, the 3D environments and types of cells are similar in both conditions.

Through applying varying strain rates to neurones and astrocytes in culture, several observations and potential mechanisms for cellular damage have been established. Cullen et al. (2007) evaluated the effect of shear strain on primary neurons and astrocytes in 3D gel environments. Strain rates of $1\ s^{-1}$, $10\ s^{-1}$ and $30\ s^{-1}$, with a maximum strain of 0.5, were applied. The strain rate of $30\ s^{-1}$ caused significantly more cell death than lower rates ($p<0.05$), and induced GFAP expression at 2 days post-injury. In the lower strain rate groups, cell density was increased. The lowest strain rate of $1\ s^{-1}$ caused expression of chondroitin-sulphate proteoglycan; a molecule associated with glial scar formation.

A similar study evaluating isolated neuronal populations found increased cell death at $30\ s^{-1}$ compared with $20\ s^{-1}$; with a controlled maximum strain of 0.5 (Cullen and LaPlaca, 2006). Across various studies, shear strain rate has been shown to induce changes in cellular permability (Cullen et al., 2011) and intracellular calcium release via NMDA receptors (Cargill and Thibault, 1996; LaPlaca et al., 1997; LaPlaca and Thibault, 1998; Maneshi et al., 2015, 2017, 2018). Applying tension to neural cells caused rate-dependent neuronal matrix re-organisation (Zhang et al., 2016) and astrocyte swelling due

to aquaporin 4 over-expression (Sturdivant et al., 2016). One study assessed the effects of compression, applying strain rates of 10 s^{-1} and 75 s^{-1} up to a strain of 0.30 (Bar-Kochba et al., 2016) to neurons. After 10 hours, neurons under both strain rates showed pathophysiological features including dendrite thinning at 10 s^{-1} and bleb formation at 75 s^{-1}; associating with membrane permeability and cell death.

Although the pathological context and strain rates are different to NTSCI, *in-vitro* brain injury models have identified that neural cell responses vary with strain rate, and have elucidated potential pathological mechanisms. This research provides the hypothesis that in NTSCI, varying the magnitude and rate of compressive strain will cause different responses in neural cell populations. The effects of changing displacement extent, force, and overall energy applied to an NTSCI model system are unknown, and need to be established.

1.5 Summary and Research Objectives

1.5.1 Summary

Clinical NTSCI has a variety of causes, most of which are associated with an ageing population. As such, these injuries are increasing in prevalence due to the changing demographics of society. In spite of this, the pathophysiological origins of NTSCI are not fully understood. This means developing or evaluating new treatments or management techniques is challenging. Furthermore, mechanics vary in both traumatic and non-traumatic injuries; but the effect of this is unknown. Due to the heterogeneity of NTSCI, and the relatively low patient numbers, clinical studies are difficult.

Experimental studies can be undertaken to evaluate the pathology of spinal cord injuries under various injury mechanics protocols. To achieve this, models must first be developed, characterised and evaluated. Previous rat models of NTSCI *in-vivo* have limitations, including timescales of over 6 months and an invasive nature. A balloon catheter model, with gradual inflation, can mimic NTSCI clinically whilst being

minimally invasive. Furthermore, simplified *in-vitro* models of the spinal cord have been established and will be used to evaluate cellular responses to injury-like scenarios. The use of a collagen hydrogel system seeded with primary neural cells ensure a mechanically relevant 3D environment initially. Subsequently, mechanical insults will be applied to the system using the BOSE 5110 bioreactor system. This allows control of force, displacement, and speed. Hence, energy can be calculated. Cellular outcomes will be established in injury scenarios with varying energy transfer.

1.5.2 Aims

The aim of this project is to evaluate biological responses to loading scenarios representative of NTSCI both *in-vitro* and *in-vivo*.

1. *In-vitro* model

    A - To develop methodology to apply displacements and forces (of varying extent and speed) relevant to non-traumatic spinal cord injury *in-vitro*.

    B - Develop and characterise a reproducible type I collagen hydrogel seeded with primary rat astrocytes, a relevant neural cell type.

    C - To evaluate the effects of clinically relevant displacement and speeds on neural cell outcomes; with a focus on astrocytes (including GFAP expression and cytokine release).

2. *In-vivo* model

    D - To develop a clinically-relevant model of non-traumatic spinal cord injury *in-vivo*; with increasing canal stenosis over an extended time frame (i.e. days) and using a ventral lesion.

    E - To assess the histological and functional outcomes which occur after long term spinal cord compression *in-vivo*.

Chapter 2

Materials and Methods

2.1   General Materials and Equipment

Details of consumable materials, equipment and reagents/chemicals used are in appendices A, B and C, respectively.

The use of the materials and methods described herein can be split into those associated with the *in-vitro* models, and those for the *in-vivo* models. *In-vitro* models will comprise astrocyte-seeded collagen hydrogels compressed by the BOSE Electroforce 5110 Biodynamic. Both the cell system and mechanical device require characterisation. Then, astrocyte outcomes will be established in control and pathological conditions, as well as after compression at various velocities. *In-vivo* a model will be developed using a modified balloon catheter, which can be implanted into rats, in order to induce a slow, graded spinal cord compression. Histological and functional outcomes will be determined.

2.2 General Methods

2.2.1 Sterilisation and Disinfection of Equipment

2.2.1.1 Class II Biological Safety Cabinet Disinfection

Cell culture was carried out using aseptic technique in a class II biological safety cabinet. Before use, fans were engaged to ensure HEPA filtered air flow. The interior of the cabinet was sprayed with 1% (w/v) Virkon, followed by 70% (v/v) ethanol. Any materials placed into the cabinet were also sprayed liberally with 70% (v/v) ethanol. While undertaking work, gloves were worn and samples were covered wherever possible. Furthermore, solutions opened within the cabinet were sterilised before use.

2.2.1.2 Sterilisation and Disinfection Methods

Autoclave (moist heat) sterilisation was used to sterilise solutions and materials wherever appropriate. This incorporated heating at 15 psi, 121°C for twenty minutes.

Filtration was used to sterilise solutions in a class II biological safety cabinet. The solution was added to a 10 mL syringe and dispensed through a 0.22 μm filter. Materials not suitable for autoclave or filtration (such as tubing, reservoir bottles, plastic components of the BOSE 5110 Electroforce apparatus) were sterilised by soaking in 1% (v/v) Trigene solution for at least 30 minutes. Before use, they were washed in sterile water.

Surgical tools used *in-vivo* were sterilised prior to surgery using dry heat sterilisation at 190°C in an oven for 4 hours. Between animals, tools were washed using soap and hot water, rinsed and left to dry. Then, tools were further sterilised using a hot glass bead steriliser. Instruments were placed in the steriliser at 300°C for 1 minute. Tools were then placed into 100% (v/v) ethanol before being allowed to air dry.

Coverslips and dissection equipment used *in-vitro* were sterilised prior to use by soaking in 70% (v/v) ethanol for at least 3 minutes, before air drying at room temperature

in a sterile biological safety cabinet.

2.2.2   pH Measurement

Measurement of pH was undertaken using a Jenway 3510 pH meter. Before changing the pH of any solutions, the pH meter was calibrated using stock solutions with pH values of 4.0, 7.0 and 11.0. Where required, the pH of solutions was altered using NaOH at 1M or 0.1M, and HCl at 1M or 0.1M. All pH measurements were taken at room temperature.

2.2.3   Stock Solutions

Ethanol: A volume of 7L of 100% ethanol was diluted with 3L of distilled water to produce 70% (v/v) ethanol. The solution was stored at room temperature for up to three months.

Virkon: A solution of 1% (w/v) Virkon was made by combining 50g Virkon powder into 5L distilled water. The solution was stored at room temperature for up to three months, or until the solution changed colour from bright pink to colourless.

2.2.4   Antibody Reagents

The antibodies used in immunocytochemistry experiments herein are described below (Table 2.1).

2.2.5   Microscopy

Bright Field Microscopy

During cell culture, an Olympus CK-40-SLP microscope was used. This optical microscope was set up for Köhler illumination to check cells visually and for total cell counts.

Widefield Microscopy

For imaging of coverslips or quick evaluation of staining, widefield microscopy was undertaken on a Zeiss Axio Imager.M2. Filters used were 49 DAPI (excitation 365, beam

splitter 395, emission 445/50 nm); 38 GFP (excitation 470/40, beam splitter 495, emission 525/50 nm); and 20 Rhodamine (excitation 546/12, beam splitter 560, emission 575-640 nm). These were used for imaging blue, green and red fluorescence respectively.

Confocal Microscopy

A Zeiss LSM880 Axio Imager.Z2 (upright) was used for confocal imaging of cellular hydrogels and slides following immunochemistry. The lasers used were Diode 405; Argon 458, 488, 514; DPSS 561; and HeNe 633. Associated colours to the wavelengths were blue, green, red and far red/violet, respectively.

Confocal imaging had benefits over widefield imaging; since confocal imaging illuminates only one single spot of light in one focal plane. Conversely, widefield microscopy illuminates the entire thickness of the specimen. Therefore, widefield

Table 2.1: **Details of antibodies used in-vitro and in-vivo.** *Including both primary and secondary antibodies.*

Antigen	Host	Isotype	Conjugate	Dilution	Details
Glial Fibrillary Acidic Protein (primary)	Rabbit IgG (anti-mouse)	Poly-clonal	N/A	1:300	Z03334, Dako, UK
Myelin Basic Protein (primary)	Rabbit (anti-mouse)	Mono-clonal	N/A	1:300	ab40390 Abcam, UK
Rabbit IgG (secondary)	Goat (anti-rabbit)	N/A	Alexa Fluor 488	1:500	Abcam, UK
CS-56 (primary)	Mouse IgM (anti-rat)	Mono-clonal	N/A	1:300	C8035 Sigma Aldrich, UK
Mouse IgM (secondary)	Goat (anti-mouse)	N/A	Alexa Fluor 568	1:500	A21043 Abcam, UK
RECA-1 Endothelial Cells (primary)	Mouse (anti-rat)	Mono-clonal	N/A	1:100	MA140240 Thermo Fisher Scientific, UK
Mouse IgG (secondary)	Goat (anti-mouse)	N/A	Alexa Fluor 647	1:500	A21236 Thermo Fisher Scientific, UK

imaging resulted in out of focus light and noise from above and below the in-plane cells in the 3D collagen hydrogel. This was not present in confocal imaging.

2.3 General *in-vitro* Materials and Equipment

2.3.1 BOSE 5110 Electroforce Biodynamic

The BOSE 5110 Electroforce Biodynamic instrument allows single-axis compression and tension of materials (Barthelat et al., 2014; BOSE, 2014). The apparatus includes a biodynamic chamber which can be sealed and flooded with media to simulate a relevant environment (Figure 2.1) (Donnay et al., 2013; Koivisto et al., 2017).
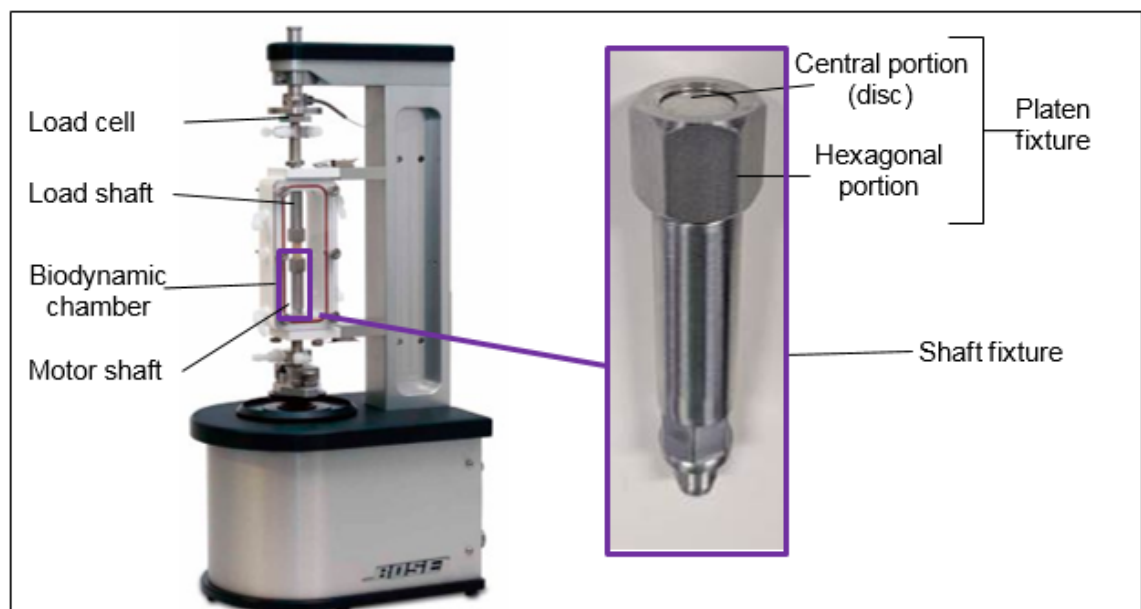
Figure 2.1: **BOSE 5110 Electroforce Biodynamic.***Entire apparatus (left), platen fixture motor shaft with disc platen (right). Both disc platens provided with the instrument had a central depressed portion (BOSE, 2014)*

Furthermore, mechanical parameters in the form of displacement, load and axial command can be controlled using WinTest® software and proportional-integral-derivative control loops; and recorded over time. The Electroforce 5110 consists of two platens. The lower motor platen moves up to a maximum of 13 mm displacement; the

upper is connected to a load cell of either 22N or 200N.

2.3.2   Primary Cells

Primary neural cells were extracted from Wistar rat pups two to three days post-natal (section 2.4.2.4) Cell culture techniques were undertaken in a class II biological safety cabinet under aseptic conditions (see sections 2.2.1 and 2.4.2).

2.4   General *in-vitro* Methods

This section describes the general methods used in *in-vitro* modelling. These methods are used in chapters 3 and 4; to develop and evaluate an *in-vitro* model of mechanical insults in NTSCI (Figure 2.2). This includes characterisation and validation of both the mechanical device (BOSE 5110 Electroforce) and 3D cellular model (primary rat astrocyte seeded collagen hydrogel). Subsequently, the 3D model will be compressed using the apparatus, and cellular outcomes established based on input velocity.

2.4.1   Cell Culture

2.4.1.1   General Cell Culture Solutions

Cell media: Primary astrocytes and mixed glia were cultured in DMEM with 4.5g.L^{-1} glucose, supplemented with 10% (v/v) FBS, 2mM L-glutamine, penicillin (100 U.mL^{-1}) and streptomycin (100 µg.mL^{-1}) (Smith, 2016). L-glutamine, penicillin, streptomycin, and serums were stored at -20ºC and defrosted prior to use. The media was stored for no longer than two weeks at 4ºC.

   Trypsin/EDTA: For cell passage, trypsin (0.05% (v/v)) and EDTA (1mM) were combined. The solution was stored in 5 mL aliquots at -20ºC and defrosted before use.

   Poly-D-lysine: For coating with poly-d-lysine (PDL), 50 µg.mL^{-1} solution was used. This was prepared by dissolving 50 µg of PDL powder per 1 mL distilled water. The solution was filter sterilised, stored at -20ºC, and defrosted as required.

*Figure 2.2: **Aims, objectives, and methods used in in-vitro studies.** Chapters are split into model development, and evaluation of neural cells in response to the model.*

Transforming growth factor beta: A stock solution of transforming growth factor beta (TGF-beta) was made up at 0.1 mg.mL^{-1} in sterile water. Aliquots were frozen and stored at -20°C for up to 3 months. When required, these were defrosted and diluted as appropriate.

2.4.1.2 Reagent Preparation for Primary Cell Isolation

Trypsin solution: A solution of 1mg.mL^{-1} (0.1% (w/v)) trypsin with activity of 13,000 to 20,000 units.mg^{-1} was prepared in sterile PBS. This was subsequently stored at -20°C in 2mL aliquots for up to one year.

DNase solution: A solution of 100 µg.mL^{-1} of DNase (0.01% (w/v), activity of 2000 units.mg^{-1}) was made up in Hanks' buffered salt solution **with** calcium and magnesium. It was subsequently stored at -20°C in 2mL aliquots for up to one year.

Triturating solution: A solution containing 10 mg.mL^{-1} (1% (w/v)) bovine serum albumin; 500 µg.mL^{-1} trypsin inhibitor (activity of 10,000 units.mg^{-1}); and 20 µg.mL^{-1} DNase (activity of 2000 units.mg^{-1}) was made up in Hank's buffered salt solution **without** calcium and magnesium. Aliquots (2mL in volume) were stored at -20°C for up to one year

2.4.1.3 Cellular Assay Solutions

Immunocytochemistry

Antibody diluent: A volume of 60 mL of antibody diluent was made up using 6 mL of 1% (v/v) sodium azide, 300 µL of 5% (w/v) bovine serum albumin (see below) in 40 mL of 1x TBS. The pH was adjusted to 7.6 before being made up to 60 mL using 1x TBS. The solution was stored at 4°C for up to three months.

Bovine serum albumin (BSA): A solution of 5% (w/v) BSA was made by adding 0.5g of BSA to 10 mL PBS, and stirred using a magnetic stirrer. The solution was sterile-filtered using a 0.2 µm filter, and stored at -20°C for up to six months.

Hoechst counterstain: Hoechst 33258 2 µg.mL^{-1} was made up of 1000 µg of Hoechst

powder in 500 μL sterile water, stored at -20°C and defrosted when required. Used at 1:1000 dilution (i.e. 2 μg.mL^{-1}).

Tris buffered saline (TBS): A total of 24g of Trizma base and 8.8g of NaCl were dissolved in 700mL distilled water. The pH of this solution was changed to 7.6 using 6M HCl dropwise. The solution was topped up to 1L using distilled water, before being autoclaved. This produced 10x concentrated TBS. Upon use, it was diluted using 100 mL 10x TBS in 900 mL distilled water for a 1x solution. The solution was kept for up to three months at room temperature.

Tris buffered saline with Tween (TBS-T): A volume of 1.5 mL of Tween 20 was added to 500 mL of 1x TBS. The solution was mixed using a magnetic stirrer, and the pH adjusted to 7.6 using 6M HCl and 6M NaOH dropwise. This solution was stored for up to three months at room temperature.

Tris no saline (TNS): A total of 3 g of Trizma base was added to 500 mL of distilled water. The pH of the solution was changed to 7.6 using 6M HCl dropwise. The solution was stored at room temperature for up to three months.

Marvel blocking solution: The blocking solution used was 0.5% (w/v) Marvel powdered milk in 50 mL 1x TBS, which was made up on the day of use and not stored. It was made up using 1 scoop of Marvel in 50 mL 1x TBS.

Triton^{TM} X-100: A volume of 1 mL Triton^{TM} X-100 was made up to 1L using sterile water. The solution was mixed and stored for up to one year at room temperature.

Dead stain from the Live/dead® assay

Ethidium homodimer (dead stain) from the live/dead® fluorescence assay was prepared as per the manufacturers instructions. This comprised 4 mL of appropriate cell culture media, 2 μL ethidium homodimer-1 were added and mixed. Where used, 4 μL of Hoechst 33258 was also added. The solution was used immediately, and the assay carried out in the dark. The method for the assay is described in 2.4.4.

Enzyme-Linked Immunosorbent Assay (ELISA)

Antibody standards: A total of 8 antibody standards were made up using serial solutions in accordance to manufacturers instructions, using standard/sample diluent provided. Diluted standard was used on the same day, and surplus standard was discarded.

  Biotin-conjugate Detection Antibody: The detection antibody was diluted at 1:100 in diluent provided. The solution was used on the same day and surplus was discarded.

  Streptavidin-horseradish peroxidase B: The streptavidin solution was diluted at 1:100 in the diluent provided. The solution was used on the same day and surplus was discarded.

  Wash Buffer: The wash buffer provided was diluted twenty-fold, as per manufacturers instructions.

2.4.2 Cell Culture Methods

2.4.2.1 Aseptic Technique

Cell methods were carried out using aseptic technique in a class II biological safety cabinet.

2.4.2.2 Primary Rat Glial Cells Culture Requirement

Primary rat glial cells were adherent to poly-D-lysine coated tissue culture plastic, and grew in a monolayer. They required 8% (v/v) CO_2 in air.

2.4.2.3 Poly-D-Lysine Coating

Coating flasks or coverslips with poly-D-lysine facilitated adhesion of primary glial cells. One 20 mL aliquot of PDL was defrosted at room temperature. Then, a sufficient volume of PDL to cover the surface was added. For a T75 flask, this was 5 mL; for a 22 x 22 mm coverslip, this was 400 μL. The flask or coverslips were then placed into a 37°C incubator for at least one hour. PDL was removed and returned to the -20°C freezer, to be re-used up to three times. Then, two 10 mL PBS washes were undertaken, followed by a final

wash with media. This media was discarded. Flasks or coverslips were left to dry for at least four hours at 37°C, 8% CO_2 (v/v) in air. Following this, PDL-coated flasks or plates were stored at 4°C for up to two weeks, sealed using parafilm.

2.4.2.4   Primary Glial Cell Isolation

Dissection of Cerebral Cortex

Details of the solutions used in this section can be found in section 2.4.1.2. Primary glia were isolated from female Wistar rat pups, between post-natal days two and three. Each rat was sacrificed using cervical dislocation. Death was confirmed before subsequent procedures were carried out; according to the UK Animals Scientific Procedures Act 1986, under Home Office Project License PPL 70/8085.

Each head was cut away from the body using scissors, and placed in a falcon tube in ice. Once all heads were removed, further dissection was carried out. Each head was sprayed with 70% (v/v) ethanol. Dissection of the brain was carried out using springbow scissors and forceps (Figure 2.3). First, bissecting the skin, then the skull, to reveal the brain (steps A to D). When the cortex was removed from the skull (step E), it was placed into a sterile petri dish containing 4°C HBSS without calcium or magnesium. Removal of the midbrain was then carried out (step F). Following this, meninges were removed from the outer layer of the cortex using a dissection microscope. The process was carried out for each hemisphere; and dissected cortices were placed into another petri dish containing HBSS without calcium or magnesium at 4°C.

Isolation of Cells from Cortex

Once dissected, the cortices were pooled to minimise intra-animal variation. Then, a straight-edged razor blade was used to chop the cortices into small pieces. Following this, the suspension was transferred to a 15 mL Eppendorf tube and centrifuged at 150g for five minutes. Then, the supernatant was removed and trypsin solution was added. This was incubated at 37°C, 8% (v/v) CO_2 for 20 minutes. Following this DNase solution was added, and the suspension was incubated for a further five minutes at 37°C, 8%
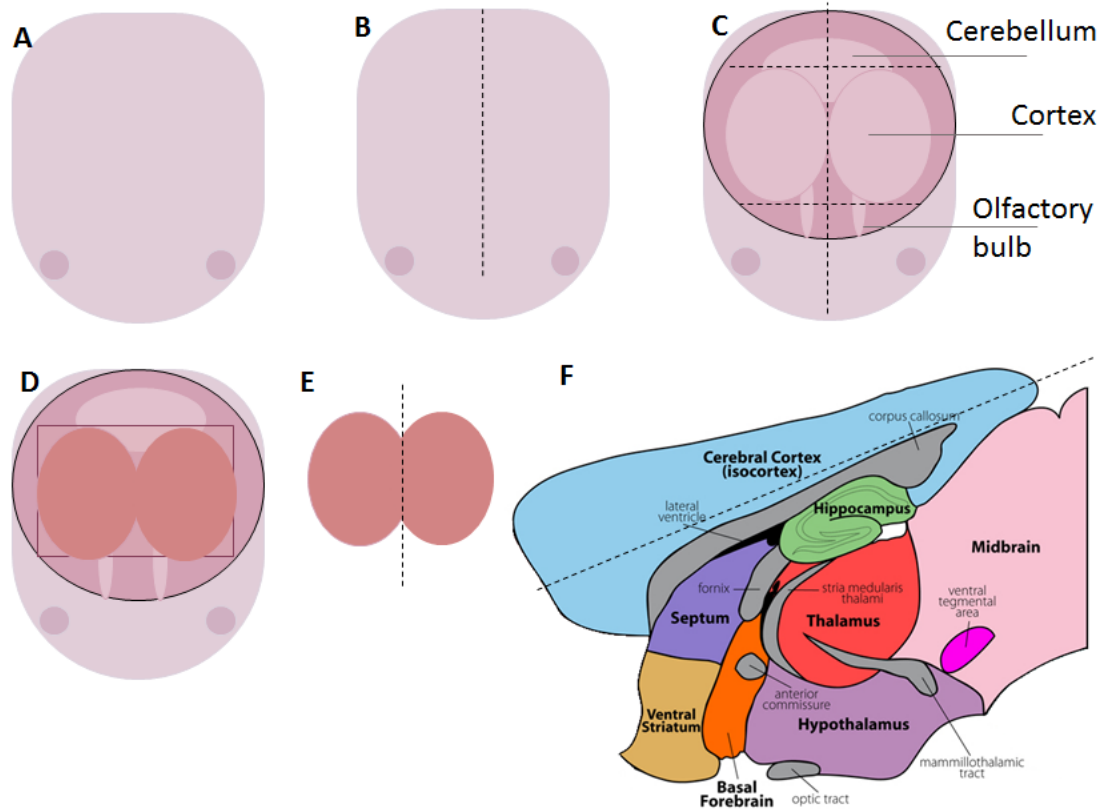
*Figure 2.3: **Steps in methodology to isolate cerebral cortex from pre-weaner rats.***
A: Wistar rats (2 to 3 days postnatal) were sacrificed using cervical distraction. The head was decapitated, and sprayed liberally with 70% (v/v) ethanol.
B: The skin was bisected sagittally using springbow scissors from the caudal surface to in line with the eyes. The skin was then pulled back to reveal the skull.
*C: The skull was cut as shown (using springbow scissors) to create flaps overlying the cortex. Care was taken to **only** cut through the skull at this stage and not damage underlying cortex.*
D: The skull was pulled back to expose the underlying cortical lobes.
E: The cortex was removed using a spatula, and placed into a petri dish containing cold medium. Here, it was cut down the mid-sagittal line; separating cerebral hemispheres.
F: View of the brain in cross-section. Using fine forceps, the midbrain and caudal parts of the cortex which fold back upon the cortex proper were removed. The cortex was retained. Image adapted from gensat.org (Heintz, 2017)

(v/v) CO_2; or longer until the suspension was no longer viscous. This indicated all the released DNA contents were degraded. The suspension was centrifuged at 150g for five minutes. The supernatant was discarded, and the pellet resuspended in triturating solution. Then, the cells were added to PDL coated T75 flasks (6 cortices into 3 flasks) containing

supplemented DMEM (section 2.4.1.1) at 37°C. Flasks were incubated at 37°C, 8% (v/v) CO_2. Media was changed the following day, and then every three to four days subsequently.

Separation of Mixed Glial Cells into Enriched Populations

Approximately ten days following isolation, or when the cells reached 80% confluency, mixed glial cells were separated into enriched populations of astrocytes and microglia. The lids of flasks were sealed, either using closed caps or parafilm. Flasks were then placed on a plate shaker at 150 rpm for 4 hours at 37°C, 8% (v/v) CO_2 in air. The media, containing a higher proportion of microglia, was added to PDL coated T75 flasks with 5mL of fresh pre-warmed (37°C) supplemented DMEM. A total of 12 mL fresh supplemented DMEM (pre-warmed to 37°C) was added to the flasks from the plate shaker, containing a higher proportion of astrocytes.

2.4.2.5   Cell Maintenance and Passage

In flasks or gels containing cells, media was removed and replaced fresh media pre-warmed to 37°C. This was undertaken using a pipette and taking care not to disrupt the cellular monolayer or the gel surface. In flasks, once the cellular monolayer reached up to 80% viability, passage was undertaken. Media was removed and two 10 mL PBS washes were undertaken to remove any traces of media. Following removal of PBS, cells were incubated with 3 mL of trypsin/EDTA at 37°C (with the appropriate percentage (v/v) CO_2 in air) for between five and ten minutes. A volume of 10 mL of pre-heated media (37°C) before a light microscope was used to check if cells had detached from the monolayer. If, after ten minutes of incubation, cells remained adherent, a cell scraper was used to manually detach the cells. Once cells were detached, the contents of the flask was transferred to a universal tube, and centrifuged at 150g for ten minutes. The supernatant was discarded and the cell pellet resuspended in 2 to 4 mL of pre-heated media. A cell count was carried out before cells were redistributed at appropriate concentrations.

2.4.2.6   Cell Count and Seeding

Cell counts were carried out using the trypan blue exclusion assay. Trypan blue is excluded from live cells by their plasma membrane, but not dead cells since their membrane is no longer intact. Upon addition of trypan blue and evaluation under light microscopy, live cells appear colourless and dead cells appear blue. For this study, a dilution factor of 2 was used i.e. 20 μL of media with cells and 20 μL of trypan blue. A volume of 20 μL of the suspension was dispensed onto the haemocytometer, below the coverslip. Corner squares were counted under phase contrast light microscopy (Figure 2.4). The number of cells in each corner square should have been between 100 and 300; otherwise the cells were resuspended in a more appropriate volume. Knowing that each corner square has a volume of 0.1 mm^3 (height 1 mm, width 1 mm, depth 0.1 mm), i.e. 0.0001 mL; the total number of live cells per mL of the original cell suspension were established according the the equation:

$$Total \ number \ of \ live \ cells \ per \ mL = \frac{Counted \ live \ cells}{No. \ of \ squares \ counted} \times Dilution \ factor \times 10^4$$

Once total number of cells was established, the volume of media required to obtain an appropriate cell concentration was added to the cell suspension. This resuspended volume was seeded into the relevant container or other material (e.g. T75 flask, coverslip or collagen gels).

For T75 flasks, cells were added to pre-warmed 37°C media to a total volume of 12 mL per flask. For coverslips, a volume of 200 μL of cells were added to each coverslip (previously PDL-coated, if required) in a 6 well plate. These were left to settle for ten minutes before the well was filled with 5 mL pre-warmed 37°C L media. For distributing cells in collagen hydrogels, see methods below.

2.4.3   Collagen Gel Production

Simple geometry collagen gels of various volumes were created in multi-well plates. The desired end volume of each gel or batch of gels was multiplied by 1.1 to account for
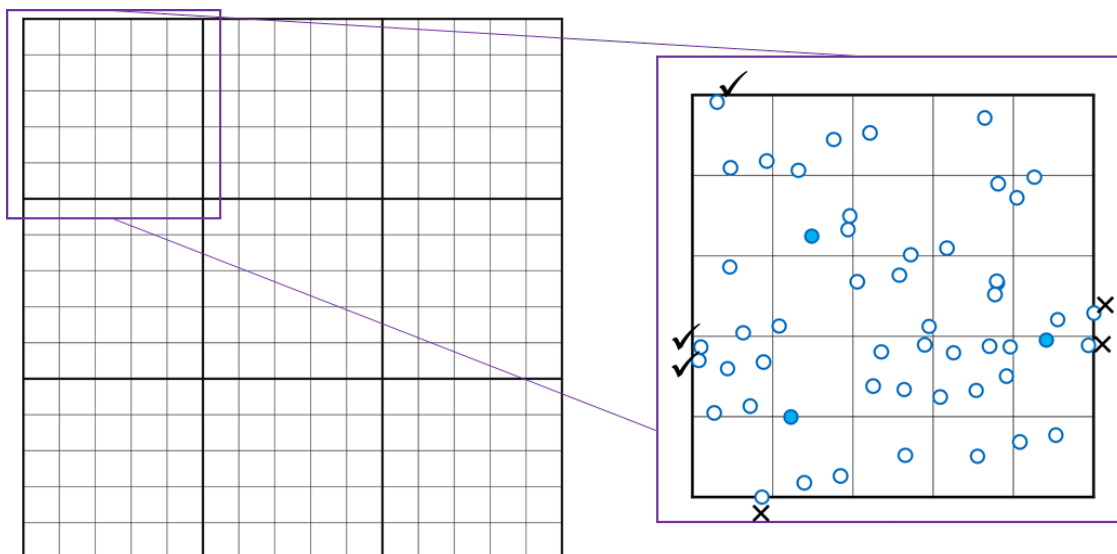
*Figure 2.4: **Haemocytometer Layout.** Only live cells (colourless with a blue 'halo' were counted). Those on the top and left edges were counted; and the bottom and right were discarded to prevent counting cells more than once. At least three corner squares were assessed*

swelling. For both cellular and acellular gels, collagen was dispensed using wide bore pipettes to facilitate smooth dispersion. Steps were taken to prevent bubble formation, such as mixing gently and dispensing reagents slowly.

For cellular gels, 80% of the total volume was rat tail collagen (type I, 2 mg.mL^{-1} in 0.6% (v/v) acetic acid), 10% was 10x minimum essential medium (MEM), 4.2% was media containing cells, and the remaining volume (approximately 5.8%) was 1M NaOH. Prior to creating cellular gels, well plates were placed on ice blocks. The cold temperature slowed the time before gelation.

Collagen and MEM were mixed in a bijou and stored on ice. Cells were then prepared to an appropriate concentration in media using the trypan blue cell count assay. This prevented cells being at a high concentration in a low volume for extended durations, minimising cell death. Collagen/MEM solutions were neutralised by adding NaOH dropwise until colour change was observed (Figure 2.5). The cellular suspension was triturated to resuspend any cells which had settled, and the appropriate volume was added to the neutralised collagen. This was then mixed gently, before being dispensed

as appropriate into a multi-well plate. Gels were left to set for up to fifteen minutes at room temperature. Then, a volume of pre-warmed 37°C media equal to the volume of gel was added to prevent the gels drying out and add nutrients. If gels contained cells, media was replaced every 3 to 4 days.

For acellular gels used in evaluating the mechanical capacity of the BOSE 5110 Electroforce system, Purecol was used. This bovine collagen I was supplied at 5 mg.mL^{-1}. As such, it was easily diluted and tested at different collagen densities. Collagen was diluted with PBS to the desired concentration. Then mixed gently and dispensed into well plates on ice blocks. Gels were left to set for 30 minutes at 37°C, as per manufacturers guidelines, before a volume of PBS equal to the gel volume was added on top to prevent dehydration.
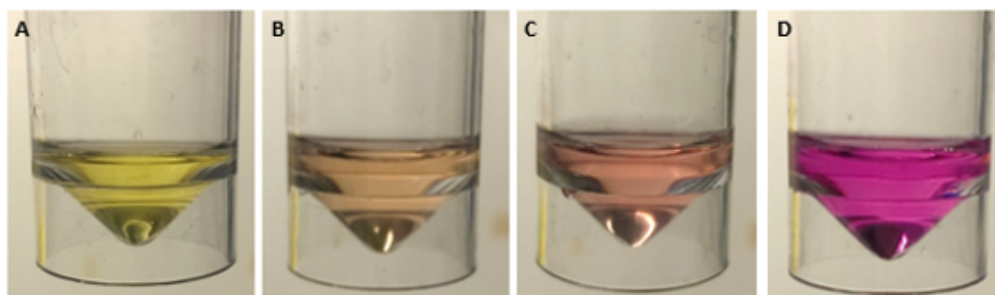
*Figure 2.5: **Creation of collagen gels**. Neutralisation of collagen and MEM using NaOH. A: collagen and MEM without NaOH. B: Incomplete neutralisation reaction, further NaOH required C: complete neutralisation. D: Excess NaOH added, discard solution*

2.4.4   Methods for Assessing Cellular Response

2.4.4.1   Ethidium Homodimer Stain from the Live/dead® Viability Assay

Ethidium homodimer is the dead stain in the Live/Dead® viability assay. It was used to visually identify dead cells. The intact plasma membrane of live cells excluded ethidium homodimer-1. Conversely, dead cells readily took up ethidium homodimer-1 due to poor membrane integrity. In dead cells, ethidium homodimer-1 could bind to nucleic acids to create red fluorescence (absorbance 528 nm, emission 617 nm) (Carpanese et al., 2014).

The solutions used in this assay are described in section 2.2.3.

2.4.4.2   Counterstain

Both Hoechst and DAPI counterstains bind to the minor groove of DNA (Estandarte, 2012). The two dyes have similar excitation and emission profiles; of 346/460 nm (Hoechst) and 354/454 nm (DAPI). Hoechst is positively charged, and as such crossed the cell membrane of viable cells. Therefore, it has been preferred for staining live cells (Demchenko, 2008). Conversely, DAPI is not charged. So, to stain living cells, incubation times had to be increased, or cells had to be fixed and permeabilised. Due to its ability to stain both living and fixed cells more easily, Hoechst was used as the counterstain throughout this research.

2.4.4.3   Immunocytochemistry in Gels

Techniques such as immunocytochemistry were used to assess cellular phenotype and spatial distribution. For each of the stages detailed below, the volume of reagent added was equal to gel volume. Wash steps were carried out for five minutes at room temperature.

First, media was removed from cells through washing with TBS three times. The fixative used was 4% (w/v) paraformaldehyde (PFA). This was defrosted from -20°C to room temperature. PFA fixed proteins through cross-linking, preventing autolysis and degradation of cellular components (Howat and Wilson, 2014). Cellular hydrogels were fixed using 4% (w/v) paraformaldehyde (PFA) for at least three hours at 4°C.

Subsequently, PFA was removed and gels were washed with TBS three times. At this point, gels could be stored for up to two weeks at 4°C. Permeabilisation was then carried out using a thirty minute incubation at room temperature with 0.1% (v/v) Triton™X-100. This allowed antibodies and stains to penetrate the cellular membrane in subsequent steps. After three further TBS washes, 0.5% (w/v) Marvel powdered milk suspension was added. The proteins in the milk powder block non-specific binding of antibodies, reducing background staining. The incubation in Marvel was carried out for thirty minutes

at room temperature. A further three TBS wash steps were carried out before primary antibody incubation. Antibodies were diluted in antibody diluent, at the appropriate concentrations. Antibody incubation was carried out in a humidified chamber at room temperature overnight. Following primary antibody incubation, two TBS-T and two TBS washes were undertaken to thoroughly remove residual antibody.

Finally, secondary antibody and counter stain were made up. Again, these were diluted in antibody diluent at appropriate concentrations; and incubated for one hour in a humidified chamber at room temperature. During this incubation, the chamber and its contents were protected from light wherever possible by covering the chamber in foil. Following incubation, two TBS-T and two TBS washes were carried out. The final, stained samples were stored at 4°C until imaged (ideally the same day, or the next day to prevent fluorophore fading). Where gels were imaged, they were placed beneath a coverslip for at least five minutes prior to imaging. Imaging was undertaken on widefield or confocal microscopes.

2.4.4.4 Immunocytochemistry of Cells on Coverslips

Immunocytochemistry of cells on coverslips was also undertaken in this research. The protocol for preparing coverslips was similar to that of gels, but with shorter incubation steps since reagents did not have to penetrate into a 3D environment. In this protocol, the volume of TBS or TBS-T used for wash steps was consistently 2 mL; whereas the volume of other reagents was 300 µL (sufficient to cover the entire 22 x 22 mm coverslip). The duration of each wash step was thirty seconds.

Initially, media was removed and three TBS washes were undertaken to remove all traces. Then, fixation using 4% (w/v) PFA was carried out for 30 minutes at room temperature. PFA was then removed with three TBS washes. Permeabilisation took place by adding 0.1% (v/v) Triton™X-100 to each coverslip, with incubation at room temperature for fifteen minutes. This was removed, and washed off with three TBS wash steps. Then, 0.5% (w/v) Marvel powdered milk suspension was added to each slide for

fifteen minutes at room temperature. This was similarly removed and washed off with three TBS washes. Primary antibodies were diluted in antibody diluent, added to each slide, and incubated for one hour at room temperature. Antibodies were washed off with two TBS-T and two TBS washes. Then, coverslips were incubated in secondary antibodies (in antibody diluent) for 1 hour at room temperature. Primary and secondary antibody incubations were carried out in a humidified chamber, covered in foil. Secondary antibody was removed with two TBS-T and two TBS washes. Coverslips were mounted on to slides using mounting medium containing Hoechst. Slides were then stored in the dark at 4°C for up to three days before imaging.

2.4.4.5   Image Analysis Following the Live/Dead® Viability Assay

Following imaging, image analysis was undertaken the software FIJI. FIJI includes ImageJ software with plugins specifically for image analysis techniques. A basic protocol (Labno, NA) was amended to incorporate FIJI plugins. In brief, the protocol comprised converting single fluorescent channel images into 8-bit images; using a local threshold to distinguish cells based on their brightness and size, whilst accounting for differences in brightness across images; splitting up multi-cellular entities and finally counting objects based on size and circularity. Several iterations of image analysis algorithm were attempted, including changing threshold techniques, incorporating watershed features, and altering size range and circularity of particles analysed. Manual cell counting was compared with automated methodology to ratify the methodology.

Manual cell counting was undertaken on cells in focus and distinguishable on each image. The RGB image was split into separate individual channel images. Using the point tool, all the stained cells on the red image (ethidium homodimer stained dead cells) were selected. The counter was reset and the cells on the blue image (Hoechst stained cells) were counted. Overall, the proportion of living cells could be calculated by knowing the total number cells (cells stained with Hoechst); and the number of dead cells (cells stained with ethidium homodimer).

2.4.4.6 Analysis of Astrocyte Reactivity using GFAP

Glial fibrillary acidic protein (GFAP) is a component of the astrocyte intermediate filament network (Hol and Pekny, 2015). As such, it is involved in cytoskeletal structure and function; with associated roles in cell motility and vesicle trafficking (Middeldorp and Hol, 2011). For this study, its role in neural injury pathogenesis was most important.

When exposed to chemical or mechanical stress, such as injuries or ischaemia, phenotypic changes occur in astrocytes, going from physiological to a reactive astrogliosis phenotype. Astrogliosis is hallmarked by upregulation of GFAP, increase number of astrocyte processes, and hypertrophy of these processes (Hol and Pekny, 2015). The degree of astrogliosis varies with injury severity, with the most severe form contributing to the glial scar in traumatic spinal cord injury (Sofroniew, 2005). The role of GFAP in astrogliosis in response to neural injury has been confirmed in knockout mice. These GFAP-null animals showed an increased susceptibility to traumatic spinal cord injuries and ischaemia (Nawashiro et al., 1998, 2000). However, the role of GFAP in non-traumatic spinal cord injury specifically has not been established. In this study, reactive astrogliosis was measured using immunocytochemistry GFAP-labelling of astrocyte populations. The number of cells expressing GFAP, area of GFAP per cell, and number of astrocytic processes were calculated using image analysis.

2.4.4.7 Image Analysis of GFAP Staining

Analysis of astrocyte reactivity, using fluorescent images of GFAP immuno-staining, was carried out in a similar manner to Smith, to facilitate comparison between studies Smith (2016). Automated image analysis minimises user bias, allows for variation in staining intensity, and increases the speed of the analysis process. Each fluorescently-labelled object could be evaluated for size and shape parameters.

First, multi-channel fluorescence images were separated by channel to show one fluorophore per image. The channel incorporating GFAP staining was selected. On this

channel, areas which were labelled for GFAP (objects of interest) were distinguished from background using an automatic threshold technique. This produced a binary image of objects of interest based on intensity. Similarly to previous studies, the 'Phansalkar Auto Local Threshold' tool was chosen to account for background noise between images (as described and rationalised in Smith (2016)). The scale was set on this binary image to conform to the original image (Figure 2.6). From the binary image, objects of interest were analysed. Objects less than 10 μm^2 were discarded as per the previous study (Smith, 2016). No maximum area was defined since the maximum area of GFAP expression per object was unknown. Outcomes measured were total area, area per object of interest, and circularity. Circularity is a measure of the shape of the object, using the equation below. A circularity of 1.0 was a perfect circle, and as the value reduced it indicates an elliptical, elongated, or irregular shape (ImageJ, 2012).

$$\text{Circularity} = 4\pi \times \frac{Area}{Perimeter^2}$$

A macro of this method was developed to facilitate analysis. This macro is in Appendix D.1. The binary image of objects was exported, and compared with the original images for quality. If the binary image did not represent the original images, for example in images with high background staining the objects of interest could not be fully distinguished, the result for that image was discarded.

2.4.4.8 Contraction Assay

At various timepoints, images were taken of the gels in each well. Gel contraction was measured using FIJI, tracing the circumference of the base of the well, followed by the perimeter of the gel. The measure tool in FIJI then provided the area of each of these, and thus percentage contraction of the gel could be calculated.

2.4.4.9 Enzyme-linked Immunosorbent Assay (ELISA)

The ELISA tests used were sandwich ELISAs with pre-coated plates. Standards and solutions were made up according to section 2.4.1.3. For IL-6 ELISA, incubations were
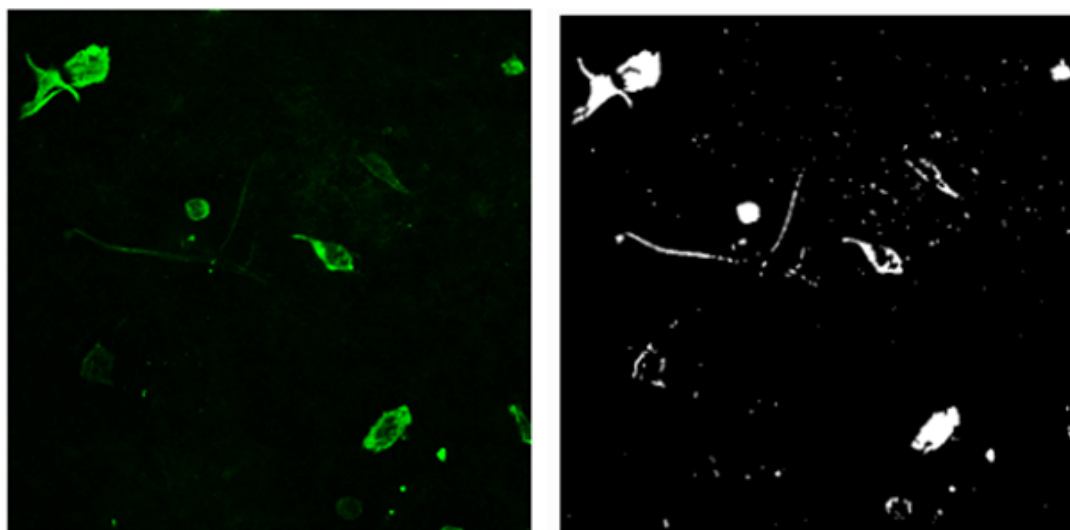
Figure 2.6: **Example of binary GFAP fluorescence image using in image analysis.** *The single channel GFAP fluorescence image (left) was separated from the multi-channel microscopy image using FIJI. The 'Auto Local Threshold' tool and 'Phansalkar' settings were used to create the binary image (right). From this image, objects with an area >10 μm² were analysed.*

carried out at 37°C. For IL-10 ELISA, incubations were carried out at room temperature, as per the manufacturers instructions.

A volume of 100 μL of standard, control or sample was added to each well. The plate was sealed with an adhesive plate sealer, and incubated for 90 minutes with gentle shaking at 50 rpm.

Solutions were then aspirated and wells washed three times with 400 μL wash buffer per well using an automatic plate washer at room temperature. The plate was blotted on paper towel to remove any residual solution.

A volume of 100 μL of biotin-conjugate detection antibody was added to each well. The plate was sealed and then incubated for 60 minutes with gentle shaking at 50 rpm. The same wash steps as above were repeated (3 x 400 μL washes and blotting).

Streptavidin solution (100 μL) was added to each well, and the re-sealed plate incubated for 30 minutes with gentle shaking at 50 rpm. The same wash steps as above were repeated (3 x 400 μL washes and blotting).

A volume of 100 μL substrate solution was added to each well. This produced a colour change at high concentrations of the cytokine being detected. The plate was sealed and covered in foil to protect from the light. The substrate solution was incubated for 15 minutes with gentle shaking at 50 rpm.

Finally, 100 μL of stop solution was added to each well, and the plate was tapped gently to ensure thorough mixing. The optical density of each well was determined using a plate reader at 450 nm.

2.5 General *in-vivo* Materials and Methods

Details of general methods, materials, equipment and reagents used can be found in 2.3. The details of each method described in this section are used in the following chapters 5 and 6, describing *in-vivo* model development and outcomes, respectively (Figure 2.7). In brief, a balloon catheter system was developed for implantation ventrally within a rat vertebral canal, which could be inflated over days to induce a NTSCI. The ventral balloon catheter system was characeterised for TSCI, and then adapted for NTSCI. Histological and functional outcomes were established in NTSCI study groups, compared to control.

2.5.1 Solution Preparation

Surgical Solutions and Perfusion

Iodine ethanol solution: A total of 1 L of iodine ethanol solution was made up using 500 mL of 100% (v/v) ethanol, and 500 mL tincture of iodine. The solution was stored for up to one year at room temperature.

Buprenorphine (Vetergesic): The analgesic solution (Vetergesic) was diluted in sterile saline to an end concentration of 0.03 mg.mL^{-1}. It was administered at 0.015 mg.kg^{-1}.

Enrofloxacin (Baytril): The antibiotic solution (Baytril) was diluted in sterile saline to an end concentration of 0.25 mg.mL^{-1}. It was administered at 0.25 mg.kg^{-1}.

	Aim	Model/apparatus	Objectives	Measurement/comparison
Chapter 5	Define NTSCI injury modality (extent, level)	CT scan	Evaluate rat anatomy	Spinal canal dimensions
		Traumatic ventral spinal cord injury study	Evaluate histological features of ventral spinal cord lesion using 12.5 µL and 15 µL, using balloon catheter	Haematoxylin and Eosin staining (lesion volume)
				Immuno-staining (location, density)
		Balloon catheter and syringe	Correspond volume injected with inflation	Catheter balloon diameter
		Balloon catheter and osmotic pump	Correspond inflation with osmotic pump outflow over time	
Chapter 6	Evaluate outcomes in NTSCI *in-vivo*	Balloon catheter rat spinal cord injury model	Assess functional, morphological, and cellular outcomes after NTSCI	Surgical procedure and animal care outcomes
				Functional outcomes: BBB open field locomotor score
				Histology: lesion morphology and cellular changes

Figure 2.7: **Aims, objectives, and methods used in in-vivo studies.** *Chapters are split into model development, and evaluation of neural cells in response to the model.*

Phosphate buffer: For one litre of phosphate buffer, 33.75 g of sodium phosphate monobasic and 7.72 g of sodium hydroxide (final concentrations 0.24 M and 0.2 M, respectively) were added to distilled water to make 2X concentrated phosphate buffer. The pH of the solution was changed to 7.4. Where 1X phosphate buffer was required, this was diluted 1:1 with distilled water. Both solutions were filtered and stored at room temperature.

8% (w/v) Paraformaldehyde: A total of 900 mL of distilled water was heated to 60°C. Then, 80 g of paraformaldehyde powder was added. Subsequently, the solution was cleared by addition of 1 M NaOH dropwise. Once the solution cooled, the pH was adjusted to 7.4 by the addition of 1 M HCl dropwise. The volume was topped up to 1 L using distilled water. The solution was stored at 4°C for up to one day.

4% (w/v) Paraformaldehyde in phosphate buffer: Paraformaldehyde solution 8% (w/v) was diluted 1:1 with 2X phosphate buffer. The solution was filtered and then immediately used.

30% (w/v) Sucrose and 0.1 % (v/v) sodium azide: A total of 30 g sucrose and 0.1 mL sodium azide were added to 99.9 mL filtered 1X phosphate buffer (0.12 M sodium phosphate monobasic, 0.1 M NaOH, pH 7.4). The solution was stored at 4°C.

Histology and Immunohistochemistry

1x TBS, 1x TNS and 0.3% (v/v) TBS-T were made up according to details in section 2.4.1.3

Blocking buffer: A solution of 10% (v/v) horse serum was made up in 0.3% (v/v) TBS-T. The solution was mixed and stored at 4°C for up to two weeks.

2.5.2   Surgical Techniques and Care

2.5.2.1   Animal Housing and Care

Animal experiments either took place in Prague, Czech Republic (Institute of Experimental Medicine); or Leeds, UK (University of Leeds). In either case, female adult (3 month old) Wistar rats were used in each experiment. In studies carried out in Prague, experiments were performed in accordance with the European Communities Council Directive of 22nd September 2010 (2010/63/EU) regarding the use of animals in research, and were approved by the Ethics Committee at the Institute of Experimental Medicine, Academy of Sciences of the Czech Republic, Prague, Czech Republic (experimental project number 53/2014). Animals were obtained from the in-house breeding facility at the Academy of Sciences of the Czech Republic, Prague. For studies carried out at the University of Leeds, animals were sourced from the University of Leeds Central Biomedical Services. Methods used complied with the UK Animals (Scientific Procedures) Act 1986, under project license PPL 70/8085, with approval from the internal University of Leeds ethics committee.

All animals were kept in a temperature controlled environment (19 to 21ºC) with a 12 hour day/night cycle (lights on at 7 AM). Each had *ad libitum* access to food and water. Animals were housed individually after surgery, with manual bladder expression twice a day if required. Any minor skin wounds or irritation were treated with a topical application of Isathal (10 mg/g fusidic acid) to prevent infections.

2.5.2.2   Spinal Cord Lesion Surgical Preparation

Anaesthesia was induced using 5% (v/v) isoflurane in oxygen at 2 L.min^{-1}. Anaesthesia was confirmed by a lack of righting reflex, toe pinch withdrawal reflex, and corneal blinking reflex. At this point, the animal was transferred to a face mask and isoflurane was reduced to 2.5% to maintain the anaesthetised state. During all subsequent surgical proceedings, the animal was on a heat mat warmed to 37°C.

The back of each animal was shaved from the base of the skull to caudal of the ribcage. Iodine solution was applied to the area using gauze. A two to three centimetre long incision was made using a scalpel, from approximately T6 to T12.

The T10 vertebra was identified by working upwards from the caudal floating rib (T13). Musculature was disrupted at this level using blunt dissection, allowing access to the vertebral bone. Once the posterior spinous process and lamina could be identified, rongeurs were used to create a partial (right-hand side only) laminectomy at T10 and expose the spinal cord (Figure 2.8A). The right hand side of the lamina were fully removed, from the midline vessel to the lateral most aspect.

Any minor bleeds during surgery were quelled using sterile cotton buds, application of saline, or use of bonewax on a sterile cotton bud. For moderate bleeds, small pieces of wet Spongostan were applied to the bleeding area to promote clotting.

At this point, isoflurane was reduced further to 2%. The patency of each balloon catheter system was tested prior to use *in-vivo*. Sterile water was used to inflate the balloon, and provided there were no leaks in the system the water was removed until the curved edges of the inflated balloon became straight again. The balloon catheter was then introduced at the laminectomy site (T10), on the right-hand lateral edge of the spinal cord within the vertebral canal. The catheter was pushed both rostro-ventrally until resistance was met. This signified the ventral surface of the vertebral body had been reached. The catheter was further advanced rostrally until a length 1 cm below the bottom of the balloon was inserted into the canal (Figure 2.8B and Figure 2.9). Based on understanding of rat

anatomy, the tip of the balloon was positioned at spinal cord level T7/8 (aligning with vertebral level T7) with the balloon itself being at T8/9 (vertebral level T7/8) (Hebel and Stromberg, 1976). The balloon was either inflated immediately and then removed, or implanted depending on the study. Subsequently, the spinal cord muscle layer was closed using resorbable Vicryl sutures. The skin was closed using Prolene sutures.
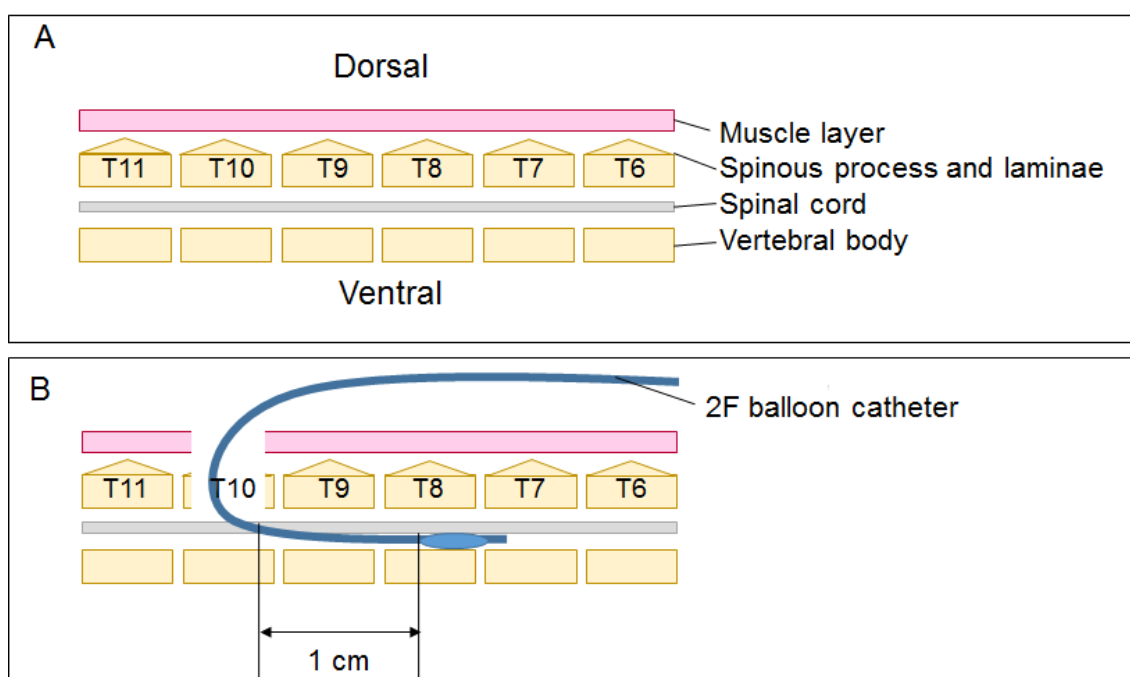
Figure 2.8: **Schematic diagram of key stages in balloon catheter surgery for inducing spinal cord injury.** *Surgery was undertaken in female adult Wistar rats. A: the native tissue in the surgical region. B: Laminectomy was performed at T10, and balloon catheter inserted ventro-laterally in the vertebral canal caudally up to 1 cm below the caudal end of the balloon (previously marked on the catheter).*

Figure 2.9: **Dimensions (mm) of portion of 2F Fogarty balloon catheter inserted into vertebral canal.** *A total length of 18 mm of the balloon catheter was inserted into the vertebral canal of rats to induce spinal cord injury. Not to scale, dimensions in mm.*

Each animal received subcutaneous injections of analgesia (Vetergesic, 0.015 mg.kg^{-1}), antibiotic (Baytril, 0.25 mg.kg^{-1}), and 5 mL pre-warmed (37°C) saline during suturing to prevent pain or infection, and facilitate animal recovery.

After suturing, isoflurane was reduced to 0%, and the animal was left breathing oxygen at 2 L.min^{-1} until they came around from anaesthesia. Then, the animal was placed in a 32°C housing chamber until they were fully recovered from the anaesthesia.

Analgesia and antibiotics were given for three days post-surgery at the same concentrations as previously stated.

2.5.3 Behavioural Testing

2.5.3.1 Open Field and BBB scale testing

Motor function was assessed according to the BBB scale (Basso et al., 1995). The scoring system is a scale of 21 (Appendix E), from 0 (complete paralysis, no movement) to 21 (normal gait, co-ordination, toe clearance, paw position, stable). This scoring took place over 4 minutes per timepoint, with the animal on an open field, radius 0.9 m. Animals were assessed in a random order.

2.5.4 Histological Preparation

To perform histology on organs and tissues, the animal had to first be perfused with fixative. It was important to remove all blood from the system prior to fixation since blood has auto-fluorescent properties and thus could have interfered with imaging and analysis.

2.5.4.1 Perfusion and Tissue Dissection

Animals were prepared for perfusion using an intraperitoneal injection of sodium pentobarbital at 200 mg.kg^{-1}. For a 300 g animal this was approximately equivalent to a 400 μL injection of 20% (w/v) Pentoject. Once toe pinch withdrawal and corneal reflexes were lost, the animal was prepared for perfusion. If these reflexes were not lost within

five minutes of the initial injection, a further volume of 200 μL was injected.

Forelimbs were spread and held in place using needles. Then, a midline incision was made just below the ribcage. The skin was detached from underlying musculature using blunt dissection. A laparotomy was performed across the entire width of the abdominal wall at this level. Then, the diaphragm was released from the thoracic wall. Subsequently, the ribs were cut on each side (lateral to the lungs) in order to lift the ribcage and sternum up over the head for access to the heart. Any remaining connective tissue was removed. The heart was positioned straight down along the midline. Iris scissors were used to make an incision just lateral of the apex of the heart, in the left ventricle. A 15 gauge blunt-tipped needle catheter was introduced to this incision, which was then pushed until it just reached the aorta. A further incision was made in the right atrium using iris scissors.

Phosphate buffer was perfused trans-cardially through the needle catheter at 8 to 12 mL.min^{-1}. This could be confirmed by movement of the animals limbs and tail, discolouration of the liver and feet. This perfusion continued until the fluid running out of the right atrium was clear. This confirmed all blood was removed from the body. Next, the catheter was transferred to 4% (w/v) PFA in phosphate buffer. The animal was perfused with fixative until the limbs and organs were stiff.

Following perfusion, the spinal cord and brain were harvested from every animal and placed in 4% (w/v) PFA in phosphate buffer for a further 24 hours to ensure complete fixation. Tissues were stored in 30% sucrose at 4°C for up to one week before histology was carried out.

If tissues were stored for a longer duration, tissues were transferred to containers with 30% (w/v) sucrose and 0.1% (v/v) sodium azide, and again stored at 4°C.

2.5.4.2 Tissue Preparation

Embedding Cryo-blocks

Spinal cords were placed into a petri dish containing fresh 30% (w/v) sucrose solution, handling gently to prevent damage. The cord was cut into approximately 2 mm slices.

Each of these was tried gently using blue roll, and subsequently placed into a cryo-mold containing a thin layer of optimum cutting temperature compound (OCT). Four spinal cord slices were placed into each cryo-mold, ensuring they all had the rostral surface facing downwards and flat. The molds were subsequently filled with further OCT. Then, they were placed into a metal tray containing a slurry of dry ice and absolute (100% (v/v)) ethanol. Again, ensuring the cryo-molds were flat. The OCT changed colour from colourless to opaque white, and changed consistency from gel-like to solid. Once the whole block had frozen, it was removed from the slurry and placed on dry ice whilst the rest of the cord was frozen. After this, cryo-blocks were stored in a zip-lock bag with air removed, at -80ºC.

Cryo-sectioning

Cryo-sectioning was undertaken at -20ºC. Each cryo-block was serially sectioned at 40 μm thickness. Torn or damaged sections were noted. Four sections were placed onto one Superfrost plus slide. Slides were left at room temperature for at least 30 minutes before being stored at -20ºC for up to one week or -80ºC for longer storage.

2.5.4.3 Histological Staining

Prior to any of the following staining procedures, slides with frozen sections were left to air dry for at least one hour at room temperature. This ensured sections were fully adherent to the slides and thus less likely to fall off during staining.

Haematoxylin and Eosin

Slides to be stained were left to thaw at room temperature for at least one hour. The slides were then placed in a slide rack and washed in running tap water for three minutes to remove excess OCT. After this, slides were immersed in Mayer's Haematoxylin for one minute, and subsequently rinsed in tap water until the water ran clear. Slides were checked under a light microscope at this point. If the haematoxylin staining was too weak, the slides were immersed again for 1 minute, followed by rinsing in tap water. This was repeated until staining was sufficient. The haematoxylin stain underwent blueing

by immersion in 1X Scott's tap water substitute for three minutes, and then a further three minute rinse in tap water. Sections were stained with eosin by immersion for thirty seconds. Eosin was washed off using tap water until the water ran clear. Then, sections were placed into 70% (v/v) ethanol for twenty seconds, followed by three immersions into fresh 100% (v/v) ethanol for one minute, two minutes and three minutes respectively. Slides were immersed into clean 100% (v/v) xylene for ten minutes, twice. Then, coverslips were mounted onto slides using DPX mountant. The xylene and DPX stages were undertaken within a fume hood. Slides were then left to dry overnight until the DPX had fully dried. Imaging was undertaken using brightfield microscopy. Subsequently, images were imported into FIJI and the area of each section was evaluated (Appendix D.2). Stained tissue was discriminated from the background using the Phansalkar auto thresholding method (Figure 2.10). The area of this tissue was then calculated.
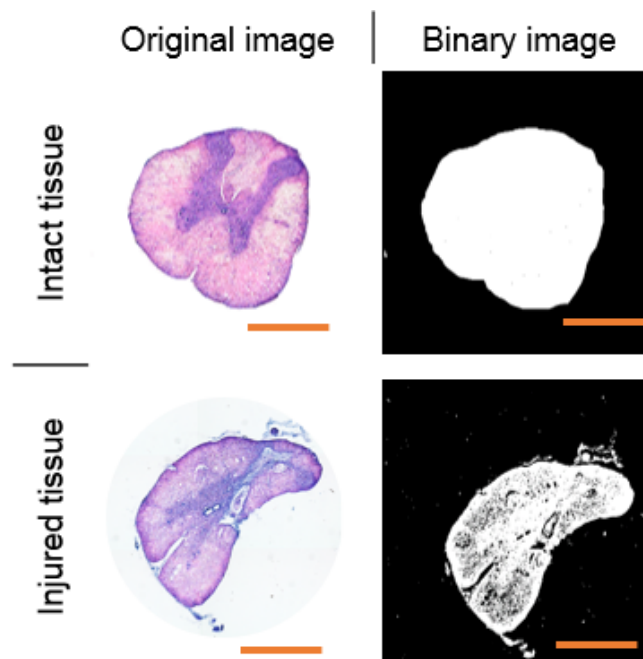
*Figure 2.10: **Example of image analysis for H&E stained spinal cord sections.** Sections 40 μm thick were stained with H&E at 1 mm intervals throughout the spinal cord. Image analysis was undertaken in ImageJ, creating a binary image using the Phansalkar image thresholding method. The stained area was then evaluated from the binary image. Scale bar = 1 mm*

Immunohistochemistry

Once the injury site was determined using haematoxylin and eosin staining, relevant sections in this region were stained using immuno-fluorescence. Three regions were imaged: central to the injury, caudal, and rostral to the injury site. Three sections were imaged in each region. Wash steps were carried out for ten minutes at room temperature, using an excess of reagent. Slides were removed from the freezer and left to thaw for at least one hour prior to staining. This ensured that all the sections were stuck to the slide. Subsequently, three washes in TBS were undertaken to remove excess OCT. Then, 400 µL of blocking buffer (8% (v/v) goat serum in 0.3% (v/v) TBS-T was added to each slide for two hours at room temperature. A piece of parafilm was placed on top of each slide to cover the sections. This ensured solutions were retained on the sections, and the solutions did not evaporate. After this, the blocking buffer was removed and 400 µL of primary antibody diluted to the appropriate concentration in the same blocking buffer was added to each slide. Again, parafilm was placed on top of each slide. Slides were incubated in primary antibody overnight at 4 °C.

The following day, primary antibody solution was removed and slides were washed three times with TBS. Secondary antibody was diluted to the appropriate concentration in blocking buffer containing Hoechst at 2 µg.mL^{-1}. A volume of 400 µL was added to each slide. Parafilm was placed on top of each slide and slides were incubated for two hours at room temperature. Subsequently, three washes were undertaken in TBS, and a final wash in TNS. Slides were mounted using Fluorsave. The slides were covered in foil and stored at 4°C until imaging was undertaken (at most three days).

Imaging was undertaken using an upright confocal microscope. For each animal, three slides were imaged (one per region): caudal to the injury region, epicentre of the injury, and rostral to the injury region. On each slide, three sections were imaged. Subsequently, images were analysed using FIJI, using a similar method to previously described for cells in hydrogels (section 2.4.4.7). Images were evaluated using an automated macro similar to that used for H&E staining (appendix D.3).
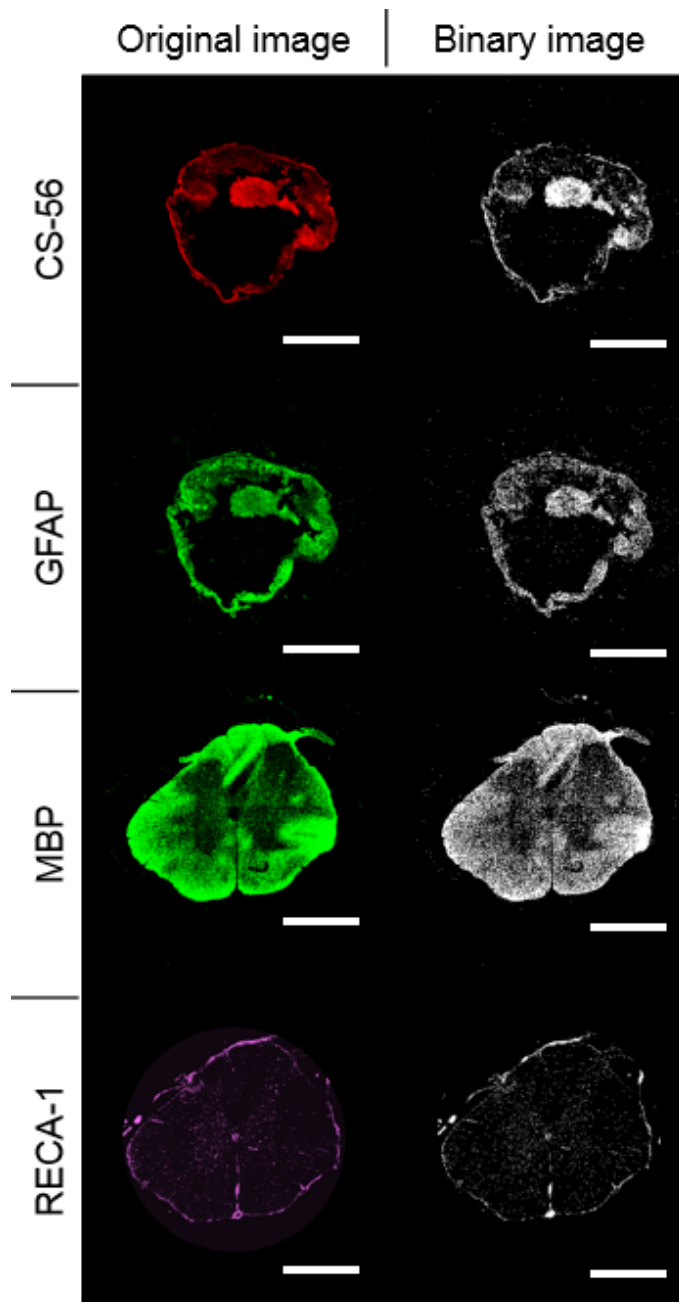
*Figure 2.11: **Example of image analysis for fluorescent labelled spinal cord sections.** Sections 40 μm thick were stained for various immuno-fluorescent markers. Imaging was undertaken on a confocal microscope. Subsequent image analysis was undertaken in ImageJ, creating a binary image using the Phansalkar image thresholding method. The stained area was then evaluated using this binary image. Scale bar = 1 mm*

In brief, for each fluorescent channel, stained regions were distinguished based on the Phansalkar local threshold method to produce a binary image (Figure 2.11). From this, the area of all the stained regions was analysed. For GFAP, CS-56 and MBP staining the area of immuno-staining was determined for each image using an automated macro, and then normalised as a percentage of the tissue present on the nearest H&E section. For RECA-1 labelling, only spinal cord parenchyma was evaluated (i.e. meninges and surrounding tissue were excluded). The average size of each stained object and the count of number of stained objects per image were assessed.

Chapter 3

In-vitro model development

3.1   Introduction

The aim of this project was to evaluate cellular responses to loading scenarios in NTSCI both *in-vitro* and *in-vivo*. The aim of this chapter in particular is to develop *in-vitro* methods to evaluate astrocyte responses to NTSCI. The introduction will outline the background, followed by methods used to develop the model, and the results of experiments using those methods. The discussion will critically appraise the wider scientific literature, describe the context of the results, and draw conclusions.

Three-dimensional environments are more physiologically relevant than two-dimensional environments for *in-vitro* models due to the presence of 3D matrix-cell interactions (Abu-Rub et al., 2010). Collagen hydrogels have been previously used to model a 3D environment to evaluate neural cell responses (East et al., 2010, 2012; Phillips, 2014a; Bar-Kochba et al., 2016; Smith, 2016; Kirk, 2018). In these studies, the collagen hydrogels supported neural cell survival, and allowed application of mechanical insults. In previous research at the University of Leeds, both the Infinite Horizon and BOSE 5110 Electroforce apparatus have been used to apply traumatic spinal cord injury insults to neural cell seeded collagen hydrogels (Smith, 2016; Kirk, 2018).

The Infinite Horizon impactor was used to model traumatic spinal cord injury in

astrocyte-seeded collagen hydrogels (Smith, 2016). However, this apparatus does not allow control of displacement and velocity parameters which are crucial in differentiating TSCI and NTSCI (Presysin, 2019). Subsequent research used the BOSE 5110 Electroforce apparatus to compress astrocyte-seeded collagen hydrogels at 3000 mm.s^{-1} (Kirk, 2018). However, no mechanical data such as load, output velocity or maximum displacement were reported from impaction experiments. Nor were mechanical outputs of the apparatus compared with input parameters, i.e. neither verification (checking the device compared to specification) nor validation (checking the device and specification captures the user's needs). Kirk (2018) described recoil of the system at impaction, leading to a secondary ramp at 3 mm.s^{-1} being required to impact the final 0.1 mm of the hydrogel. The cause of this was hypothesised to be recoil due to the elastic properties of the gel, but the system was not tested in air, which would have determined if the recoil was indeed due to the gel properties, or inherent to the apparatus. Questions remain regarding the mechanical outputs of the apparatus at high velocity parameters, and no testing or characterisation has been carried out at low velocity parameters. Accurate and precise application of velocity is core to differentiating TSCI and NTSCI.

This chapter aimed to estbalish a reliable method for using the BOSE 5110 Electroforce to apply controlled and reproducible uniaxial compression to hydrogels to mimic relevant loading scenarios in spinal cord injury (both TSCI and NTSCI). If this was the case, the displacement and velocity profiles input into the apparatus would closely match the output mechanical data. This would be apparent at every velocity tested, and both with and without gels present in the system.

Astrocytes are core to the pathology of TSCI, forming the glial scar (section 1.3.1). The effects of injury mechanics on astrocyte morphology have been studied *in-vitro* in a TSCI context (Section 1.4.2.2). The aim of this chapter was to establish a 3D astrocyte culture model.

To assess the cells in 3D culture, they were seeded into collagen hydrogels. In previous studies, collagen hydrogels have been seeded with primary astrocytes, with

cells remaining viable for up to 14 days (East et al., 2009; Smith, 2016; Kirk, 2018). Transforming growth factor beta (TGF-beta) has been used in several studies to induce spinal cord injury phenotypes in astrocytes (Table 1.6 in section 1.4.2). Treatment with TGF-beta induced reactive astrogliosis and glial scar formation (Logan et al., 1994; Vogelaar et al., 2015). Astrocytes in a 3D hydrogel environment treated with TGF-beta have previously shown increased GFAP expression (area per cell) and hydrogel contraction (Cullen et al., 2007; East et al., 2009). In this study, as in the previous research, the astrocyte-seeded hydrogels were treated with TGF-beta as a positive control for astrogliosis. By reproducing previous research, this can further validate the phenotype of the cell population; specifically in the context of spinal cord injury.

3.2 Aims

The aims of this chapter specifically were to develop methods of evaluating biological responses to loading scenarios representative of NTSCI *in-vitro*. This links to the aim of this whole project, which is to evaluate biological responses to loading scenarios representative of NTSCI both *in-vitro* and *in-vivo* (Figure 3.1). Specific objectives for this chapter:

1. To develop methodology to apply displacements and forces (of varying extent and speed) relevant to non-traumatic spinal cord injury *in-vitro*:

    A Determine the maximum velocity of the BOSE 5110 Electroforce apparatus.

    B Determine the effects of newly designed novel platens on mechanical outputs (displacement and maximum velocity) of the system.

    C Identify the optimal gel volume for use within the BOSE 5110 Electroforce apparatus.

    D Determine the effect of incorporating acellular collagen hydrogels at 2

mg.mL^{-1} and 5 mg.mL^{-1} into the system on displacement and velocity at various velocities (1000, 100, 10, 1 and 0.1 mm.s^{-1}).

E Determine the effect of working distance on displacement and velocity when hydrogels are incorporated into the system.

2. Develop and characterise a reproducible type I collagen hydrogel seeded with primary rat astrocytes, a relevant neural cell type:

A Evaluate the percentage of cells isolated from rat primary mixed glial cell preparations which are positive for GFAP expression (using immuno-labelling), and cell death using ethidium homodimer and Hoechst staining on coverslip culture after three days in culture.

B Evaluate cell viability using ethidium homodimer and Hoechst staining of primary astrocytes at days 1, 4, 7, 11 and 14 after seeding in rat collagen I hydrogels.

C Evaluate the effects of 10 ng.mL^{-1} TGF-beta treatment on primary rat astrocyte viability in 3D rat collagen I hydrogels using ethidium homodimer and Hoechst staining, and area using GFAP immuno-labelling at days 1, 4, 7, 11 and 14 post-seeding.
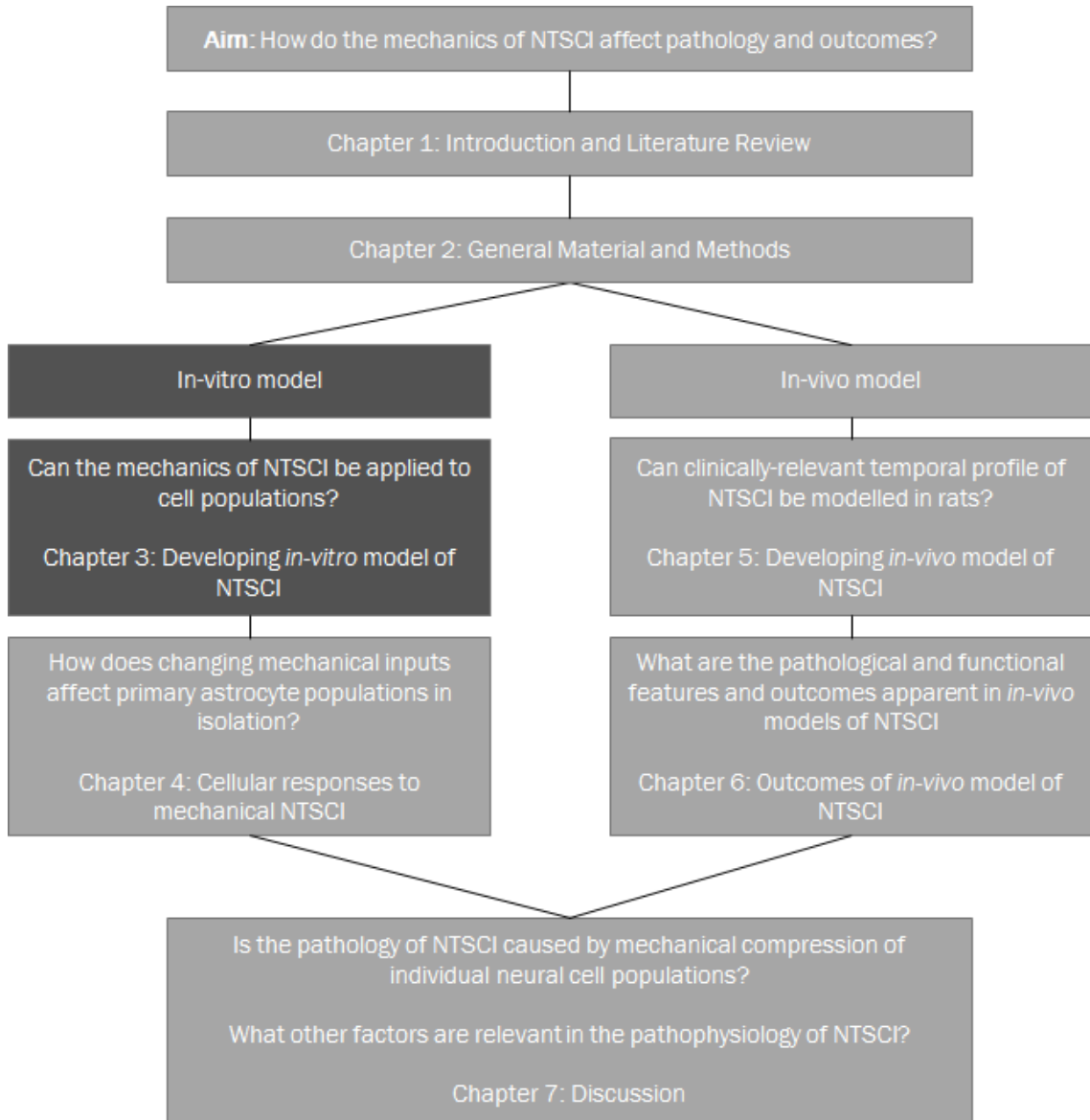
Figure 3.1: **Hypothesis and research questions asked in Chapter 3, relating to the whole study.**

3.3   Experimental Setup

An overview of the methods used in relation to the aims and objectives provides further detail and context for this chapter, developing models of spinal cord injury *in-vitro*. This chapter has two parts: verification and characterisation of the BOSE 5110 Electroforce system, and evaluation of the astrocyte cell population. Each will be discussed in turn. (Figure 3.2).

3.3.1   Characterisation of the BOSE 5110 Electroforce System

Methods used in this section, and relation to objectives, are detailed in Figure 3.2.

The BOSE 5110 Electroforce system (described in section 2.3.1) allows uni-axial compression or tension of a material, with control using a P.I.D tuning system. A schematic representation of the apparatus depicts the setup with connection to a reservoir bottle with media (Figure 3.3). Upon initial setup of the apparatus, the zero position was noted as the displacement when the motor and load platens touched (as determined by a change in load of over 0.1N). These were subsequently moved apart using the WinTest software, the sample loaded in, and chamber closed. The platens were subsequently moved slowly together using the WinTest software in increments of 1 to 10 μm until surface tension caused the sample to adhere to the load platen. This meant gel height could be recorded relative to the zero position.

Figure 3.2: ***Aims, objectives, and methodologies used in Chapter 3: Verification of the BOSE 5110 Electroforce and evaluation of astrocyte populations.***
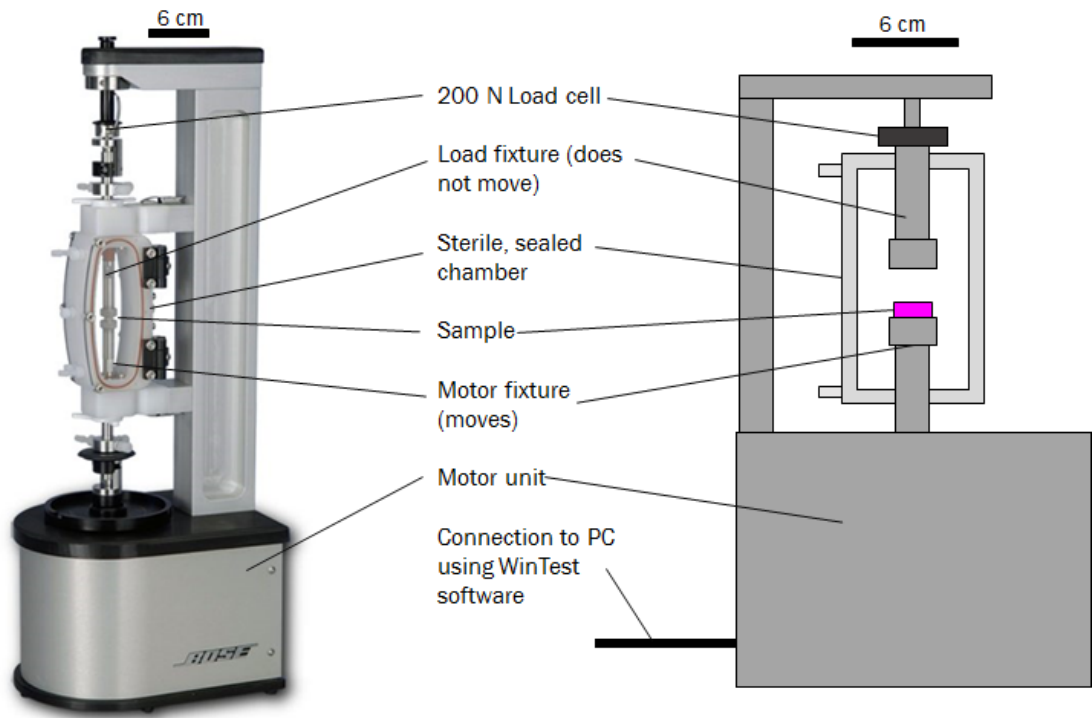
Figure 3.3: **Photograph and schematic diagram of the BOSE 5110 Electroforce apparatus loaded with hydrogel sample.** *Photograph from suppliers website (TAInstruments, 2016)*

3.3.1.1 Evaluation of BOSE 5110 Electroforce Mechanical Parameters with New Platen Fixtures

The original platen fixtures for the BOSE 5110 Electroforce were not flat, and the outer portion of the platen surface was raised compared with the internal disc portion (Figure 2.1 in section 2.3). This could have lead to discrepancies in measuring gel height. Further, during compression experiments the outer edges of the gel would have been compressed more than the central portion i.e. compression would not be uniform across the sample. New platens were designed and manufactured to overcome these issues (Figure 3.4). Platens A and B were provided with the apparatus. Platen C was a new platen for the upper load fixture to apply the compression uniformly. Platen D and E were two new platens for the motor fixture where the sample was loaded. Platen E was completely flat. Platen D had a central indented portion, to prevent sideways slippage of the sample.
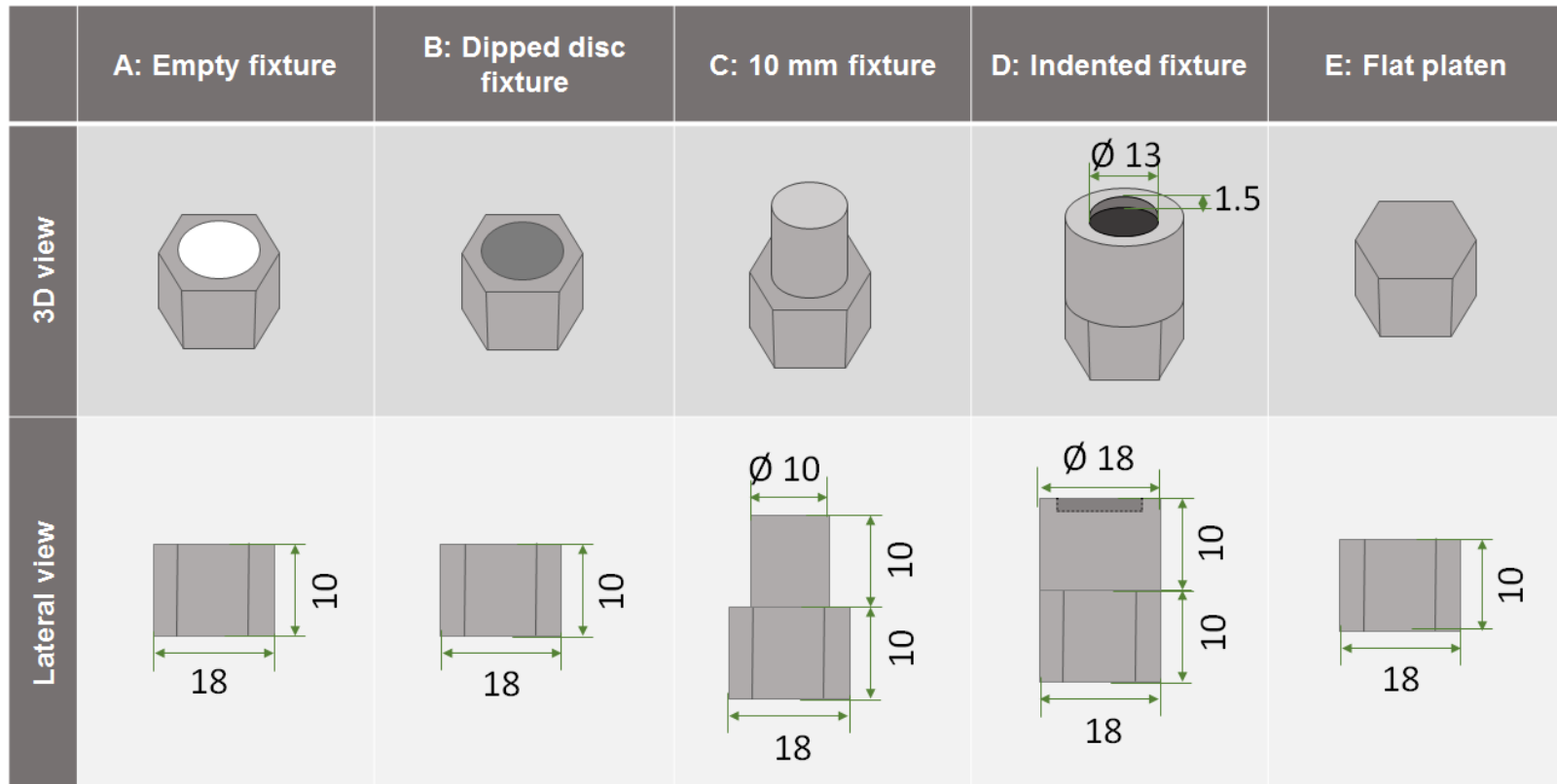
*Figure 3.4: **Platens designed for the BOSE 5110 Electroforce.** The 'disc' (B) and 'empty' (A) platens were provided with the instrument itself, and the others were designed and manufactured in house at the University of Leeds. Platens were made of 316L stainless steel. All measurements are in millimetres*

The proportional, integral, and derivative (P.I.D.) control system of the apparatus was calibrated from the supplier, with tuning undertaken in air at 1000 mm.s^{-1} over 12 mm. P.I.D. values were 0.536222, 0.008357 and -2.26814 respectively. Using these P.I.D. values, the inertia of novel platen fixtures were tested. They were first weighed three times each; and then affixed to the motor plate in turn. A trapezoid displacement profile was used; comprising a 0.1 second dwell, ramp to a displacement of 10 mm at 3000 mm.s^{-1}, a 10 second dwell, then ramp back by -10 mm at 3000 mm.s^{-1}. This was repeated four times for each platen fixture. Displacement over time was recorded, and from this velocity was calculated. Statistical analysis was undertaken using two-way ANOVA with Tukey's post-hoc test. Mass and displacement correlation was determined using linear regression in Microsoft Excel. The standard error of the correlation coefficient was determined using the following equation, where y was the true value of y (velocity), $\hat{y}$ was the predicted value of y, and n was the number of data points.:

$$\text{Standard error of the correlation coefficient} = \sqrt{\frac{\sum(\hat{y}-y)^2}{n-2}}$$

3.3.1.2 Use of Hydrogels in the BOSE 5110 Electroforce System

Evaluating Gel Height: Varying Well Plate Size and Gel Volume

This preliminary experiment created individual acellular collagen gels of various volumes, using the methods described in section 2.4.3. The gels were made of neutralised rat collagen I, and were acellular; substituting media alone for media containing cells. Gels were created with the end volumes of 250 µL, 500 µL and 750 µL in a 48 well plate, and 300 µL, 600 µL and 1000 µL in a 24 well plate (n = 1 per condition). Gels were placed in to the BOSE 5110 Electroforce, and their heights measured using methods described in section 3.3.1. Linear regression between volume and gel thickness was determined using Microsoft Excel. The standard error of the correlation coefficient was determined using the equation described in the previous section.

Reproducibility of Gel Height

In all subsequent studies where hydrogels seeded with rat primary astrocytes at 1x10^6

cells.mL^{-1}, gel volume and corresponding gel heights were measured. This allowed evaluation of variation of the gel heights based on gel volume. All of the gels were made in a 48 well plate, and either comprised a volume of 300 or 400 μL.

3.3.1.3 Mechanical Outputs of the BOSE 5110 Electroforce System Incorporating Hydrogels

Mechanical outputs of the BOSE 5110 Electroforce system were determined with hydrogels present compared with air alone. The gels used were acellular bovine collagen hydrogels with a volume of 400 μL and a collagen density of either 2 mg.mL^{-1} or 5 mg.mL^{-1}. Four gels were seeded for each data point. The motor platen used was entirely flat (platen E, figure 3.4), and the load platen had a 10 mm diameter (platen C in figure 3.4). The experimental profile was a symmetric trapezoid; comprising movement to the desired displacement at the desired velocity, a 0.1 s dwell, and return to initial displacement at the same velocity. Displacement and time were recorded throughout each test. During the initial displacement ramp, maximum velocity was noted and mean velocity was calculated. Statistical analysis was undertaken using two-way ANOVA with Tukey's post-hoc test.

Gels were set in a 48 well plate, thus had a diameter of 11 mm (Corning, 2008). The load platen with a diameter of 10 mm compressed over 80% of the gel cross-sectional area. Theoretical velocities of 0.1, 1, 10, 100 and 1000 mm.s^{-1} were used. Preliminary testing (data not shown) identified that a working distance of 1.5 mm was sufficient to reach all maximum velocities except 1000 mm.s^{-1}; where a working distance of at least 8 mm was required. Therefore, hydrogel compression was carried out at two working distances; from 6.5 mm above the upper gel surface (i.e. total working distance 8 mm) and from 0 mm above the gel surface (i.e. touching the gel, total working distance 1.5 mm). The same working distances of 8 mm and 1.5 mm were used in air.

3.3.2   Methods for Evaluating Astrocyte Cell Populations

Before experiments could be undertaken which evaluated astrocyte responses to varying mechanical inputs, the cell population itself required evaluation (Figure 3.2). This included assessing the proportion of astrocytes in the cell population, cellular viability and growth within hydrogels, and response to TGF-beta (a compound previously shown to induce spinal cord injury-like phenotypes in astrocytes (East et al., 2009), Table 1.6 in section 1.4.2). Further, these studies allowed characterisation of the assays to monitor cellular responses.

3.3.2.1   Determination of the Proportion of Astrocytes in Enriched Mixed Glial Populations

Astrocytes were the neural cell used in this study, since they have a role in sensing mechanical changes in the local environment (section 1.2.2). The primary cell isolation method used the entire cortex of a rat to extract mixed glial cell populations (described in section 2.4.2.4). Even after enriching astrocyte populations, there was a possibility that the primary cells isolated could include microglia from brain tissue, fibroblasts from the meninges, or other cellular contaminants. Therefore, the proportion of astrocytes in enriched mixed glial populations had to be established.

Mixed glial cells were isolated from four P3 pre-weaner rats (Section 2.4.2.4). These were seeded into two PDL-coated T75 flasks, and after 14 days astrocytes were enriched using methods described in section 2.4.2.4. The remaining cell population was further cultured for two days before being dispensed on to six PDL-coated 22 mm^2 coverslips at 3.6×10^4 cells per mL (as per previous study (Smith, 2016), methods described in section 2.4.2.6). After a further three days in culture, coverslips were stained with a combination of the live/dead assay and immunocytochemistry. This comprised ethidium homodimer (the dead component of the live/dead assay) incubation for one hour (methods in section 2.4.4), followed by immunocytochemistry for GFAP expression with Hoechst

counterstain (methods in section 2.4.4.3). The experiment was repeated in triplicate. Controls included a positive cell death control, where staining was preceded by a 30 minutes 70% (v/v) ethanol incubation; and negative antibody controls including using TBS instead of the primary antibody, and using an IgG isotype control.

Coverslips were imaged on the widefield microscope (Zeiss, Axio Imager M2), identifying all cells with Hoechst staining; dead cells with ethidium homodimer staining, and cells expressing GFAP using antibody-labelling. Image analysis took place using automatic tools (counting Hoechst and ethidium stained cells) and manual counting (number of cells stained with GFAP).

3.3.2.2 Astrocyte Viability and GFAP Expression in 3D Collagen Hydrogels

After evaluation in 2D, the cells isolated using the same methods were evaluated in a 3D collagen hydrogel environment. Positive control samples were treated with TGF-beta; a chemical known to stimulate astrocyte reactivity. Over two weeks, the astrocyte response (GFAP expression and viability) were recorded with and without TGF-beta treatment. The total number of cells were also recorded. This was carried out using Hoechst staining (total number of cells), ethidium homodimer staining (number of dead cells) and GFAP immuno-labelling.

Primary mixed glial cells were isolated from six P3 pre-weaner rats. After 14 days, microglia were removed using shaking at 250 rpm for four hours (as described in section 2.4.2.4) to obtain astrocyte-enriched cultures. These cells were seeded into 300 μL collagen hydrogels in a 48 well plate at 1×10^6 cells.mL^{-1}. This cell concentration has been used previously in the literature for astrocytes in 3D hydrogel matrices. For instance (Smith, 2016) used an astrocyte density of 1×10^6 cells.mL^{-1} in a collagen hydrogel model, and (Cullen et al., 2007) used an astrocyte density of 1.25×10^6 cells.mL^{-1} in Matrigel.

Time points used were days 1, 4, 7, 11 and 14 post-seeding. Six gels were seeded per timepoint, three untreated and three treated with 10 ng.mL^{-1} TGF-beta within the media. Staining was visualised using the confocal microscope (10x objective), 5 random fields of

view were evaluated per gel, with each comprising a 7 x 10 μm Z stack (total depth 60 μm). Additionally, images were taken of one treated and one untreated gel at 20x magnification per time point. These images comprised a 9μm Z stack (10 x 1 μm slices) and allowed evaluation of GFAP expression phenotype at higher resolution. Image analysis was carried out on images taken with the 10x objective, identifying dead cells (ethidium-stained), all cells (Hoechst-stained) and GFAP expression. Image analysis was undertaken using automatic cell count tools in FIJI to determine the number of nuclei (Hoechst staining) and number of dead cells (ethidium staining). To quantify area of GFAP per image, the green channel image (due to the secondary antibody used) was used. Areas with staining were distinguished from the background using the Phansalkar method (as described by Smith (2016)). Further details are described in Section 2.4.4.7. Total area of staining per image was evaluated. Statistical analysis used two-way ANOVA comparing untreated and treated gels over time. A p value of <0.05 was deemed significant, and Tukey's post-hoc test was used to subsequently identify significant differences.

A contraction assay was used to characterise the gel contraction over time (methods described in section 2.4.4.8). Gel contraction by astrocytes is indicative of reactivity. To achieve this, photographs were taken of the treated and untreated gels at day 11 and day 14. These were the longest timepoints for the experiment, and other studies have shown that TGF-beta response is greatest at longer timepoints (up to 15 days after cell seeding) (Cullen et al., 2007). Percentage gel contraction was measured by measuring the area of the well itself, and the gels contained within. This was achieved using FIJI software, manually drawing around each feature, and using the 'measure' tool to quantify area. Mean percentage differences in area between the well and gel were then calculated.

Statistical analysis was carried out in Microsoft Excel, using the Real Statistics add-in. Two factor regression ANOVA was used for image analysis data, with Tukey's post-hoc test (significance level of p <0.05). Comparisons were made between the total area of GFAP expression; and proportion of viable cells. For contraction assay results, an unpaired t-test was carried out with a significance level of p <0.05.

3.4   Results

3.4.1   The BOSE 5110 Electroforce was accurate at low velocities, but less accurate at over 100 mm.s^{-1}

The BOSE 5110 Electroforce apparatus was able to compress collagen hydrogels with control of either load or displacement parameters. However, the system had not been validated in the literature to have been used for this purpose. Input and output parameters had not been compared to evaluate the accuracy of the apparatus. Nor had the optimal gel height for working with the apparatus been established. The initial aims of this study were to characterise the mechanical output of the BOSE 5110 Electroforce system, test new fixtures, and optimise the use of collagen hydrogels in terms of gel volume and height.

3.4.1.1   Maximum velocity of the BOSE 5110 Electroforce did not match the input velocity, but did not change with introduction of new platens

The experiment described in this section aimed to determine the mechanical outputs of the BOSE 5110 Electroforce apparatus using previously supplied and newly manufactured platens. This included maximum velocity, displacement and inertia correlated this with mass (see chapter 2, methods section 3.3.1.1; Figures 2.1 and 3.4). Platens were weighed and then affixed to the motor shaft. Outputs were determined by recording displacement and time using input parameters of 10 mm displacement at 3000 mm.s^{-1}. Displacement and velocity were correlated with mass.

The velocity profile output did not reach the theoretical velocity input parameters The maximum input velocity was 3000 mm.s^{-1}, whereas the output velocity was 1440 mm.s^{-1} (across all platen fixtures). Further, a positive velocity (i.e. movement of the platen upwards) was observed in the output velocity. Comparing the different platens to each other, there was no significant difference in maximum output velocity (p >0.05).

The theoretical input and experimental output displacement profiles matched more closely than the velocity profiles (Figure 3.5). The maximum displacement of -10 mm was achieved in all tests, although there was a time delay of approximately 0.08 seconds in all cases. There was an effect of displacement recoil with all platens.
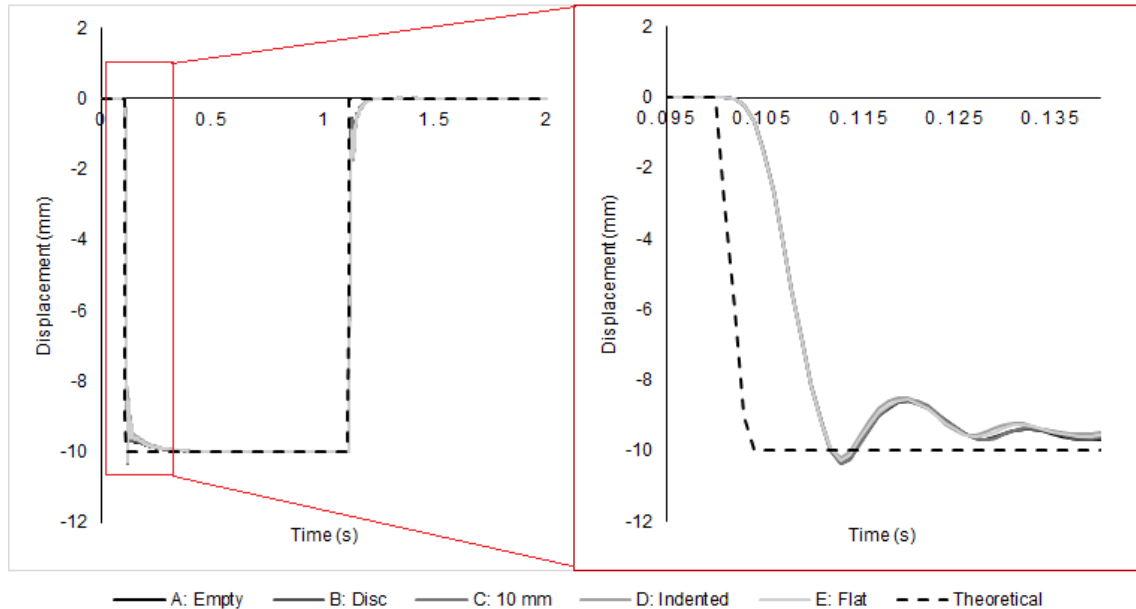
Figure 3.5: **Experimental displacement profiles of various platen fixtures in the BOSE 5110 Electroforce.** *Data series for platens overlap and are not distinguishable on the graph. The theoretical experimental profile was upward displacement of 10 mm at 3000 mm.s^{-1}; dwell for 10 seconds, downward displacement of 10 mm at 3000 mm.s^{-1}.*

At the timepoint when theoretical displacement first reached 10 mm (0.107 seconds), experimental displacement for each platen was noted. An increase in mass was associated with a reduction in displacement, with a linear correlation coefficient of 0.76 and (Figure 3.6). The largest difference in displacements at this timepoint was just 49 μm, and differences were not statistically significant (p >0.05). These values were recorded at a velocity of 1440 mm.s^{-1}.
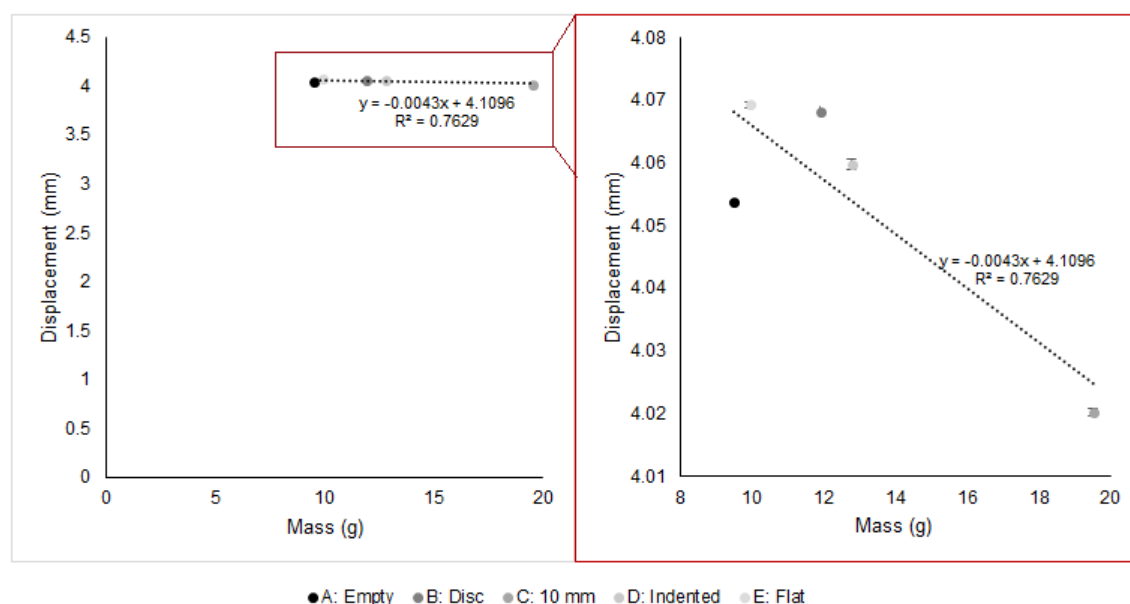
Figure 3.6: ***The effects of mass on the displacement of various platen fixtures in the BOSE 5110 Electroforce at a single time point.*** *Time point selected was 0.107 seconds; when theoretical displacement first reached 10 mm. Data shown with the y-axis from zero (left) and, for clarity, with a modified y-axis scale (right). n = 4 each data point. Data shown is mean ± S.E.M. (S.E.M. is in the order of 0.0001 to 0.001 mm)*

3.4.1.2 Hydrogels were easily incorporated and optimised for use within the BOSE 5110 Electroforce system

To characterise the BOSE 5110 Electroforce system mechanical outputs using collagen hydrogels, gels had to be of sufficient height to account for the precision of the apparatus; as well as to allow handling (loading and unloading from the apparatus itself). The first subsection herein describes a preliminary experiment for assessing collagen hydrogel height; and the second describes the apparatus mechanical outputs of the apparatus when hydrogels were in place.

To evaluate reproducibility in gel thickness, along with how gel volume equated to gel height, acellular gels of varying heights were produced as previously described (for methods, see section 3.3.1.2). Photographs of the gels in the BOSE 5110 Electroforce apparatus can be observed in Figure 3.7. The heights of gels fabricated in the 48 well

plate followed a linear regression with a correlation coefficient (R^2) of 0.9987, and a standard error of the estimate of 0.069. The correlation was lower for 24 well plate gels ($R^2 = 0.8963$, standard error of the estimate 0.64) (Figure 3.8). Based on the equations describing gel height, a volume of 400 µL in a 48 well plate, or 470 µL in 24 well plate was required for a gel height of 2 mm.

48 well plate			24 well plate		
250 µL	500 µL	750 µL	300 µL	600 µL	1000 µL
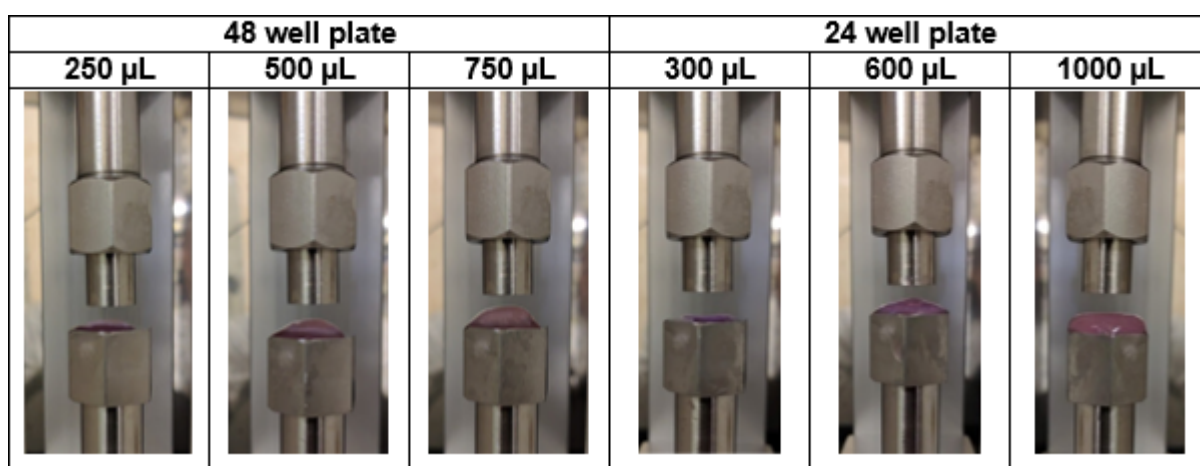
Figure 3.7: **Images of collagen hydrogels of varying volumes made in 24 or 48 well plates.** *Various gel sizes were created with the aim of creating a hydrogel between 2 and 3 mm in thickness. Gel height was assessed in the BOSE 5110 Electroforce*

The smallest gel volumes in each plate (250 µL in a 48 well plate, and 300 µL in a 24 well plate) were difficult to handle and remove from the plate. All other gel volumes were successfully handled; placed into and removed from the BOSE 5110 Electroforce without damage.
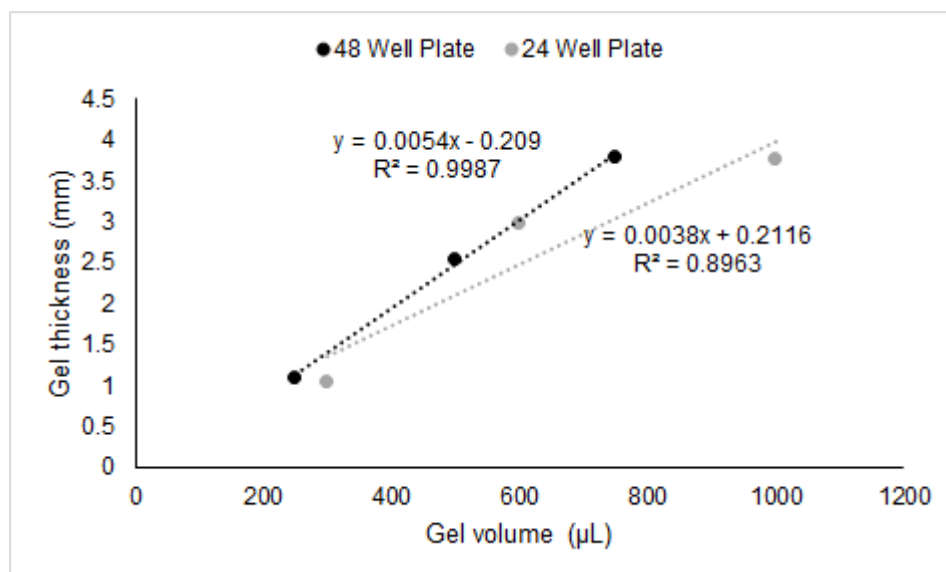
Figure 3.8: **Thickness of collagen hydrogels of varying volumes fabricatee in either 24 or 48 well plates.** *As measured using the BOSE 5110 Electroforce, by moving the motor platen upwards until the gel was touching the load platen (n=1 for each data point).*

Gel heights were reproducible

Gel height reproducibility was established by measuring gel heights in all subsequent studies where hydrogels were seeded with primary astrocytes at $1\text{x}10^6$ cells.mL^{-1}. Gel height was measured using the method described in section 3.3.1, and box plots of the data were established (Figure 3.9). The first six tests used gels 400 μL in volume in a 48 well plate, and had a mean gel height of 2.79 ± 0.047 mm. Subsequently, two following tests used gels of 300 μL in volume in a 48 well plate. These gels had a mean gel height of 2.05 mm $\pm$ 0.055 mm (73% of 2.79 mm). In both volumes, gel heights were consistently within 30% of the mean.
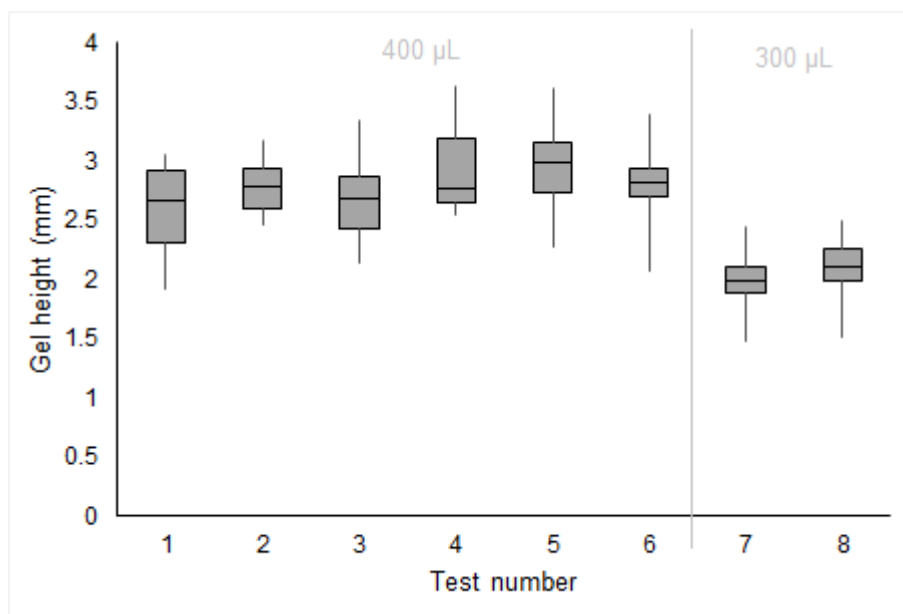
Figure 3.9: ***Box plot of gel heights of 300 and 400*** μ ***L collagen hydrogels.*** *The height of rat type I collagen hydrogels, seeded with primary astrocytes at 1x10^6 cells.mL^{-1} were measured using the BOSE 5110 Electroforce apparatus. Experiments 1 to 6 (inclusive) used 400 μL gels, and experiments 7 and 8 (inclusive) used 300 μL gels. n = at least 10 gels per experiment*

3.4.1.3 The mechanical outputs of the BOSE 5110 Electroforce system did not differ when 2 mg.mL^{-1} collagen hydrogels were introduced

A study was undertaken to characterise the BOSE 5110 Electroforce system, specifically comparing theoretical input and experimental output velocities over a variety of working distances.

The mechanical outputs of the BOSE 5110 Electroforce were tested using acellular collagen hydrogels (method described in section 3.3.1.3). Two densities of collagen I hydrogels were tested, 2 mg.mL^{-1} and 5 mg.mL^{-1}. Five theoretical velocities were tested 1000, 100, 10, 1 and 0.1 mm.s^{-1} at two working distances: 1.5 mm (from the top of the gel surface) and 8 mm (from 6.5 mm above the gel surface). Tests with gels were run four times, and tests in air (no gels) were run three times. In some gel tests, the gels slipped off the platens during compression and as such their results could not be included. The

number of samples per test were as follows:

- 5 mg.mL^{-1} collagen gels (all velocities and working distances) n=4

- Air (all velocities and working distances) n=3

- 2 mg.mL^{-1} collagen gels: 1000 and 100 mm.s^{-1} n=4

- 2 mg.mL^{-1} collagen gels: 10 and 1 mm.s^{-1} n=2

- 2 mg.mL^{-1} collagen gels: 0.1 mm.s^{-1} n=3

The target displacements (from 1.5 to 8 mm) were reached under every condition, velocity and working distance (Figure 3.10). Recoil of apparatus was observed at both working distances at 1000 mm.s^{-1}, and to a lesser extent at 1.5 mm at 100 mm.s^{-1} (A, B, C in Figure 3.10).

Maximum theoretical input velocity was reached in all but six tests (Table 3.1). Five of these were at 1000 mm.s^{-1}. The sixth was at 100 mm.s^{-1}, at a working distance of 1.5 mm with 5 mg.mL^{-1} collagen hydrogel present. At high velocities ($>$10 mm.s^{-1}), exceeding the theoretical velocity was due to overshoot on the compression ramp. At low velocities ($\leq$ 10 mm.s^{-1}), theoretical velocity was exceeded due to noise in the system.

In all tests, standard error of the mean compression velocity was small (errors bar in A to E, Figure 3.11). At 0.1 and 1 mm.s^{-1}, there were no significant differences in mean and theoretical velocities, nor based on working distance or condition. At 10 mm.s^{-1}, velocity was reached at both working distances for air and 2 mg.mL^{-1} collagen hydrogel. For the 5 mg.mL^{-1} collagen hydrogel, velocity was not reached at 1.5 mm, but was reached at 8 mm. At 100 mm.s^{-1}, increasing the working distance significantly increased mean velocity outputs from 92.5 to 96.5 mm.s^{-1} (p $<$0.05). With the working distance of 8 mm, theoretical velocity was reached in all conditions. At 1000 mm.s^{-1}, increasing working distance increased mean velocity output by 738 mm.s^{-1} (p $<$0.05). With a collagen hydrogel at 5 mg.mL^{-1}, this was still insufficient to reach the theoretical input value. In spite of the overshoot observed at the higher velocities, overall the displacement over time was maintained and stable for the duration of the experiment.

Table 3.1: **Maximum velocity output of the BOSE 5110 Electroforce apparatus, at various theoretical velocities, with and without hydrogels.** *Velocities were recorded with and without bovine type I collagen hydrogels present (collagen at 2 mg.mL^{-1} and 5 mg.mL^{-1}), at various combinations of theoretical velocity and working distance. Data shown are mean $\pm$ S.E.M. for between n = 2 and n = 4 tests. All data are significantly greater than the input velocity apart from those denoted by *: these are significantly lower than the input velocity (p <0.05)*

Distance	Condition	Theoretical input velocity (mm.s^{-1})				
		0.1 mm.s^{-1}	1 mm.s^{-1}	10 mm.s^{-1}	100 mm.s^{-1}	1000 mm.s^{-1}
1.5 mm	Air	0.18 ± 0.02	1.83 ± 0.17	15.00 ± 0.01	118.33 ± 1.67	241.67 ± 1.67*
	2 mg.mL^{-1} hydrogel	$0.32 \pm 3.4 \times 10^{-3}$	2.00 ± 0.02	15.00 ± 0.02	105.00 ± 2.04	215.00 ± 0.01*
	5 mg.mL^{-1} hydrogel	0.34 ± 0.02	2.00 ± 0.01	$15.00 \pm 1.6 \times 10^{-3}$	96.25 ± 1.25*	228.75 ± 1.25*
8 mm	Air	0.16 ± 0.01	1.98 ± 0.14	$12.00 \pm 1.9 \times 10^{-3}$	114.17 ± 0.83	963.33 ± 1.67*
	2 mg.mL^{-1} hydrogel	0.17 ± 0.01	1.79 ± 0.12	12.00 ± 0.01	116.25 ± 1.25	1022.50 ± 1.44
	5 mg.mL^{-1} hydrogel	0.17 ± 0.008	1.93 ± 0.09	12.00 ± 0.03	111.25 ± 1.25	992.50 ± 6.61*
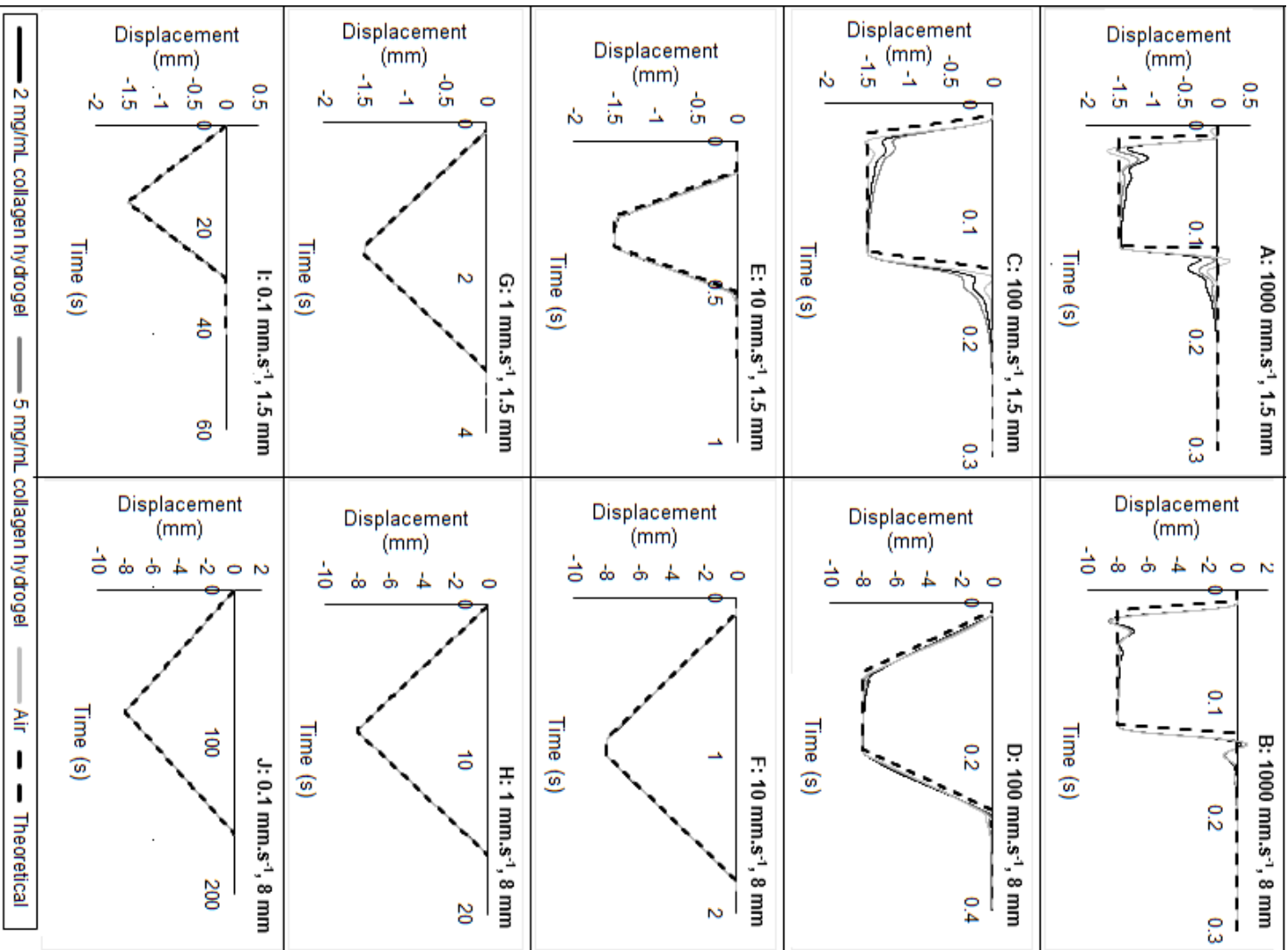
Figure 3.10: **Displacement profiles from the BOSE 5110 Electroforce, at various theoretical velocities, with and without hydrogels present.** *Displacement was recorded with and without collagen hydrogels present (collagen at 2 and 5 mg.mL⁻¹), at various combinations of theoretical velocity and working distance.*
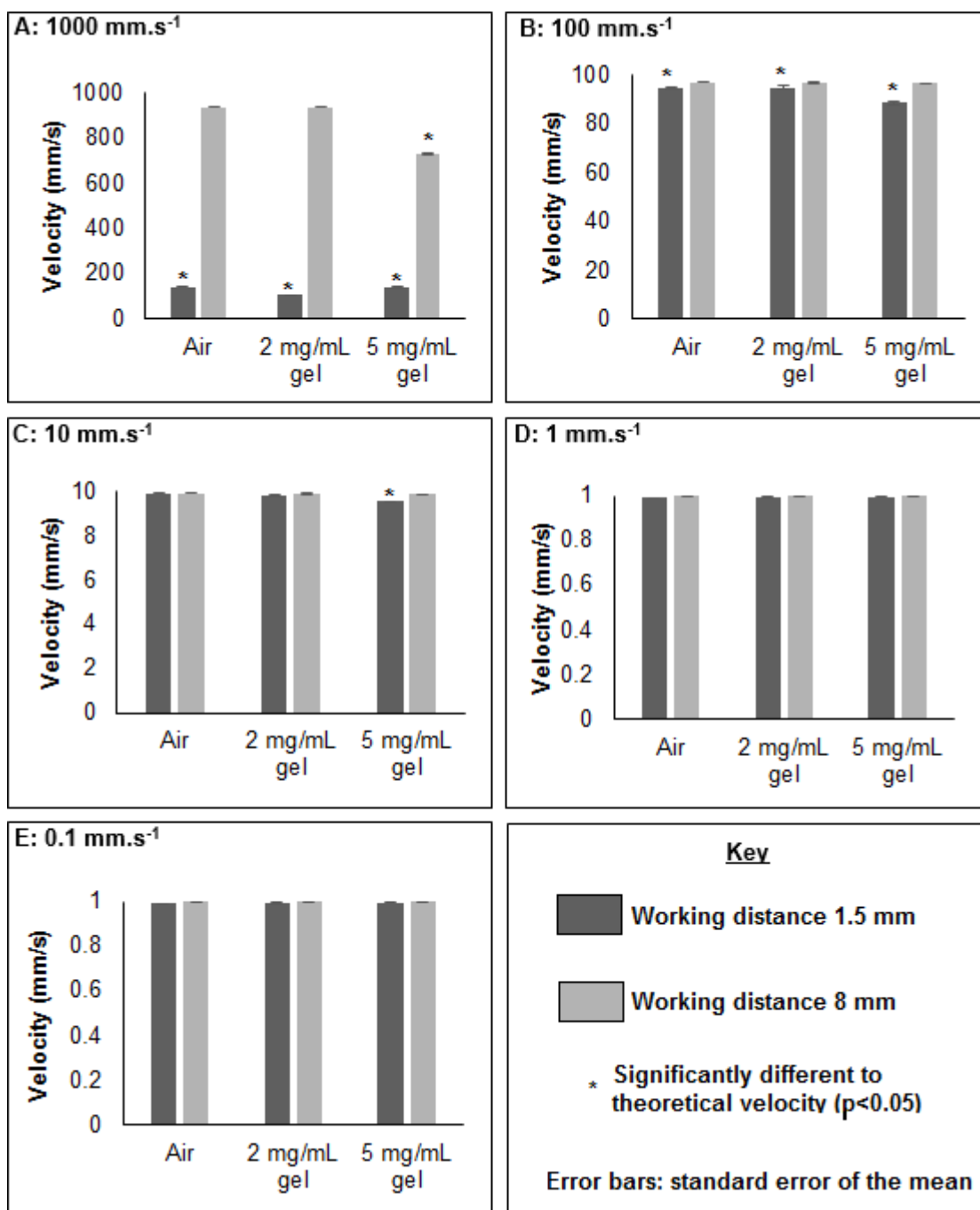
Figure 3.11: **Velocities produced by the BOSE 5110 Electroforce apparatus, with and without collagen hydrogels present.** *Theoretical velocities of 1000 (A), 100 (B), 10 (C), 1 (D), and 0.1 (E) mm.s^{-1} were tested in the BOSE 5110 Electroforce system, without gels present and with collagen hydrogels at 2 and 5 mg.mL^{-1}. Two working distances were used: 1.5 mm (from gel surface) and 8 mm (from 6.5 mm above gel surface). Data shown are mean values for the displacement ramp $\pm$ S.E.M.*

3.4.2   Establishment of 3D astrocyte culture model

The aim of this study was to evaluate neural cell responses to varying mechanical inputs. The cell type of interest was primary rat astrocytes. Before use in experimental studies applying mechanical insults, the cells themselves had to be evaluated in both 2D and 3D scenarios. For instance, identifying whether the extracted primary cells were predominantly astrocytes; evaluating cellular density in collagen hydrogels; and assessing physiological and pathological changes in GFAP expression.

3.4.2.1   Astrocytes in hydrogels were activated by TGF-beta.

The proportion of astrocytes was determined in a population of cell isolated from mixed glial cells which had been subjected to shaking for 4 hours at 250 rpm to remove microglia. Cells were seeded onto coverslips, and immuno-stained for GFAP. Cells which stained positively for both Hoechst and GFAP were considered to be astrocytes, whereas cells stained with Hoechst only were other cell types. Methods are described in section 3.3.2.1.

A total of 89.7 $\pm$ 3.5% of all cells were stained with GFAP. In the 70% (v/v) ethanol control, 100% of cells were stained with both ethidium-homodimer and Hoechst (i.e. were dead). Across the remaining samples, an average of 11.7 $\pm$ 2.9% of all cells were dead.

In order to characterise the 3D hydrogel astrocyte-seeded model used in this study, an experiment was undertaken evaluating cellular responses to TGF-beta treatment. Methods described in section 3.3.2.2. In brief, at 5 timepoints over 14 days, GFAP expression (a marker of astrocyte reactivity) was evaluated alongside ethidium homodimer staining (a marker of dead cells) in astrocyte seeded collagen gels treated with TGF-beta or untreated (n = 3 per timepoint for each condition).

In test gels incorporating cells treated with TGF-beta, the morphology of astrocytes changed from rounded (day 1) to increasingly ramified (day 14) (Figure 3.12). The area of GFAP expression per field of view was quantified using FIJI software. With TGF-beta

treatment, total area stained with GFAP increased by 227% over the 14 day experiment; conversely GFAP expression in untreated gels remained relatively constant (Figure 3.13). There was significantly more GFAP expression in TGF-beta treated cells versus untreated cells at day 14 ($p < 0.05$).

In untreated and TGF-beta treated gels, $13.5 \pm 3.3\%$ and $13.6 \pm 3.5\%$ (mean $\pm$ S.E.M) of cells were dead, respectively. Between days 1 and 14, the proportion of dead cells decreased by 90.8% for untreated cells, and 82.5% for TGF-beta treated cells (Figure 3.14). In both conditions, there was a significantly greater proportion of viable cells on day 14 than days 1 and 7 ($p < 0.05$). In TGF-beta treated cells, there were significantly more viable cells on day 14 vs day 4; and in untreated gels there were significantly more viable cells on day 11 vs day 7 ($p < 0.05$). There was no significant difference in viability between untreated and TGF-beta treated cells at any time point.
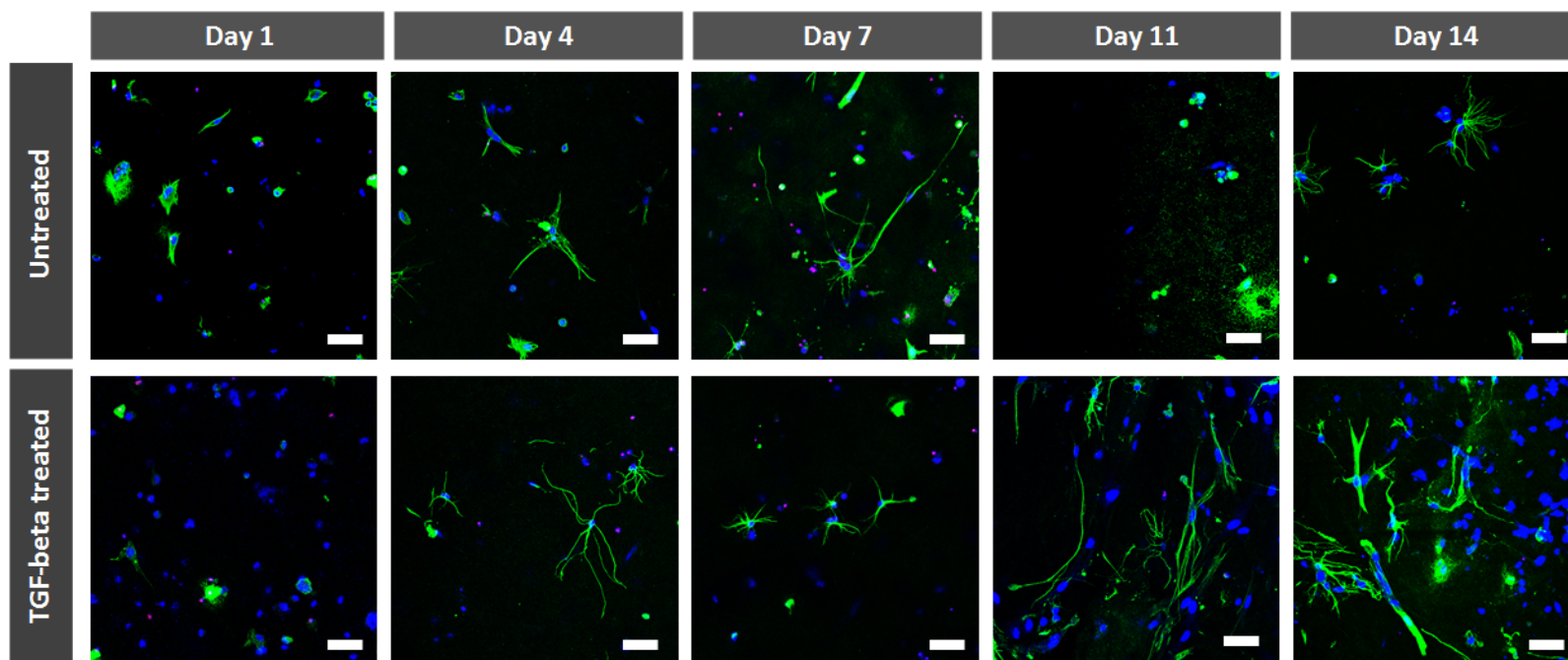
20X objective. Scale = 50 μm. Key: Hoechst(all cells) | GFAP (astrocytes) | Ethidium homodimer (dead cells) |

Figure 3.12: **Confocal microscope images, taken using 20x objective, of primary astrocytes in collagen gels, treated with TGF-beta** *Collagen hydrogels were seeded with primary astrocytes at $1x10^6$ cells.mL^{-1}; and immunostaining carried out at 5 timepoints over 14 days. GFAP expression is a marker of astrocyte reactivity*
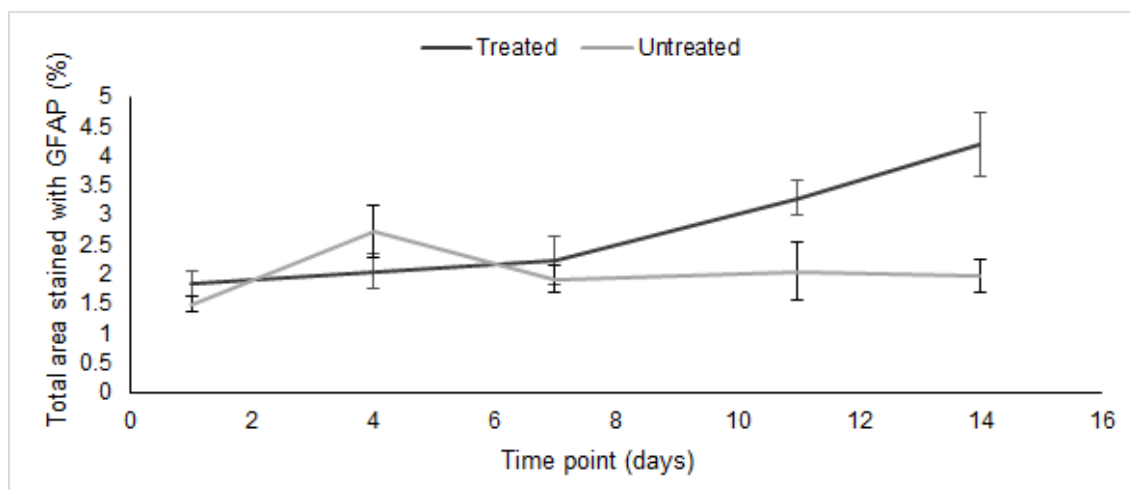
Figure 3.13: **Proportion of image stained positively for GFAP, in astrocyte seeded hydrogels** *Collagen hydrogels were seeded with primary astrocytes at $1x10^6$ cells.mL^{-1}; half of which were treated with 10 ng.mL^{-1} TGF-beta. Immunostaining was carried out at 5 timepoints over the 14 day experiment for GFAP; a marker of astrocyte reactivity. Area stained with GFAP was calculated using FIJI software. For each data point, n=3. Data shown is mean $\pm$ S.E.M.*
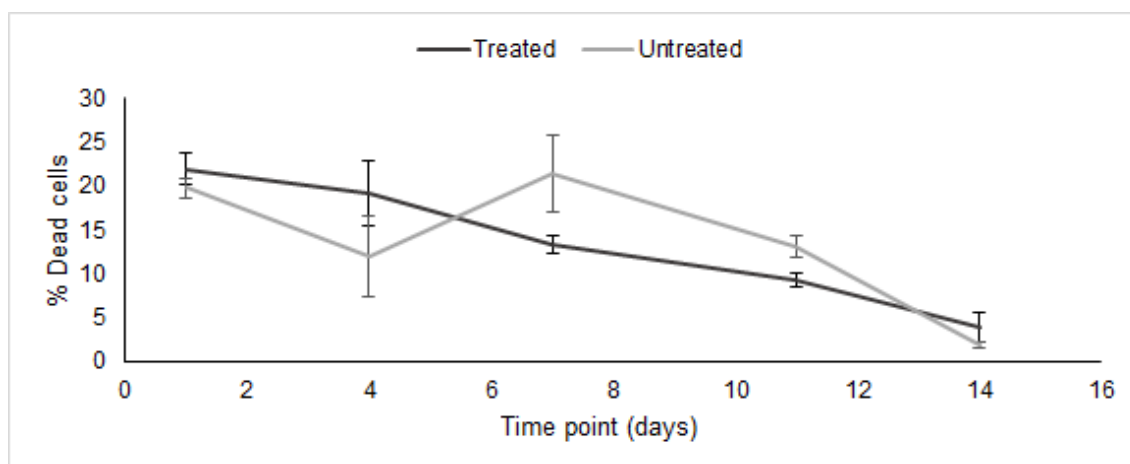
Figure 3.14: **Proportion of dead cells per image, in astrocyte seeded hydrogels** *Collagen hydrogels were seeded with primary astrocytes at $1x10^6$ cells.mL^{-1}; half of which were treated with 10 ng.mL^{-1} TGF-beta. Staining was carried out at 5 timepoints over the 14 day experiment for ethidium homodimer and Hoechst; markers of dead cells, and all cells, respectively. Dead cells were identified by both ethidium homodimer and Hoechst staining; whereas living cells stained with Hoechst only. Proportion of dead cells was calculated using FIJI image analysis software. For each data point, n=3. Data shown is mean $\pm$ S.E.M.*

3.4.2.2   Activated astrocytes induced hydrogel contraction

Hydrogel contraction, as a marker of cellular reactivity, was also measured in both untreated and TGF-beta treated astrocyte-seeded collagen gels on day 11 and day 14. On average over both days, TGF-beta treatment led to gel contraction of $48.6 \pm 2.77\%$ (mean $\pm$ S.E.M.) compared to their original gel diameter; whereas untreated gels contracted by $9.14 \pm 1.99\%$ compared to their original diameter at both timepoints (Figure 3.15), p <0.05 on both days).
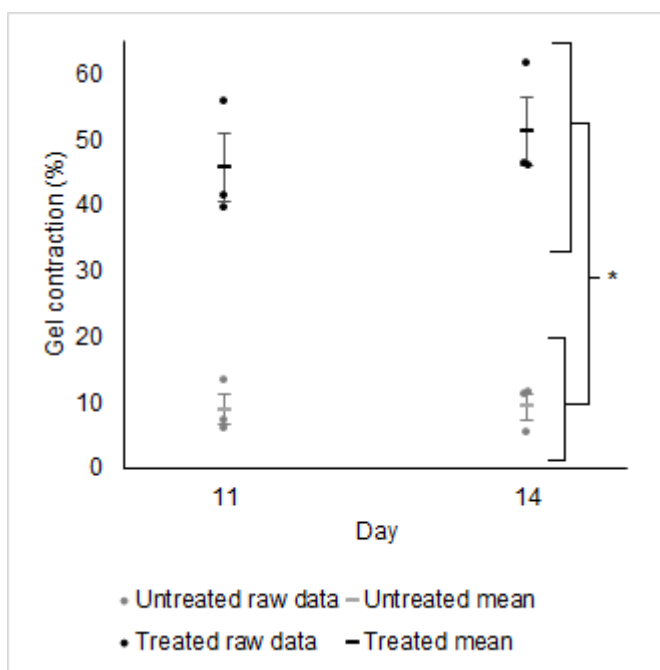
*Figure 3.15: **Gel contraction in TGF-beta and untreated collagen hydrogels, seeded with primary astrocytes** Collagen hydrogels were seeded with primary astrocytes at $1x10^6$ cells.mL^{-1}; half of which were treated with TGF-beta. Gel contraction was measured by taking photographs of the gels in a 48 well plate at day 11 and day 14 post-seeding. Images were analysed using FIJI; where gel area was compared with well area. For each data point, n=3. Data shown is mean $\pm$ S.E.M. * denotes p <0.05*

3.5 Discussion

3.5.1 Characterisation of the BOSE 5110 Electroforce Biodynamic System

It was hypothesised that the BOSE 5110 Electroforce Biodynamic system could be used to apply clinically relevant loading scenarios to seeded collagen hydrogels; mimicking spinal cord injury. This hypothesis was used in previous research to apply mechanical insults to neural cell seeded collagen hydrogels in the context of spinal cord injury (Kirk, 2018). However, the previous study did not characterise the actual mechanical outputs of the apparatus. To characterise the apparatus, mechanical outputs were recorded in air and with gels introduced into the system. The optimal gel size was established.

3.5.1.1 BOSE 5110 Electroforce Mechanical Parameters with New Platen Fixtures

The original platen fixtures for the BOSE 5110 Electroforce system had slightly indented central portion. To apply load and displacement with an even spatial distribution across the hydrogel surface, and to prevent gels slipping, new platens were manufactured. The volume and mass of these platens varied based on design specifications. The output displacement and velocity of the apparatus with each platen were recorded. Platen fixtures were attached to the motor platen, and a displacement profile comprising upwards motion at a theoretical velocity of 3000 mm.s^{-1}, and a displacement of 10 mm was applied. A displacement of 10 mm was applied since this gave 1 mm at either end of the displacement profile for uncontrolled movement without reached the limits (the total theoretical working distance of the apparatus was 12 mm).

At the maximum output velocity (1440 mm.s^{-1}), the effect of differences in platen mass led to a minimal difference in displacement of 49 μm. This was not statistically significant. As such, the mass of the platens will have little effect in the study, and any can be used in future experiments.

Displacement data closely matched between theoretical and experimental values. A recoil effect was seen in displacement profiles, as described in previous research (Kirk, 2018). This was identified as an effect of collagen hydrogels, and hypothesised it was due to elastic recoil of the gel. The results herein identified the recoil without any hydrogel present (i.e. in air). Therefore, it was due to workings of the apparatus, regardless of material present. One explanation is due to the abrupt change in momentum of the apparatus at high velocities. The apparatus cannot immediately change from 1000 mm.s^{-1} to stationary, and instead recoil occurs.

In velocity data, the theoretical maximum velocity was 3000 mm.s^{-1} whereas maximum recorded velocity was 1440 $\pm$ 1.27 mm.s^{-1}. By contrast, in previous research a velocity of 3000 mm.s^{-1} was stated but not tested (Kirk, 2018). Impact velocity is important in NTSCI, and distinguishes it from TSCI. Further evaluation of theoretical input and experimental output velocities of the BOSE 5110 Electroforce apparatus was required over a range of velocities.

3.5.1.2 Using Hydrogels in the BOSE 5110 Electroforce System

The ideal gel would be substantial enough to minimise the effects of errors in measuring gel height, and have sufficient mechanical properties to physically load and unload the gels from the BOSE 5110 Electroforce apparatus without damage. A lower volume would be beneficial in terms of maximising the use of reagents, and reducing the number of animals required in primary cell experiments.

In an experiment varying the volume and diameter of gels, those with a height of less than 2 mm were difficult to handle and were easily damaged when moving from the well plate into the BOSE 5110 Electroforce apparatus. The minimum suitable volume was 400 μL in a 48 well plate, or 470 μL in a 24 well plate. The low N number and use of acellular gels in this experiment meant further testing was needed to confirm the gel height requirement using repeated measurements of cellular gels. Since the 48 well plate used lower reagent quantities per gel to achieve the height, 400 μL was carried forward

due to its cost-effectiveness.

In cellular 400 μL gels from a 48 well plate, the mean height was 2.79 mm. In cellular 300 μL, the mean height was 2.05 mm. If the gels were perfectly cylindrical the difference would be 15% (based on the volume of a cylinder). A difference of 27% was observed, where the gels were unlikely to be perfectly cylindrical. At least n = 4 gels were measured per test, and at least 3 tests were carried out for each volume (i.e. n = 12). The cellular hydrogels had a greater height than acellular hydrogels. This may be because the cellular components in the gel facilitate fluid retention and therefore height is maintained. Further, the initial study using acellular hydrogels had n = 1 per volume and well plate variation. Conversely, the cellular hydrogel study had a greater number of gels created at each volume. As such, the cellular study is more relevant and has greater power.

The volume of 300 μL gels in a 48 well plate used the least reagents but had sufficient height, and hence was used in all future experimental studies.

3.5.1.3   Mechanical Outputs of the BOSE 5110 Electroforce System

Experiments were undertaken to characterise velocity and displacements outputs by the BOSE 5110 Electroforce system, at a variety of theoretical velocities and working distances. Further, the effect of incorporating gels into the system (as opposed to experiments carried out in air) was evaluated. Bovine collagen was used as opposed to rat collagen, in order to preserve the rat collagen reagent and save costs (bovine collagen was cheaper). Further, the bovine collagen was purchased at a greater concentration (5 mg.mL^{-1}), allowing evaluation of a more concentrated collagen concentration than used previously (Smith, 2016; Kirk, 2018). Further, two collagen concentrations were tested: 2 and 5 mg.mL^{-1}.

The mechanical properties of various densities of collagen hydrogels have been examined in the literature, repeatedly showing that elasticity reduces with increased density (Roeder et al., 2002; Ahearne et al., 2010; Lopez-Garcia et al., 2010). For instance, in one study, 5 mg.mL^{-1} collagen gels had a shear modulus three to six times

greater than 2 mg.mL^{-1} collagen gels (Valero et al., 2018). In this research, there was no consistent difference in displacement, maximum or mean velocity of the BOSE 5110 Electroforce using 2 mg.mL^{-1} collagen gels compared to air. Differences were present when using 5 mg.mL^{-1} collagen gels, at a working distance of 1.5 mm. At 1000, 100 and 10 mm.s^{-1}, incorporation of 5 mg.mL^{-1} collagen hydrogels led to a significant reduction in mean output velocity versus the theoretical input. No differences were observed between air and 2 mg.mL^{-1} collagen hydrogels.

Throughout each test, displacement was tightly controlled. Maximum and mean velocity values of each test had low standard errors of the mean. This indicated that apparatus could apply precise and reproducible profiles to air and gels. The BOSE 5110 Electroforce apparatus used a displacement control setting to achieve this.

Maximum output velocity exceeded input velocity at 10, 1 and 0.1 mm.s^{-1}, with a greater effect at lower working distances. In these tests, the number of data points collected during their duration was the same as at greater working distances (e.g. 2000 data points over 8 mm displacement; and 2000 data points over 1.5 mm displacement). Due to limitations in the apparatus precision this resulted in an increase in noise.

Working distance affected velocity outputs at 1000 and 100 mm.s^{-1} input velocities. For 100 mm.s^{-1}, increasing the working distance from 1.5 to 8 mm led to an increase in mean output velocity from 92.5 to 96.5 mm.s^{-1}. At 1000 mm.s^{-1}, increasing the working distance led to a significant increase in mean output velocity from 128.6 to 866.5 mm.s^{-1}. The reason for the greater working distance required at greater velocities was the acceleration capacity of the device (as mentioned by Kirk (2018)), which was not incorporated into the apparatus software when designing the theoretical experimental profiles (Figure 3.16). According to the supplier's website, the BOSE 5110 Electroforce has a maximum deformation rate of 740 mm.s^{-1} (TAInstruments, 2016). The fact that 1000 mm.s^{-1} input velocity exceeded the suppliers expectations for the apparatus could have contributed to the reduced accuracy of the instrument at such velocities; it may have been out of the range of the apparatus. As such, 1000 mm.s^{-1} was not used in future
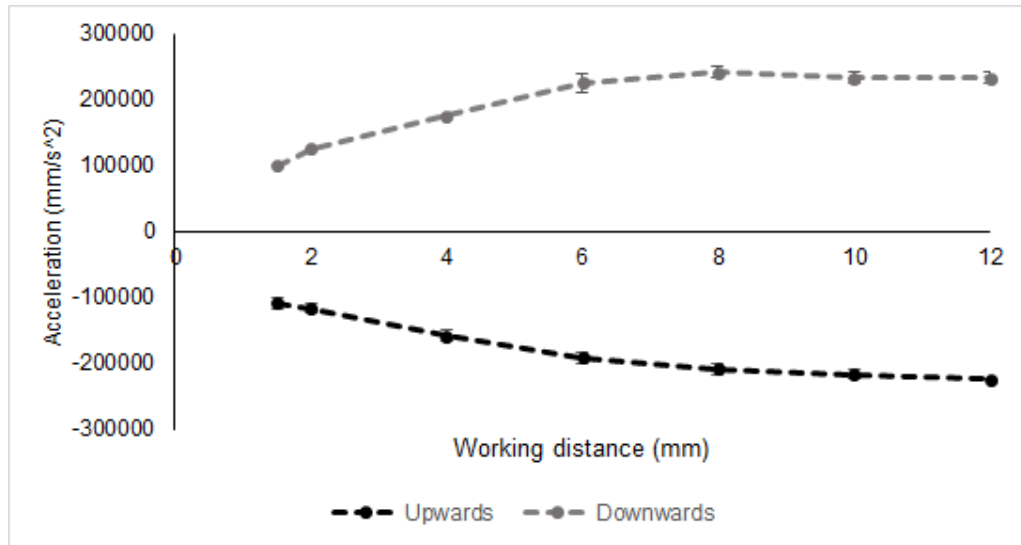
*Figure 3.16: **Acceleration upwards (negative values) and downwards (positive values) elicited by the BOSE 5110 Electroforce at 1000 mm.s^{-1}** At a theoretical velocity of 1000 mm.s^{-1}, acceleration was recorded for both upwards and downwards motion at a range of working distances.*

experiments to prevent damage. For 100 mm.s^{-1}, the mean velocity of 92.5 mm.s^{-1} at 1.5 mm was deemed sufficient for future studies.

One issue that arose during this experiment was gels falling off the flat platen. This indicated that in future experiments the indented platen should be used.

The research so far has been in verification of the BOSE apparatus, i.e. checking the device is working according to the manufacturers specification. Subsequent chapters describe validation of the device, i.e. the utility of the device in the context of spinal cord injury. It is not known whether work done, load, displacement, maximum velocity, mean velocity or another factor will have the greatest effect on neural cell responses to mechanical compression. These factors will be recorded in all future experiments so outcomes can be established.

3.5.1.4   Comparison of the BOSE 5110 Electroforce with other Impactor Systems

Only one other hydrogel compression study has been carried out using the BOSE 5110 Electroforce, and this used an input velocity of 0.167 mm.s^{-1} (Koivisto et al., 2017). The

findings of the research herein identified that the BOSE 5110 Electroforce apparatus was both accurate and precise at such low velocities. However, the previously published study did not describe the output velocity, its precision, accuracy or reliability (Koivisto et al., 2017). Similarly, three studies using the BOSE 5110 Electroforce to test materials in tension did not describe tuning values, or accuracy and precision of data (Avril et al., 2013; Banks et al., 2014; Garcia and Stewart, 2016).

Other apparatus from the same manufacturer has been used in the scientific literature for *in-vitro* compression experiments (Sparrey and Keaveny, 2011; Busby et al., 2013; Bartlett et al., 2016b; Andriakopoulou, 2016). Across these papers, mechanical input parameters varied. Strain rates tested ranged from 0.005 to 5. in two studies (Sparrey and Keaveny, 2011; Busby et al., 2013). Another used a velocity parameter of 0.1 mm.s^{-1} (Andriakopoulou, 2016), and a final tested dynamic mechanical analysis (i.e. a variety of velocities, all at a frequency of 1 Hz) (Bartlett et al., 2016b). None the these studies reported precision, reliability or accuracy of the output mechanical parameters.

No *in-vitro* studies performed to date using any other device from any other supplier reported impact mechanics or evaluation of the accuracy, precision or reliability of impact apparatus (Cullen and LaPlaca, 2006; Cullen et al., 2007; Bar-Kochba et al., 2016). Conversely, impact mechanics are more often reported for *in-vivo* studies. For instance, one study using the University of British Columbia multi-mechanism injury system reported both the input velocities and displacements, as well as output data (Lam et al., 2014). These authors identified a small difference in input vs output displacement of under 3%. The difference in impact velocity was greater, varying between 4.75 and 9.96%. This corresponds with results found in this study, where displacement was consistently reached to a high level of accuracy, whereas variation between theoretical input and experimental output velocities was greater.

A further study used a BOSE Testbench system to induce spinal cord injury *in-vivo*, first tuning the apparatus using a silicone polymer to represent the spinal cord (Salegio et al., 2016; Sparrey et al., 2016). The desired impact velocity *in-vivo* was 1000 mm.s^{-1},

which was the maximum deformation rate of the system. However, experimental recorded impact velocities were between 420 and 530 mm.s^{-1}. This difference may have been due to the fact that surrogate spinal cords were less stiff than the cord *in-vivo* (Sparrey et al., 2016). The study does not comment on the velocities achieved during surrogate testing. This highlights the importance of recording output velocities in every case.

It has been established that impact mechanics can affect spinal cord injury and neural cell outcomes (see literature review sections 1.4.1.2 and 1.4.2.2). During *in-vivo* studies, these effects have been noted and impact mechanics are reported. This is not the case for *in-vitro* studies, where there is a paucity of understanding of the precision, accuracy and reliability of impact apparatus. These factors must be understood to fully comprehend the effects of changing impact mechanics on injury outcomes. Overall, the results herein show the BOSE 5110 Electroforce apparatus is precise, can elicit reproducible displacements both in air and in collagen hydrogels. The accuracy of the device is less well-established with output velocities sometimes falling beyond 20% of the theoretical values. However, the biological significance and consequences of this are unknown, since neural cell responses to impacts at a variety of speeds have not been established. In each test going forwards, output velocities will be recorded and neural cell responses compared.

3.5.2   Evaluating Astrocyte Cell Populations

The aim of this section was to develop and characterise a reproducible type I collagen hydrogel seeded with primary rat astrocytes (a relevant neural cell type). Three factors had to be established; firstly the proportion of primary cells which were astrocytes, secondly astrocyte growth in collagen hydrogels at the previously used density, and thirdly whether the astrocytes could elicit known responses to a chemical stimulant causing reactivity (TGF-beta). The cell population was evaluated using ethidium homodimer, a marker of cell death, and GFAP immuno-labelling.

3.5.2.1 Proportion of Astrocytes in Enriched Mixed Glial Populations

Mixed glial populations isolated from neo-natal rats contain astrocytes, microglia, and oligodendrocyte cells. By shaking the mixed glial cells in low oxygen conditions at 250 rpm, the less strongly attached microglia and oligodendrocytes come away from the surface and into suspension; whereas astrocytes remain attached (Mecha et al., 2011).

In astrocyte-enriched populations seeded onto coverslips, $89.7 \pm 3.5\%$ (mean $\pm$ S.E.M.) of cells expressed GFAP. Previous studies have described that if 85 to 90% of cells are stained with GFAP, then the population can be described as astrocytes (East et al., 2009; Kerstetter and Miller, 2012; Smith, 2016). The proportion of cells expressing GFAP in this study met the required threshold, and therefore the population were determined to be astrocytes.

In this experiment, 11.7% of astrocytes stained with a dead cell marker (ethidium homodimer) in 2D culture. In a similar 2D astrocyte study, cell death was estimated to be 7% (East et al., 2009). The results are similar, suggesting concurrency between studies. Differences may be due to slight variations in primary astrocyte isolation protocols, in the staining itself, or in image analysis. This study used ethidium homodimer to mark dead cells and automated image analysis was carried out using FIJI. Conversely, the previous study used propidium iodide and image analysis used Olympus Analysis Pro software.

Overall, the implications of this experiment are that there a similar proportion of GFAP-expressing cells (astrocytes) to previous studies, and the cells behave as expected in 2D culture.

3.5.2.2 Astrocyte Activation and Hydrogel Contraction

TGF-beta is a chemical known to induce reactive astrogliosis and glial scar formation in astrocytes (Logan et al., 1994; Vogelaar et al., 2015). By culturing astrocytes in collagen hydrogels with TGF-beta over a period of 14 days, the cell population and responses were further evaluated. If the cells were in fact astrocytes, and behaved in a relevant

manner, TGF-beta would have increased reactivity as measured by GFAP expression and gel contraction.

When astrocytes were seeded into rat type I collagen hydrogels at 1×10^6 cells.mL^{-1}, neither the area labelled with GFAP nor number of dead cells (as determined by ethidium homodimer staining) significantly increased over the course of 14 days (P >0.05). Over the course of 14 days, total GFAP area per image significantly increased in TGF-beta treated samples (P <0.05). The proportion of dead cells did not change over time (P >0.05). Other studies found that in response to TGF-beta treatment, astrocyte GFAP expression per cell significantly increased over 14 days; with increased ramifications over the same time period (compared with untreated control cells) (East et al., 2009; Kimura-Kuroda et al., 2010; Smith, 2016). Qualitative analysis of the images showed the same trend of increasing ramification over a two week period (Figure 3.12). Furthermore, another study using astrocytes in Matrigel showed TGF-beta treatment caused increased density of hypertrophic processes, but no significant changes to cell death compared with untreated control samples (Cullen et al., 2007). Overall, the effect of TGF-beta treatment on astrocytes identified in this study was similar to published research in the literature; with increased area of GFAP expression, increased ramification of astrocytes, and no change in cell viability.

Ideally, ramification of astrocytes and GFAP area per cell would also have been evaluated. This was not possible since many cells present seemingly did not express GFAP, therefore complicating image analysis. This was either due to cells not being GFAP-positive astrocytes, the antibody not penetrating the gel, or the astrocyte phenotype producing a low level GFAP expression. Antibody diameter is in the range of 7 to 10 nm (Dong and Shannon, 2000). Previous studies have found that for 1 to 2 mg.mL^{-1} rat type I collagen gels, pore size ranged from 5 to 17 μm (Banerjee et al., 2008; Yang et al., 2010). Even at collagen concentrations between 8 and 20 mg.mL^{-1}, pore size was in the range of 500 to 1000 nm (Antoine et al., 2015), therefore the antibody should have been able to penetrate the gel. Previous experiments in this research indicated that in 2D, 90%

of the cells expressed GFAP in 2D cultures, whereas in images from this 3D study, this figure was not reached (images in Figure 3.12). Primary astrocytes are less reactive in 3D environments than in 2D (East et al., 2009). In 3D, astrocytes at the upper surface of collagen hydrogels have the greatest reactivity and therefore GFAP levels (Smith, 2016). During imaging, setting the laser power for this highly reactive surface meant that GFAP expression in less reactive astrocytes deeper into the gel was not identified due to its weaker signal. However, the nuclei were identified due to the 60 μm z-stack depth, and Hoechst staining. As such, many cells were present which did not show GFAP expression. The large number of cells present per image also meant GFAP area per cell could not be accurately quantified. To overcome this in future studies, a smaller z-stack, 20 μm in depth, will be used where only one plane of cells are present (East et al., 2009). Previous research also identified that cells on the uppermost surface elicited the greatest response to mechanical injury (Smith, 2016); perhaps due to the fact that these cells undergo the greatest displacement. Therefore, in future studies only the upper surface cells will be imaged. This will facilitate evaluation of GFAP expression per cell; which will allow for gel contraction.

Gel contraction was measured at days 11 and 14 in this study. When astrocytes become increasingly reactive, they elicit mechanical strain on the surrounding matrix, causing it to contract. TGF-beta treated samples were contracted by 48.5% on days 11 and 14. Comparing this contraction with previous research; when astrocytes were seeded at the same density in the same collagen hydrogel, contraction of approximately 40% was found at day 1 (Smith, 2016). These values for contraction are similar, and the differences identified may be due to the difference in time points, or differences in cell isolation protocols. In future studies where mechanical insults are applied to collagen hydrogels, gel area and subsequent contraction will be evaluated at every time point.

3.5.3   Conclusion

Overall, each of the objectives set out in the aims were achieved (Table 3.2). Therefore the methods used within this chapter are suitable for future studies to evaluate the effects of varying input mechanics on astrocyte responses.

Table 3.2: ***Conclusions of Chapter 3: In-vitro model development***

Aim	Objective	Result and Implications
Develop methodology for mechanical impacts	Maximum velocity of BOSE 5110 Electroforce	Maximum velocity was 1440 mm.s^{-1}. This exceeds the manufacturers guidelines (740 mm.s^{-1}) and therefore should not be used in future experiments
	Effects of new platens on mechanical outputs	Minimal effect of new platens in terms of mechanical outputs. Any platen would suffice. The indented platen would prevent gels slipping off.
	Optimal gel volume	A volume of 300 µL in a 48 well plate was the minimum volume to allow handling and gel height measurement.
	Effect of incorporating collagen hydrogels	Minimal observed effect of using the BOSE 5110 Electroforce with gels or in air.
	Effect of working distance and velocity with hydrogels	A working distance of at least 8 mm was required to achieve 1000 mm.s^{-1}. For all other velocities (100, 10, 1, 0.1 mm.s^{-1}), a distance of 1.5 mm was sufficient to allow the velocity to be reached.
Characterise astrocyte population	Evaluate percentage of astrocytes from a mixed glial population	Approximately 90% of cells expressed GFAP in 2D culture.
	Assess cell viability of astrocytes in collagen hydrogels	Astrocytes remained viable and non-reactive over two weeks in collagen hydrogels.
	Evaluate the effect of TGF-beta treatment on astrocytes in collagen hydrogels	TGF-beta treatment elicited astrocyte reactivity (GFAP expression) and hydrogel contraction, as expected.
	Image astrocytes in collagen hydrogels	A z-stack depth less than 60 µm should be used to image astrocyte-seeded collagen hydrogels in the future, to ensure only one plane of cells is imaged.

Chapter 4

Responses of Neural Cells to Varying Mechanical Inputs

4.1 Introduction

This chapter aims to evaluate responses to loading scenarios in NTSCI *in-vitro*, and compare outcomes to TSCI. This chapter uses the BOSE 5110 Electroforce Biodynamic to apply mechanical insults at varying velocities to astrocyte-seeded collagen hydrogels. Cellular outcomes measured include astrocyte-mediated gel contraction (a measure of reactivity), GFAP expression, cell ramifications, and both pro- and anti-inflammatory cytokine release.

In TSCI, the pathological cascade can be split into primary and secondary injury. Primary injury is the mechanical trauma itself, and secondary injury is a further, more complex, cascade of events such as inflammation, glial scar formation and demyelination (see Section 1.3.1, (Anwar et al., 2016; Morin, 2018)). In TSCI, the response is co-ordinated by astrocytes and microglia (Anwar et al., 2016). Since NTSCI is not caused by trauma, but instead by quasi-static compression of the spinal cord, this distinction between primary and secondary injury cannot be made. There is little understanding of how the pathology of NTSCI develops (Kurokawa et al., 2011; Yu et al., 2011;

Karadimas et al., 2013; Newcombe et al., 2015; Zhou et al., 2015). In NTSCI, it is unclear in the literature how mechanical compression of the spinal cord and neural cells therein result in symptoms; whether this is due to the mechanical compression of cells themselves, or due to other mechanisms such as compression of the vasculature leading to hypoxia. Clinically, several days after high velocity injuries (TSCI), astrocytes undergo hypertrophy and reactive astrogliosis to form the glial scar (Norenberg et al., 2004; Sofroniew and Vinters, 2010). Further, there are elevated levels of GFAP in the serum of patients with TSCI, indicating increased astrocyte reactivity (Ahadi et al., 2015). *In-vivo* and *in-vitro*, increased astrocyte reactivity and increased GFAP expression are observed in TSCI models (Cullen et al., 2007; Weightman et al., 2014; Smith, 2016; Sturdivant et al., 2016; Kirk, 2018). *In-vivo*, astrocyte reactivity peaks at 1 to 4 weeks post-injury (Hu et al., 2010; Kawano et al., 2012; Wanner et al., 2013). The effects of NTSCI on astrocyte reactivity and GFAP expression have not been established in the literature.

There is evidence from both *in-vitro* and *in-vivo* studies that injury mechanics affect spinal cord injury outcomes (sections 1.4.1.2 and 1.4.2.2). These studies have predominantly focussed on TSCI, using either scalpel blades to induce injury, or high strain rates and/or velocities (Sypecka et al., 2015; Smith, 2016; Kirk, 2018; Pandamooz et al., 2019). There is a lack of consensus regarding which mechanical parameter(s), specifically, are responsible for differences in injury outcomes in TSCI, and there is no data for how injury mechanics induce or affect NTSCI. Some TSCI studies report that displacement is the core factor in determining injury severity, independent of velocity (Kearney et al., 1988; Kwo et al., 1989; Kim et al., 2009), whereas others state a combination of factors, such as work done, are most important (Jakeman et al., 2000; Seki et al., 2002; Lam et al., 2014). There is a gap in the literature regarding injury mechanics in NTSCI, and directly comparing outcomes in such injuries with TSCI.

In-vitro models of spinal cord injury allow evaluation of an individual cell population in isolation to understand intricacies of the injury (Abu-Rub et al., 2010; East et al., 2010; Bar-Kochba et al., 2016). They offer greater control and minimisation of confounding

factors compared with *in-vivo* studies. No parametric studies have been undertaken evaluating the velocity of compression in the context of NTSCI, or directly comparing with TSCI velocities. In two *in-vitro* studies of TSCI undertaken at the University of Leeds, astrocyte GFAP expression was evaluated (Smith, 2016; Kirk, 2018). These studies used either the BOSE 5110 Electroforce or the Infinite Horizon impactor. It is worth noting that only the BOSE 5110 Electroforce apparatus allows control of displacement and time (and therefore velocity); which are crucial in distinguishing TSCI from NTSCI.

Kirk (2018) compressed simple disc-shaped collagen hydrogels using focal lesions in the BOSE 5110 Electroforce, with a reported velocity of 3000 mm.s^{-1}. After 24 hours, Kirk found there were significantly more GFAP-labelled pixels per area than in non-compressed controls. The number of GFAP-labelled pixels increased with displacement depth, with 80% and 100% displacement exceeding lipopolysaccharide treated control samples. Smith (2016) compressed aligned collagen hydrogels using focal lesions in the Infinite Horizon (under load control to 2N). In the region closest to the impact site GFAP-stained area per cell increased over 10 days, although these differences were not statistically significant due to the small sample size. These results indicate that TSCI can be modelled using astrocyte-seeded collagen hydrogels and mechanical impaction. The question remains whether astrocyte compression at slow velocities could induce a different phenotype, representing NTSCI.

The previous chapter has established the suitability of the BOSE 5110 Electroforce in inducing controlled impaction on hydrogels. This chapter aimed to investigate the effect of low velocity injuries to astrocytes seeded in 3D hydrogels. The displacement used was 70%, based on functional deficits observed *in-vivo* and in clinical studies (Penning et al., 1986; Steurer et al., 2011; Yang et al., 2015; Iwahashi et al., 2016; Weber et al., 2016; Kadanka et al., 2017; Martin et al., 2018; Witiw et al., 2018)

4.2   Aims

The aims of this chapter were to characterise biological responses to loading scenarios representative of NTSCI *in-vitro* (Figure 4.1). The results of this chapter will be used to determine the mechanistic pathway and phenotype of astrocyte responses to NTSCI, directly compared to TSCI. NTSCI and TSCI will be distinguished by the compression velocity. Specific objectives for this chapter:

1. To evaluate how mechanical inputs affect primary neural astrocyte responses in the context of spinal cord injury, comparing high and low velocities (TSCI and NTSCI, respectively)

   A Determine the accuracy of the BOSE 5110 Electroforce Biodynamic in applying 70% displacement to astrocyte-seeded collagen I hydrogels at 0.1, 1, 10 and 100 mm.s^{-1}

   B Assess astrocyte responses to the various input velocities detailed above: GFAP expression, gel contraction and cytokine release.
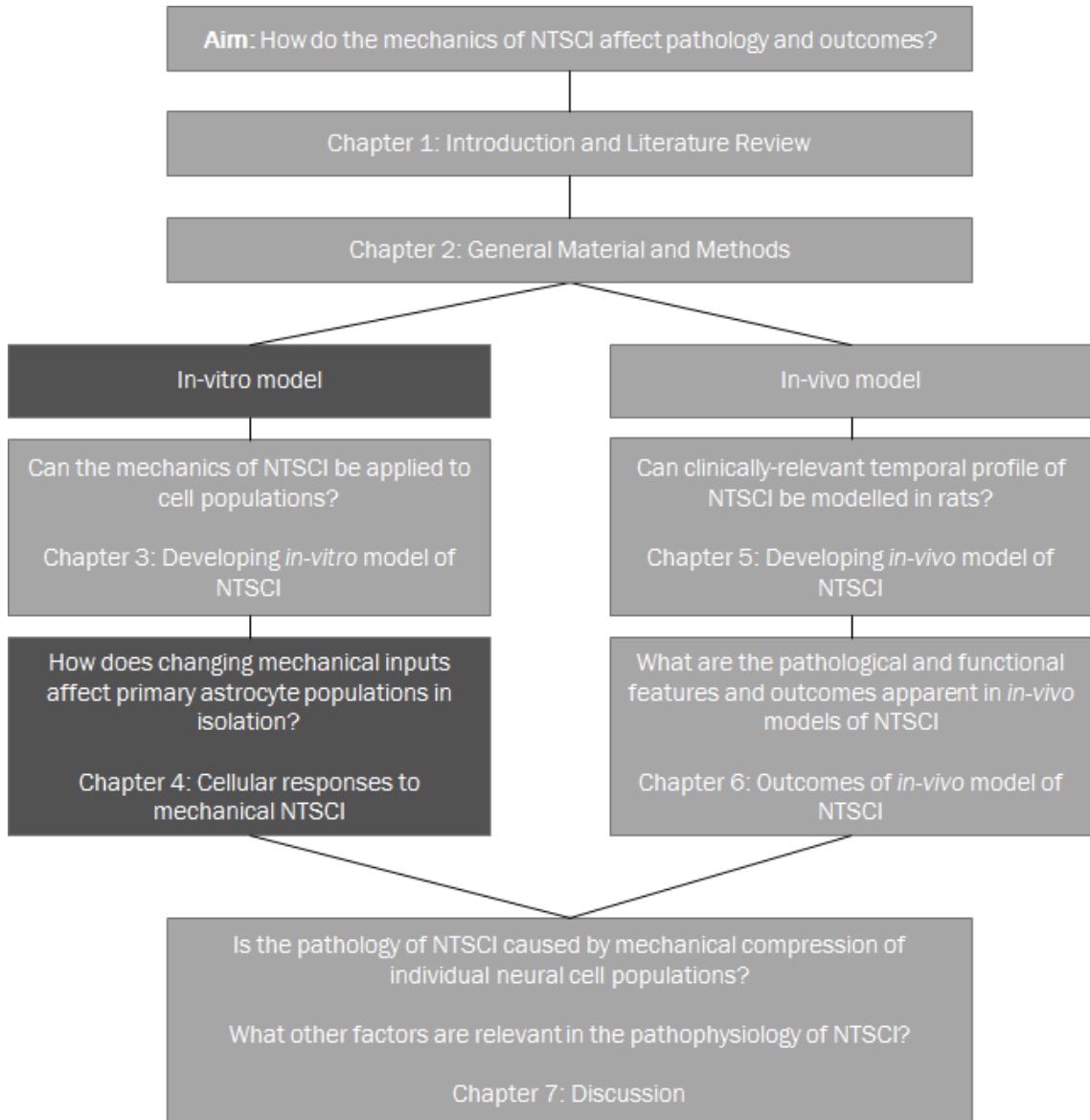
Figure 4.1: **Hypothesis and research questions asked in Chapter 4, relating to the whole study.**

4.3 Experimental Setup

4.3.1 Mechanical Compression of Astrocyte-Seeded Hydrogels

The aim of this study overall was to evaluate neural cell responses to varying mechanical inputs; specifically using astrocytes seeded in collagen hydrogels, compressed in the BOSE 5110 Electroforce system (section 2.3.1).

4.3.1.1 Rationale for Method Details

TSCI occurs in the range of metres per second (Wilcox et al., 2003). However, due to the manufacturers guidelines and capability of the apparatus (as discussed in the previous chapter), a maximum velocity of 100 mm.s^{-1} was used in this study for the TSCI condition. The choice of lower velocities was to model NTSCI, rather than TSCI. Matching the clinical velocity or strain rate of NTSCI in *in-vitro* models would mean compression over months to years. This was not suitable for the timescale of this project, nor the apparatus requirements. The absolute values of velocity for inducing NTSCI are not established, but are inherently several orders of magnitude lower than those in TSCI. As such, 0.1 mm.s^{-1} was the lowest velocity used, and was used to model NTSCI.

In this study, the indented motor platen was used to prevent gels slipping (platen D figure 3.4, section 3.3.1.1), and the load platen was 10 mm in diameter (platen C figure 3.4, section 3.3.1.1). The reason for the selection of the 10 mm diameter load platen was due to the nature of compression in NTSCI. Previous TSCI studies have used a 2.5 mm and 3.34 mm diameter (Smith, 2016; Kirk, 2018). However, NTSCI is often multi-level, with compression occurring at more than one vertebra (Park et al., 2010; Wu et al., 2013; Li et al., 2015). Therefore, the compression is more likely to be diffuse as opposed to focal. The diameter of the compression is important as it would alter the pressure transmitted to the cells. For a given force, pressure would be greater with a smaller diameter, and vice versa. Since NTSCI is multi-level, the diameter of compression is greater and therefore pressure lower than in a TSCI where, for instance, a bone fragment from one vertebral

level would induce injury.

4.3.1.2   Method Setup

These experiments aimed to evaluate astrocyte responses to being compressed at various velocities to model NTSCI and TSCI. To achieve this, primary astrocytes were separated from primary rat (P3 post-natal) mixed glia 14 days post-isolation (methods section 2.4.2.4). Cells from 8 rat pups were pooled to reduce the effects of inter-animal variation. The cells were seeded into neutralised collagen hydrogels at a final concentration of $1x10^6$ cells per mL of gel (see methods section 2.4.3). Each gel was 300 μL in volume and gels were manufactured in 48 well plates. Four plates were set up, with one being evaluated at each timepoint (day 1, 4, 11, and 14). Positive control gels were also seeded, incorporating 10 ng.mL^{-1} TGF-beta. Each experiment was carried out twice.

The BOSE 5110 Electroforce apparatus was set up according to the details described in section 3.3, but with an additional reservoir bottle attached to fill the chamber with media (Figure 4.2). After measuring gel height, the chamber was filled with pre-warmed media using a peristaltic pump. The reservoir bottle was attached to a sterile filter which contained a 0.20 μm pore size for sterile air transfer. After compression, the chamber was drained of the media before each sample was removed.

The gels were placed on to the motor platen, gel height measured, and the bio chamber was filled with pre-warmed (37°C) HEPES (10 mM) supplemented DMEM complete media at 80 mL.min^{-1}. The gels were compressed in the BOSE 5110 Electroforce using a trapezoid experimental profile; with compression to 70% displacement (based on gel height) at four velocities: 0.1, 1, 10 and 100 mm.s^{-1}. The gels were compressed, followed by a 30 second dwell, then decompressed at 1 mm.s^{-1}. Media was removed from the chamber, and the gel was removed and returned to the 48 well plate. Control gels were placed into the apparatus, the bio chamber filled with media, gel height measured, but not compressed. They remained in the apparatus for up to 5 minutes, before the bio chamber was emptied and gels were moved back into the 48 well
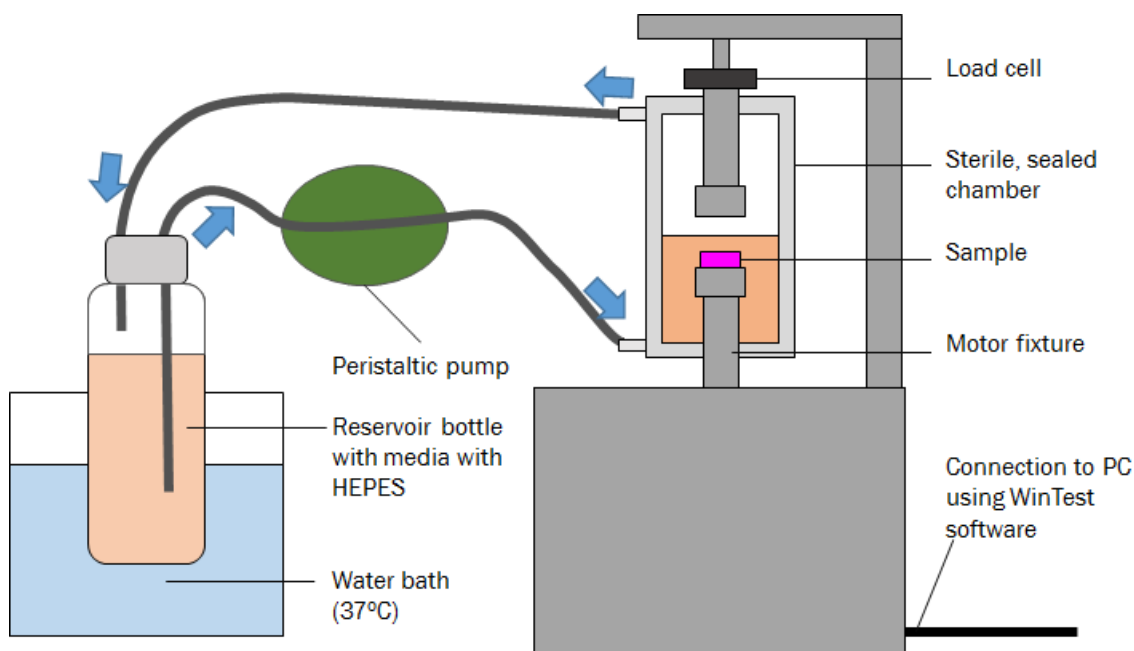
Figure 4.2: **Schematic diagram of the BOSE 5110 Electroforce apparatus connected to peristaltic pump and reservoir bottle.** *Blue arrows denote direction of flow for filling the sealed chamber. For emptying, the peristaltic pump was reversed.*

plate along with fresh media. Neither negative nor positive (TGF-beta at 10 ng.mL^{-1}) control gels were removed from the plate, but media was changed. The plates containing gels were cultured at 37ºC, 8% (v/v) CO_2 in humidified air. Every three to four days media was replaced.

4.3.1.3   Compression Mechanics Calculations

Displacements and loads were recorded over time. Further, work done was calculated. Work done is a function of load and displacement. To calculate work done, non-uniform numerical trapezoid integration was carried out using the following equation (where x was displacement, y was load; n was the timepoint gathered in each experiment; N was the final time at the end of the experiment):

$$Work\ done = \tfrac{1}{2} \sum_{n=1}^{N} ((x_{n+1} - x_n)(y_n + y_{n+1}))$$

4.3.2 Evaluation of Astrocyte Responses to Compression at Various Velocities

A total of four gels were evaluated per condition at each of four timepoints over 14 days: day 1, 4, 11 and 14 (n=20 gels per condition total per experiment). At each timepoint, media was collected and frozen at -80ºC, and a contraction assay was undertaken (section 2.4.4.8). Contraction assay data was analysed in Microsoft Excel, using two-factor ANOVA with regression for unbalanced groups, and Tukey's post-hoc test. A p-value of less than 0.05 was deemed significant.

Further, at each time point, gels were fixed in 4% (w/v) PFA. Subsequently, wells were covered with Parafilm, and plates were stored at 4ºC until the end of the two-week experiment.

Staining was undertaken after all gels had been fixed. Methods were the same as in the previous chapter (section 3.3.2). Immuno-staining for GFAP, and ethidium homodimer and Hoechst staining were undertaken. Then, hydrogels were moved from the well plate onto slides. Coverslips were placed on top for a flat imaging surface.

Images were taken at 20x magnification on a confocal microscope. In the microscope, the upper surface of each gel was identified as the point in the z plane where cells first become visible. The centre point of the gel was identified by the midway point between the edges of the gel (x and y directions). Images were only taken within a radius of 3.5 mm in the x and y directions of the centre point to ensure they were within the impacted region. Four z stacks were taken, one approximately at the centre of each quadrant (as shown in figure 4.3). A z stack 20 μm deep, comprising of 7 individual images, was taken at each position. Raw image files were saved, and maximum intensity projection at each position were also exported. Laser settings were configured for the brightest TGF-beta (10 ng.mL^{-1}) treated samples on each day, and maintained for all the gels from the same timepoint. Image analysis was undertaken in FIJI as per the methods previously described (Section 2.4.4.7). Area per object of interest and circularity were

extracted. Use of area per object, as opposed to overall area per image, accounted for changes in hydrogel contraction between conditions. Subsequent statistical analysis was carried out in Microsoft Excel using one-way ANOVA with Tukey's post-hoc test, at a significance level of $p < 0.05$.
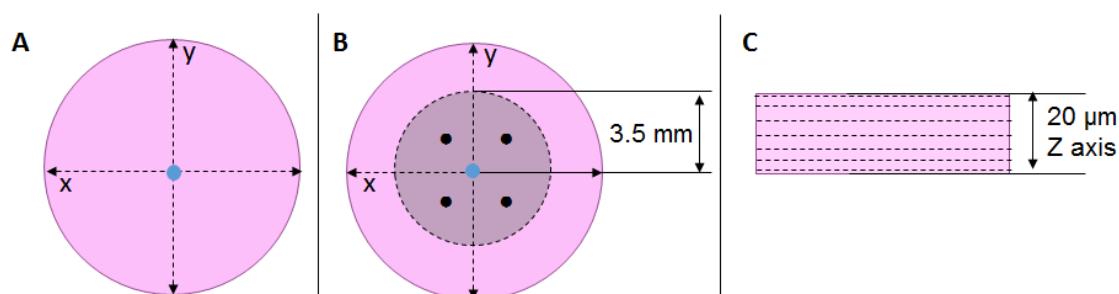
Figure 4.3: **Location of imaging regions in hydrogels.** *A: The centre point (blue dot) was determined using the midpoint between edges of the gel in the x and y planes. B: Four locations were imaged (black dots), within 3.5 mm (x and y direction) from the centre of the gel to ensure they were in the compressed regions. C: Each imaging location comprised a 20 µm z stack of 7 individual images.*

4.3.2.1 Enzyme-linked immunosorbent assay (ELISA) for cytokine release

The general methods used for this section are described in Section 2.4.4.9. Two cytokines were investigated: IL-6 (pro-inflammatory) and IL-10 (anti-inflammatory). For IL-6, standard concentrations were 31.25, 62.5, 125, 250, 500, 1000, 2000 and 4000 pg.mL^{-1}. The plate had 96 tests, and so not all conditions could be tested.

The following conditions and time points were excluded:

- Media from day 7

- Media from day 10

- The following experimental conditions:

    - 70% compression at 10 mm.s^{-1}
    - 70% compression at 1 mm.s^{-1}

The following conditions and timepoints were included in the ELISA assay:

- Media from day 1

- Media from day 14

- The following experimental conditions:

  - TGF-beta (10 ng.mL^{-1}) treated (positive control)
  - 70% compression at 100 mm.s^{-1}
  - 70% compression at 0.1 mm.s^{-1}
  - Control gels loaded into BOSE apparatus but not compressed
  - Negative, untouched control

The same conditions as above were used in an IL-10 ELISA. In this test, standard concentrations were 15.625, 31.25, 62.5, 125, 250, 500, 1000 and 2000 pg.mL^{-1}.

4.4 Results

Astrocyte-seeded collagen hydrogels were compressed to 70% of their gel height, at velocities from 0.1 to 100 mm.s^{-1}. Mechanical data from each compression was recorded (displacement and load versus time). At day 1, 5, 11 and 14 after compression, a contraction assay was carried out, and hydrogels were fixed. After the experimental time course was complete, astrocytes were stained for GFAP using immunocytochemistry (immunofluorescence).

4.4.1 Impact mechanics increased in proportion to input velocity.

Displacement profiles were consistent with input axial command values at all velocities (Figure 4.4). Load and work done both increased with velocity. Load increased from 0.16 $\pm$ 0.02 N (mean $\pm$ S.E.M.) at 0.1 mm.s^{-1} to 1.51 $\pm$ 0.10 N at 100 mm.s^{-1}. The maximum loads applied at 10 and 100 mm.s^{-1} were similar, at 1.45 $\pm$ 0.03 N and 1.51 $\pm$ 0.10 N respectively. Work done ranged between 0.05 $\pm$ 0.02 mJ at 0.1 mm.s^{-1} to 1.12 $\pm$ 0.13 mJ at 100 mm.s^{-1}. Work done at 10 mm.s^{-1} was 0.78 $\pm$ 0.1 mJ. More detailed compression mechanics data are included in appendix F.
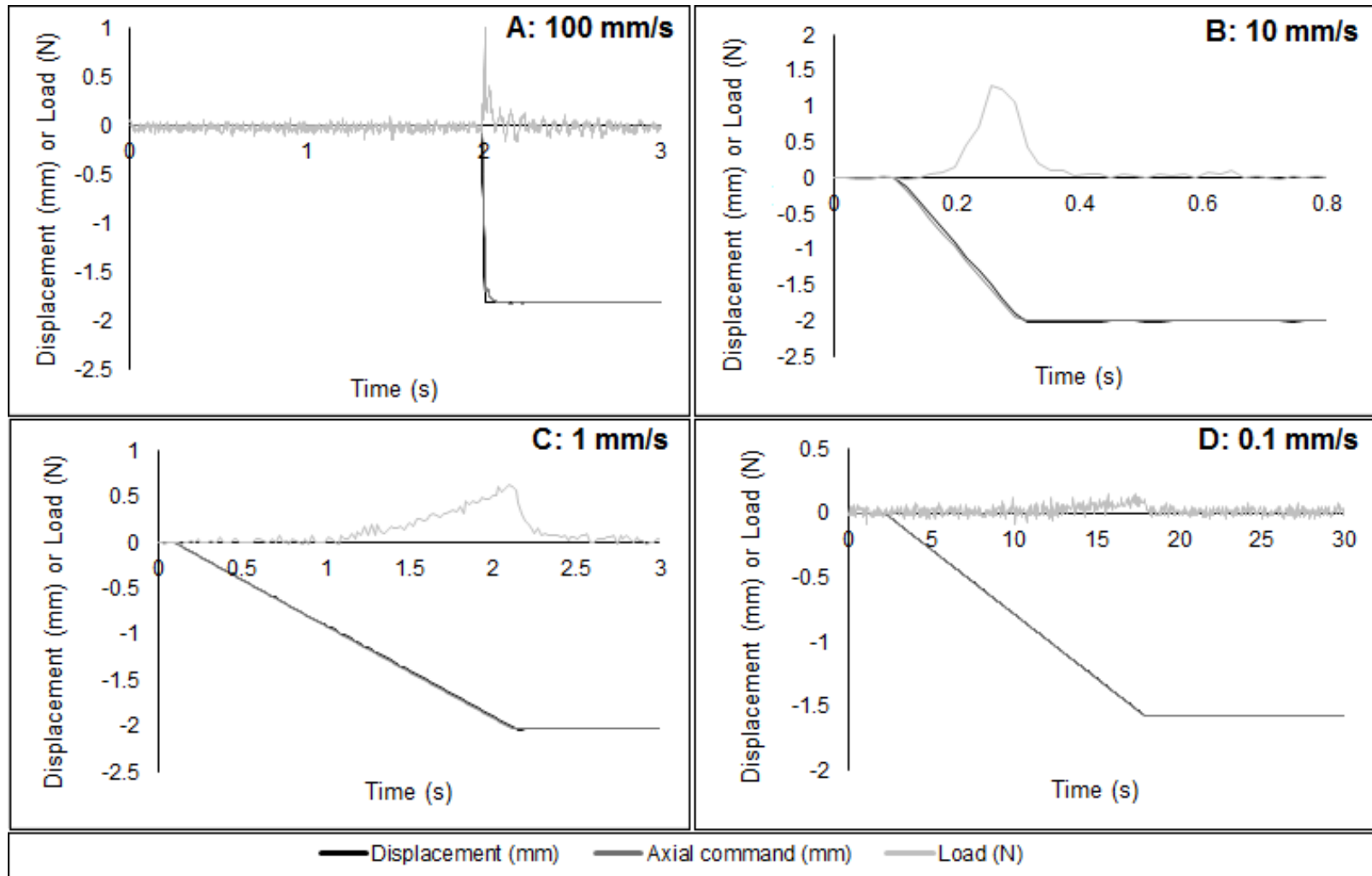
Figure 4.4: **Displacement and load data over time for compression of astrocyte-seeded hydrogels at four velocities.** *Rat type I collagen hydrogels (2 mg.mL^{-1}) were seeded with rat primary astrocytes at 1x10^6 cells.mL^{-1}. Each hydrogel was compressed to 70% of its height in the BOSE 5110 Electroforce apparatus. Displacement (negative) and load (positive) over time were recorded.*

4.4.2   Astrocyte responses varied based on mechanical inputs

4.4.2.1   Hydrogel contraction was only observed in TGF-beta control samples

Photographs of gels were taken at day 1, 5, 11 and 14, and gel contraction was calculated by their ratio between gel and well diameter. With TGF-beta treatment at 10 ng.mL^{-1}, gels contracted by a maximum of 61.99% over the time course (Figure 4.5). Across all velocities tested, the maximum gel contraction was 25.43% (1 mm.s^{-1}, day 14). For apparatus (BOSE) control samples and negative control samples, maximum gel contraction was 14.8% (day 5) and 15.40% (day 1), respectively. TGF-beta treated samples contracted significantly more than all other conditions at day 5, 11, and 14 (p <0.05).
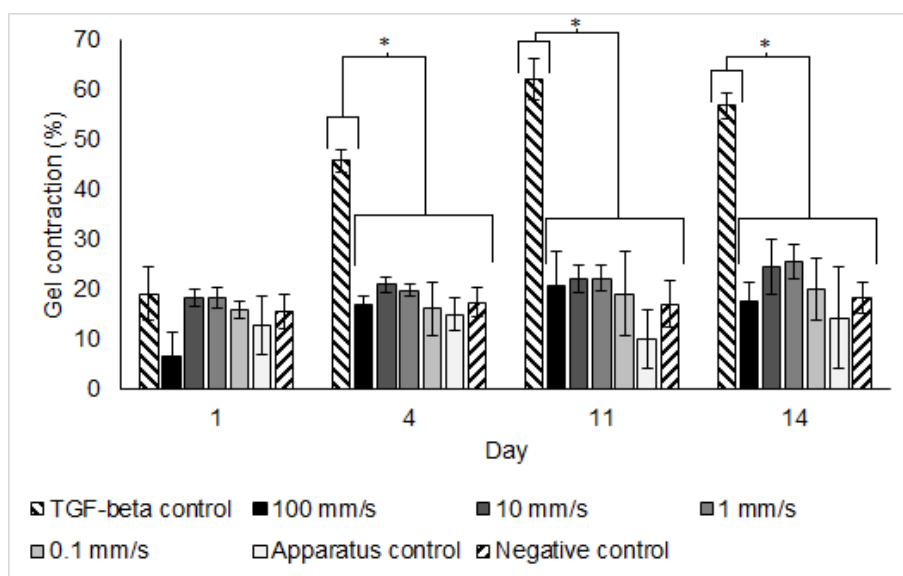
*Figure 4.5: **Astrocyte-seeded hydrogel contraction over 14 days after treatment with TGF-beta (10 ng.mL^{-1}) or compression to 70% of gel height at various velocities.** Test gels were compressed using the BOSE 5110 Electroforce. Positive controls were treated with TGF-beta at 10 ng.mL^{-1}. Control gels were placed into the BOSE 5110 Electroforce apparatus but not compressed. Negative control gels were not removed from the wellplate. n = 4 per timepoint for test gels, and n = 3 per timepoint for control gels. Asterisks denote statistical significance after a two way ANOVA with Tukey's post-hoc test (p <0.05).*

4.4.2.2   Astrocyte viability could not be assessed

Ethidium homodimer did not specifically label any cells, instead diffuse staining was seen throughout each hydrogel imaged.

4.4.2.3   Astrocytes were activated 11 days after 100 mm.s^{-1} compression

A representative set of images of astrocyte-seeded collagen hydrogels compressed at various velocities are illustrated in Figure 4.6. Compression at 100 mm.s^{-1} resulted in increased ramification of astrocytes at days 11 and 14 compared with days 1 and 5. This trend was not visible in the other velocities tested.

Astrogliosis was characterised by increased size and ramifications of astrocytes

Quantification of images of GFAP-stained astrocytes in collagen hydrogels allowed evaluation of average size per object and circularity, indicating hypertrophy and reactive processes, respectively. For average size per stained object, there were no significant differences between conditions on day 1 (Figure 4.7). On day 5, the greatest object area was in hydrogels that had been compressed at 100 mm.s^{-1}, although this was not significantly different from any other group. On day 11, the conditions of TGF-beta treatment and compression at 100 mm.s^{-1} resulted in significantly greater area per object compared with all lower velocities, along with apparatus and negative control conditions (p <0.05). On day 14, the same trend was seen, with TGF-beta treatment and compression at 100 mm.s^{-1} resulting in significantly greater area per object than 10, 1, 0.1 mm.s^{-1} compression velocities, apparatus control and negative control conditions (p <0.05).
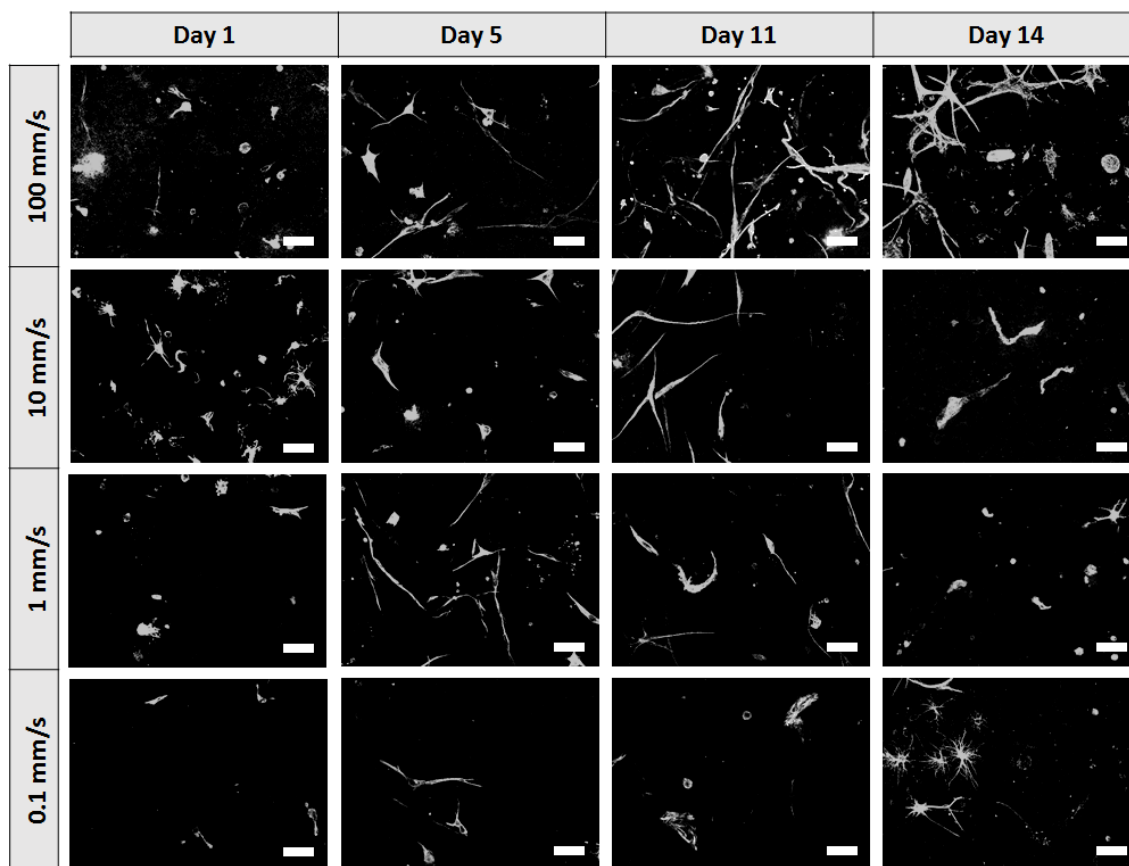
*Figure 4.6: **Sample images of GFAP labelled primary astrocytes seeded in collagen hydrogels, after compression to 70% of gel height at various velocities.** Rat type I collagen hydrogels (2 mg.mL^{-1}) were seeded with rat primary astrocytes at 1x10^6 cells.mL^{-1}. At the timepoints shown, collagen hydrogels were fixed with 4% (v/v) PFA. Immuno-staining for GFAP was carried out. Images taken at 20x magnification, scale bar 50 μm. Contrast in these images has been enhanced for visualisation and printing purposes.*
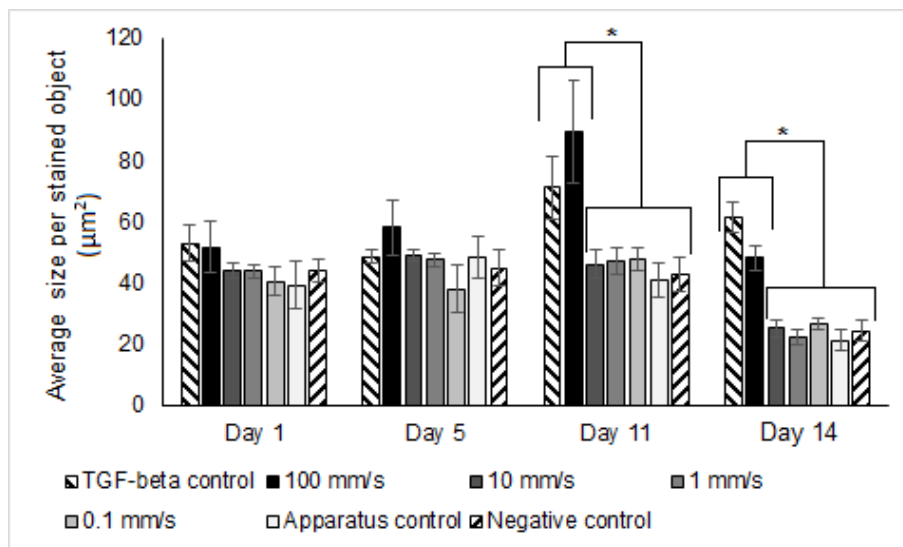
Figure 4.7: ***Average area per stained object of GFAP-labelled rat primary astrocytes seeded in collagen hydrogels.*** *Positive control was 10 ng.mL^{-1} TGF-beta. Control gels were loaded in to the apparatus but not compressed. Negative control remained in the multi-well plate. Image analysis in FIJI. Mean ± S.E.M. One way ANOVA at each timepoint, and Tukey's post hoc test (* = p <0.05).*
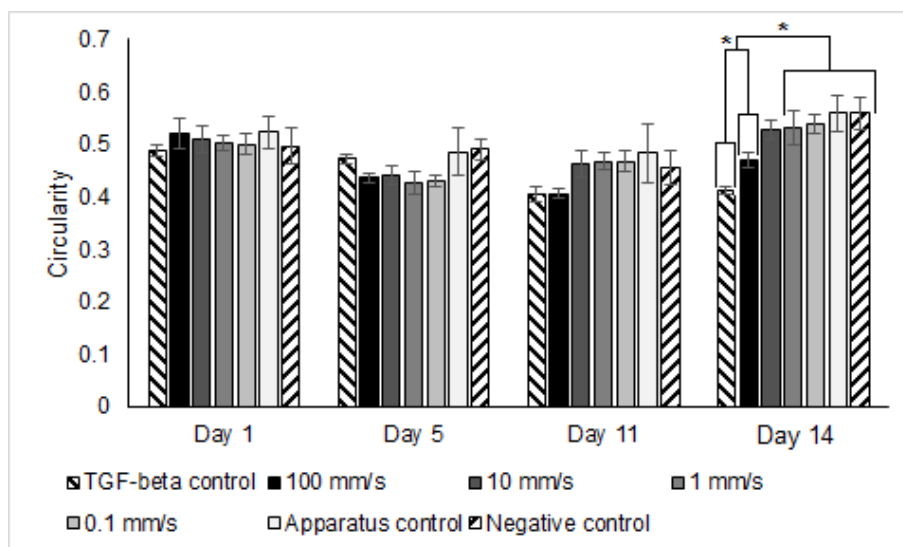
Figure 4.8: ***Circularity of GFAP-labelled rat primary astrocytes seeded in collagen hydrogels.*** *Positive control was 10 ng.mL^{-1} TGF-beta. Control gels were loaded in to the apparatus but not compressed. Negative control remained in the multi-well plate. Image analysis in FIJI. Mean ± S.E.M. One way ANOVA at each timepoint, and Tukey's post hoc test (* = p <0.05).*

Circularity is the ratio between area and perimeter^2 of each stained object, where a value of 1 would be perfectly round (Chapter 2, section 2.4.4.7). The lower the circularity, the less regular the shape.

There were no differences between conditions on day 1 (Figure 4.8). On day 5, objects in the TGF-beta treatment condition had a greater circularity than all of the compressed hydrogels, but this was not statistically significant (p >0.05). On day 11, circularity was reduced in TGF-beta treatment and 100 mm.s^{-1} compression conditions compared to all other conditions, but this was not statistically significant (p >0.05). On day 14, TGF-beta treatment resulted in a significantly reduced circularity compared to all other conditions (p <0.05). Circularity in the 100 mm.s^{-1} compression group was significantly greater than TGF-beta treatment, but significantly less than lower velocities and negative control conditions (p <0.05).

4.4.3 High velocity mechanical compression resulted in significant IL-6 release, but no differences in slower velocity compression.

4.4.3.1 IL-6 release was observed at day 14 with 100 mm.s^{-1} compression only

A standard curve was plotted using the IL-6 standards with known concentrations (Figure 4.9). As per manufacturers guidelines, the log of concentration against log of absorbance produced a linear regression.

Using the linear regression equation provided in the standard curve, IL-6 concentrations for experimental conditions could be evaluated (Figure 4.10). On day 1, TGF-beta treatment induced a significant increase in IL-6 expression compared to all other conditions (p <0.05). On day 14, the same trend was seen with media from TGF-beta treated cells containing significantly more IL-6 than the slow velocity (0.1 mm.s^{-1}), apparatus and negative control conditions (p <0.05). Additionally, at day 14, media collected from astrocyte-seeded hydrogels compressed at 100 mm.s^1 contained significantly increased IL-6 concentrations compared to slow velocity (0.1 mm.s^{-1}),
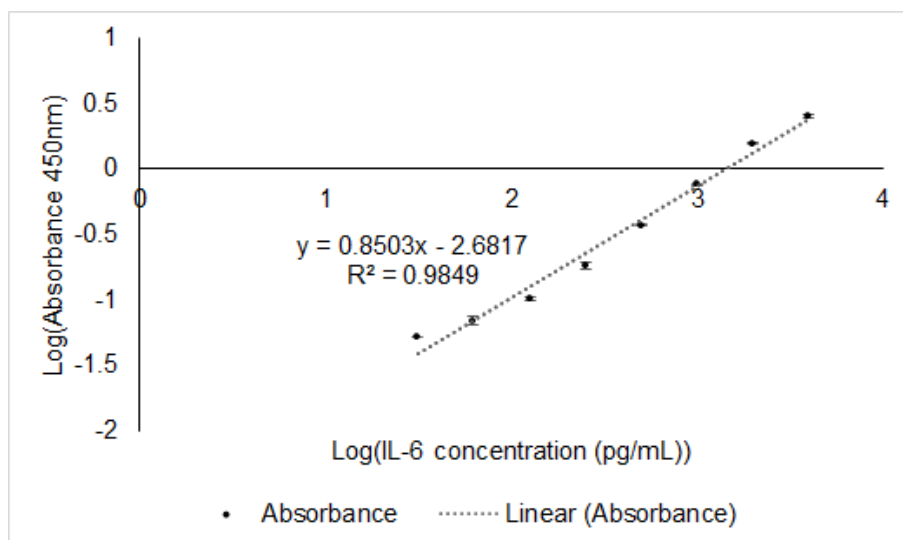
*Figure 4.9: **Standard curve of IL-6 ELISA.** IL-6 standards were diluted to the concentrations defined in the datasheet. A sandwich ELISA was undertaken, and absorbance at 450 nm was tested. Data shown are mean $\pm$ S.E.M. (n=2 per data point).*

apparatus and negative control conditions (p $<$0.05).

4.4.3.2 No significant differences in IL-10 release were observed under any condition

A standard curve was plotted using the IL-10 standards with known concentrations (Figure 4.11). As per manufacturers guidelines, the log of concentration against log of absorbance produced a linear regression with correlation coefficient of 0.9686.

At day 1, there was a significantly greater concentration of IL-10 in the media from astrocyte-seeded hydrogels which had been compressed at 0.1 mm.s^{-1}, compared to those compressed at 100 mm.s^{-1} (Figure 4.12, p $<$0.05). However, the concentration of IL-10 was not significantly different between these conditions and negative controls.
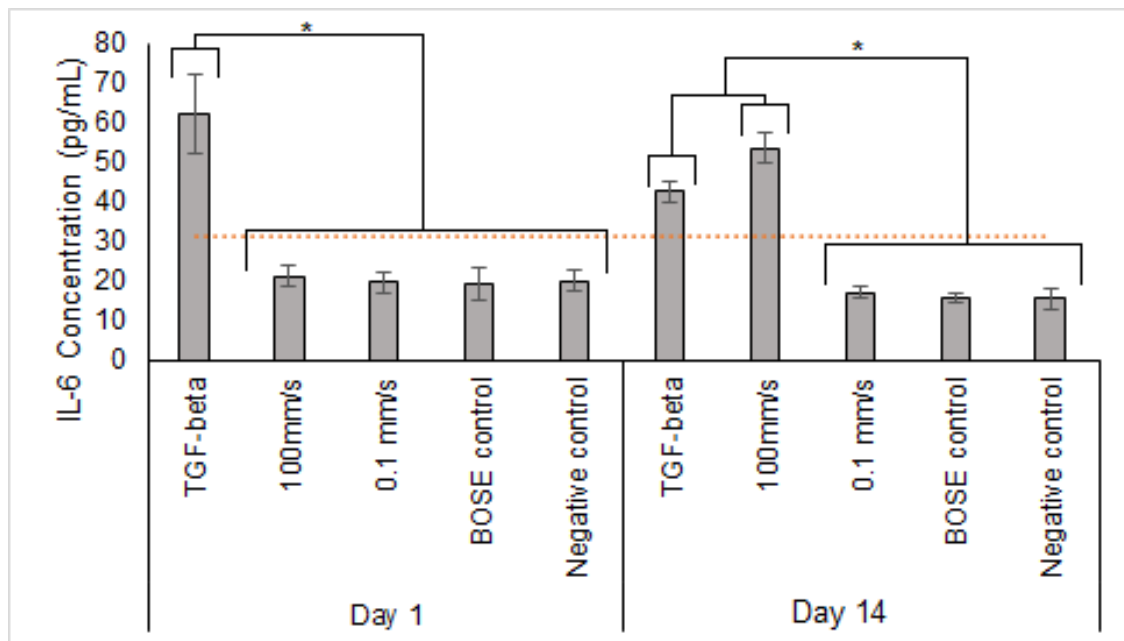
Figure 4.10: **IL-6 release from astrocyte-seeded collagen hydrogels days 1 and 14 post-compression.** *Data obtained using a sandwich ELISA with absorbance at 450 nm. Data presented is mean $\pm$ S.E.M., n=6 per datapoint. Statistical significance (asterisks) was determined using two-way ANOVA with Tukey's post-hoc test (p <0.05).*
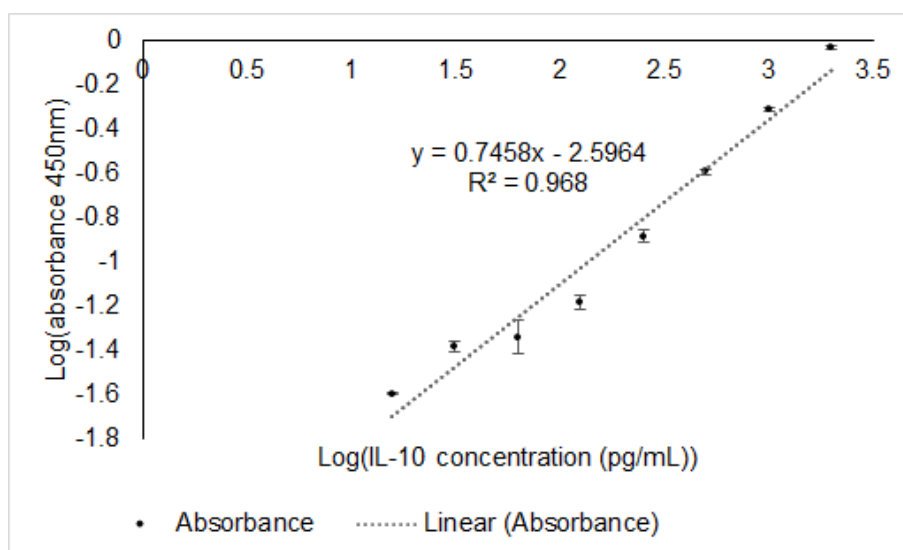
Figure 4.11: **Standard curve of IL-10 ELISA.** *IL-10 standards were diluted to the concentrations defined in the datasheet. A sandwich ELISA was undertaken, and absorbance at 450 nm was tested. Data shown are mean values with standard error of the mean error bars (n=2 per data point).*
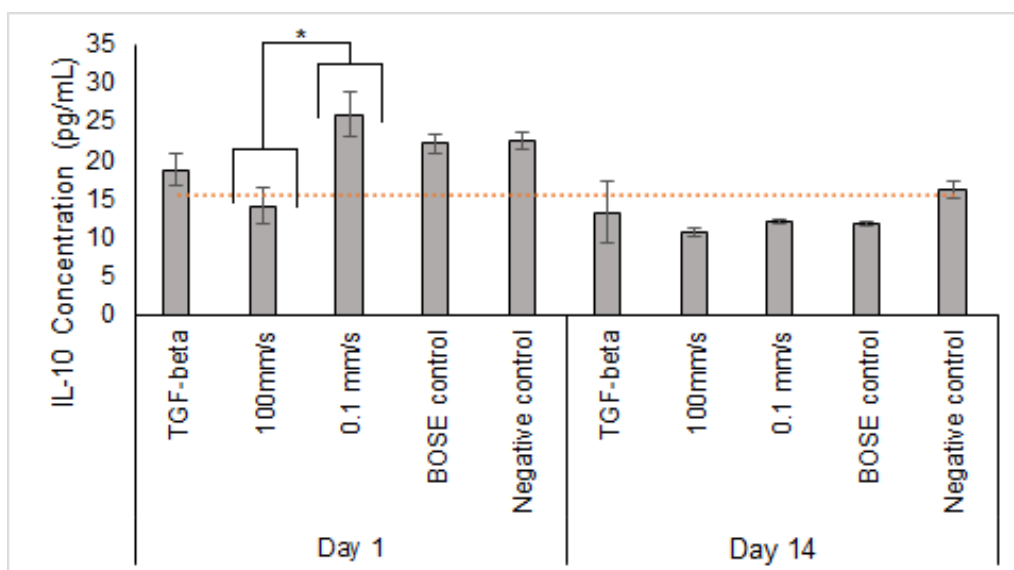
Figure 4.12: **IL-10 release from astrocyte-seeded collagen hydrogels days 1 and 14 post-compression.** *Data obtained using a sandwich ELISA with absorbance at 450 nm. Data presented is mean ± S.E.M., n=6 per datapoint. Statistical significance (asterisk) was determined using two-way ANOVA with Tukey's post-hoc test (p <0.05).*

4.5 Discussion

The aims of this chapter were to characterise biological responses to loading scenarios representative of NTSCI *in-vitro*, in particular comparing them to TSCI responses. The BOSE 5110 apparatus accurately applied mechanical insults to astrocyte-seeded hydrogels at velocities from 0.1 to 100 mm.s^{-1}. Load increased with velocity, indicating a greater force imparted onto cells with increasing velocity. NTSCI and TSCI were distinguished based on velocity. The key findings of this chapter were that astrocyte responses varied based on impact velocity. With high velocity impacts (100 mm.s^{-1}), astrogliosis (increased size and ramification) of astrocytes was observed from day 11, in conjunction with increased expression of the inflammatory cytokine IL-6. Conversely, at all velocitiy less than 100 mm.s^{-1}, no significant differences were observed in IL-6 or IL-10 release, nor in astrocyte shape and morphology.

4.5.1 Low velocity insults and NTSCI pathology

At day 1, significantly more IL-10 was released from astrocytes compressed at a low velocity than high velocity. However, no changes were observed compared to negative controls. There were no differences in IL-6 release at slow velocities at the timepoints tested. Similarly, there were no differences observed in astrocyte reactivity (GFAP expression). Therefore, the phenotype observed in NTSCI was different to TSCI. Patients with NTSCI experience a range of symptoms which are due to neurological tissue damage. However, the pathological mechanisms are not fully understood. It is important to evaluate each result of this chapter and their relevance to clinical NTSCI, which can elucidate pathological mechanisms and drive future research. Clinically, NTSCI involves prolonged compression of the spinal cord, over a timescale of weeks or months (Quinn, 2005; Karadimas et al., 2013). Herein, the compression was a one off event with a dwell of only 30 seconds. The extended chronic timeframe in clinical NTSCI may lead to a different phenotype in astrocytes to that observed herein. Use of an alternative apparatus

such as the ComCell device, adapted to apply a single compression over long term culture in multiple wells, may also fulfil this requirement (Matthews et al., 2001; Michalopoulos et al., 2012).

One possible reason for the lack of changes in astrocytes to observed herein, compared to clinical symptoms, is the duration of compression. Clinically, constant compression is sustained, and over extended timescale. *In-vitro* herein, it was a one-off event.

There have been no studies evaluating cytokine release in NTSCI patient populations. However, due to the inherent features of NTSCI (plasticity and remodelling in low velocity compression), it was hypothesised that there may be increased cytokine expression involved in remodelling of neural tissue. The cytokine IL-10 is widely described as an anti-inflammatory, cerebroprotective immunosuppressive cytokine (David and Kroner, 2011; Gensel and Zhang, 2015; Burmeister and Marriott, 2018; Ren et al., 2018; Jayaraj et al., 2019). It is involved in minimising cell death and inflammation, and promoting remodelling after TSCI (as summarised by Ren et al. (2018)). For example, Ishii et al. (2013) injected an IL-10 neutralising antibody into the CNS of mice after a TSCI, and observed a suppression in motor recovery compared to control groups. Further, a dichotomy in neural cell activation (pro- versus anti-inflammatory) has been described in the literature based on chemical activation of microglia and astrocytes (Jang et al., 2013a,b).

This study is the first to define astrocyte responses using cytokine release in a low velocity *in-vitro* mechanical compression study in astrocytes in isolation. Cullen et al. (2007) applied slow shear strain ($1.s^{-1}$) to hydrogels seeded with astrocytes and microglia, and did not observe any changes in astrocyte GFAP expression. The research herein did not observe significant differences in IL-10 release or astrocyte reactivity after low velocity (strain rate $0.142.s^{-1}$). injuries. This suggests either that these outcomes are not core to responses to low velocity compression, or the pathology in NTSCI is not mediated by reactive astrocytes alone, or that the mechanics of the compression tested in this study

were insufficient to show any pathological phenotype. Clinical studies evaluating cytokine release in patients with NTSCI would provide direction for outcomes *in-vitro*.

In the limited literature describing clinical and rat *in-vivo* studies of NTSCI, none have evaluated GFAP expression (Kubota et al., 2011; Kurokawa et al., 2011; Zibly et al., 2012; Long et al., 2013; Yang et al., 2015; Sun et al., 2016; Xu et al., 2017). In two studies which evaluated GFAP levels in rabbit models of lumbar stenosis through herniated discs, one found an increase in astrocyte reactivity at day 3 and 14 (Shunmugavel et al., 2013); whereas the other did not find significant differences to sham controls at day 10 (Cho et al., 2015). One study on post-mortem tissue from patients with NTSCI showed no glial scar formation (Someya et al., 2011). Therefore, the effects of NTSCI on astrocytes *in-vivo* have not been fully established. The study herein suggests direct mechanical compression of astrocytes does not cause astrogliosis in NTSCI. In future clinical studies, astrogliosis should be evaluated. This would allow evaluation of whether astrocytes are involved in the injury process, to provide direction for future research.

The roles of distinct populations of neural cells have not been established in NTSCI pathology. Astrocytes are core to the injury cascade in TSCI, but this research shows that mechanical compression of astrocytes alone is insufficient to induce NTSCI phenotypes. Clinically, this means in patients with NTSCI, direct mechanical compression of astrocytes is not the factor which induces symptoms. One possible reason for this is that cells other than astrocytes are damaged. Incorporation of other cell types into the model such as macrophages or microglia could cause a different response. Being immune cells, these cells classically have two types of activation: pro-inflammatory or anti-inflammatory (axonal regeneration and repair) (Gensel and Zhang, 2015). Although their roles have not been defined in NTSCI, their incorporation could result in greater pro- or anti-inflammatory changes in the *in-vitro* model.

Ischaemia is hypothesised to be involved in NTSCI, and may be the factor which results in damage to cells, as opposed to direct mechanical compression. When objects compress the spinal cord from the ventral approach, the ventral median artery in the

ventral median sulcus is first to be compressed. Compression of this major vessel results in ischaemia to the cord, which could cause hypoxic cell death. If this is the case, astrocytes may not be core to the pathology in NTSCI. Astrocytes may be involved in releasing molecules to control angiogenesis, remodelling the spinal cord to overcome ischaemia, and modifying vasculature permeability, which are secondary to the vasculature compression in the neurovascular unit (Mishra, 2017; McConnell et al., 2017). This would not be the same response as seen in TSCI, i.e. not a pro-inflammatory, reactive astrogliosis response. Instead, this would be an anti-inflammatory phenotype, which could be exacerbated by the presence of immune cells.

The inflammatory and pathological process in NTSCI is slow, and not similar to acute spinal cord injuries (Beattie and Manley, 2011). TSCI is characterised by gross structural damage, haemorrhage, immediate inflammatory cell infiltration, astrogliosis and scar tissue formation (Anwar et al., 2016; Morin, 2018). Conversely, the slow velocity of NTSCI means this gross damage and resulting pathology is not observed (Karadimas et al., 2013, 2015). The findings of the research herein correspond with this difference in pathology. Nevertheless, the changes observed in NTSCI were minimal compared to those in TSCI. This may be due to a more complex pathological cascade in NTSCI, where mechanical compression of astrocytes is not the core factor. Studies suggest microglia initiate and control astrocyte response after neural injury (Shinozaki et al., 2017). The injury cascade in NTSCI is hypothesised to be caused by hypoxia/ischaemia due to blood vessel compression, resulting in oligodendrocyte apoptosis and subsequently neuronal degeneration (Dolan et al., 2016). Therefore the use of this model with astrocytes alone would be insufficient to fully model NTSCI.

Overall, the results of this chapter suggest that direct mechanical compression of astrocytes at low velocities is not core to NTSCI pathology. In order to further explore the pathology of low velocity mechanical compression, further complexities should be added to the model. This should include cell populations such as microglia, oligodendrocytes and neurones. The effects of hypoxia should also be tested by modification of culture

conditions, and longer timepoints should be used. The use of the established *in-vitro* model will allow evaluation of each of these additions in isolation and in combination with one another. This, in turn, will increase understanding of the complexities of NTSCI, which could aid in developing future treatments.

4.5.2 Astrocyte Outcomes in Other Velocities Tested

10 and 1 mm.s^{-1}

Compression at the greatest velocity (100 mm.s^{-1}) caused a significant increase in GFAP labelled area per object at day 11 and 14. No such trend was observed at 10 mm.s^{-1} compression, or below. For all hydrogels compressed at velocities less than 100 mm.s^{-1}, there were no significant differences to negative control samples or to one another. These results suggest there is a threshold value, above which astrocytes become reactive, but below which no changes in reactivity are observed. This threshold value cannot be in load, since was similar between the two greatest velocities (10 and 100 mm.s^{-1}, but cellular outcomes were different. This may have been due to the recoil of the apparatus at high velocities once the target displacement was reached (as described in Chapter 3), resulting in data not forming one smooth peak.

Displacement was also the same for all samples. The two factors which differed were velocity and load. Collagen hydrogels are viscoelastic materials (Antoine et al., 2014). The same is true of the spinal cord (Bilston and Thibault, 1996; Ichihara et al., 2003; Fradet et al., 2016). It is well established that at high velocities or strain rates, viscoelastic materials have an increased stiffness (Dogliotti and Yelland, 1964; Hussein, 2018). Therefore, at high velocities, the maximum load recorded was greater and the cells would have been subject to a greater force. It is difficult to decouple these factors experimentally.

Few studies have evaluated the effects of changing velocity on astrocyte outcomes in the context of spinal cord injury. Cullen et al. (2007) evaluated the effect of increasing

shear strain rate on astrocytes, and found that the greatest strain rate tested resulted in increased GFAP expression at 2 days post injury, whereas lower strain rates did not. The strain rates used were $30.s^{-1}$, $10.s^{-1}$ and $1.s^{-1}$. By contrast, the strain rates used herein were $142.s^{-1}$, $14.2.s^{-1}$, $1.42.s^{-1}$ and $0.142 .s^{-1}$. Only at the greatest strain rate (equivalent to 100 $mm.s^{-1}$) were similar changes in astrogliosis observed. The results of the Cullen study study as well as the research herein suggest a threshold in velocity or strain rate, above which astrogliosis occurs, but below which astrocytes remained quiescent.

In terms of mechanics, slow velocity compression of a viscoelastic material allows it to change shape and stress to reduce (stress-relaxation). This would occur clinically, but only up to a threshold value of depth. After this depth, the spinal cord would not be able to relax further as it would have filled any surrounding space in the vertebral column. This would mean that increased stress was then applied directly to the cells. This could be tested *in-vitro* by using a greater displacement depth. Compression of 70% of the original gel height was chosen based on clinical studies showing that spinal cord compression greater than 15 to 50% of the cross-sectional area is required for symptoms to occur (Penning et al., 1986; Matsunaga et al., 2008; Iwahashi et al., 2016; Kadanka et al., 2017; Lim et al., 2017). It is possible that when applying forces to astrocytes alone, without other cells and components such as vasculature, a greater compression could be required to elicit cellular responses.

100 $mm.s^{-1}$, TSCI

This study found that high velocity (TSCI) impacts resulted in a larger area of GFAP staining per each stained object on day 11 and 14, along with increased ramifications of astrocytes at day 14. The larger area of GFAP per object can be interpreted as astrocytes being larger or expressing more GFAP, which is indicative of astrogliosis. Similarly, increased ramifications of astrocytes also indicate an astrogliotic response. Astrogliosis is characterised by an upregulation of GFAP, increased number of processes and process hypertrophy (Hol and Pekny, 2015). In TSCI, the degree of astrogliosis is a marker of

injury severity (Wanner et al., 2013). Reactive astrocytes form the glial scar, a physical barrier to neuronal regeneration. This has been observed clinically (Norenberg et al., 2004; Sofroniew and Vinters, 2010) as well as in various experimental models (Cullen et al., 2007; Kawano et al., 2012; Wanner et al., 2013; Weightman et al., 2014).

At day 14, there was an increase in IL-6 release, a pro-inflammatory cytokine. These results indicated the high velocity impact at day 1 (primary injury) resulted in a secondary injury comprising inflammatory response and astrogliosis at day 11 and day 14. It is worth noting that intensity of GFAP staining could not be measured in this study due to over-exposure of some images because of variation in staining intensity, but this could be used in future studies as another marker of astrogliosis.

IL-6 is a pro-inflammatory cytokine core to the secondary inflammatory injury cascade in TSCI (Okada, 2016; Paterniti et al., 2015). In a mouse study, blocking the IL-6 receptor *in-vivo* resulted in attenuation of astrogliosis and the secondary injury (Okada et al., 2004; Tan et al., 2013). The finding herein of increased IL-6 expression after high velocity mechanical compression indicates that a secondary injury comprising astrocyte inflammation was induced.

Two previous studies at the University of Leeds used the same cell type in the same collagen hydrogel system, and evaluated GFAP (Smith, 2016; Kirk, 2018). Kirk (2018) compressed the hydrogels with a focal, high velocity impact in the BOSE 5110 Electroforce apparatus. Findings from that study were that after 24 hours, i.e. within the primary injury timeframe, there were significantly more GFAP positive pixels in each image than negative controls. The area of GFAP staining per cell was not described. Therefore, differences in GFAP staining could have been due to an increased number of cells present. A measure of luminescence, indicating ATP levels, also indicated increased metabolism 24 hours after impaction, which again could indicate an increased number of cells. The research herein normalised GFAP staining per object (i.e. normalising based on the number of cells), and did not find significant differences at day one post-impaction. It is worth noting that the Kirk study used the same primary antibody for

GFAP at the same concentration, facilitating comparison. Kirk evaluated cytokine release at 4 and 24 hours post-impaction, and found significantly more IL-6 in media from astrocyte-seeded hydrogels than media only controls. However, with increasing impact displacement, IL-6 levels decreased. The differences between the research herein and the Kirk study may have been due to differences in methodology, including the focal nature of the lesion, varying displacement depth, timepoints evaluated and differences in analysis methodology.

Smith compressed the hydrogels with a focal impact, using the Infinite Horizon impactor (Smith, 2016). Similarly to the Kirk study, the Smith study also evaluated astrocyte responses using the same GFAP primary antibody at the same concentration as the study herein. The velocity of the impaction device could not be controlled. Instead, load control was used, applying a 2 N load. In test sample collagen hydrogels, where a 2 N input was defined, the output was 3.95 N. Accuracy of the device was not determined in the impacted samples, but was likely to be poor as reflected in the load input and output discrepancy. Upon impaction, material in the centre of the impact site was lost, but could not be seen as debris. This could have indicated the material was retained in the sample and pushed to the edge of the impaction site. At day 1, 5, and 10 post-impaction, there was increased GFAP-stained area per cell closest to the impaction site (although these differences were not statistically significant). The difference was greatest at day 10, but there was only one sample tested at this datapoint. No ELISA data was presented in the Smith study. The research herein identified increased GFAP staining per cell at day 11 and day 14. These findings are supported by the Smith study, in spite of limitations such as accuracy, and differences in the methodology used.

No studies have used organotypic spinal cord slices with varying mechanical insults to evaluate astrocyte reactivity. A weight drop method has been used to induce TSCI, but reactivity of astrocytes was not established (Krassioukov et al., 2002; Pandamooz et al., 2019). Weightman et al. (2014) used an organotypic spinal cord slice in combination with a scalpel blade to induce TSCI. Optical density was used as a measure of the amount of

fluorescent GFAP labelling, and this was increased in the nearest 100 μm to the lesion at 6 days post-injury. This corresponded with hypertrophic astrocytes with elongated processes, although these were not quantified. In more distant locations, astrocytes had a quiescent morphology and reduced GFAP labelling was observed. Astrogliosis in the Weightman study was observed at an earlier timepoint than the study herein (7 vs 11 days). This may be due to the presence of other cell types within the slices, which enhanced the astrogliotic response; such as microglial infiltration to the injury site and activation. The drawbacks of spinal cord slice studies are that astrocytes cannot be evaluated in isolation, therefore it is unclear whether responses were elicited by astrocytes themselves or as part of a more complex cascade involving other cell types.

Various *in-vivo* studies have evaluated the impact of mechanical factors on injury outcomes, however none have evaluated the effect of impact mechanics on astrogliosis specifically. Interestingly, Kim et al. (2009) evaluated the effects of three impacts speeds using different impactors on spinal cord injury, with a matched displacement. For the three velocities tested (100, 200 and 400 mm.s^{-1}), there were no significant differences in injury outcomes (behavioural or histological). This suggests that above a threshold, the value of which is below 100 mm.s^{-1}, velocity is not the most important factor in outcomes. A similar outcome was described by Lam et al. (2014) who used two displacements and three velocities (8, 80 and 800 mm.s^{-1}). Lam describes a threshold between impact depth and speed in determining injury outcomes. The load and work done imparted onto the spinal cords was not described in either study, so it is not possible to say whether the outcomes themselves were definitely due to differences in velocity. By contrast, Scheff et al. (2003) used three forces: 1, 1.5 and 2N, to induce spinal cord injury. There was a significant increase in injury severity in terms of behavioural outcomes and injured tissue area between groups, but there was also a significant difference in displacement as well as load. Therefore, it was not possible to determine if the effects were due to increased load in isolation.

Overall, the trend within the literature is that injuries with a greater mechanical

impact result in worse functional outcomes and greater area of injured tissue. The most important mechanical factor itself is debated, and difficult to isolate due to the inherent complexities of *in-vivo* models. None of the studies have assessed the effect of impact mechanics on astrogliosis specifically.

The results of this study herein support those of aforementioned research at the University of Leeds, addressing their limitations, and filling research gaps in *in-vivo* studies. The present study indicates that astrocytes alone in collagen hydrogels can model TSCI with high velocity impaction. High velocity TSCI-like primary injury astrocytes in collagen hydrogels stimulates a delayed secondary injury response incorporating astrogliosis, increase GFAP expression, and pro-inflammatory IL-6 release. The secondary injury cascade has been established herein, but no differences were observed at the primary injury stage. It would be of use to evaluate cell viability and metabolism at early timepoints in particularly, as this has been shown in a similar model to characterise the primary injury response (Kirk, 2018).

4.5.3 Conclusion

Progress made in this chapter in relation to the aims are described (Table 4.1). The results have the following implications in terms of causal mechanisms for TSCI and NTSCI:

- TSCI pathology is caused by high velocity mechanical compression of astrocytes: this primary mechanical trauma results in the secondary injury cascade of astrogliosis and inflammation.

- Reactive astrogliosis after mechanical insults is non-linear, with a threshold not based on displacement alone or load. Work done or velocity are core factors in distinguishing TSCI.

- The causal mechanism for NTSCI is not slow velocity mechanical compression of astrocytes.

- Further study is required using the same model with increased complexity and more cell types to fully characterise NTSCI.

Table 4.1: ***Conclusions of Chapter 4: Responses of Neural Cells to Varying Mechanical Input***

Aim	Objective	Result and Implications
Evaluate the effects of displacement and speeds on astrocytes	Seed collagen I hydrogels with astrocytes	Hydrogels were successfully seeded with primary rat astrocytes
	Compress hydrogels to 70% displacement at 0.1, 1, 10 and 100 mm.s^{-1}	The BOSE 5110 Electroforce was used to accurately apply high and low velocity mechanical insults to astrocyte-seeded collagen hydrogels
	Evaluate astrocyte responses for TGF-beta treatment (positive control)	TGF-beta treatment caused IL-6 release on day 1 and day 14; hydrogel contraction from day 5 onwards; and astrogliosis on day 11 and 14 (reduced circularity, and increased area of GFAP per cell).
	Evaluate high velocity (100 mm.s^{-1}) astrocyte responses	Compression at a velocity of 100 mm.s^{-1} caused increased area of GFAP expression per cell at day 11 and day 14, and IL-6 release at day 14.
	Evaluate lower velocity (10 and 1 mm.s^{-1}) astrocyte responses	Compression at velocities of 10 mm.s^{-1} or less did not significantly change GFAP expression. This is in spite of similar load between 100 and 10 mm.s^{-1} velocities.
	Evaluate low velocity (0.1 mm.s^{-1}) astrocyte responses	Compression at 0.1 mm.s^{-1} resulted in significantly more IL-10 release than compression at 100 mm.s^{-1}, however neither of these were significantly different to controls. No changes were observed in GFAP labelling.
	Evaluate astrocytes responses for negative controls	No differences were identified between apparatus and negative controls, i.e. in the assays used, there was no effect of physically removing the hydrogels from the plate and loading them in to the BOSE 5110 Electroforce apparatus.

Chapter 5

In-vivo NTSCI model development

5.1 Introduction

This chapter developed an *in-vivo* model of NTSCI based on a modification of a previous method used for TSCI, using a balloon catheter in rats. Three factors were considered to modify the method: directionality of the lesion (i.e. ventral as opposed to the traditional dorsal injury), the degree of stenosis required particularly in relation to balloon volume, and to adapt the method to allow inflation over a longer timeframe.

Whether NTSCI is caused by metastatic tumours in the vertebral body, osteophytes, or disc herniation, the origin of the mechanical insult is most often ventral to the cord (Ferrara, 2012; Tetreault et al., 2015; Martin et al., 2018). This is important since the spinal cord is not symmetrical about the z axis, i.e. the ventral and dorsal halves of the cord are different both geometrically and functionally. This is true of white matter, grey matter, and overall shape (Watson et al., 2009). For instance, the ventral surface of the spinal cord has the anterior median fissure, and the surrounding white matter is home to the reticulospinal and spinothalamic tracts, which are important in balance and sensory information (Sengul and Watson, 2015; Mitchell et al., 2016).

In spite of the clinical relevance, lesion directionality is often overlooked in TSCI and NTSCI *in-vivo*. Methods such as impaction or material implantation induce injury from

the dorsal approach. If a ventral approach could be developed, it would be important to understand how the histology of a traumatic lesion from the ventral approach differs from traditional dorsal methods.

A balloon catheter model for TSCI (such as used by Vanicky et al. (2001)) has been adapted to induce a ventral lesion by Institute of Experimental Medicine, Czech Academy of Sciences of the Czech Republic (henceforth IEM), although this is currently unpublished. A partial laminectomy is undertaken at T10, and a 2 French (2F) Fogarty balloon catheter is introduced and advanced ventrally and then cranially by 1 cm to spinal cord level T8/9. This means the catheter is theoretically ventral or ventro-lateral to the spinal cord. Existing research collaborations between academics at the University of Leeds, and IEM (Prague) facilitated development of the model herein. The findings of the research group at IEM (Prague) are currently unpublished. Therefore, this chapter first evaluates the histopathology of a TSCI ventral balloon catheter lesion in the rat spinal cord, at one week post injury. The purpose of this study was to assess the histology of such a lesion compared to the wider literature, and determine if the lesion was ventral.

In terms of developing the ventral balloon lesion model for NTSCI, stenosis progression is important. The pathology of NTSCI develops as stenosis increases: initially with an asymptomatic phase, followed by symptom onset and then deterioration (Karadimas et al., 2012, 2013). Understanding stenosis and cord compression extent in the animal model could further elucidate pathological mechanisms. Clinically, increasing canal stenosis is associated with an increased risk of developing symptomatic NTSCI (Penning et al., 1986; Steurer et al., 2011; Iwahashi et al., 2016; Weber et al., 2016; Kadanka et al., 2017; Martin et al., 2018; Witiw et al., 2018). If there is a threshold for cord compression to initiate symptoms this has not been established in the literature. It is particularly important to investigate canal stenosis and cord compression from the ventral approach, as this is where NTSCI originates from clinically.

To understand compression extent and stenosis, the geometry of both the injury-causing device and the rat vertebral canal must be established. In both NTSCI and TSCI

studies, these values are not often reported. In TSCI balloon catheter studies, the volume of injury-causing object varied between approximately 13 mm^3 (equating to 13 μL) at spinal cord level C5/6, and 10 to 50 μL at spinal cord level T8/9 (Vanicky et al., 2001; Kim et al., 2004; Lonjon et al., 2010; Chung et al., 2013). One study using the same 2F Fogarty balloon catheter as used in the current study described a diameter of 2.5 mm with a volume of 15 μL (Lonjon et al., 2010). However, the method to ascertain this dimension, and the corresponding balloon diameter for any volume other than 15 μL, were not described. A figure in another study using the same balloon catheter showed that the balloon diameter is 2.9 to 3 mm (Vanicky et al., 2001). This dimension must be taken as an estimate, as the value was interpreted from a photograph using crude measurement techniques. These volumes did not correspond with cord compression, and it is not known whether similar volumes would induce functional and histological changes in slow velocity NTSCI lesions.

Yang et al. (2015) carried out a rat study wherein a polymer was introduced at the thoracic level which increased in volume to a maximum of 8.4 mm^3. This induced spinal cord compression of 70%, and caused functional deficits. The timeframe of material expansion was not established. Conversely, Kim et al. (2004) used a similar polymer at the cervical level. The volume change described was 24% increase over 24 hours, but the dimensions of the polymer were not defined. This resulted in 11% cord compression but no functional deficits. Few other spinal cord injury studies *in-vivo* describe the resulting canal stenosis, and how that affects functional or histological outcomes (Hu et al., 2011; Kurokawa et al., 2011; Long et al., 2013; Xu et al., 2017).

There is a paucity of data describing the relationship between canal stenosis and outcomes in TSCI and NTSCI. In NTSCI, canal stenosis is particularly important as the increasing stenosis over time is core to the injury progression. The relationship between the geometry of the rat vertebral canal, compared with volume and geometry of the balloon catheter is a critical step in model development, and as such had to be characterised. This data could be used to determine canal stenosis in future studies of

NTSCI.

Martin et al. (1992) used the balloon catheter model in a traumatic injury study, but noted that the method could be modified to characterise progressive spinal cord compression by inflating the balloon progressively and leaving in place for longer timeframes. This has not yet been attempted in the literature. To model NTSCI *in-vivo*, the injury extent must increase over a temporal profile over weeks to days in a rat. Due to the time scale of this research, a temporal profile of injury lasting up to three days in a rat was selected. This means the device inducing the injury must be able to be implanted, as the animal could not be under anaesthetic for three days whilst inflation took place. A ventral balloon catheter model has been used to model TSCI *in-vivo*, and has the capacity to be adapted for NTSCI studies.

It was hypothesised that the balloon catheter system could be adapted for NTSCI studies. The system had to be able to be implanted (i.e. able to be sterilised, reasonable size), and the diameter of the balloon had to increase in a controlled manner over time after implantation. The geometry of the balloon could be tailored in terms of cross-sectional area of the vertebral canal, as defined in the previous experiment.

5.2   Aims

The aims of this chapter were to develop methods to model NTSCI *in-vivo*. This links to the overall aim of the project, to evaluate responses to NTSCI *in-vitro* and *in-vivo* (Figure 5.1). Specific objectives for this chapter:

1. To develop a clinically-relevant model of non-traumatic spinal cord injury *in-vivo*; with increasing canal stenosis over an extended time frame (i.e. days) and using a ventral lesion:

    A Characterise histology of balloon catheter inflation ventral lesion in traumatic spinal cord injury (rat, T8/9 spinal cord level).

    B Evaluate rat spinal column anatomy, in particular the diameter of the vertebral canal at thoracic vertebral levels T6 to T13.

    C Assess 2F Fogarty balloon inflation volume with increasing diameter.

    D Develop method for 2F Fogarty balloon inflation model for a non-traumatic injury context.
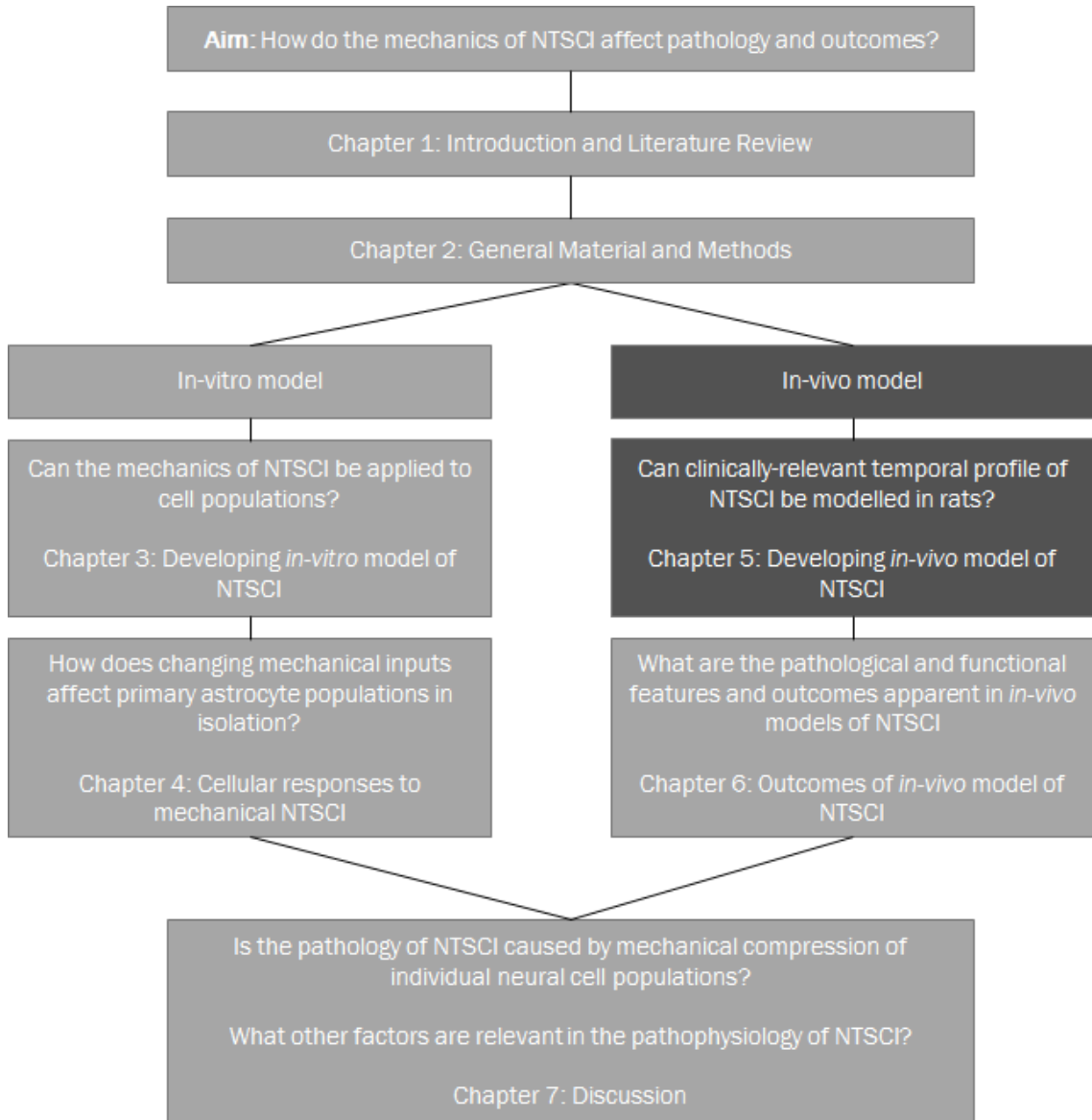
Figure 5.1: **Hypothesis and research question in Chapter 5, relating to aims of the whole study**.

5.3   Experimental Setup

5.3.1   Ventro-Lateral Balloon Spinal Cord Lesion

Four Wistar rats, 250 to 300g were operated upon in the Institute of Clinical and Experimental Medicine in Prague, using a currently unpublished ventral balloon catheter TSCI lesion model. This was modified from a previous dorsal balloon catheter model (Vanicky et al., 2001). In brief, a right-sided laminotomy was performed at T10, and a 2F Fogarty balloon catheter was introduced on the right hand side of the spinal cord, and advanced cranially, up to 1 cm below the proximal end of the balloon, so the centre of the balloon was at spinal cord level T8/9 (vertebral level T7/8). The balloon was inflated *in-situ* during surgery with either 12.5 μL or 15 μL of water using a Hamilton syringe (n=2 for both conditions). The balloon was left in place for 5 minutes before being fully deflated and removed. The incision was then closed using non-resorbable sutures. One week after injury, animals were perfused and spinal cords excised and their gross morphology briefly examined. Cords were then stored in 30% (w/v) sucrose with 0.1% (v/v) sodium azide at 4ºC for up to four months. Subsequently, spinal cords were embedded into OCT and frozen using a dry ice and ethanol slurry. Cryo-blocks were stored at -80ºC. The blocks were sectioned serially at 40 μm, and stored at -20ºC.

Sections every 1 mm were stained with haematoxylin & eosin to evaluate cross-sectional area of the tissue. Subsequently, sections were stained using immuno-labelling for GFAP (staining astrocytes) and CS-56 (staining chondroitin sulphate proteoglycans). These markers are upregulated in TSCI (Norenberg et al., 2004; Sofroniew and Vinters, 2010; Wanner et al., 2013; Hol and Pekny, 2015; Tachi et al., 2015; Alizadeh et al., 2019; Muir et al., 2019). For each animal, this comprised three regions: the lesion epicentre, and rostral, and caudal to the epicentre. Three sections per animal were imaged at each location using a confocal microscope, and the microscope settings were maintained throughout. Images were subsequently analysed using an automated macro in

FIJI (ImageJ) to evaluate the proportion of area which was stained. This was normalised as a percentage to the tissue cross-sectional area as determined using the H&E sections.

5.3.2 Evaluation of Rodent Anatomy: Computed Tomography Scan

5.3.2.1 Methods

CT scanning of a rodent spine was undertaken for guiding *in-vivo* experiments and gaining understanding about the anatomy of the vertebral column. Scans were undertaken using an Xtreme CT, with images taken along the length of the thoracic and lumbar spine in the transverse plane. Measurements were taken in the plane of the CT scan and in the anatomical plane using the 'volume viewer' plugin, allowing slices to be made in any orientation. Transverse slices were viewed, however due to spinal curvature the images obtained from the CT scan were out of plane, i.e. the whole vertebral foramen was not in plane on the individual image. The images were tilted using FIJI so that the entire vertebral foramen was in-plane and not tilted (Figure 5.2).
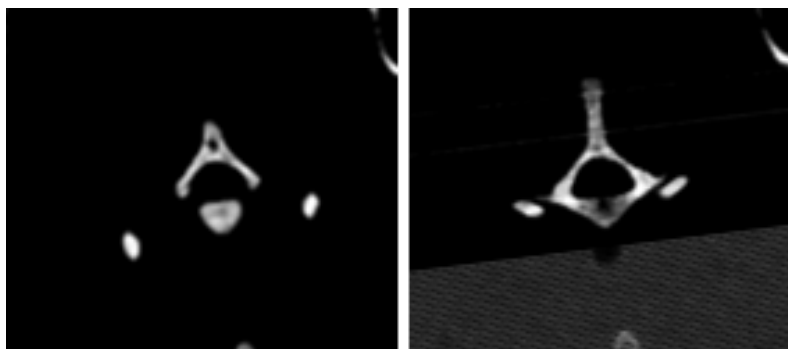
*Figure 5.2: **Evaluation of transverse out-of-plane measurements from microCT images of a rodent spine.** Left: x = 0, y = 0, z = 0; shows the image taken from the CT scan. Neither the full dimensions of the vertebral canal, nor the spinous process could be visualised. Right: x = 16, y = -2, z = 0; shows the same level now in plane, with the entire spinous process and vertebral canal surrounded by bone.*

Measurements from the thoracic and lumbar vertebrae were taken using FIJI (Figure 5.3). In order to estimate the cross-sectional area of the vertebral foramen, it was assumed

to be an ellipse, and was therefore calculated by the equation below:

$$\text{Ellipse Area} = r1 \times r2 \times \pi$$
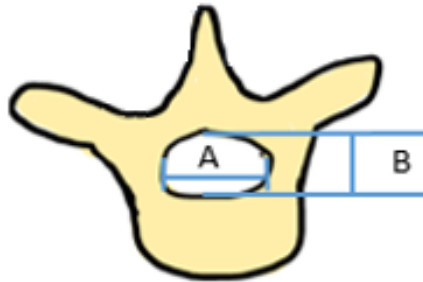
Figure 5.3: **Dimensions of the rodent spine taken from CT scans.** *Transverse plane dimensions were evaluated in thoracic and lumbar regions. A: width of vertebral foramen; B: depth of vertebral foramen.*

5.3.2.2 Experimental Setup

One cadaveric adult female Wistar rat was used to spare resources. The rodent was placed in a supine position, and scanned using the Xtreme CT, with a resolution of 40 μm on each image. The scan incorporated 126.6 mm (the length of the animal from neck to tail regions) and 3088 slices. The region from T2 to L6 was evaluated.

5.3.3 Evaluation of Balloon Catheter System

5.3.3.1 Methods

The specification and dimensions of the 2F balloon catheter, and other catheters, needle and cannulae used in this study are detailed below (Table 5.1). The balloons are designed to inflate uniformly and symmetrically in every direction (Lifesciences, 2019).

Prior to inducing the lesion *in-vivo* using a 2F balloon catheter, the volume-diameter relationship of the balloon had to first be established. Air was removed from the system

and replaced with water using a needle and 10 mL syringe with a small volume of sterile water. The needle formed a tight seal with the inner catheter walls. Air was drawn back through the syringe to form a vacuum, then water was added. Further manipulation of volume was carried out using a 50 µL Hamilton syringe, 30G needle and sterile water. Balloon diameter was measured by affixing the balloon to a graticule, and viewing under a dissection microscope.

Subsequently, a system was developed and characterised to inflate the balloon over a period of days which was suitable for *in-vivo* implantation. The balloon catheter was either attached to 3 French polyethylene tubing with an osmotic pump or 21G needle; or the 2F balloon catheter was affixed to a 22 gauge venous cannula. Air was replaced with sterile water in each system, and sterile water was used to inflate the balloons. The diameter of the balloon was measured as above, using a graticule and microscope.

Table 5.1: **Specification of catheters, cannulae and needles used in this study** *NB balloon liquid volume is not available as they are not tested for this purpose*

Item	Inner diameter (mm)	Outer diameter (mm)
Edwards 2F balloon catheter (deflated)	Unknown	0.667
Edwards 2F balloon catheter (inflated)	Unknown	4 (maximum)
Osmotic pump tubing requirement	0.76	N/A
Polyethylene (PE-60) tubing	0.76	1.14
Sentrawin 22G cannula tubing	0.41	0.72
21G needle	0.51	0.82
30G needle	0.31	0.16

5.3.3.2 Experimental Setup

Balloon Catheter Volume and Diameter

For initial balloon volume and diameter characterisation, two setups comprising a 5 cm length of 2F balloon catheter affixed to 5 cm of 3F PE-60 polyethylene tubing were manufactured. The seal between catheter and tubing was created using silicone 3140, and left to dry overnight. A 21G needle was inserted into the open end of the PE-60 tubing, and air was replaced with water in the system using a 10 mL syringe. In both systems, the

balloons were fully inflated to check patency. In the first system, the balloon was deflated until the sides of the balloon **just** became straight again (A and B in Figure 5.4). In the second system, the balloon was deflated fully. Subsequently, in both systems the needle was detached from the 10 mL syringe and attached instead to an airtight 50 µL Hamilton syringe filled with sterile water and no air bubbles. The balloon was affixed to a graticule and placed under a dissection microscope. Volume increments of 1 µL were added to the balloon and the diameter was measured, up to a total volume of 50 µL. Subsequently, the balloon was deflated in 5 µL increments, and the diameter was recorded.
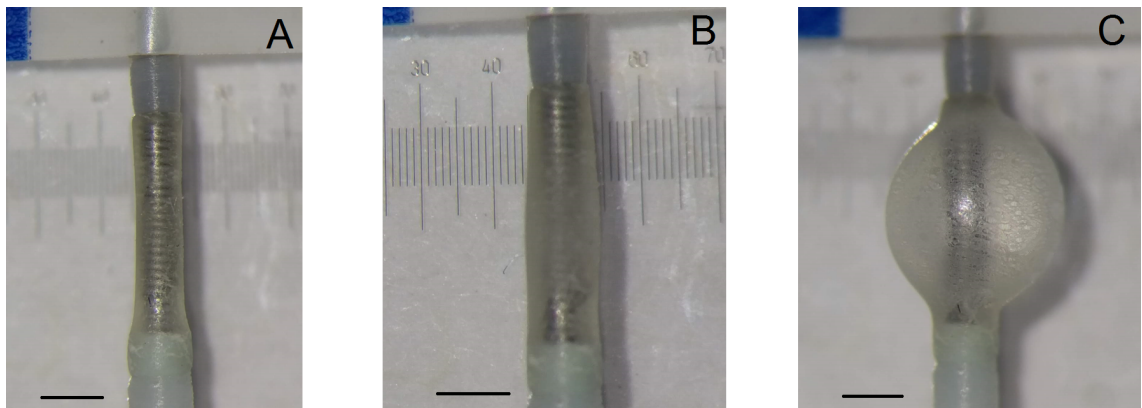
*Figure 5.4: **Photographs of balloon component of 2F balloon catheter at various stages.** A: completely deflated, B: sides of the device **just** straight, C: inflated with 15 µL. Scale bar 1 mm. Measurements taken using a graticule and microscope setup.*

Setup of Injection Port for Balloon Catheter NTSCI System

The balloon catheter/PE-60 catheter system (as previous, but a total of 10 cm of catheter and 10 cm of PE-60 tubing was used) was manufactured. Again, air was replaced with sterile water. The balloon was inflated to its maximum, and then deflated until the sides of the balloon were **just** straight. This was then attached to an osmotic mini pump (Figure 5.5).
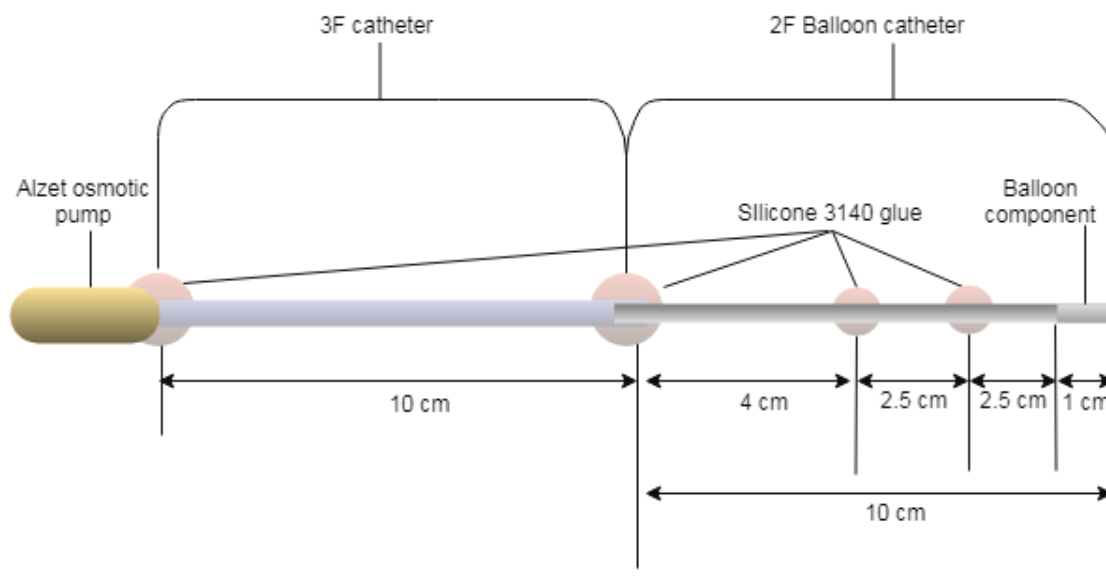
*Figure 5.5: **Schematic diagram showing the setup of balloon catheter with an osmotic pump system** Air was removed from the catheter tubing and replaced with sterile water before affixing the osmotic pump (also filled with sterile water). A total catheter length of 15 cm was affixed to an Alzet 1002 osmotic mini-pump using silicone 3140 cured at room temperature overnight. The whole system was submerged in phosphate buffered saline at 37^oC for inflation experiments*

The pump was filled with 100 μL sterile water, and this was confirmed by measuring the concurrent change in mass of the pump before and after adding water. The pump was primed in PBS at 37^oC for 24 hours before being sealed overnight to the catheter system using silicone 3140. The pump-catheter system was submerged in PBS at 37^oC for at least one week. The balloon diameter was measured prior to incubation, and then at 10, 25, 50, 100 and 168 hours (1 week).

An injection port was developed using either the PE-60 system with a 21G needle inside; or by affixing the injection port to a 22G venous cannula (Figures 5.6 and 5.7, respectively). In this latter setup, a length of 15 cm of 2F balloon catheter tubing was attached to a 22G venous cannula using silicone 3140 which was dried overnight at room temperature. To insert the catheter into the cannula, a 21G needle was pushed into the end of the cannula to widen it slightly, to allow the 2F balloon catheter to fit inside. Seals were made with silicone 3140. An airtight seal within the luer slip of either the needle or

venous cannula was developed.
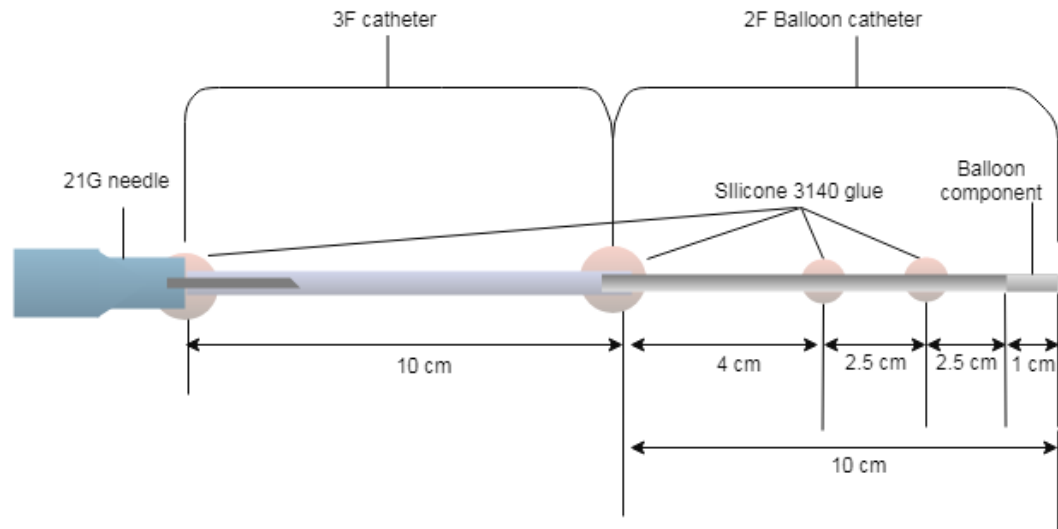
Figure 5.6: **Schematic diagram showing the setup of balloon catheter with 3F tubing** *Air was removed from the catheter tubing and replaced with sterile water. A total balloon catheter length of 10 cm was affixed to 10 cm of 3F polyethylene tubing. A 21G needle was then inserted into the 3F catheter. Joins were affixed with silicone 3140 and cured overnight.*

In repeat injection studies using the injection port, the 22G venous cannula system was set up as above. The luer slip was blocked using the materials defined in the previous test. Patency of the system was tested, the balloon was inflated to maximal volume (40 μL), and then deflated until the sides of the balloon were **just** straight. Then, the system was affixed to a graticule under a dissection microscope. A 30G needle attached to 50 μL airtight Hamilton syringe was inserted through the injection port. A set volume was dispensed. The needle was subsequently removed. Balloon diameter was measured at each step.

5.3.3.3 Developing an Injection Port

In order for the balloon to retain its diameter and volume once implanted, the whole catheter system had to be closed to the air and without leaks. To develop a model where repeat injections could be applied to the balloon catheter system over a period of days, an injection port needed to be developed. Two setups were tested: 2F balloon catheter with
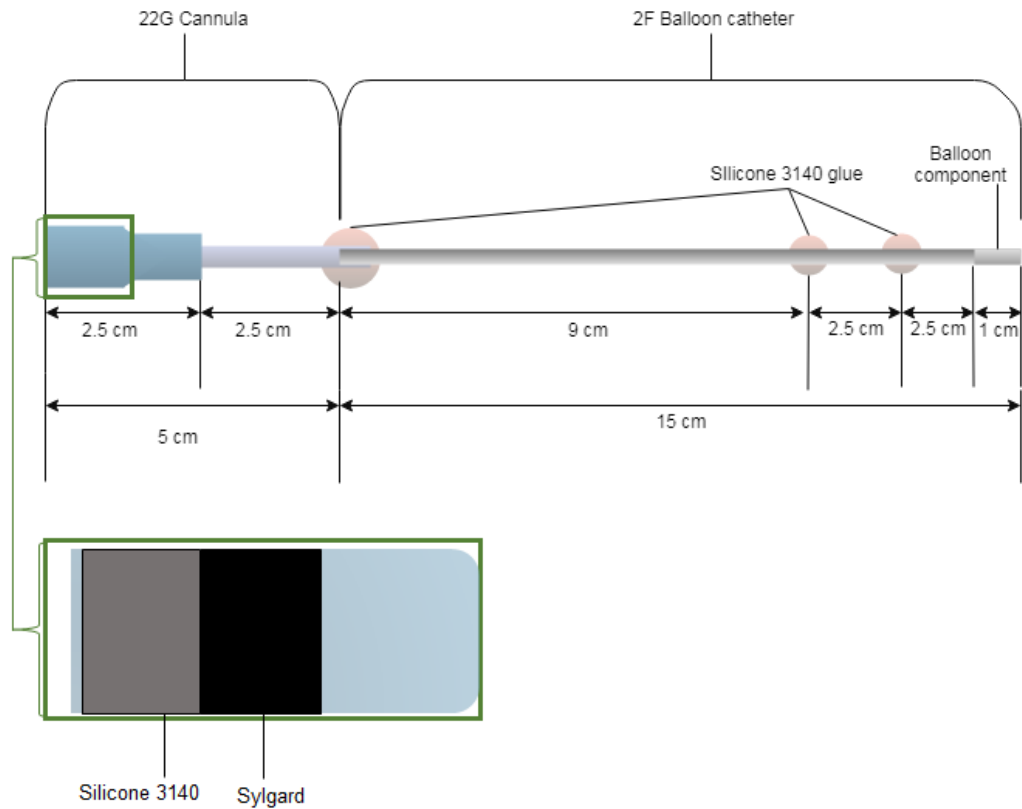
Figure 5.7: **Schematic diagram showing the setup of balloon catheter with cannula system and an injection port** *This setup was tested with materials to create a seal in the distal end of the setup. Air was removed from the catheter tubing and replaced with sterile water before inflation experiments were undertaken. System modified from previous publication (Fiebig et al., 2013).*

PE-60 tubing and a 21G needle; or 2F balloon catheter with 22G venous cannula. The material used for the port had to allow needle puncture, but then seal after the needle was removed. A previous study developed an injection port system using a venous cannula with an a rubber material inside it (Fiebig et al., 2013). The method used in this previous study was adapted.

The inside diameter of both the 22G cannula tubing, and 3F polyethylene tubing, were too narrow to allow any repeat injections; one injection, even with a 30G needle, would have completely disrupted the port. As such, the cannula luer slip was left attached the system. For the 3F tubing, a 21G needle was inserted into the tubing and attached using silicone 3140. This gave two options for forming an injection plug, the luer slip tips

of either the cannula or 22G needle.

Sylgard and silicone 3140 both alone and in combination were tested. Discs of Sylgard were punched out of a larger sheet using borers of various diameters. These were then pushed into the luer slip tips of both systems. A disc with a diameter of 4.23 mm fitted into the tips, and formed a visible seal around the diameter. When injecting through the material, it did not dislodge upon insertion or removal of the needle. The discs were pushed 2 mm down into the luer slip tips. The 2 mm gap above the discs was filled with silicone 3140, taking care to remove air bubbles, as a secondary means to ensure a closed system (Figure 5.7). This was left to cure overnight at room temperature.

Both the cannula and 3F catheter/needle system were sealed using the combination of Sylgard and silicone 3140. The two materials allowed needle puncture and injection without excess force. When the needle was removed, the puncture hole immediately sealed and no backflow of the injected solution was noted. The needle within the 3F catheter system had the capacity to easily puncture the catheter tubing without the user knowing. Further, the needle and 3F tubing system had three joins, which introduced more opportunities for leaks. Therefore, only the 22G cannula system was carried forward.

5.4 Results

5.4.1 Tissue damage and reduced cross-sectional area at the injury epicentre was observed in all animals

Ventral traumatic spinal cord injuries were introduced in four rats at T9 spinal cord level (approximately) using a 2F balloon catheter, which was inflated with either 12.5 or 15 μL water. The balloon was left in place for five minutes, then subsequently deflated and removed. The animals were perfused one week after surgery, and subsequently spinal cords were sectioned at 40 μm and stained with H&E.

The spinal cords did not appear flattened or deformed after dissection. Lesion sites could be identified by faint red bands on the tissue.

Many of the sections were damaged, but without cellular response, indicating damage occurred after perfusion. The tissue from one of the two animals injured with a volume at 12.5 μL was too damaged to clearly identify the lesion.

In the remaining three animals there was a clear lesion site, with a reduced volume of tissue in each transverse section area. The balloon component of the catheter was 5.5 mm long. As such, the evaluation of cross-sectional area of 10 mm should have been sufficient to identify the lesion caused by the balloon. There was a difference in cross-sectional area between the two injury volumes of 12.5 and 15 μL. (Figure 5.8). At the epicentre, there was approximately 11% less tissue in the 15 μL injury group compared with 12.5 μL.

The H&E stain used did not distinguish between healthy spinal cord parenchyma, inflammatory cell infiltration, or scar tissue. Therefore, the absolute values for cross-sectional area of the spinal cord at the injury site may be lower than those determined by this study.

For the lesion of 12.5 μL, there was minimal tissue remaining at the epicentre. However, at 2 mm rostral or caudal to the lesion, the grey and white matter of the cord could be distinguished, with only the dorsal white matter having been damaged (Figure
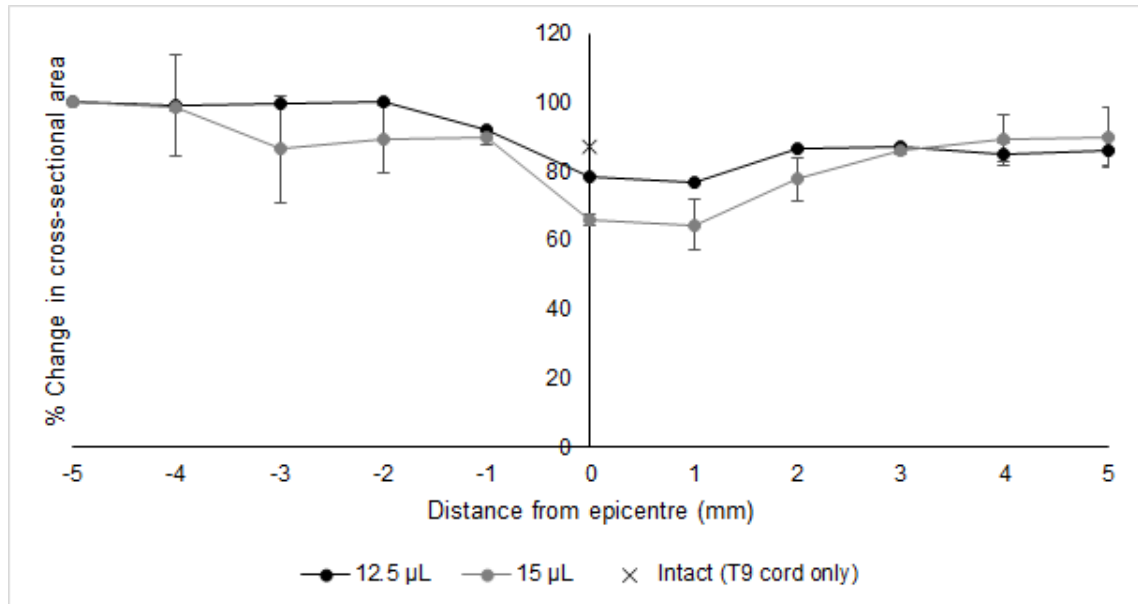
*Figure 5.8: **Transverse cross-sectional area of TSCI rat spinal cord, normalised to 5 mm rostral from the injury epicentre.** Animals underwent a T10 laminectomy and balloon catheter insertion and inflation at T8/9, with a volume of either 12.5 (n=1) or 15 µL (n=2). Cross-sectional area was determined using 40 µL sections, 1 mm apart, stained with haematoxylin and eosin. Subsequently, area was determined using an ImageJ macro.*

5.9). At 5 mm rostral and dorsal to the epicentre, there was a lesion present within the dorsal funiculus of the white matter, in a circle or oval shape. This was also present at 8 mm rostral and dorsal, although the lesion was smaller.

For the lesion of 15 µL, there was significant tissue damage at the epicentre, and both 2 mm rostral and caudal to the lesion (Figure 5.9). At these points, white matter and grey matter could not be distinguished. At 5 mm rostral and caudal to the epicentre, the white and grey matter of the cord could be distinguished, although there was still considerable damage to the dorsal region. At 8 and 10 mm rostral to the epicentre, a circular/oval lesion could be observed in the dorsal white matter, similar to that seen at 5 and 8 mm rostral in the 12.5 µL lesion (Figure 5.10).

In total, lesions could be observed a total distance of 16 mm rostrocaudally for the 12.5 µL lesion, and 18 mm rostrocaudally for the 15 µL lesion.
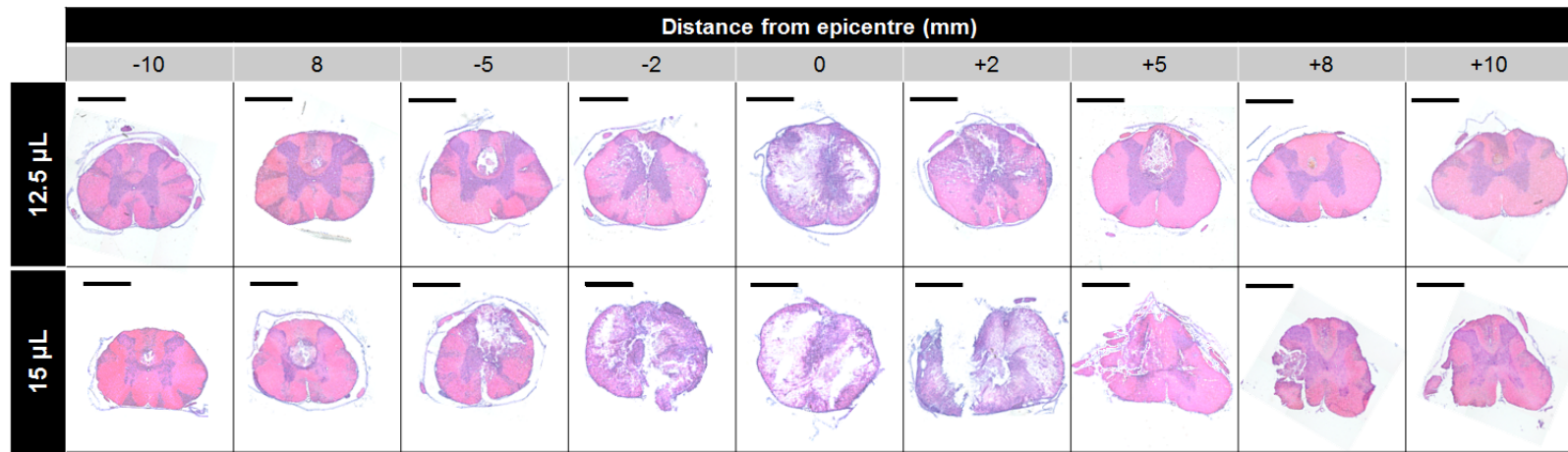
Figure 5.9: **Sample cross-sections of spinal cord from TSCI balloon catheter lesions with two volumes.** *Animals underwent a T10 laminectomy and balloon catheter inflation at T8/9 with a volume of 12.5 or 15 μL. Animals were perfused one week after the injury. Sections 40 μm thick were stained with H&E. Negative distance values denote rostral to the epicentre, and positive distance values denote caudal. Scale bar = 1mm.*

The balloon component itself was 5.5 mm long, with rostral catheter 2 mm further. The catheter and deflated balloon were 667 μm in diameter. The circular/oval lesion observed in injuries induced by both volumes extended beyond this 2 mm. These circular cavities were larger closer to the injury epicentre, with a smaller diameter the further from the epicentre. At 9 mm rostral to the lesion epicentre for a 15 μL lesion, the cavity measured approximately 500 μm laterally, and 750 μm dorso-ventrally (Figure 5.10). Here, the cavity was contained some cells with a yellow colour indicated ongoing necrosis. At 8 mm rostral to the 12.5 μL lesion, the cavity measured approximately 220 μm laterally, and 260 μm dorso-ventrally (Figure 5.11). Here, there was no yellow colour observed, instead the tissue comprised loose connective tissue matrix with some cells, indicating necrosis had already taken place.

Vacuoles were observed in white matter both rostral and caudal to the lesion epicentre (Figure 5.12). These were present in lateral and ventral regions of the white matter, where the dorsal white matter was no longer present.

At the lesion epicentre, three tissue types were present (Figure 5.13). At the penumbra of the spinal cord in cross-section, a small amount of conserved white matter remained. Within the main cross-sectional area of the spinal cord, there were two further types of cells. The central region contained high density cells. Between this high density region and the white matter were regions containing no cells or debris, and loose regions of debris with macrophage infiltration.
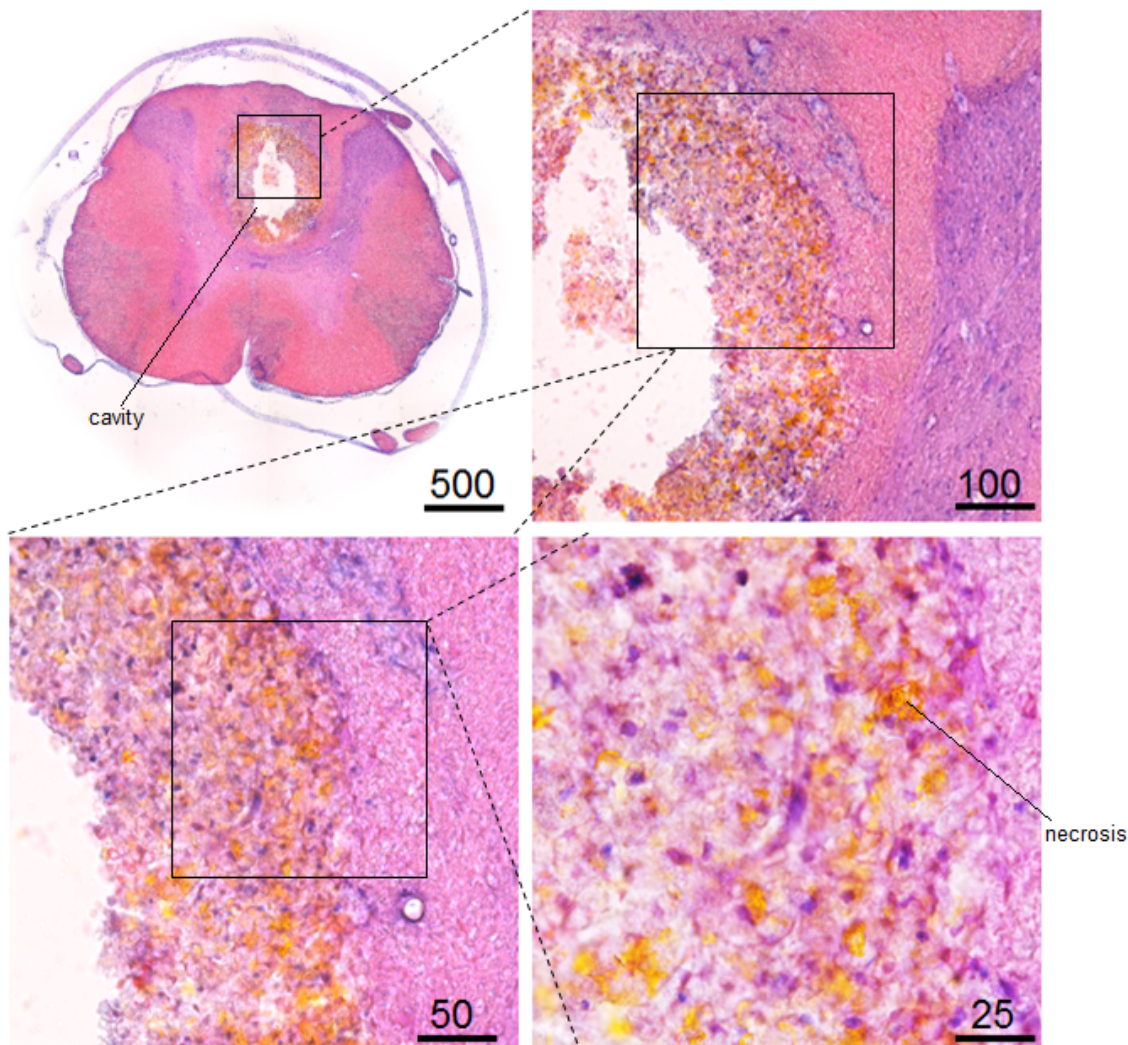
Figure 5.10: **H&E image of lesion cavity 8 mm rostral from lesion epicentre in 15 µL balloon-induced TSCI.** *Animals underwent a T10 laminectomy and balloon catheter inflation at T8/9 with a volume of 15 µL. Animals were perfused one week after the injury. Sections 40 µm thick were stained with H&E. Scale bar for each image is in µm.*
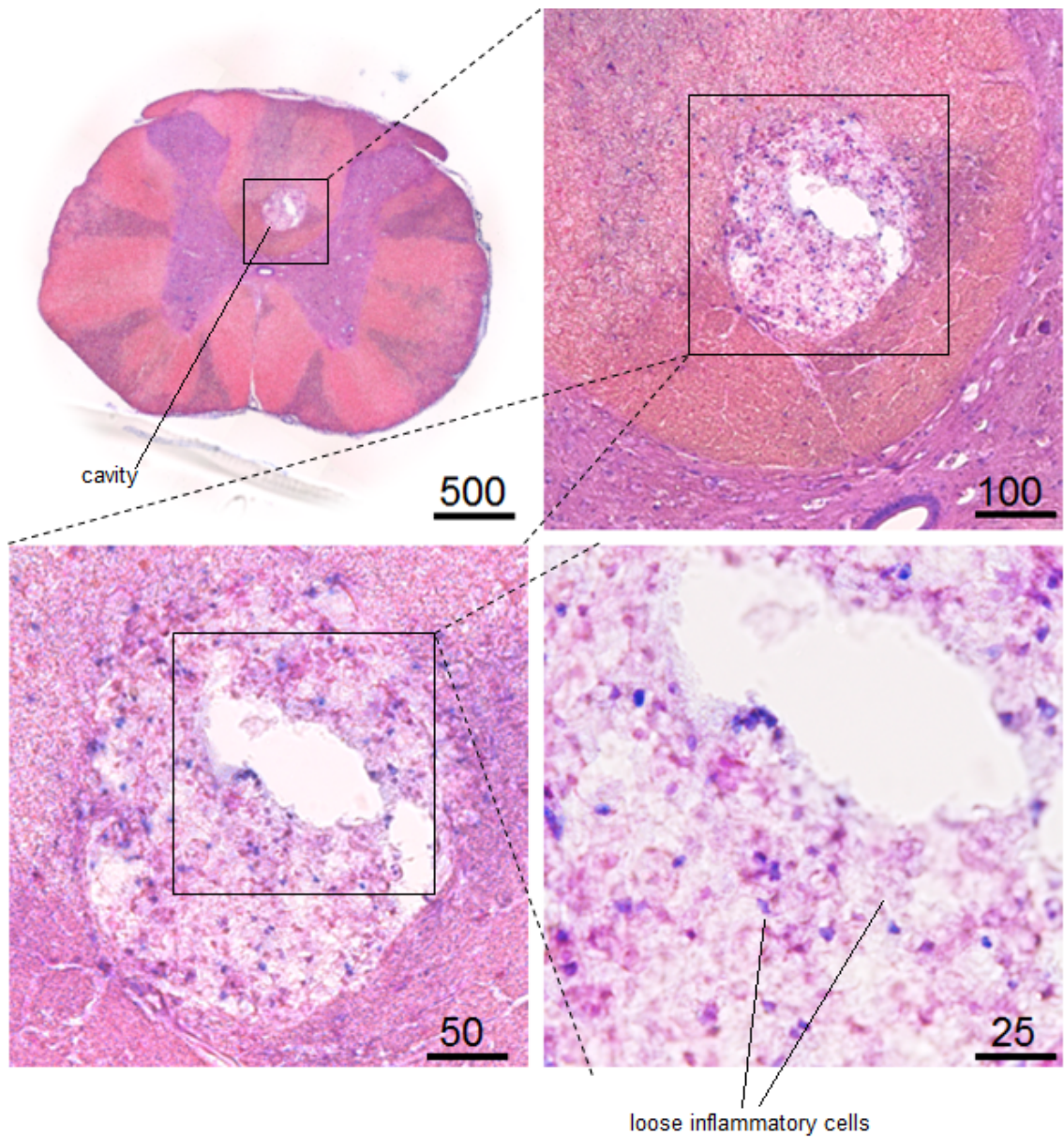
Figure 5.11: **H&E image of lesion cavity 8 mm rostral from lesion epicentre in 12.5 μL balloon-induced TSCI.** *Animals underwent a T10 laminectomy and balloon catheter inflation at T8/9 with a volume of 12.5 μL. Animals were perfused one week after the injury. Sections 40 μm thick were stained with H&E. Scale bar for each image is in μm.*
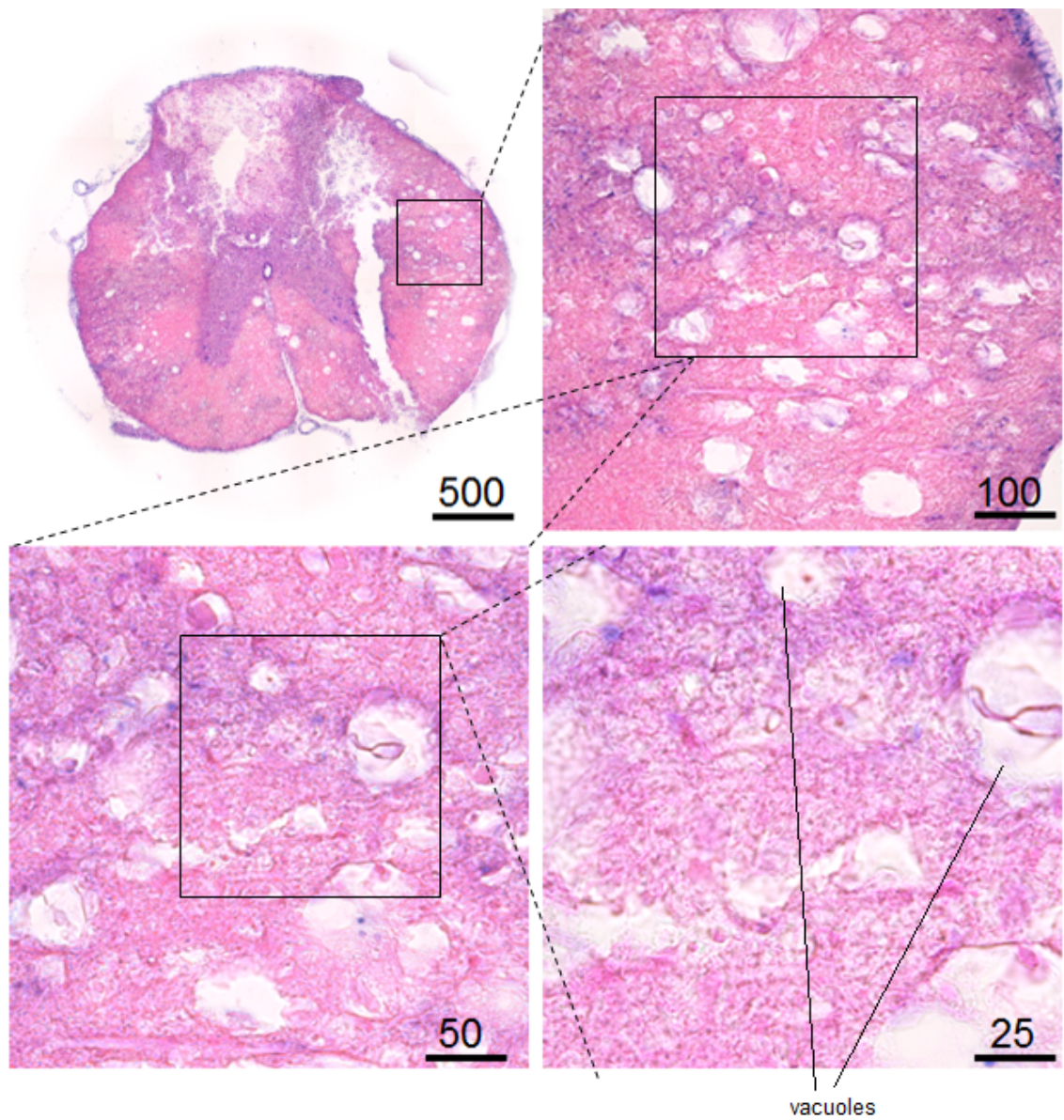
Figure 5.12: ***Vacuoles in white matter rostral to TSCI lesion epicentre.*** *Animals underwent a T10 laminectomy and balloon catheter inflation at T8/9 with a volume of 15 μL. Animals were perfused one week after the injury. Sections 40 μm thick were stained with H&E. Scale bar for each image is in μm.*
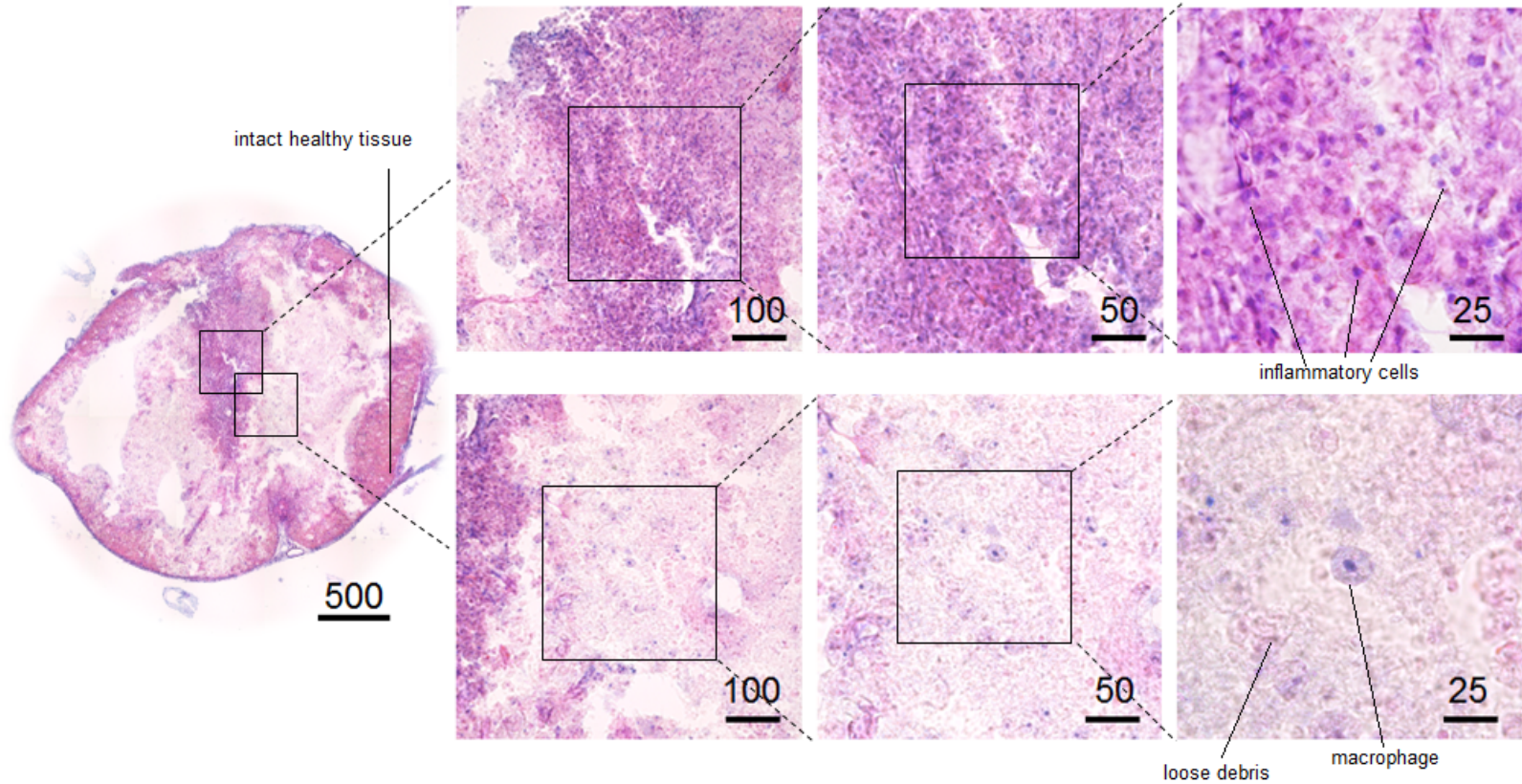
Figure 5.13: ***Lesion epicentre one week after TSCI induced by balloon catheter.*** *Animals underwent a T10 laminectomy and balloon catheter inflation at T8/9 with a volume of 15 μL. Animals were perfused one week after the injury. Sections 40 μm thick were stained with H&E. Scale bar for each image is in μm. Two types of cell or tissue regions can be identified, a high density cellular infiltrate (above row), and a loose matrix of macrophages and debris (below row), and*

5.4.1.1 Traumatic balloon injury resulted in increased GFAP and CSPG expression at the injury epicentre

It is worth noting that due to damage to the tissue during histological preparation, N = 1 for a balloon volume of 12.5 μL. This meant that statistical analysis using two-way ANOVA could not be undertaken and volumes could not be compared (Figure 5.14A). Instead, results were pooled and one-way ANOVA was carried out with Tukey's post-hoc test, comparing spinal cord regions. There was a greater area of GFAP staining at the epicentre than either rostral or caudal to the lesion (p $<$0.05, Figure 5.14B). In rostral and caudal regions, GFAP labelling was observed predominantly at the edge of the cord, i.e. the white matter (Figure 5.15). At the injury epicentre GFAP labelling was observed in both the central fibrotic region as well as in the remaining white matter.
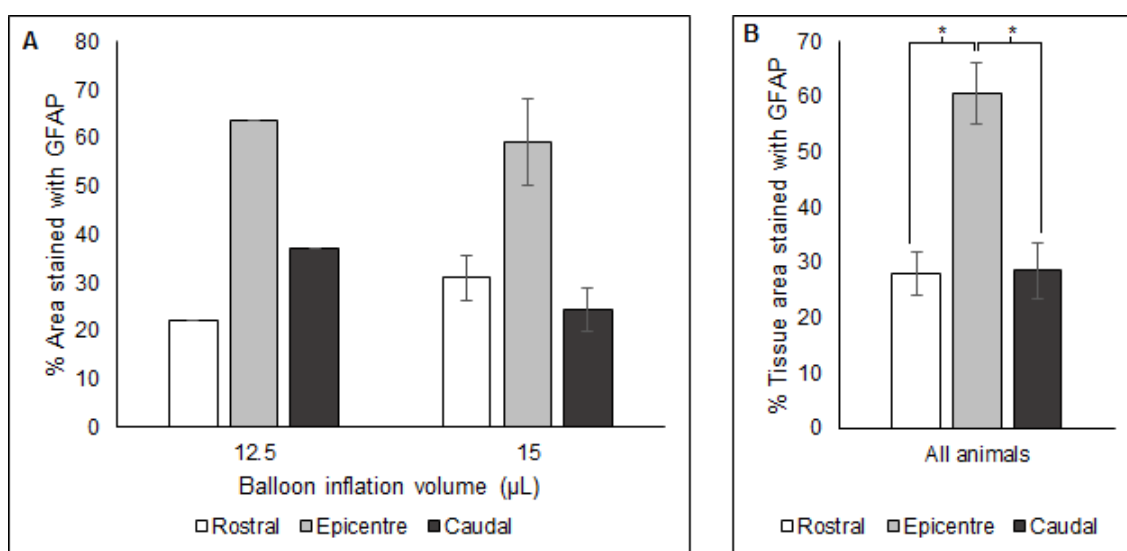
*Figure 5.14: **Proportion of tissue stained with GFAP in balloon catheter induced TSCI.** Animals underwent a T10 laminectomy and balloon catheter inflation at T8/9 with a volume of 12.5 (N=1) or 15 (N=2) μL. Animals were perfused one week after the injury. Sections 40 μm thick were stained with GFAP and the stained area (determined using FIJI) was given as a percentage of the total area determined using H&E staining. Three sections per animal were stained at each location. Data is mean ($\pm$ S.E.M for 15 μL).*
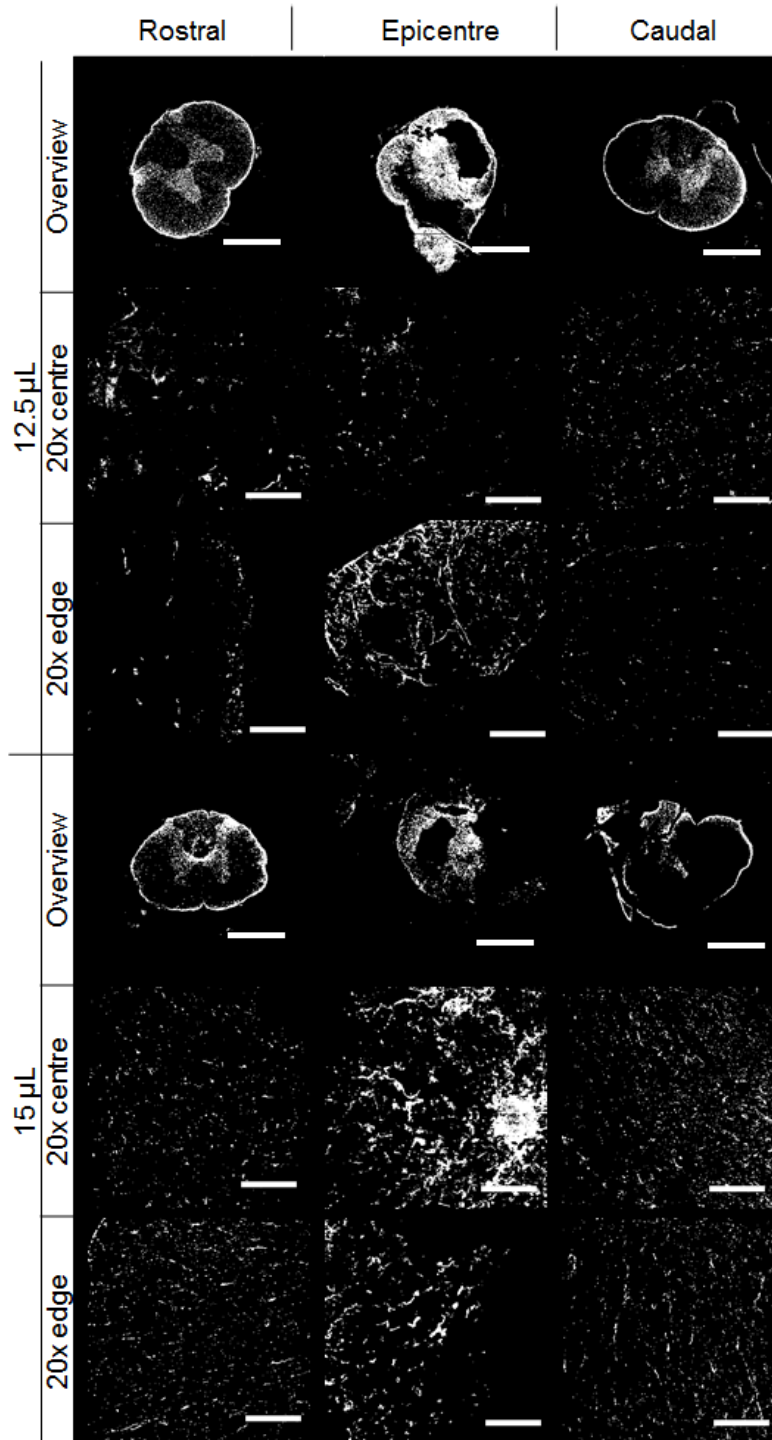
Figure 5.15: **Representative images of GFAP staining in ventral balloon catheter-induced TSCI.** *Animals underwent a T10 laminectomy and balloon catheter inflation at T8/9 with a volume of 12.5 or 15 µL. Animals were perfused one week after the injury. A total of three sections 40 µm thick were stained and imaged at each location. In overview images, scale bar is 1 mm, in 20x images, scale bar is 100 µm*

Similarly to GFAP, pooled data for CS-56 expression was required for statistical analysis due to N=1 for 12.5 μL (Figure 5.16A). Using a one-way ANOVA, there was a significantly greater area stained with CS-56 at the epicentre than at rostral and caudal regions (p <0.05, Figure 5.16B). There was minimal observable CS-56 staining in rostral and caudal regions, and staining was only present in the central grey matter (Figure 5.17). Conversely, at the epicentre there was strong specific staining for CS-56 in the central fibrotic regions as well as in the remaining white matter at the edge of the tissue.
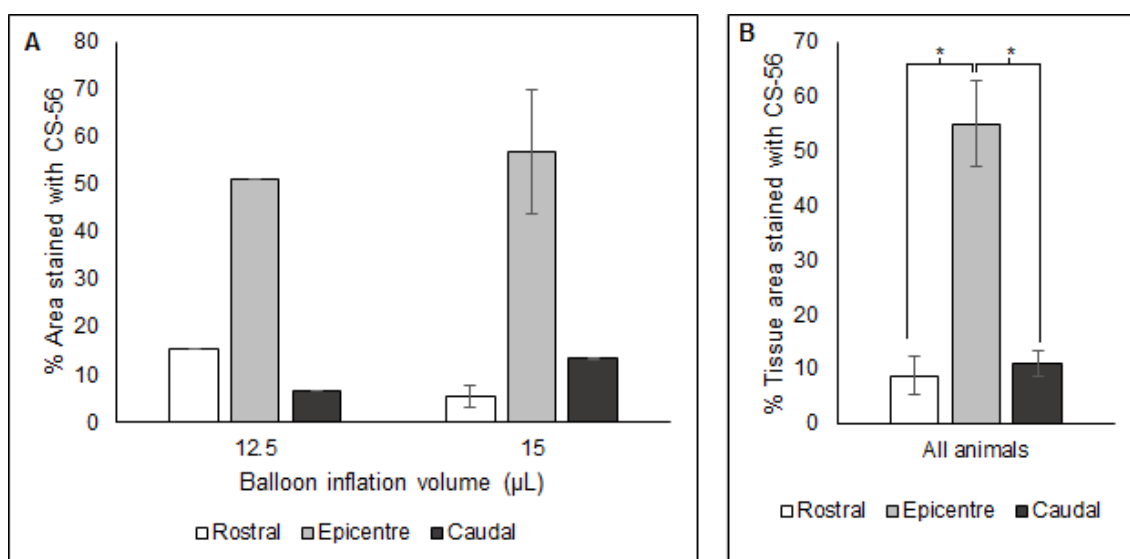
Figure 5.16: **Proportion of tissue stained with CS-56 in balloon catheter induced TSCI.** *Animals underwent a T10 laminectomy and balloon catheter inflation at T8/9 with a volume of 12.5 (N=1) or 15 (N=2) μL. Animals were perfused one week after the injury. Sections 40 μm thick were stained with CS-56 and the stained area (determined using FIJI) was given as a percentage of the total area determined using H&E staining. Three sections per animal were stained at each location. Data is mean (± S.E.M. for 15 μL).*
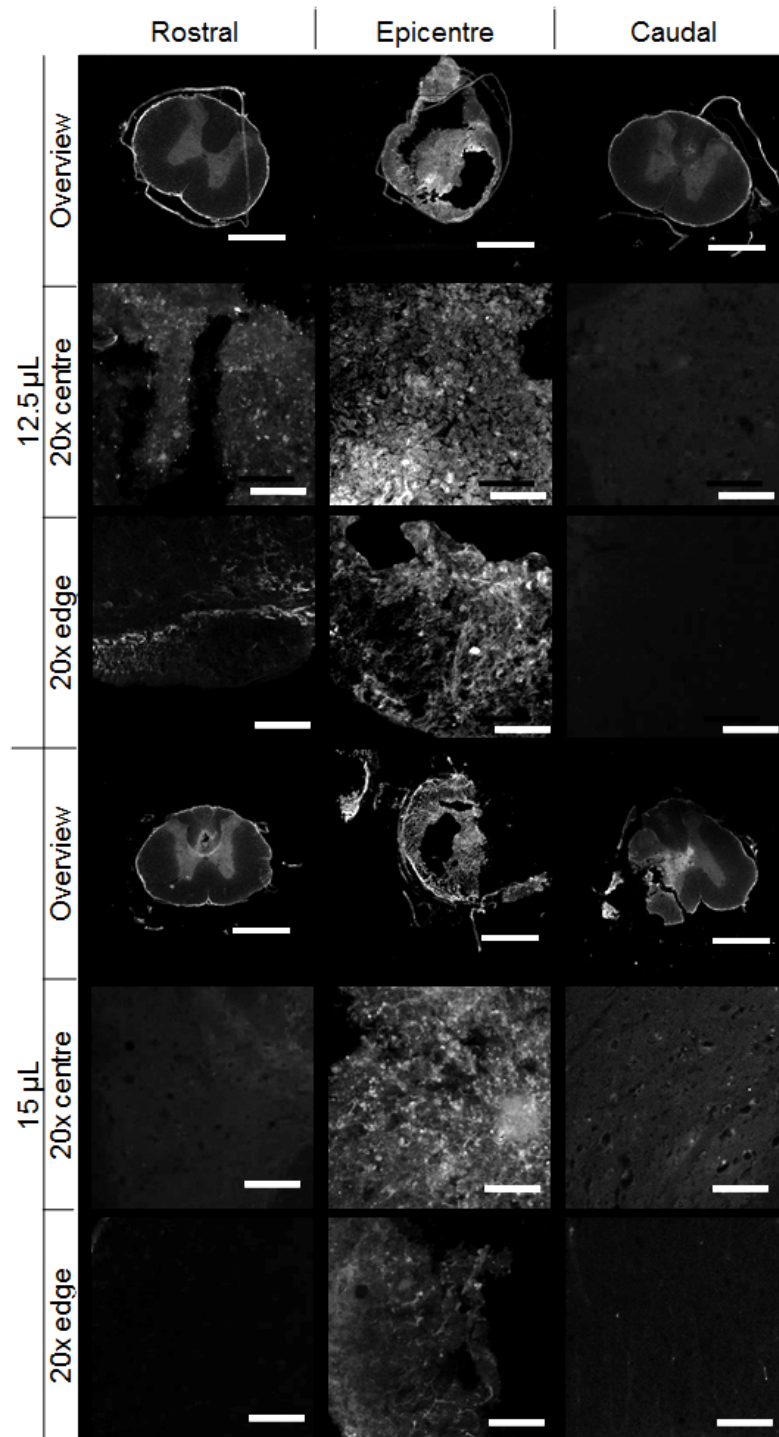
Figure 5.17: **Representative images of CS56 staining in ventral balloon catheter-induced TSCI.** *Animals underwent a T10 laminectomy and balloon catheter inflation at T8/9 with a volume of 12.5 or 15 µL. Animals were perfused one week after the injury. Sections 40 µm thick were stained with CS56 to identify chondroitin sulphate proteoglycans. In overview images, scale bar is 1 mm, in 20x images, scale bar is 100 µm*

5.4.2 Vertebral foramen area was greatest at T7/8

For *in-vivo* experiments, a greater understanding of rat spinal anatomy was required to identify appropriate compression extent. Further, the balloon catheter system required evaluation and development prior to implantation. Prior to developing methodology for *in-vivo* experiments, it was useful to first develop an understanding of the spinal anatomy of the rat. This was undertaken by a CT scan of a rat post-mortem (methods in section 5.3.2). The thoracic region of the spine had an anatomical curvature which could not be straightened due to rigor mortis (Figure 5.18).

The width of the vertebral foramen generally decreased from T2 to L6, with exceptions at T13, L1, and L3 (Table 5.2). The depth of the vertebral foramen increased from T2 to T7, and then decreases to L6. Cross-sectional area was on average 7.9 ± 0.21 mm^2 for the thoracic region, and 4.5 ± 0.86 mm^2 for the lumbar region. The maximum cross-sectional area was 8.9 mm^2 at T7/8.

*Figure 5.18: **3D renditions of 2D CT scans of rat skeletal anatomy.** Rendered in ImageJ, scale bar = 5 mm. Sagittal view (left, yz plane); frontal view (right, xy plane).*

Table 5.2: **Rodent vertebral dimensions, from the second thoracic to last lumbar vertebrae.** *Dimensions from female Wistar rat CT scan, with image analysis using the FIJI volume viewer plugin VF = vertebral foramen, D = depth; W = width, CSA = cross-sectional area (assuming the vertebral foramen is an ellipse)*

		Vertebral level																
		T2	T3	T4	T5	T6	T7	T8	T9	T10	T11	T12	T13	L1	L2	L3	L4	L5	L6
Measurement	VFW (mm)	4	3.8	3.6	3.5	3.3	3.3	3.3	3.5	3.1	3.3	3.4	3.8	3.8	3.6	3.3	3	2.5	2.2
	VFD (mm)	2.5	2.5	2.6	3.1	3.1	3.4	3.4	3	2.9	2.8	2.5	2.8	2.6	2.1	1.9	1.6	1.4	1.2
	CSA (mm^2)	7.9	7.5	7.2	8.4	8.0	8.9	8.9	8.4	7.2	7.2	6.6	8.3	7.7	5.9	4.8	3.6	2.7	2.1

5.4.3 2F balloon volume-geometry characterisation could be fitted to a polynomial curve

Methods used in this section are described in section 5.3.3. An initial experiment was undertaken to assess how adding volume to the balloon catheter system affected balloon diameter. Subsequently, a similar study was undertaken in the sealed system with repeat injections over time.

This part of the study evaluated how additional volume affected balloon diameter using a 2F balloon catheter, PE-60 tubing and 21G needle attached to 50 μL Hamilton syringe. Starting with a completely empty balloon (inflation 2, A and B, Figure 5.4 in Section 5.3.3.2) resulted in a lag before inflation began. Ultimately, the same maximum diameter was achieved in both systems. The reported maximum diameter of the balloon was 4 mm, with a cross-sectional area of 12.57 mm^2 (section 5.3.3). The maximum diameter achieved was 4.1 mm, with a cross-sectional area of 13.36 mm^2 (Figure 5.19).

At a volume of 15 μL, the catheter diameter was 2.8 mm. In both tests, inflation and deflation matched one another. Fitting the mean of these datapoints to a polynomial trendline gave the following output equation describing balloon diameter (y) in terms of volume (x), with an R^2 value of 0.98:

$$Y = -0.017x^2 + 0.149x + 0.738$$

5.4.3.1 An osmotic pump was not sufficient to inflate the balloon

This part of the study used a 2F balloon catheter, affixed to PE-60 tubing, which was in turn affixed to an Alzet osmotic pump (Figure 5.20). Based on the equation corresponding balloon volume and diameter, and knowing the dispensing rate of the pump from the manufacturers details (0.25 μL per hour) it was estimated that after one week inflation (168 hours), 42 μL would have been added into the balloon. This would have resulted in a theoretical diameter of approximately 4 mm (Figure 5.21). However, over the course of one week attached to the pump, the balloon diameter did not increase.
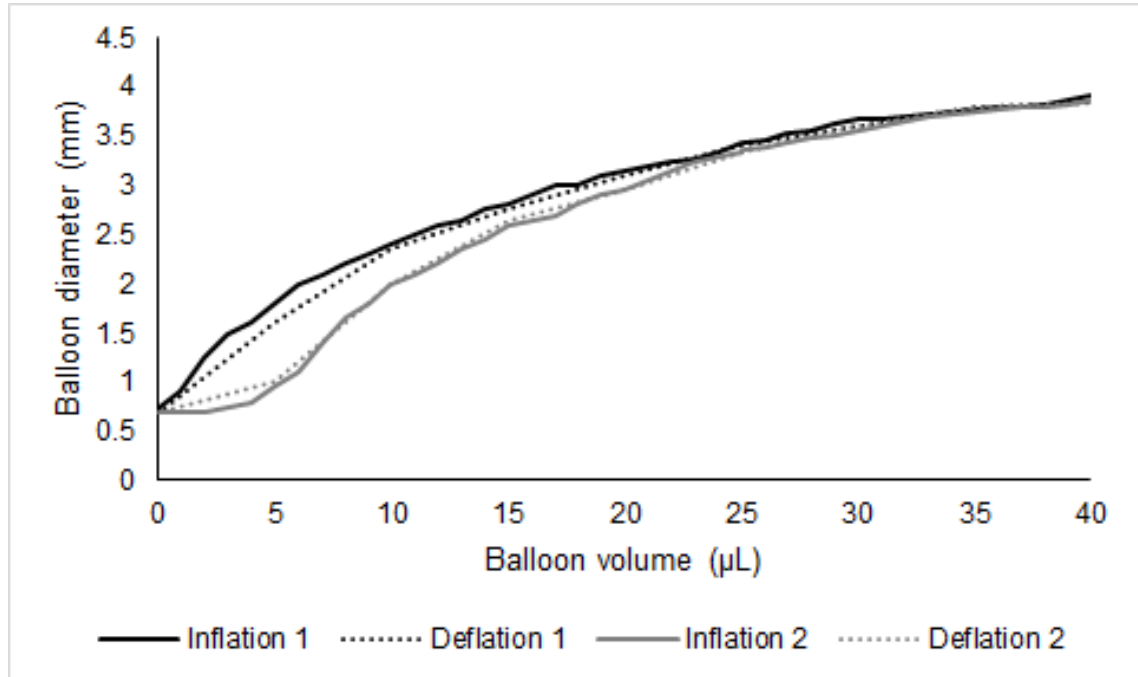
*Figure 5.19: **Volume-diameter inflation and deflation mechanics of a 2F balloon catheter.** A 2F balloon catheter was inflated in 1 μL increments up to a volume of 50 μL, measuring diameter using a graticule and microscope. The system was then deflated in increments of 5 μL, similarly measuring diameter. Inflation/deflation 1 began when the sides of the balloon were straight. Conversely, inflation/deflation 2 began when the balloon was completely empty.*
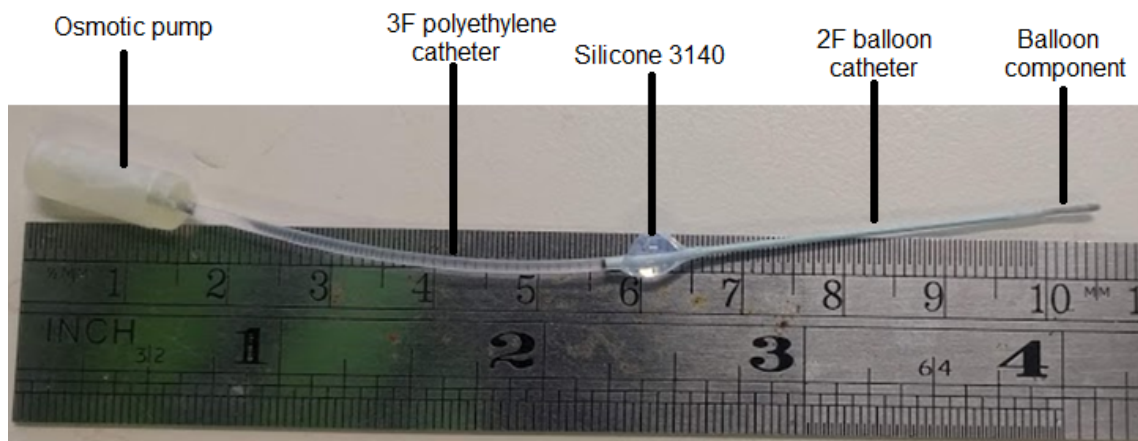
*Figure 5.20: **Annotated photograph of osmotic pump setup with balloon catheter.** The osmotic pump (Alzet 1002 model) had to be connected to 3F polyethylene tubing; which was subsequently connected to the 2F balloon catheter. Seals were made using silicone 3140. The osmotic-pump 3F catheter tubing seal is not annotated in the photograph, but this join was also sealed with silicone 3140.*
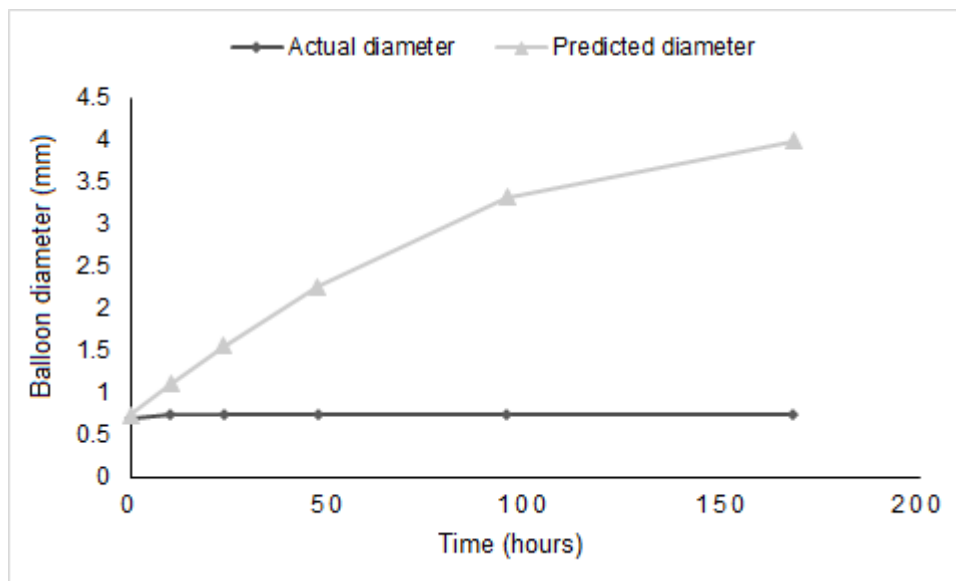
*Figure 5.21: **Predicted and measured balloon diameter of 2F catheter connected to osmotic mini pump.** The whole system was placed in PBS at 37ºC for one week, with regular measurements of the balloon diameter. Predicted balloon diameter values were based on a previous study using a Hamilton syringe to add volume to the same catheter system.*

5.4.3.2 Over 3 injections, 7.5 μL (a total of 22.5 μL) matched the end diameter of 2.8 mm

The catheter and 22G venous cannula system, with injection port, was used for this part of the study (Figure 5.22). The aim was to understand how repeat injection of various volumes resulted in changes in balloon diameter. The injection process (inserting needle, adding volume, removing needle) was repeated three times. Volumes dispensed ranged from 6 μL to 10 μL per injection. The aim was to achieve a diameter of 2.8 mm (matching that used in previous studies) after three repeat injections, equating to T9 vertebral canal stenosis of approximately 75%. This was achieved using a volume of 7.5 μL per injection (Figure 5.23). Diameter was maintained when the needle was removed from the system, but dropped when the needle was subsequently added back into the system.
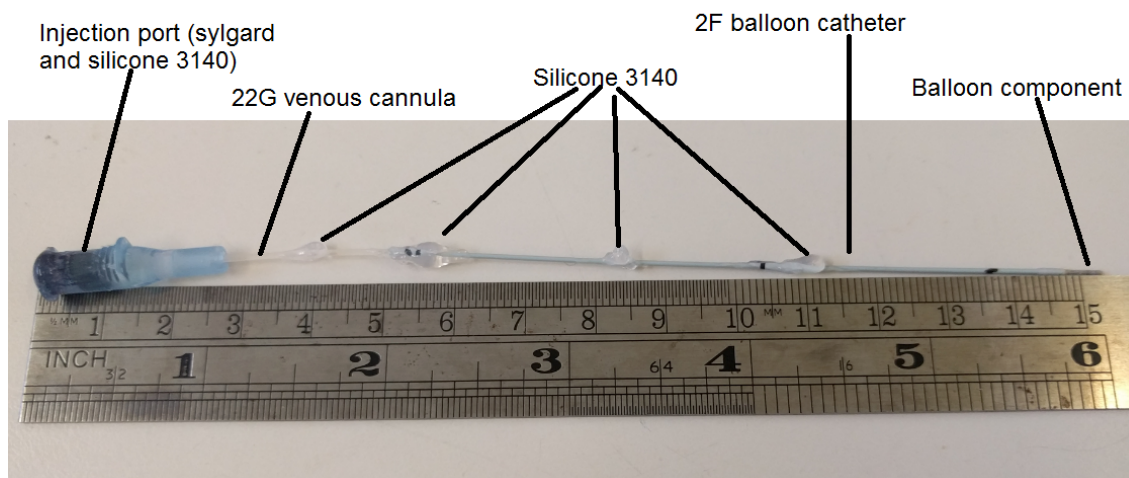
Figure 5.22: **Annotated photograph of injection port setup with balloon catheter.**
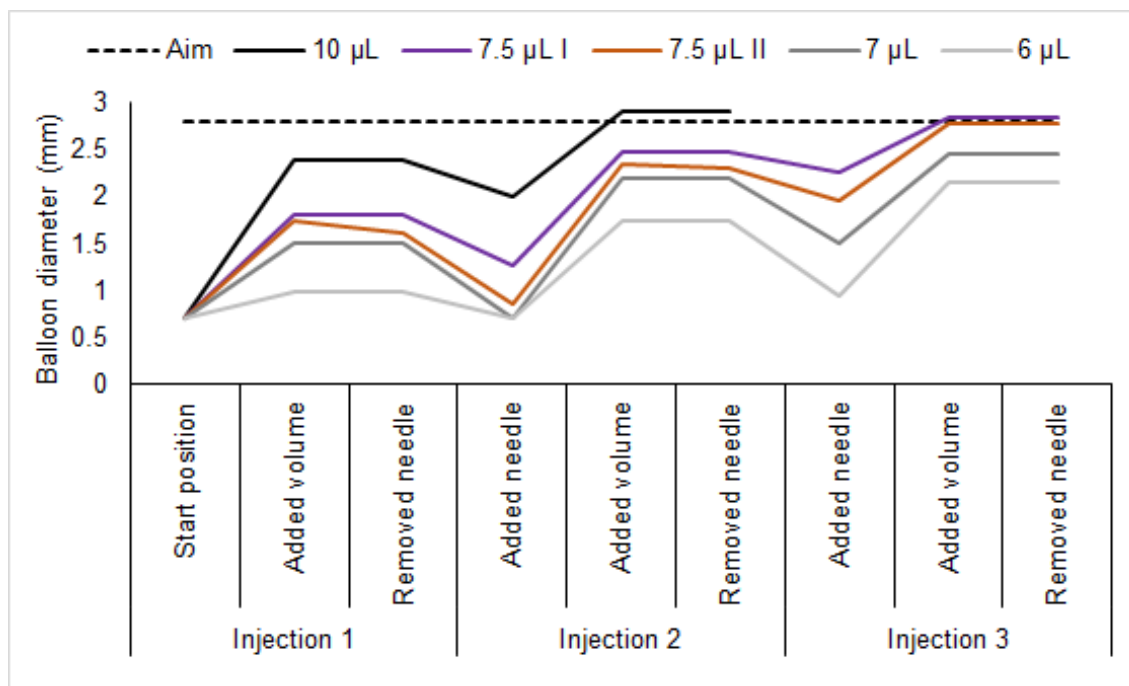
Figure 5.23: **Balloon catheter diameter when inflated with various volumes over repeat injections with an injection port.** *The 2F balloon was subsequently inflated using repeat injections through the slip tip injection port using various volumes. Diameter was measured with an aim of 2.8 mm after three repeat injections. Results shown are from one catheter setup only, except for 7.5 μL where two setups were tested.*

5.5   Discussion

It was hypothesised that a ventral balloon catheter lesion (method developed by IEM, Prague, Czechia) could induce TSCI, and be adapted to induce injury over a longer timescale (NTSCI). This hypothesis was tested by evaluating the histopathology of lesions in a rat (T8) using the ventral balloon catheter lesion in a TSCI context. Subsequently, work was carried out to define the optimum compression extent of the system by evaluating both rat vertebral column dimensions, and geometry of the balloon itself with changing volume. Tests were then carried out *in-vitro* to adapt the balloon catheter for use in NTSCI implantation studies, evaluating the diameter of the balloon over a period of two to three days. Three days in a rat is equivalent to approximately three months in man, mimicking the prolonged timescale of NTSCI (Andreollo et al., 2012; **?**).

Balloon catheters have been used in dorsal TSCI studies, to induce histological and functional deficits at T8 to T9 spinal cord level. A laminotomy or partial laminectomy is performed at spinal cord level T10, and a 2F Fogarty balloon catheter is introduced, then advanced cranially 1 cm to reach spinal cord level T8 to T9 (as confirmed by imaging by Martin et al. (1992); Chung et al. (2013)). Benefits include only a partial laminectomy or laminotomy, and no need to stabilise vertebrae using forceps, which minimises soft and bone tissue damage. Further, the lesion site itself is closed, which more closely mimics the human condition. This is in contrast to weight drop or impactor studies where the lesion site is open. The lesion severity for both early (5 days) and chronic (up to 7 weeks) outcomes can be controlled using the volume of the balloon, and a dose response curve for the dorsal balloon lesion has been established (Martin et al., 1992; Vanicky et al., 2001; Lonjon et al., 2010; Chung et al., 2013). At spinal cord level T8/T9, a volume of 15 µL was determined to cause an injury which had the capacity to both improve or deteriorate (Vanicky et al., 2001).

5.5.1 Ventro-Lateral Balloon Spinal Cord Lesion

A ventral TSCI was induced at spinal cord level T8/9 using a balloon catheter lesion, in four animals. Two of these had a lesion with a volume of 12.5 μL, and two with 15 μL. All four animals survived the surgery. Both volumes of 12.5 and 15 μL showed a clear histological lesion site. Functional testing was not carried out herein, and further characterisation of ventro-lateral balloon catheter traumatic spinal cord lesions are being undertaken by collaborators in Prague.

In this study, transverse sections of spinal cords at one week post-injury showed significant disruption to the central canal, white matter and grey matter for both balloon volumes at the lesion epicentre. Due to tissue damage during perfusion or histological preparation, one of the animals injured with 12.5 μL had to be excluded from histological assessment. In the animal with a 12.5 μL lesion there was a greater area of normal white matter parenchyma at the epicentre than in the two animals with a 15 μL lesion.

The cross-sectional area of the spinal cord was evaluated within 10 mm of the epicentre (5 mm rostral, 5 mm caudal). This distance was decided based upon the balloon length itself (5.5 mm). The greater balloon volume induced a larger lesion size (i.e. smaller cross-sectional area) at the epicentre $\pm$ 1 mm rostro-caudally. No statistics could be undertaken due to the N of 1 in the 12.5 μL group. Evaluating the images of the spinal cord, damage was greater in the 15 μL lesion group both at the epicentre and over a wider rostro-caudal distance from the epicentre. However, this was not reflected in the cross-sectional area results since the H&E staining used does not distinguish normal and damaged tissue, only the presence of tissue. Alternative stains such as fast blue could distinguish white matter parenchyma from other tissues (grey matter parenchyma, connective tissue, inflammatory cell infiltrates).

Remaining cellular material in the spinal cord contained high density inflammatory and fibrotic cells centrally, whereas the surrounding tissue contained cystic cavities with cellular debris and macrophages. Similar findings were observed in dorsal weight drop

contusion models of TSCI and balloon catheter models, with ablation of grey matter, presence of cellular debris, minimal haemorrhage, and development of a cystic cavity at one week (Mao et al., 2016; Sutherland et al., 2016). In dorsal TSCI balloon catheter studies, a similar pathology was identified, with increasing tissue disruption and lesion extension with greater volumes (Vanicky et al., 2001; Lonjon et al., 2010; Chung et al., 2013). Where white matter was present in a transverse section with significant tissue damage, vacuolisation was apparent. This was also in keeping with other dorsal TSCI balloon catheter studies (Martin et al., 1992; Chung et al., 2013).

Across all three animals, there was a greater proportion of tissue stained with GFAP and CS-56 at the epicentre than rostrally and caudally. There was no difference observed in GFAP or CS-56 staining between balloon volumes; this is likely to be due to the low N numbers in each group. The increase in GFAP-stained area directly reflects reactive astrogliosis at the lesion epicentre, which was not present in the rest of the spinal cord. Reactive gliosis is core to the pathology of TSCI both clinically and *in-vivo*, as part of the formation of the glial scar (Norenberg et al., 2004; Sofroniew and Vinters, 2010; Wanner et al., 2013; Hol and Pekny, 2015; Alizadeh et al., 2019). Although several studies have used a 2F balloon catheter to induce TSCI in rats, only two have incorporated evaluation of reactive gliosis or the fibrotic scar (Martin et al., 1992; Chung et al., 2013). In both of these studies, fibrotic scar formation and an increase in GFAP area was observed at the lesion epicentre, but not quantified in either case. The findings of the research herein validate that the ventral 2F balloon catheter method of causing TSCI can induce reactive astrogliosis at the injury epicentre, whilst the rest of the spinal cord remains quiescent, in keeping with the wider TSCI literature.

In the research herein, a greater area was stained with CS-56 at the epicentre than at intact rostral and caudal regions. Chondroitin sulphate proteoglycans (CSPGs, stained by CS-56) are a core component of the glial scar, and are produced by reactive astrocytes and other spinal cord cells after injury (Buss et al., 2009; Anderson et al., 2016; Sofroniew, 2018). For example, after hemisection injury in a rat model, CS-56 expression increased

between day 4 and day 14 (Tachi et al., 2015), corresponding with glial scar formation. The CSPG molecules are components of the perineuronal nets which usually surround neurones, and restrict plasticity (Sobel, 1998; Kwok et al., 2011; Burnside and Bradbury, 2014; Haggerty et al., 2017; Irvine and Kwok, 2018). Such is the effect of over-expression of CSPGs in spinal cord injury to inhibit neuronal regeneration, that enzymes which digest CSPGs have shown potential in treatment (Bradbury et al., 2002; Muir et al., 2019). The findings of increased CSPG expression at the injury epicentre compared to intact rostral and caudal levels further validate the experimental model.

Lesion extension was observed rostral and caudal to the injury epicentre, predominantly comprising a cystic cavity with cellular debris in the dorsal funiculus of the white matter. The extent of lesion extension in both groups was greater than the length of the balloon itself, and therefore was due to biological extension as opposed to mechanically induced by the balloon. Lesion extension was greater in the 15 µL group compared with the 12.5 µL group, although statistics could not be undertaken. This finding is in keeping with previous studies where a greater volume of the balloon induced a longer (rostro-caudal) lesion (Vanicky et al., 2001; Lonjon et al., 2010; Chung et al., 2013). A similar shape and location cavity was observed in these previous studies where the balloon catheter TSCI model was used in a dorsal lesion (Martin et al., 1992; Lonjon et al., 2010; Chung et al., 2013). There are several explanations for the location of this cavity being in the dorsal funiculus rather than ventrally. The cavity could be inherent to the severe balloon-induced TSCI, independent of whether the injury itself was dorsal or ventral. Alternatively, the cavity could be dependent on direction and the balloon could have been positioned dorsally instead of ventrally in all of the animals tested. Finally, the cavity could be as a result of damage occurring during balloon insertion or removal, as opposed to inflation of the balloon. These explanations could be tested in future studies using imaging techniques to identify balloon position, or by creating an injury with a smaller volume to identify better the position of the balloon at the lesion epicentre. Ideally, in future studies, the catheter should remain in place in the spinal canal until the end of

the experiment (perfusion). This would prevent damage occurring when the catheter is removed.

Due of the extent of tissue disruption at the lesion epicentre, it was not apparent whether the injury induced was in fact ventral or dorsal to the spinal cord. The low number of animals per group in this study mean that this study could not fully characterise the lesion. Further work is being carried out by the developers of the method at IEM, Prague. In this study, a lesion was clearly present in all four animals, which was similar to that seen in other TSCI studies. Therefore, the balloon catheter method was appropriate for inducing spinal cord injury in a rat model.

In relation to the volumes used, a 12.5 μL lesion resulted in less tissue damage than a 15 μL lesion. However, statistical analysis could not be fully undertaken due to the N of 1 in the 12.5 μL group. Vanicky et al. (2001) deduced that a 15 μL lesion was optimal as it allowed for determining both deterioration and improvement of the lesion. For reasons of continuity with this study and the wider literature, future NTSCI studies will match the diameter of a 15 μL 2F balloon catheter. It will be important to determine the geometry of this volume balloon in relation to the vertebral canal.

5.5.2 Evaluation of Rodent Spinal Anatomy to Provide Direction for *in-vivo* Studies

Several studies have used balloon catheters to induce spinal cord injury, relying on increasing volume to compress the spinal cord. In the previous TSCI balloon catheter study, both volumes tested (12.5 μL and 15 μL, at spinal cord level T8/9, vertebral level T8) caused a histological defect, but the compression extent was unknown. In NTSCI, compression extent increases over time. Initially, this does not result in symptoms, but after compression exceeds a tissue threshold, tissue damage and symptoms result. The exact value of this threshold is not well established clinically. Compression extent is determined by the area of the injury-causing object in relation to the geometry of the vertebral column. Understanding these two measurements is important to determine

compression extent. This study carried out a CT scan of a rat vertebral column in order to better understand compression extent.

Lumbar measurements were compared with a previously published study to determine accuracy of the findings herein (Jaumard et al., 2015). Jaumard used a different subspecies and gender of rat, and only evaluated the lumbar spine. Therefore percent changes through the lumbar spine were compared instead of absolute values (normalised to L1) (Figure 5.24). It is worth noting that the rat spinal cord terminates at approximately L3 to L4 (Hebel and Stromberg, 1976; Gelderd and Chopin, 1977).
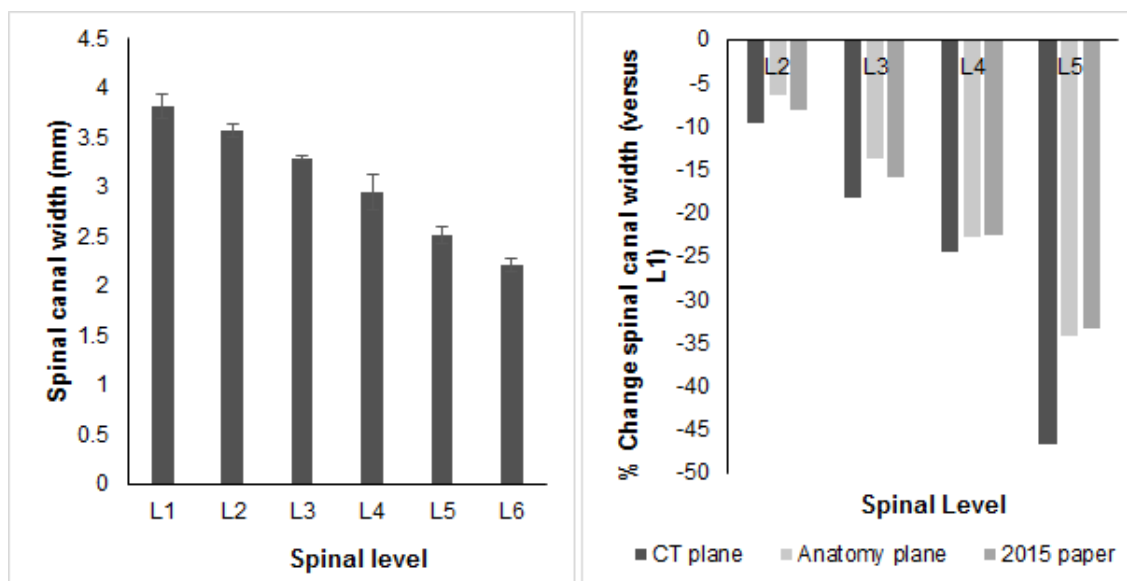
*Figure 5.24: **Assessment of reproducibility and validation of lumbar vertebral canal width dimensions.** Left: mean ± 95% CI measurements of lumbar vertebral canal width, over technical repeats (n=3). Right: comparison of proportional changes in vertebral canal width in the lumbar vertebrae compared with L1/2 compared with previously published data (Jaumard et al., 2015)*

The 95% confidence intervals for all data ranged from 0.003 to 0.201 mm. Dimensions were evaluated in the original x-plane of the CT scan; as well as altering the x-plane position to mimic the anatomical plane. Using dimensions from the original CT plane caused a consistent over-estimation of vertebral canal width of $5 \pm 3\%$ (mean $\pm$ SEM), and an under-estimation of vertebral canal depth of $9 \pm 2\%$, compared with a previous study (Jaumard et al., 2015). Conversely, when measurements were taken

in the anatomical plane, changes were -1 $\pm$ 1% for vertebral canal width and -3 $\pm$ 2% vertebral canal depth compared with the previous study. This gives confidence that measurements were accurate to within 5% of previously reported values. Furthermore, the narrow confidence intervals on technical repeats using this method are indicative of its reliability. The experiment was used to gain an approximate understanding of vertebral canal dimensions, which can guide future studies. As such, only one animal was evaluated. For a more thorough investigation, more animals would be required.

Data of dimensions of the rat spinal cord exists, as does information on how the vertebral levels and spinal cord levels align (Hebel and Stromberg, 1976; Watson et al., 2009). By comparing this information with the vertebral canal measurements herein, on average 75% of the vertebral canal is occupied by spinal cord (Table 5.3). Shrinkage of the spinal cord measurements was minimised through the use of CryoJane tape (Watson et al., 2009). Nevertheless, shrinkage could have still occurred and therefore the value of 75% described above may be an underestimate. Further, this is only an approximation as the strain, age and gender of animals used for each piece of information may differ. If vertebral canal stenosis to 25% of cross-sectional area induces symptoms, the spinal cord must occupy more than 75% of the total cross-sectional area. These findings should be further validated through experiments.

Table 5.3: **Dimensions of vertebral canal and spinal cord in the lower thoracic region.** *Alignment between vertebral and spinal cord level calculated from Hebel and Stromberg (1976). Vertebral canal measurements were obtained herein. Spinal cord measurements taken from frozen sections in Watson et al. (2009).*

Level		Cord Dimensions (Watson et al., 2009)			Vertebral Canal Dimensions (Hebel & Stromberg, 1976)			Comparison
Vertebral	Spinal cord	Lateral (mm)	Ventro-dorsal (mm)	Cross-sectional area (mm^2)	Lateral (mm)	Ventro-dorsal (mm)	Cross-sectional area (mm^2)	Cord vs Canal (%)
T5	T6	3.18	2.53	6.32	3.50	3.10	8.52	74.15
T6	T7	3.03	2.29	5.45	3.30	3.10	8.03	67.83
T7	T8	2.87	2.34	5.27	3.30	3.40	8.81	59.86
T8	T9	2.86	2.34	5.26	3.30	3.40	8.81	59.65
T9	T10	2.92	2.39	5.48	3.50	3.00	8.25	66.46
T10	T11	2.86	2.45	5.50	3.10	2.90	7.06	77.94
T10	T12	3.37	2.48	6.56	3.10	2.90	7.06	92.96
T11	T12	3.37	2.48	6.56	3.30	2.80	7.26	90.45

5.5.2.1   Implications of Findings for NTSCI Studies

TSCI is induced by a high velocity high impact mechanical insult to the spinal cord, resulting in gross haemorrhage and tissue damage from the primary injury, which is followed by a secondary injury cascade (Rowland et al., 2008; Alizadeh et al., 2019). Conversely, NTSCI is characterised by chronic compression of the spinal cord with increasing stenosis. There is no clear distinction between primary and secondary injury (Karadimas et al., 2015).

One method used in the literature to induce NTSCI *in-vivo* is by inserting a polymer into the vertebral canal, which absorbs water and increases in volume, resulting in spinal cord compression over an increased timeframe compared to TSCI (Kurokawa et al., 2011; Hu et al., 2011; Long et al., 2013; Xu et al., 2017). Only two rat NTSCI studies directly evaluated the change in geometry of the polymer and functional deficits. Yang et al. (2015) measured the cross-sectional area (x and z planes) of a polymer at T8/9 to increase from 2 to 8.4 mm^2, and corresponded this with a decrease in spinal cord cross-sectional area of 70%, and both functional and histological changes. However, the timeframe over which the material expansion occurered was not noted. Kim et al. (2004) used a similar method at C5/6 and with an increase in volume from 10.4 to 13 mm^3 over 24 hours, spinal cord cross-sectional area reduced by 11%, and no functional deficits were observed over 5 weeks. These studies give some insight into the degree of spinal cord compression required to elicit functional deficits in animal models of NTSCI. The timeframe required to induce NTSCI as opposed to TSCI is not established in these, or other studies.

There is a paucity of literature describing canal stenosis and the resulting functional deficits. To better understand the effect of compression extent in NTSCI, four ideal canal stenosis points should be incorporated at distinct timepoints:

- **0% canal stenosis, equivalent to 0 mm^2 at T7/8**: Baseline value

- **25% canal stenosis, 2.20 mm^2 at T7/8**: based on the evaluation of spinal cord and

vertebral column area in Table 5.3, this should cause minimal compression of the spinal cord itself.

- **50% canal stenosis, 4.41 mm^2 at T7/8**: clinical studies have identified that somewhere between 25 and 50% spinal cord compression induces symptoms. If the spinal cord takes up 75% of the vertebral canal, these values equate to between 43.75 and 62.5% canal occlusion. However, Kim et al. (2004) found that 48% occlusion of the vertebral canal did not cause functional deficits. To further investigate whether 50% canal occlusion does cause damage to the spinal cord and symptoms, canal stenosis of 50% should be further investigated.

- **>75% canal stenosis, 6.61 mm^2 at T7/8**: The final canal stenosis value of 75% exceeds the minimum symptomatic canal occlusion identified in man. Ideally, this maximum canal occlusion should match that of previous traumatic 2F Fogarty balloon catheter studies, i.e. using a balloon inflated with 15 μL.

These canal occlusion values need to be characterised in terms of 2F Fogarty balloon catheter volume. Further, a method had to be developed to inflated the balloon in the NTSCI context must be able to achieve this increase in cross-sectional area over a relevant time frame in the range of days in a rat, which corresponds to months in humans (Andreollo et al., 2012; **?**).

5.5.3 Evaluation of Balloon Catheter Implantation System

As described previously, understanding compression extent relies on both vertebral canal and balloon volume dimensions in balloon catheter models of spinal cord injury. Balloon catheters have been previously used in *in-vivo* models of traumatic spinal cord injury in both rats and rabbits, with several rat studies at the T8/9 spinal cord level (Martin et al., 1992; Vanicky et al., 2001; Sedy et al., 2008; Lonjon et al., 2010; Pedram et al., 2010). The volume and corresponding diameter of the balloon has not been fully characterised in these studies.

The initial, deflated balloon diameter was 0.667 mm (according to manufacturers details). This equates to 8% of T7/8 vertebral canal. This is greater than the ideal of 0%, but should not compress the spinal cord, and therefore, is suitable for the first cross-sectional area of 0% defined in the previous section. Volumes of 12.5 and 15 μL, used in the preliminary traumatic injury study, equated to 63 and 72% canal stenosis respectively, and caused significant disruption to the spinal cord.

The herein study showed that in a T7/8 (T8/9 spinal cord level) ventro-lateral lesion, 15 μL produced a consistent histological defect similar to TSCI. For improved understanding of the model, balloon diameter had to be characterised with respect to volume. Using a simple inflation study, the setup described had a diameter of 2.8 mm at a volume of 15 μL. A diameter of 2.8 mm with a volume of 15 μL is similar to the 2.5 mm (Lonjon et al., 2010) and approximate 3 mm (estimated from Figure 2 in Vanicky et al. (2001)) previously reported. This volume equated to a cross-sectional area of 6.16 mm^2, and approximate percent vertebral canal stenosis of 72% based on previous experiment. This value of canal stenosis is slightly less than that defined in the previous subsection for maximal compression. However, using the cross-sectional area of 6.16 mm^2 (volume of 15 μL) will facilitate comparison between outcomes in previous studies.

To achieve the intermediate 25 and 50% canal stenosis, and model NTSCI as opposed to TSCI, the balloon system had to be adapted to inflation over time as opposed to one acute inflation.

5.5.4   Development of NTSCI Balloon Catheter Method

Use of the osmotic pump would have been optimal to induce NTSCI, since it would mean the balloon inflated slowly over the course of days without manual input. However, when the osmotic pump was attached to the balloon catheter, the balloon did not inflate. The pressure needed to keep the balloon inflated is inversely proportional to the radius. With a low radius, the osmotic gradient produced by the osmotic pump to expel fluid was less than the pressure required to fill the balloon, and thus it did not expand.

As an alternative method, an injection port was developed and connected to the balloon catheter. Injection ports have been used in venous injection studies (Fiebig et al., 2013; Figueiredo et al., 2015). The injection port facilitated manual filling of the balloon over a controlled time course. Repeat injection mechanics were first established *in-vitro* to determine how much volume was required per injection over three repeat injections to achieve a final diameter of 2.8 mm, matching that of the previous experiment. Three injections of 7.5 µL each was optimal of the conditions tested. The total volume injected into the system (22.5 µL) was greater with repeat injections than with a single injection (15 µL) due to loss from the system upon needle insertion. This loss may have been due to air in the system that could not be removed, or due to pressure differentials within the syringe and balloon causing the balloon to deflate slightly.

Using three injections, the increase in cross-sectional area and canal stenosis were as follows:

- 0 injections, 0.38 mm^2, 8% canal stenosis

- 1 injection, 2.38 mm^2, 28% canal stenosis

- 2 injections, 4.52 mm^2, 53% canal stenosis

- 3 injections, 6.25 mm^2, 73% canal stenosis

5.5.5   Conclusion

This chapter has completed work towards the aims previously described (Table 5.4). This includes characterisation of a TSCI ventral balloon catheter lesion in relation to the wider literature. The work described herein has evaluated the dimensions of the vertebral canal in order to give direction for future NTSCI stenosis studies. Further, the 2F balloon catheter system has been evaluated and a method has been developed to used this system in an NTSCI context.

Table 5.4: **Conclusions of Chapter 5: In-vivo model development**

Aim	Objective	Result and Implications
Develop *in-vivo* models of ventral NTSCI	Characterise histology of balloon catheter ventral lesion in TSCI	A volume of 15 μL caused a more severe lesion than 12.5 μL, in terms of increased tissue disruption over an increased rostro-caudal length.
		GFAP and CS-56 expression increased at the epicentre compared to the closest intact rostral and caudal region; this indicated glial scar formation as expected.
		It could not be determined whether the injury was induced ventrally or dorsally to the cord, due to the extent of tissue damage and low N Number.
		Future studies should match the diameter of a 15 μL 2F balloon, to facilitate comparison with other research.
		In NTSCI studies, the catheters should not be removed from the spinal canal during the study itself, only at dissection. This will allow evaluation of the balloon injury itself as opposed to any damage caused by removing the catheter.
	Evaluate the diameter of the rat vertebral canal from T6 to T13	Vertebral canal stenosis extent and the effects on spinal cord compression and functional effects are not established in the literature for TSCI or NTSCI.
		At spinal levels T8, T9 and T10, vertebral canal cross-sectional area was 8.81, 8.25 and 7.06 mm^2.
	Assess 2F Fogarty balloon inflation volume with diameter	In a simple inflation study adding 1 μL at a time to the balloon catheter, a volume of 15 μL equated to a diameter of 2.8 mm. Assuming the balloon is a sphere, this is a cross-sectional area of 6.16 mm^2.
		There was an effect of having the balloon system completely empty before inflation, compared to filled with water before balloon inflation. Future studies should begin with the system filled with water.
		Future NTSCI studies should aim to recapitulate the same ultimate cross-sectional area as 15 μL in a traumatic balloon lesion (6.16 mm^2).
	Develop method for 2F Fogarty balloon inflation model for a non-traumatic injury context	An osmotic pump could not inflate the balloon.
		Three injections of 7.5 μL through an injection port resulted in cross-sectional areas corresponding to 8%, 28%, 53% and 73% canal stenosis at T7/8 (the latter of which was 6.16 mm^2).

Chapter 6

Outcomes of NTSCI *in-vivo* Studies

6.1   Introduction

Understanding of the pathology of non-traumatic spinal cord injuries is limited. This is in contrast to traumatic spinal cord injuries, where a core primary and secondary injury cascade have been established (Rowland et al., 2008; Alizadeh et al., 2019). This study concentrated on developing a rat model of NTSCI, incorporating a ventral graded lesion which increased in extent over time. To achieve this, a balloon catheter was implanted into the vertebral canal using a ventro-lateral method, and balloon was inflated based on the stenosis extents described in the previous chapter. This took place with one increase in stenosis (inflation) per day, over a total of three days.

There are three key factors characterising NTSCI, and distinguishing it from TSCI, as described by Karadimas et al. (2015):

1. No acute mechanical insult, slow velocity compression

2. Absence of gross haemorrhagic necrosis

3. Chronic and progressive nature (likely induces compensatory mechanisms)

Clinical cadaver studies on patients with NTSCI are limited in number, since NTSCI is secondary to other underlying diseases and is not the cause of death. Those which

have been undertaken focus on cervical NTSCI (spondylotic myelopathy). In cadaver studies, glial scars are not reported (Someya et al., 2011). The hypothesised pathological mechanism in NTSCI is cord compression resulting in compression of the vasculature structure and resulting in ischaemia (Shingu et al., 1989; Kameyama and Hashizume, 2003; Baptiste and Fehlings, 2006). However, experimental studies supporting this are lacking (Karadimas et al., 2015). One study evaluating six post-mortems of patients with metastatic cord compression observed demyelination, apoptosis of oligodendrocytes and neurones, and cystic necrosis in severe compression (Newcombe et al., 2015). There is also evidence of neuroinflammation, corresponding to symptom severity (Yu et al., 2011; Du et al., 2018). The mechanism of how slow velocity spinal cord compression results in physiological changes remains unclear, as do the cellular and tissue outcomes themselves.

Animal studies allow greater evaluation of histological and functional changes in NTSCI. Long et al. (2013) implanted an agarose gel polymer into the epidural space at spinal cord level C5/6 in a rat. The polymer had been modified to expand to seven times its original volume over three timescales: immediately; over two hours; or over one day. In the instant compression group, within 24 hours the BBB score had reduced to 6. Conversely, for the other two groups the BBB score was 15.6 after 24 hours, and 17 after one week. In terms of histological outputs, in the immediate compression group, haemorrhage, central canal deformation and oedema were observed within 24 hours. Conversely, in the two gradual compression groups, spinal cord central canal deformation was observed but haemorrhage, necrosis, and oedema were not. These NTSCI histological findings have been reported in other *in-vivo* studies using a screw or line around the spinal cord, finding spinal cord compression, white matter degradation and vacuolisation, and central canal deformation (Kubota et al., 2011; Sun et al., 2016).

Although the methods and spinal cord levels are different to those used herein, previous NTSCI studies highlight that with the same compression extent, and different timeframes (TSCI vs NTSCI), functional and histological outcomes are different.

There are limitations to previous NTSCI *in-vivo* models, including the timeframe

being too long (line around the spinal cord), too fast and difficult to control (expanding material), and too invasive (screw). Further, the capacity to induce a lesion from a ventral aspect would show greater affinity with clinical NTSCI (Ferrara, 2012; Tetreault et al., 2015; Martin et al., 2018).

In the balloon catheter model, these factors are all controlled: a moderate timeframe, control over the balloon inflation via volume, and minimally invasive, requiring only a partial laminectomy. Further, the balloon catheter model has also been used in a dorsal and traumatic method to evaluate the efficacy of novel treatments, including mesenchymal stem cells, curcumin, and induced pluripotent neural progenitor cells in a hydrogel construct (Lonjon et al., 2010; Ruzicka et al., 2018, 2019). In a traumatic context, the method is well established and reproducible.

It was hypothesised that NTSCI could be modelled in rats using an implanted balloon catheter and cannula injection port, which was characterised in the previous chapter. Upon implantation of the balloon catheter, there would be minimal functional deficit. After each inflation of the balloon, functional deficit would increase in magnitude. A functional deficit would be sustained over the duration of the study. Further, histological findings from the compressed spinal cord would not show gross haemorrhage, oedema, parenchyma ablation, or necrosis, and instead show compression and a change in shape of the spinal cord with damage predominantly affecting the white matter.

6.2 Aims

The aims of this chapter were to characterise responses in the *in-vivo* model of NTSCI, in order to better understand the pathobiological mechanisms in NTSCI. The aims of this chapter are in the context of the whole project (Figure 6.1). Specific objectives of this chapter:

1. To assess the histological and functional outcomes which occur after long term

spinal cord compression *in-vivo*:

A Surgical implantation of the balloon and subsequent inflation over 3 days, and monitoring for 14 days post-maximal inflation.

B Characterise functional deficits using BBB scale.

C Characterise histological outputs using H&E and immunohistochemistry.

    i. Shape and area of tissue at the lesion site

    ii. Changes to the spinal cord parenchyma

    iii. Evaluation of astrocyte reactivity using GFAP and CSPG staining

    iv. Assess demyelination using myelin basic protein (MBP) labelling

    v. Changes to the vasculature using RECA1 labelling
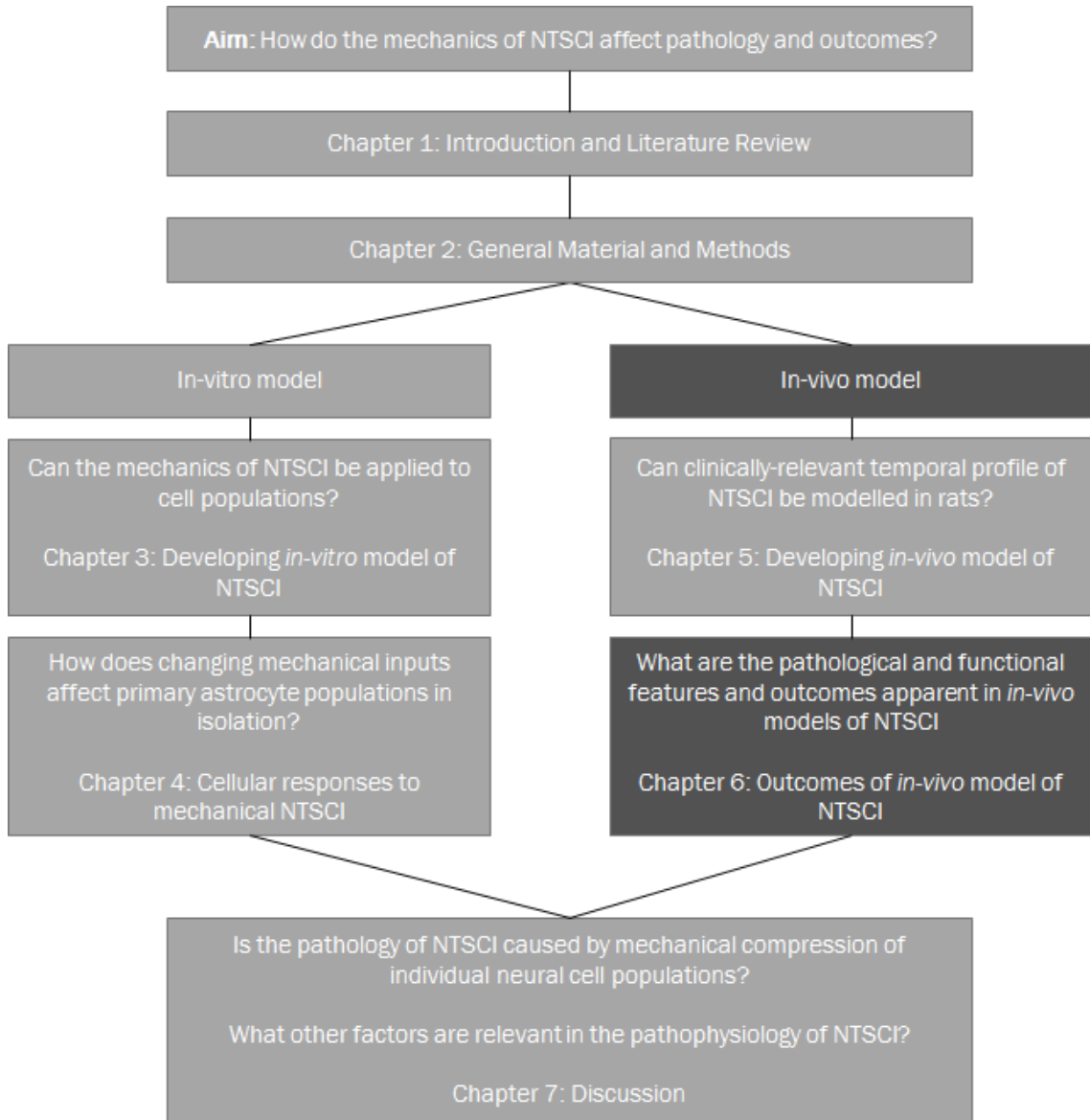
Figure 6.1: **Hypothesis and research question in Chapter 6, relating to aims of the whole study**.

6.3   Experimental Setup

6.3.1   Surgical Approach and Behavioural Analysis

The study described herein had three aims: to determine whether the balloon catheter system could be implanted without host response, to determine whether a ventral lesion could be reliably established, and to characterise whether the balloon catheter system could be used to produce a non-traumatic spinal cord injury (histologically and functionally).

A total of ten female Wistar rats (200 to 250 g) were operated upon in two cohorts. A total of three animals were shams, and their balloon catheters were not inflated. The patency of each balloon catheter was tested immediately prior to implantation. Those implanted into injury group animals were patent at this point.

The balloon-catheter system was implanted so that the balloon position was approximately T8/9 spinal cord level (vertebral level T7/8, Figure 6.2). Additionally, for a transcutaneous injection port, another 1 cm incision was made at the shoulder blade level. Blunt dissection was used to separate the skin from connective tissue in the thoracic region, and up to the rostral incision. The catheter was affixed in place at T10 using resorbable Vicryl sutures into the spinal column musculature. Tubing connecting the balloon to the injection port was fed subcutaneously from T10 to the incision between the shoulder blades. The port was fed through the skin here and held in place using Vetbond surgical adhesive. Subsequently, the skin was closed using Prolene sutures. In sham animals, the port was positioned subcutaneously rather than transcutaneously.

The balloon catheter length was 15 cm, with the cannula and port being an additional 5 cm. The balloon was inflated with 7.5 µL per day on days 1, 2 and 3 post-surgery. each animal was anaesthetised briefly using 5% isoflurane in oxygen at 2 L.min^{-1}. Subsequently, the animal was moved on to a face mask with 2% isoflurane in oxygen at 2 L.min^{-1}. A 50 µL airtight Hamilton syringe was filled with sterile water, and a 30G

needle was attached. The needle was pushed through the silicone seal on the injection port, and the volume required was injected into the system in one smooth motion. The needle was removed, any observations were noted, and isoflurane was turned off. Once the animal had recovered from anaesthesia, they were returned to their home cage.
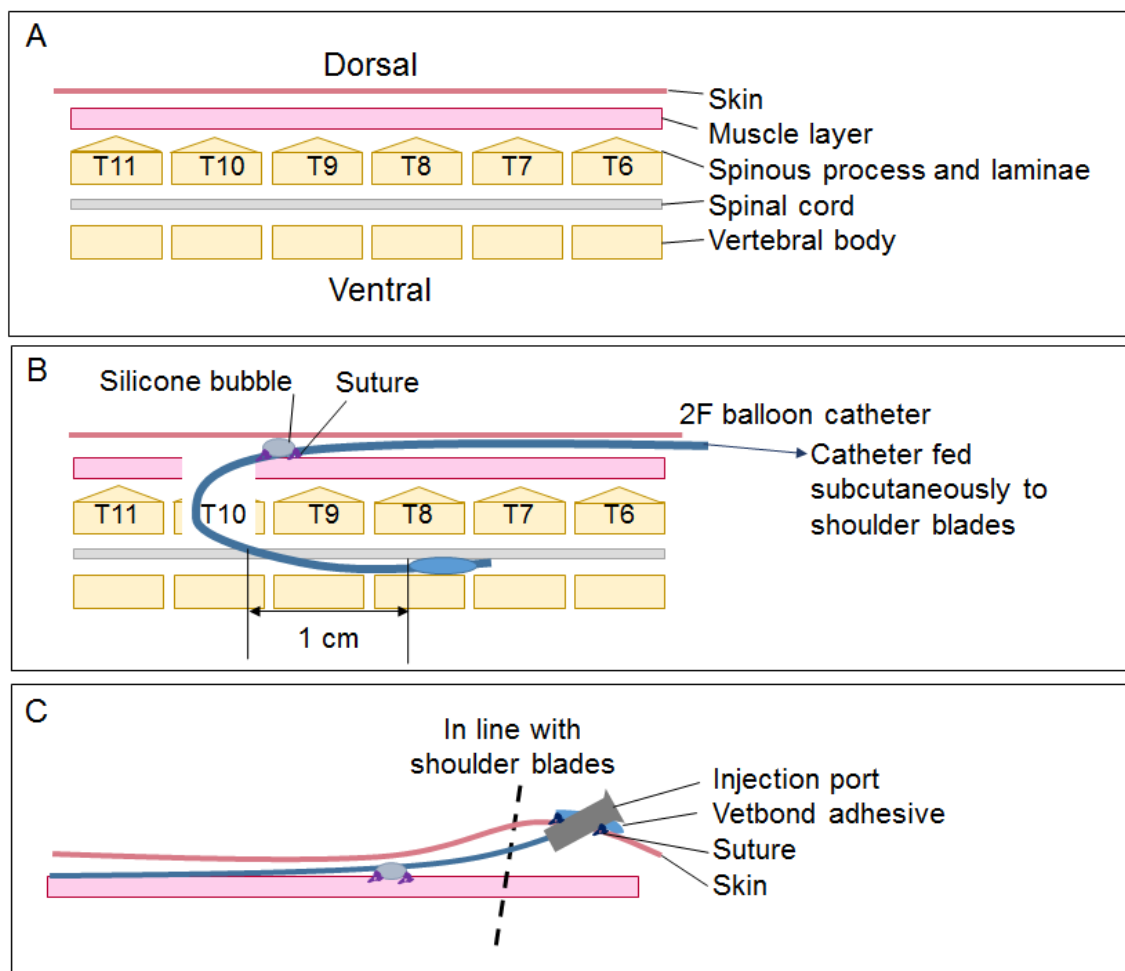
Figure 6.2: **Schematic diagram of key stages in balloon catheter implantation surgery for inducing spinal cord injury.** *Surgery was undertaken in female adult Wistar rats. A: the native tissue in the surgical region. B: Laminectomy was performed at T10, and balloon catheter inserted ventro-laterally in the vertebral canal caudally up to 1 cm below the caudal end of the balloon (previously marked on the catheter). The catheter was held in place by resorbable sutures around a silicone bubble. C: The catheter was fed up to the region of the shoulder blades subcutaneously, where a further incision was made in the skin to allow for the injection port. The port was fitted using sutures and vetbond adhesive.*

For the total duration of the experiment, functional locomotor behaviour was

evaluated using the open-field BBB score system (Appendix E). For the first six days, this was undertaken daily in the mornings, prior to balloon inflation in the afternoons. For example, the third balloon inflation occurred on day 3 post-initial surgery, then the subsequent BBB test was undertaken on the morning of day 4. Subsequently, the test was carried out every other day until 14 days post maximal inflation (18 days post initial surgery), when animals were terminated using an overdose of intra-peritoneal anaesthetic, perfused with PFA and spinal cords dissected.

6.3.2   Histological Analysis

At 2 weeks post-injury, animals were trans-cardially perfused and fixed with 4% (w/v) PFA. Spinals cords were excised and stored in 4% (w/v) PFA for a further 24 hours, before being stored in 30% (w/v) sucrose and 0.1% (v/v) sodium azide for up to 3 months before histology was undertaken.

For histological evaluation, spinal cords were cut into transverse slices approximately 2 mm thick, which were then embedded into OCT and stored at -80°C. Transverse slices were serially sectioned at 40 μm using a cryostat, and stored at -20°C. H&E staining was undertaken every 1 mm along the length of the spinal cord to evaluate cross-sectional area and identify the injury site.

Subsequently, immunohistochemistry was undertaken at three regions: rostral to the injury epicentre, at the injury epicentre, and caudal to the injury epicentre. Sections were stained with GFAP (astrocytes), CS-56 (chondroitin sulphate proteoglycans), MBP (myelin), and RECA-1 (endothelial cells). Three sections were imaged at each region per animal using a confocal microscope, and the laser settings were kept the same between all images. These images were then analysed using FIJI (ImageJ). An automated macro determined the area stained with each antibody, and this area was calculated as a percentage of the overall tissue area observed on the nearest H&E stained section. Dura and other meninges were present on some of the sections, but were excluded from analysis by only evaluating objects less than 0.01 mm^2.

6.4 Results

6.4.1 Changes and mass and complications observed were different in shams and injured animals

Of the ten animals operated upon, none required bladder expression until the third balloon inflation (diameter 2.8 mm, total volume 22.5 µL), i.e. neural circuits controlling bladder expression were not damaged until this point. After this, three of the animals (animals 4, 5 and 6) required bladder expression twice daily for up to 10 days. One of these (animal 6) had haematuria for 2 days following maximal inflation. The greatest reduction in weight was seen in animal 6 (-13.0%, day 6, Figure 6.3A), who had the smallest mass initially (207 g on day of surgery). The weight of the injured animals reduced by -3.73 ± 1.93% by day 6 (mean ± S.E.M.), corresponding with 4 days post maximal inflation (Figure 6.3B). The other injured animals weighed at least 215 g on the day of surgery, and maximum weight loss was -7.95%. After 9 days post-surgery, the mass of the animals recovered to pre-operative levels, and exceeded pre-operative levels for the remainder of the timecourse.

A total of 5 of the 7 injured animals (6, 7, 8, 9 and 10) in the injury group had irritation around their port (Figure 6.4). These were either destroyed by the animal, or cut off manually, and the wound sutured closed. This occurred between one and two weeks post-surgery.

At perfusion, all of the injured animals' catheters remained within the vertebral canal. The Vicryl sutures had not degraded substantially and were still visible. At perfusion, all of the balloons were intact. One had a volume of 4.5 µL remaining, with a diameter of 1.7 mm.
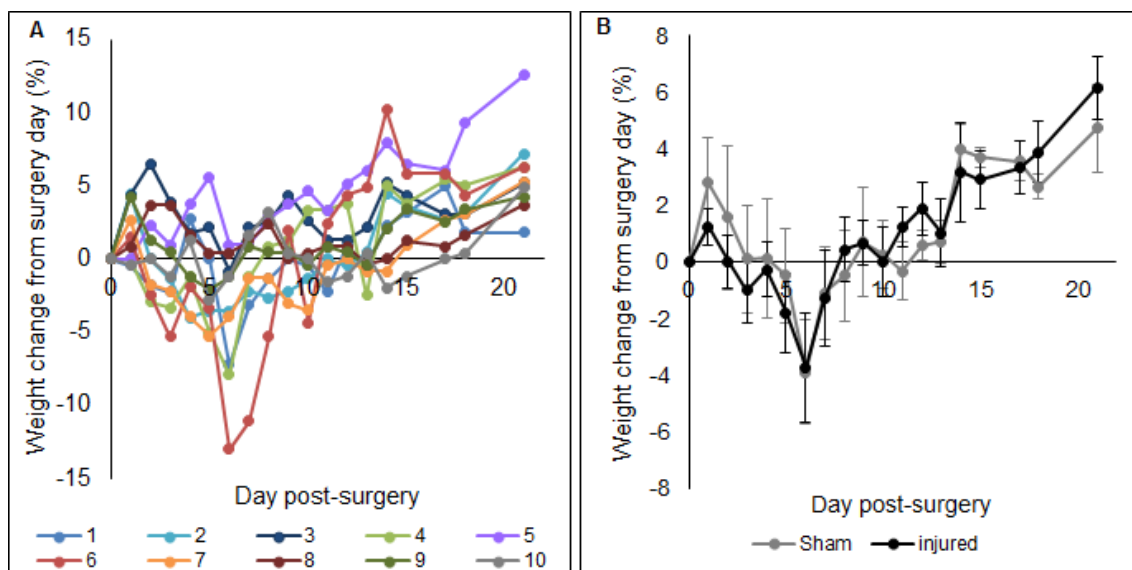
*Figure 6.3: **Percent change in weight of animals after spinal cord injury using repeat injections and balloon catheter lesion.** Animals underwent a T10 laminectomy and balloon catheter implantation rostral to this level. Day 0 was post-surgery, but prior to balloon inflation. Day 1 had one balloon inflation, day 2 had two inflations, day 3 onwards had the maximal three inflations. A: individual animals, 1, 2 and 3 were shams. B: grouped into sham and injured, mean ± S.E.M.*
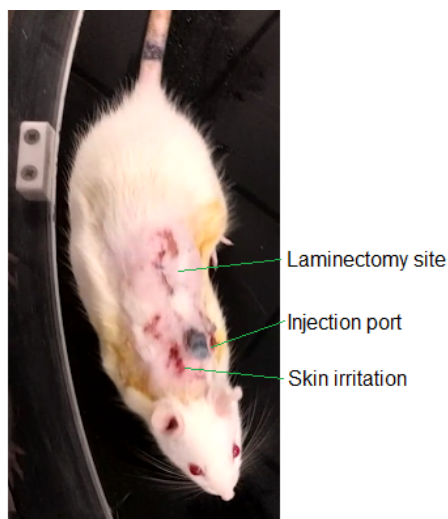
*Figure 6.4: **Annotated photograph of animal 12 days after balloon catheter repeat injection surgery.** Animals underwent a T10 laminectomy and balloon catheter implantation rostral to this level. Animals showed signs of skin irritation around the injection port from day 3 post-surgery.*

6.4.2 Open field locomotor score reduced with concurrent inflations, but the scores varied

Motor function declined for each of the injured animals with each inflation (as measured by the open field BBB test, Figure 6.5A). Animals were grouped based on functional deficits observed (Figure 6.5B):

- **Sham (no inflation)**: animals 1, 2 and 3

- **Mild injury**: animals 7, 8, 9 and 10

- **Severe injury**: animals 4, 5 and 6
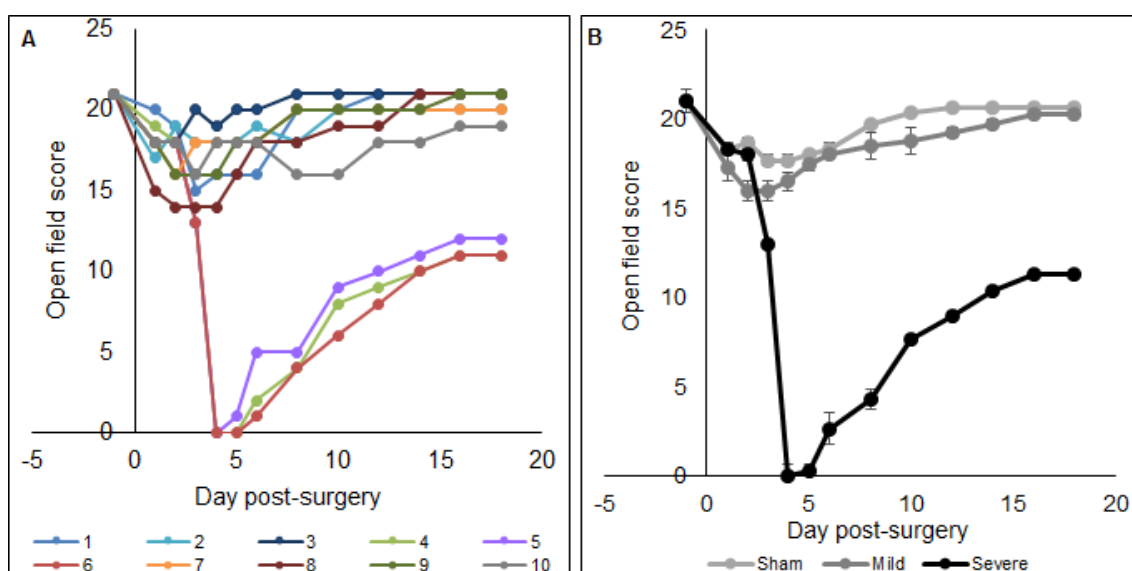
*Figure 6.5: **Minimum open field locomotor scores of animals after balloon catheter spinal cord injury.** Animals underwent a T10 laminectomy and balloon catheter implantation rostral to this level. Day 0 was post-surgery, but prior to balloon inflation. Inflations were undertaken 1x per day on day 1, 2, and 3. Sham animals had the balloon inserted but not inflated (animals 1, 2 and 3). A: individual animals. B: grouped by BBB score, mean ± S.E.M.*

Initially, one day after surgery (0 inflations), the mean BBB score was 18.0 ± 0.406 for all ten animals. This equated to a functional deficit of rotated paw position at lift off only. On day 2 (1 inflation for injury groups), mean BBB score remained similar at 17.4

$\pm$ 0.50. In severely injured animals, the second inflation caused a reduction of 5 points on the motor scale, and the third inflation reduced the BBB score to either 0 or 1, indicating complete hindlimb paralysis. Recovery then took place over the remaining timecourse of the experiment. In this severe injury group motor function plateaued at a BBB score of 11 or 12; denoting full range of motion of hindlimbs and weight-supported plantar stepping, but with no or occasional co-ordination (respectively). In animals with a mild injury, the second inflation caused a reduction of approximately 2 points to a BBB score of 16; denoting toe clearance only occurring 51-94% of the time, as well as paw rotation at lift off. This remained constant at the 3rd inflation. Over the following two weeks, motor function recovered to almost normal in the mild injury group. Sham animals did not show decreased motor function after two or three inflations.

6.4.2.1 No consistent functional differences were observed between left and right hindlimbs across injury groups

In sham injuries, there was a slight effect observed of greater function in the left hindlimb than the right, but the variation was high (Figure 6.6). This effect was greater in animals with a mild injury, and was observed between days 1 and 8 post-surgery. For severely injured animals, this effect was only observed at day 6 post-surgery.

6.4.3 Severe injury resulted in a greater degree of compression and histological damage than mild injury and sham groups

Sections taken every 1 mm were stained with H&E and their area evaluated. The results of both studies were pooled together using the same groups described above. Animal 5 had to be excluded due to damage during dissection.

The transverse area of the spinal cord in shams was significantly greater than both injury groups (Figure 6.7, p $<$0.05). The transverse area of the spinal cord in severe injuries was significantly less than mild injuries (p $<$0.05). The greatest reduction in cross-sectional area was observed at the epicentre for each group. The severe injury group
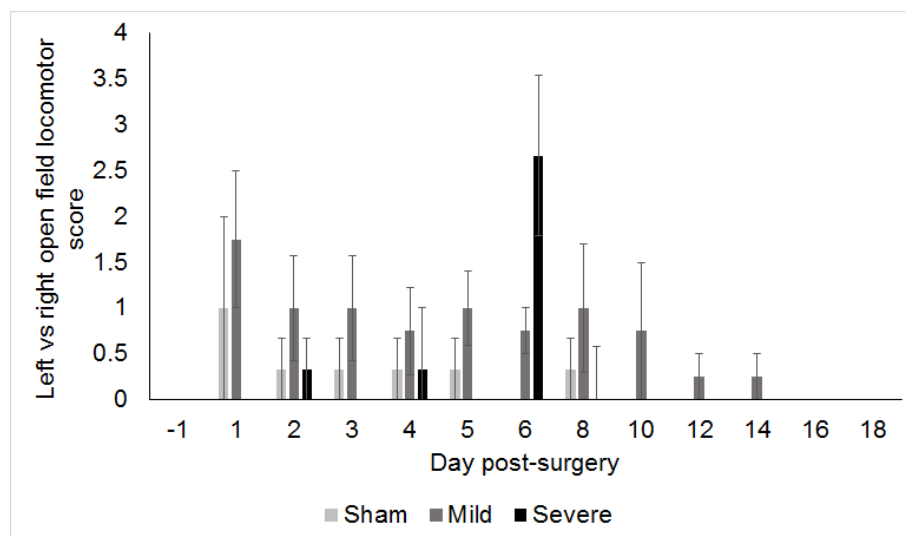
*Figure 6.6: **The difference between left and right hindlimb open field locomotor scores after NTSCI**. Animals underwent a T10 laminectomy and balloon catheter implantation rostral to this level. Day 0 was post-surgery, but prior to balloon inflation. Day 0 was post-surgery, but prior to balloon inflation. Inflations were undertaken 1x per day on day 1, 2, and 3. Grouped by maximum functional deficit. N=3 for sham, N=4 for mild injury, N=2 for severe injury.*

had approximately 36% spinal cord compression compared to an intact sample, and the mild injury group had 21% spinal cord compression.

Cross-sections of the spinal cord at the injury site allowed evaluation of both catheter position and descriptions of the injury (Figure 6.8). In all groups, at the epicentre, the white matter on the lateral right funiculus was compressed. This compression was greater in mild injury groups, where the spinal cord tissue was a 'C' shape, compared to a slightly flattened oval of the sham group. In these two groups the 'H' shape of the grey matter remained observable, although was distorted in the mild injury group. The severe injury group had even greater compression, affecting the dorsal and ventral funiculi, and the grey matter. The 'C shape' could be observed rostral and caudal to the severe lesion. In the mild injury, and to a lesser extent in the sham injury, different areas were affected rostrally and caudally. Caudal to the lesion the area of compression was more ventral, whereas rostral to the injury the area of compression was more dorsal.
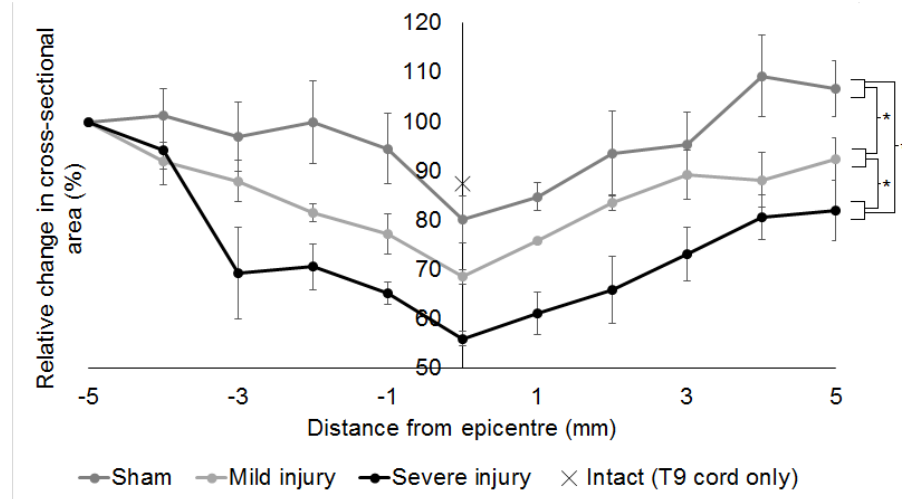
*Figure 6.7: **Cross-sectional area of NTSCI rat spinal cord, normalised to 5 mm rostral from the injury epicentre.** Animals underwent a T10 laminectomy and balloon catheter implantation at T8/9. This balloon was inflated over the course of three days to match a volume of 15 μL. Sham animals (n=3) had implantation but no inflation. The injured animals were grouped into mild (n=4) and severe (n=2) based on BBB score. Cross-sectional area was determined using 40 μm sections, 1 mm apart, stained with haematoxylin and eosin. Subsequently, area was determined using an ImageJ macro.*

Lesion extensions observed rostro-caudally in this study were 10 ± 0.58 mm (mean $\pm$ S.E.M) for sham animals, 14.5 ± 1.26 mm for animals with a mild injury, and 15.0 ± 1.0 mm for animals with a severe injury. These differences between groups were not significantly different (p >0.05).

Overall, after NTSCI, the spinal cords were deformed but the majority of the parenchyma was intact, indicating no gross haemorrhagic necrosis had occurred. Spinal cords after a severe injury had vacuoles at the epicentre of lesion in white matter, and in nearby tissue (Figure 6.9). Further, at epicentre of severe injuries there was loss of grey matter parenchyma and inflammatory cell infiltrate. In these severe lesions, from 2 mm to 5 mm caudal to the lesion, a dorsal white matter cavity was observed (Figure 6.10A). The cavity was present at up to 6 mm caudal to the injury and 6 mm rostral. These findings were not observed in any animal in the sham or mild injury groups (Figure 6.10B).
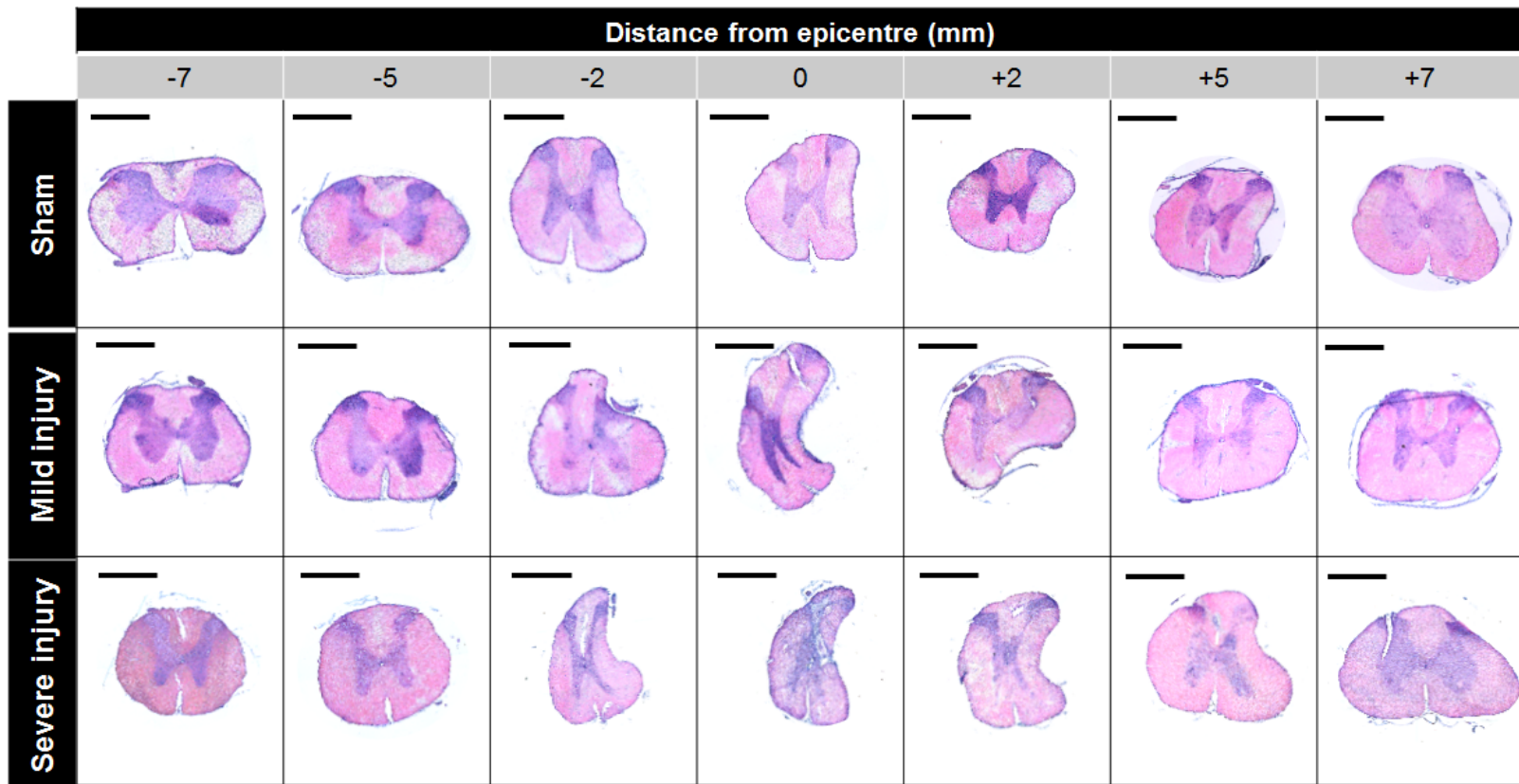
Figure 6.8: ***Sample transverse sections of spinal cord from NTSCI balloon catheter lesions.*** *Animals underwent a T10 laminectomy and balloon catheter inflation at T8/9 over three days, with a maximum diameter to match a volume of 15 μL. Sham animals had the balloon implanted but not inflated. Animals were perfused two weeks after the injury. Sections 40 μm thick were stained with H&E. Negative distance values denote rostral to the epicentre, and positive distance values denote caudal. Scale bar = 1mm.*
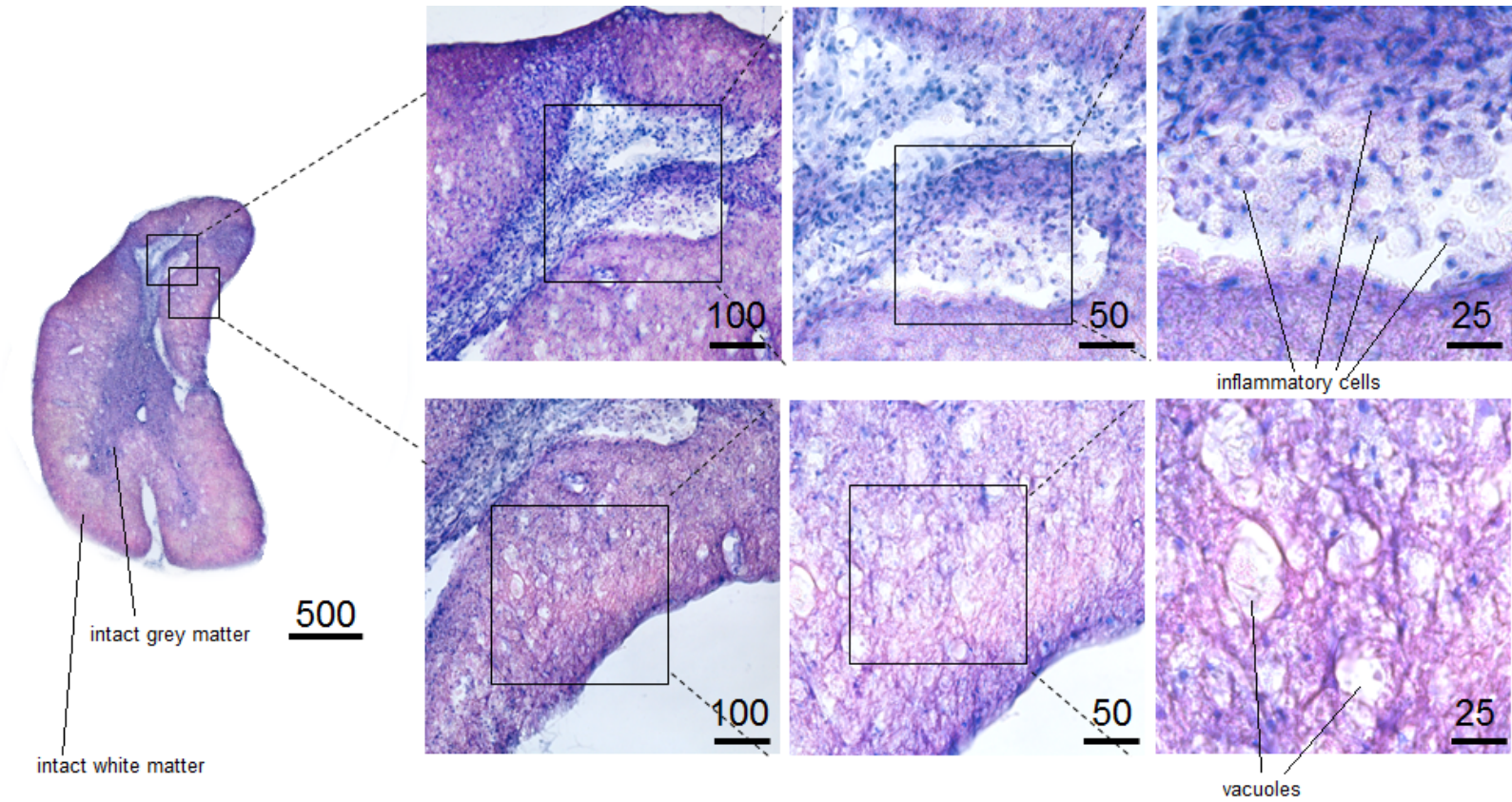
Figure 6.9: **Histological H&E stained images from the epicentre of a severe NTSCI lesion.** *Showing cellular infiltration (above), and white matter vacuoles (below). Animals underwent a T10 laminectomy and balloon catheter implantation at T8/9, and inflation to match a diameter of a volume of 15 µL. Animals were perfused two weeks after the injury. Sections 40 µm thick were stained with H&E. Scale bar for each image is in µm.*
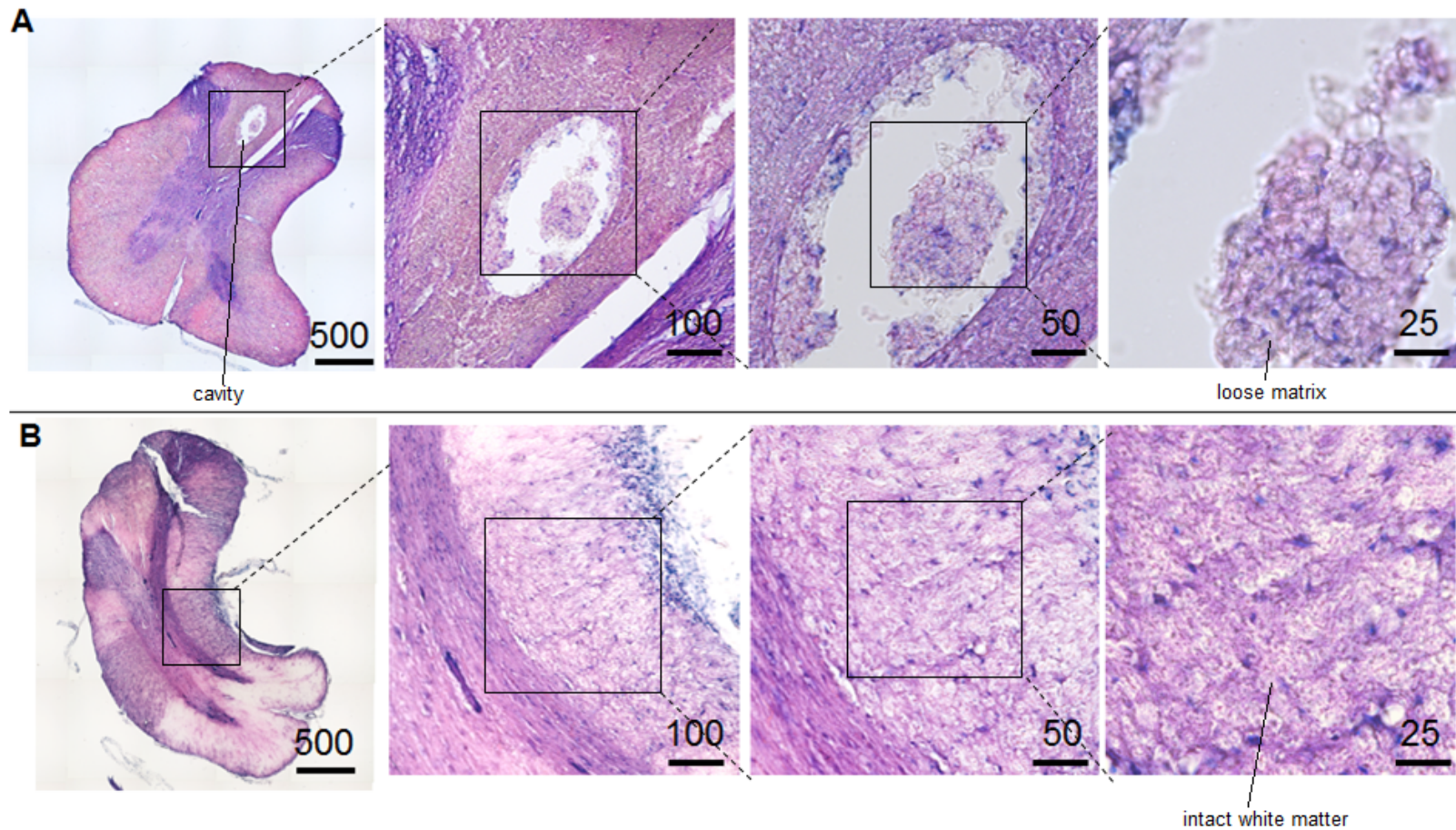
Figure 6.10: **Further histological H&E images from NTSCI lesions.** *A: cystic cavity 2 mm caudal to the lesion epicentre, severe lesion. B: white matter in mild injury epicentre. Animals underwent a T10 laminectomy and balloon catheter inflation at T8/9 over three days, with a maximum diameter to match a volume of 15 μL. Sham animals had the balloon implanted but not inflated. Animals were perfused two weeks after the injury. Sections 40 μm thick were stained with H&E. Scale bar for each image is in μm.*

There was a positive trend between minimum motor function score and minimum transverse cross-sectional area, although this was not linear (Figure 6.11). When ranked, the Spearman correlation coefficient was 0.633, and the p value was 0.05.
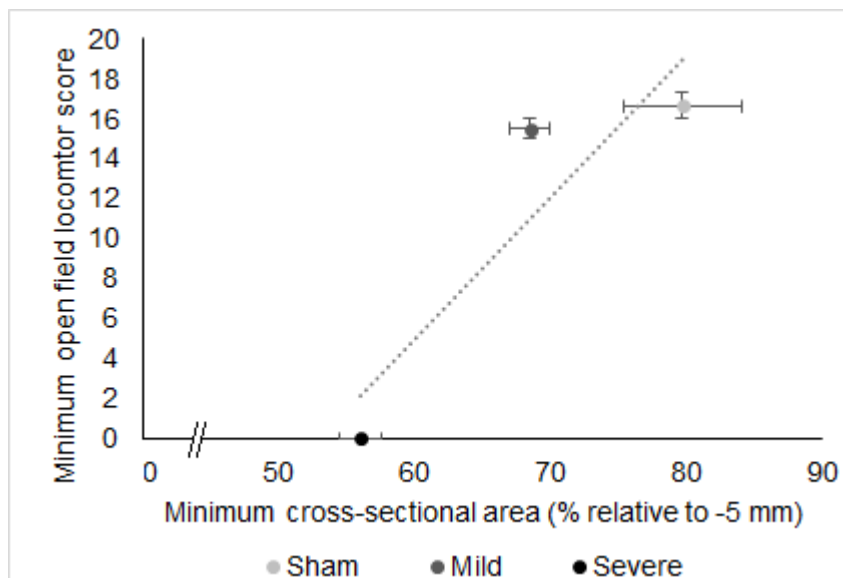
Figure 6.11: **The relationship between minimum open field locomotor score (BBB) and minimum cross-sectional area (CSA) of the spinal cord.** *Animals underwent a T10 laminectomy and balloon catheter inflation at T8/9 with a maximum diameter of 2.8 mm. Sham animals had the system implanted but not inflated. Minimum cross-sectional area was determined using image analysis of H&E stained transverse spinal cord sections. Linear trendline shown. N=2 for severe, N=4 for mild, N=3 for sham.*

6.4.4 Differences were observed in GFAP and myelin labelling at the epicentre of severe NTSCI injuries

6.4.4.1 NTSCI induced increased GFAP staining in severe injuries only

In mild and sham groups, the proportion of tissue stained with GFAP at all three regions was similar (Figure 6.12). This is in contrast to the severe group, where a greater proportion of GFAP staining was observed at the epicentre than at rostral and caudal regions. This corresponded with a loss of central grey matter at the severe epicentre (Figure 6.13). There was an N of 2 for the severe group, leading to a large S.E.M. and no statistical significance between these groups.
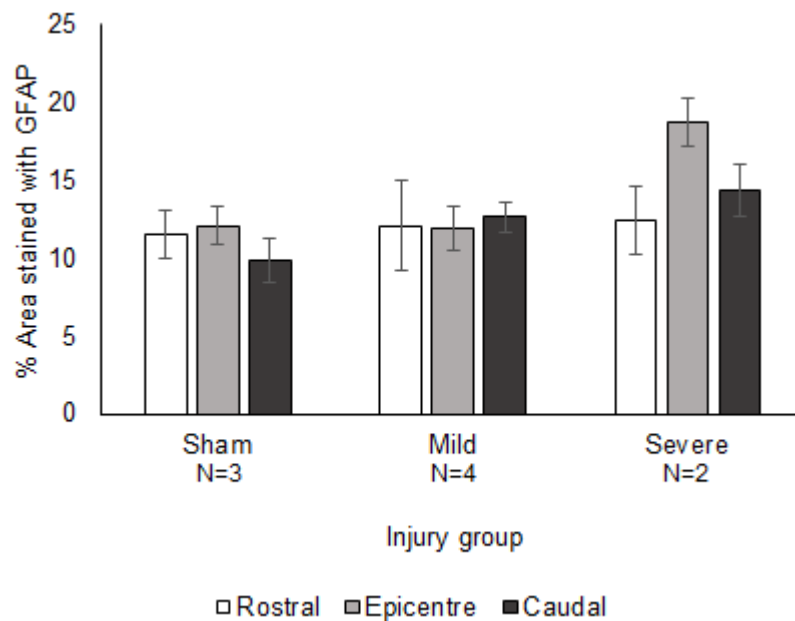
*Figure 6.12: **Proportion of tissue stained with GFAP in NTSCI lesions.** Animals underwent a T10 laminectomy and balloon catheter inflation at T8/9 over 3 days. Animals were perfused two weeks after the maximal inflation, and were grouped based on the functional deficit obtained. A total of three sections were stained and imaged for each animal at each location, mean $\pm$ S.E.M.*
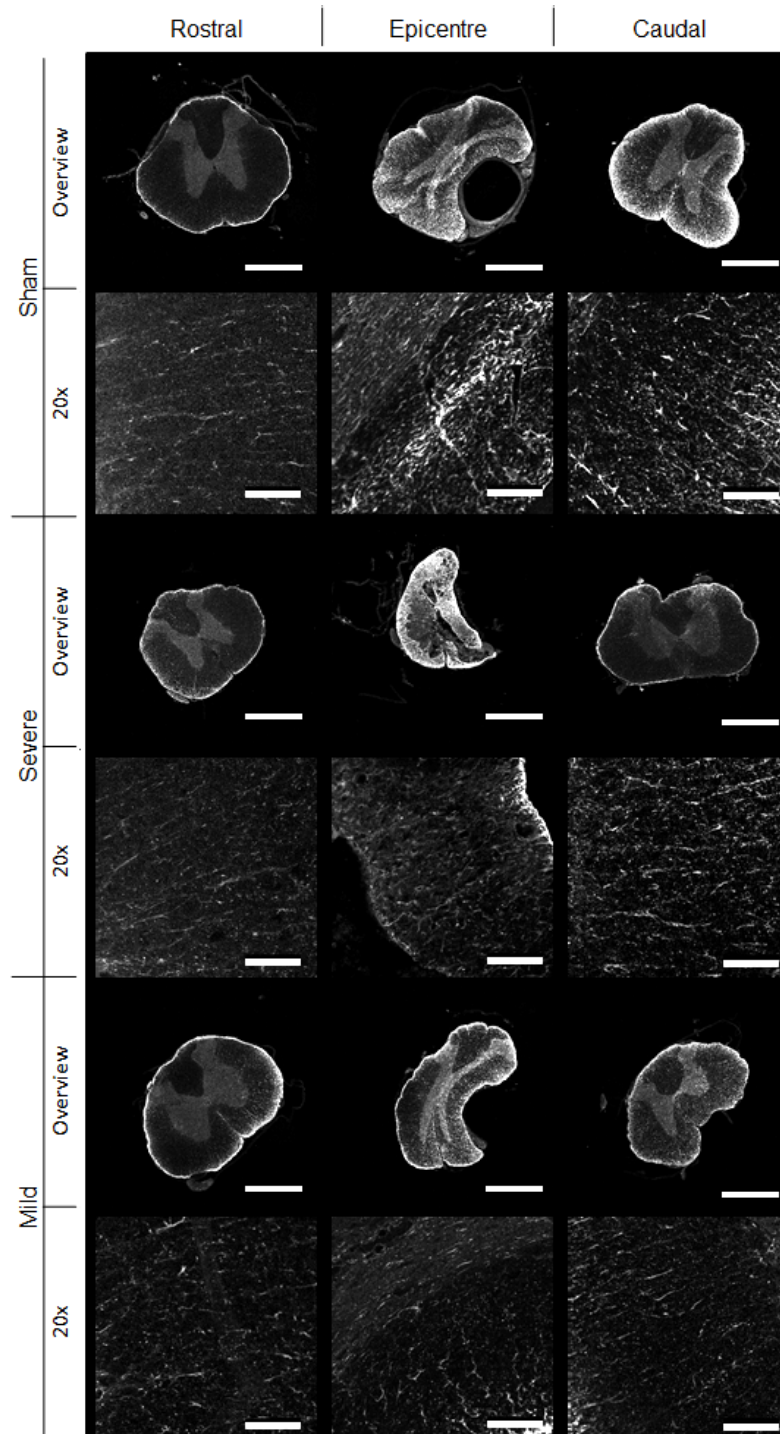
Figure 6.13: **Representative images of GFAP staining in ventral balloon catheter-induced NTSCI.** *Animals underwent a T10 laminectomy and balloon catheter inflation at T8/9 over 3 days, then perfused two weeks after maximal inflation. Animals were grouped based on their functional deficit. In overview images, scale bar is 1 mm, in 20x images, scale bar is 100 μm. 20x images were taken of the right lateral white matter.*

6.4.4.2   NTSCI did not cause substantial changes in chondroitin sulphate labelling

Chondroitin sulphate proteoglycans (CSPGs, stained by CS-56) are a core component of the glial scar in TSCI. For all regions and injury severity groups, less than 10% of the tissue was stained with CS-56, with no significant differences (Figure 6.14). This lack of staining can be observed in representative images (Figure 6.15).
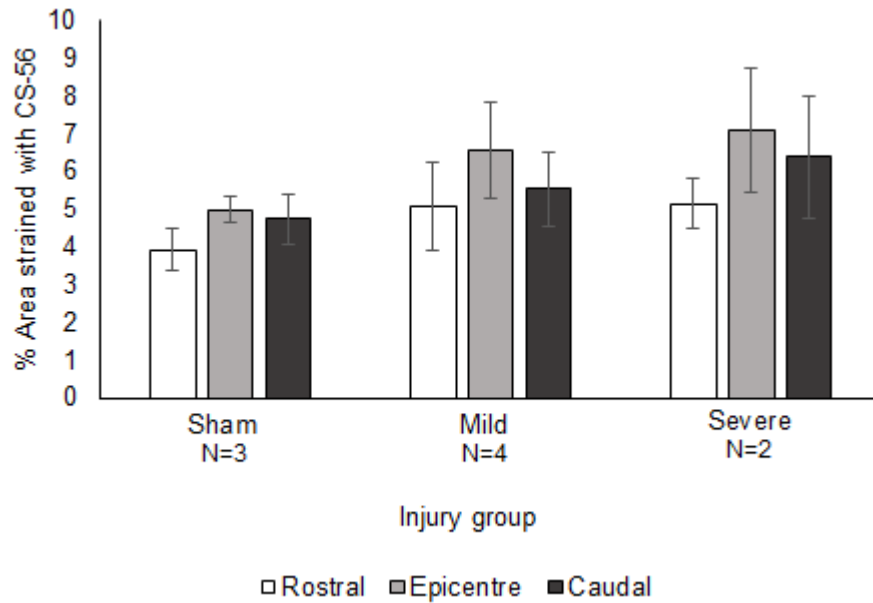
Figure 6.14: **Proportion of tissue stained with CS-56 in NTSCI lesions.** *Animals underwent a T10 laminectomy and balloon catheter inflation at T8/9 over 3 days. Animals were perfused two weeks after the maximal inflation, and were grouped based on the functional deficit obtained. A total of three sections were stained and imaged at each location. Data is mean $\pm$ S.E.M.*
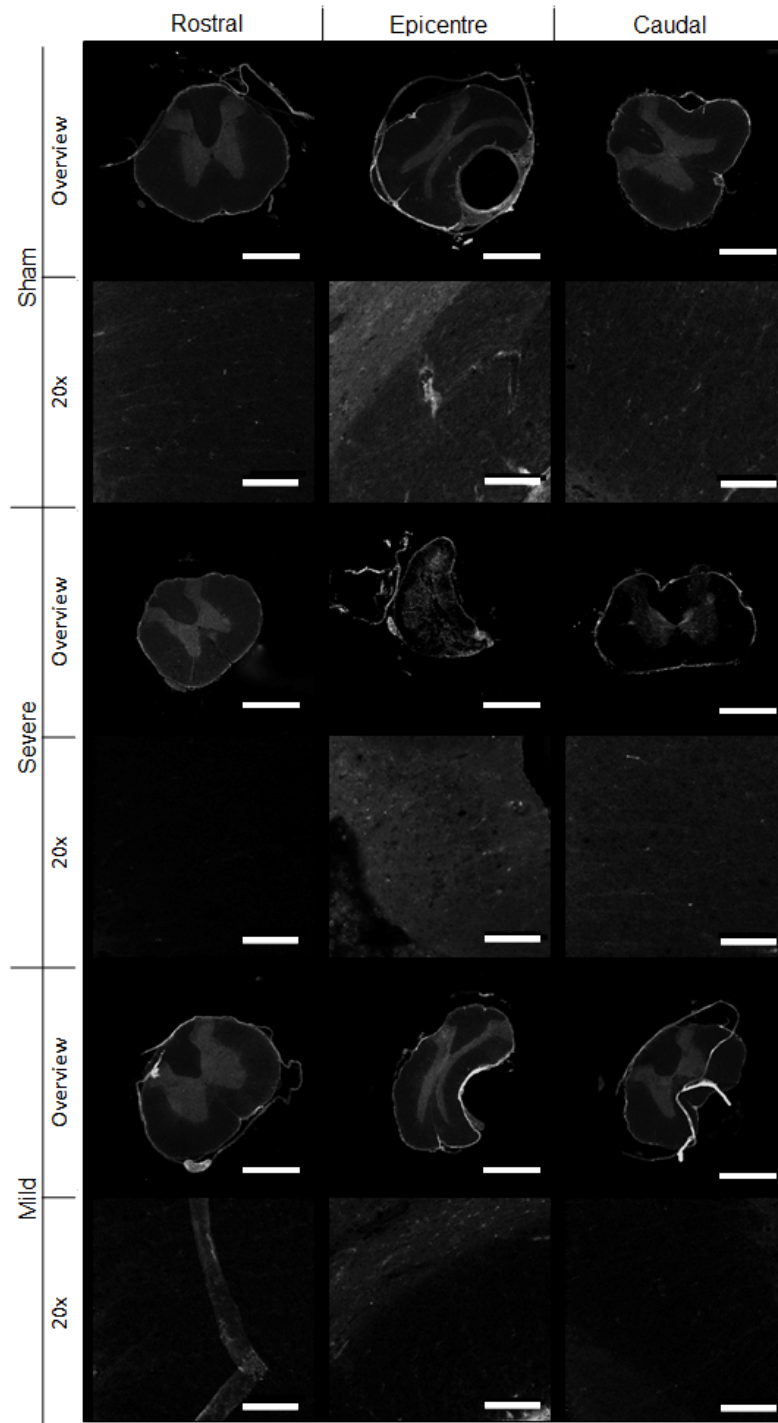
Figure 6.15: **Representative images of CS-56 staining in ventral balloon catheter-induced NTSCI.** *Animals underwent a T10 laminectomy and balloon catheter inflation at T8/9 over 3 days, then perfusion two weeks after maximal inflation. Animals were grouped based on the functional deficit. In overview images, scale bar is 1 mm, in 20x images, scale bar is 100 μm (right lateral white matter).*

6.4.4.3 Severe NTSCI injury resulted in moderate demyelination at the injury epicentre

For animals in the sham group, the area stained with myelin was similar at all three locations (Figures 6.16 and 6.17). In mild and severe groups, there was a slight reduction in the area stained with MBP at the epicentre, but this was not statistically significant (N=2 for severe injury, Figure 6.16).
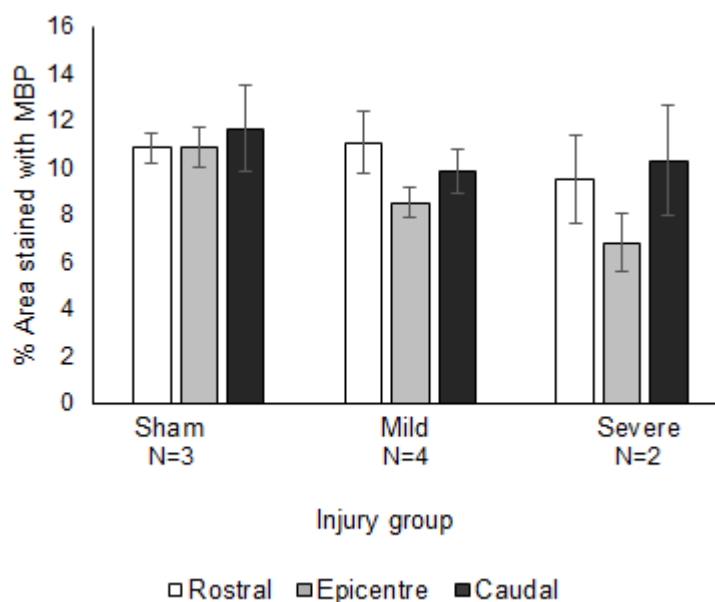
Figure 6.16: **Proportion of tissue stained with MBP in NTSCI lesions.** *Animals underwent a T10 laminectomy and balloon catheter inflation at T8/9 over 3 days. Animals were perfused two weeks after the maximal inflation, and were grouped based on the functional deficit obtained. A total of three sections were stained and imaged at each location. Data is mean ± S.E.M.*
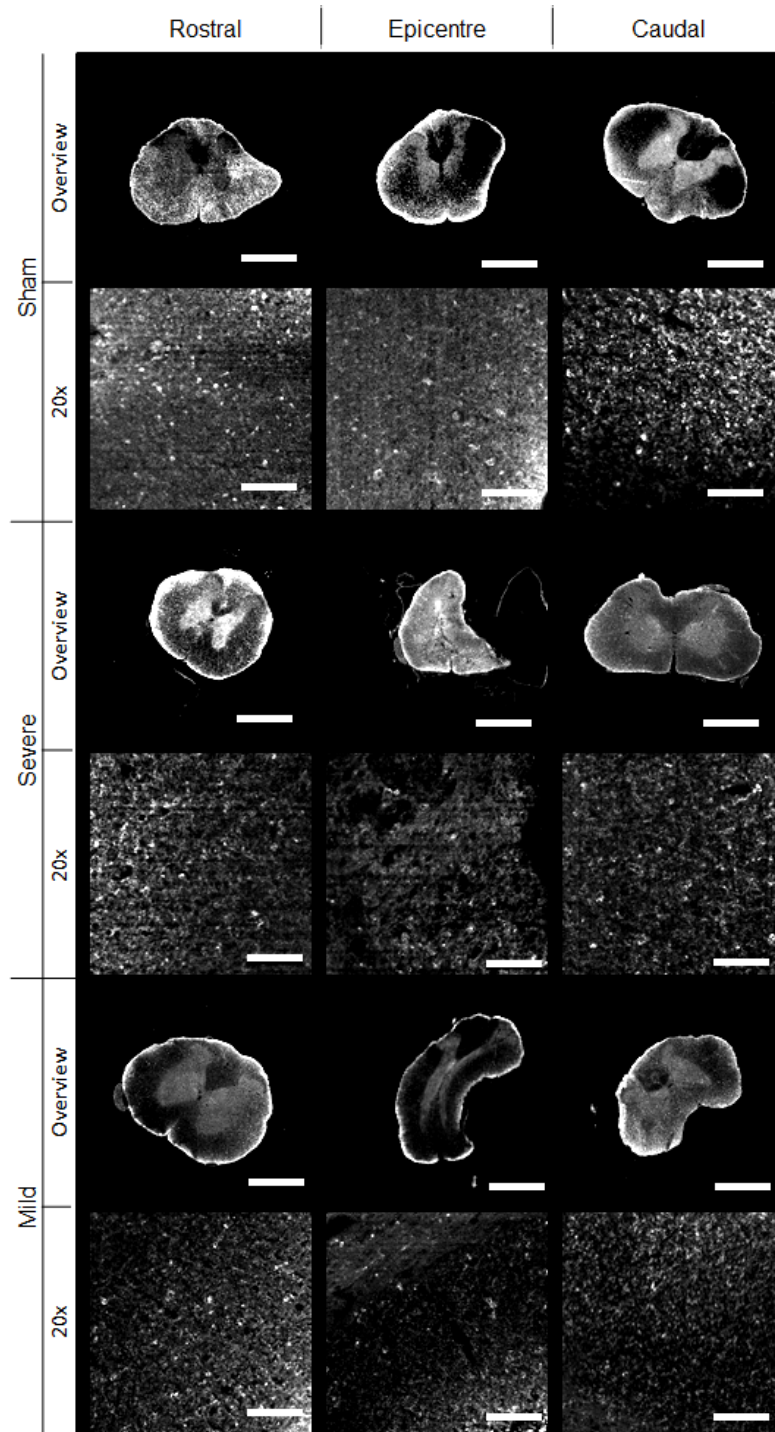
Figure 6.17: **Representative images of MBP staining in ventral balloon catheter-induced NTSCI.** *Animals underwent a T10 laminectomy and balloon catheter inflation at T8/9 over 3 days, and were perfused two weeks after the maximal inflation. Animals were grouped based on the functional deficit obtained. In overview images, scale bar is 1 mm, in 20x images (right hand side white matter), scale bar is 100 μm*

6.4.4.4 Severe NTSCI caused narrowing of the vasculature, with no difference to the number of vessels

For RECA-1 labelling, two outcomes were measured: the average size of each stained object (vessel), and the number of stained objects counter per unit area.

In terms of the number of vessels counted per each spinal cord section (normalised to the tissue area), there were no observable differences between locations and groups (Figure 6.18). Conversely, for the average size of vessels, there was a decrease at the epicentre for severely injured animals only (Figure 6.19). This difference was observable on images from this region compared to others (Figure 6.20).
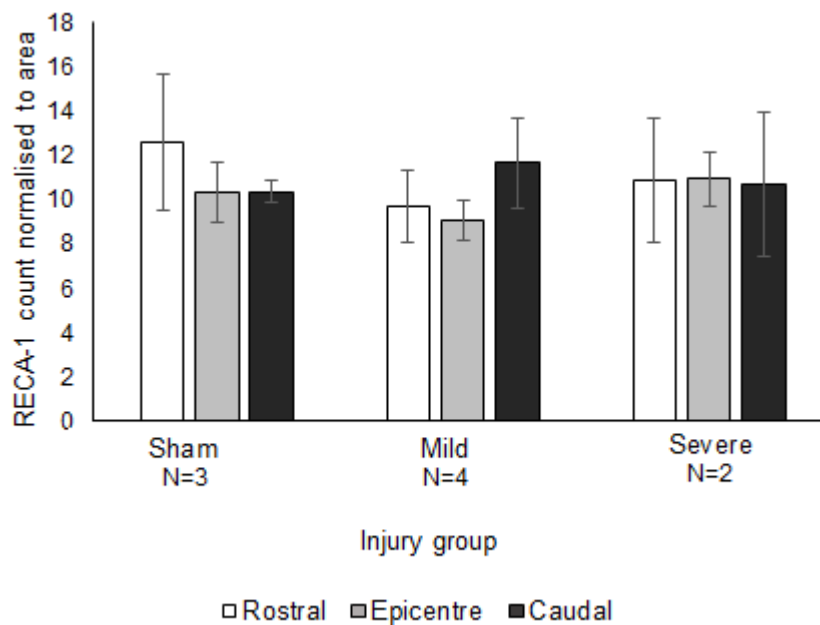
*Figure 6.18: **Number of RECA-1 stained objects in NTSCI spinal cords normalised to area.** Animals underwent a T10 laminectomy and balloon catheter inflation at T8/9 over 3 days. Animals were perfused two weeks after the maximal inflation, and were grouped based on the functional deficit obtained. A total of three sections were stained and imaged at each location. Data is mean ± S.E.M.*
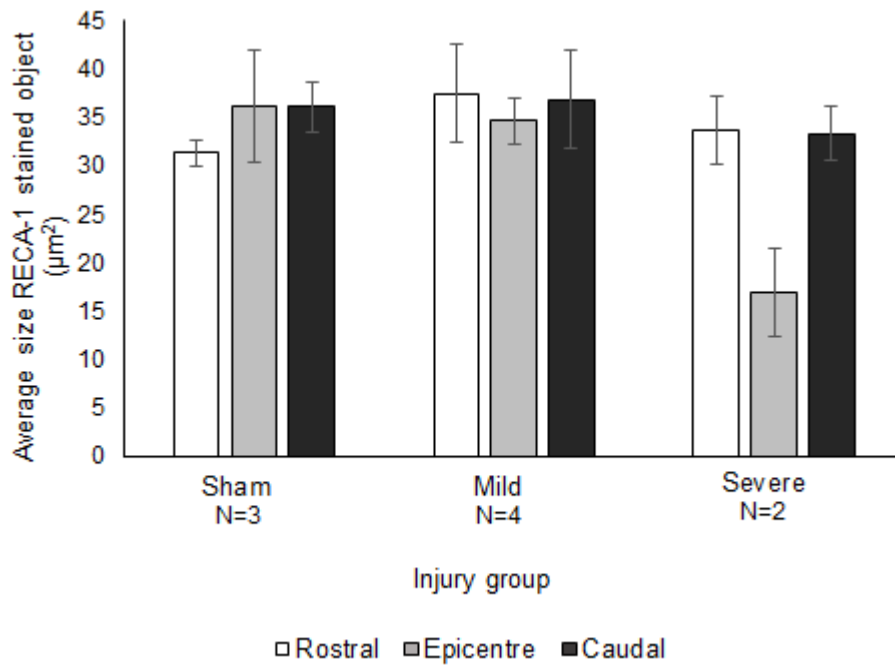
Figure 6.19: ***Average size of each object stained with RECA-1 from NTSCI spinal cords.*** *Animals underwent a T10 laminectomy and balloon catheter inflation at T8/9 over 3 days, then were perfused two weeks after the maximal inflation, and grouped based on the functional deficit obtained. A total of three sections were stained and imaged at each location. Data is mean ± S.E.M.*
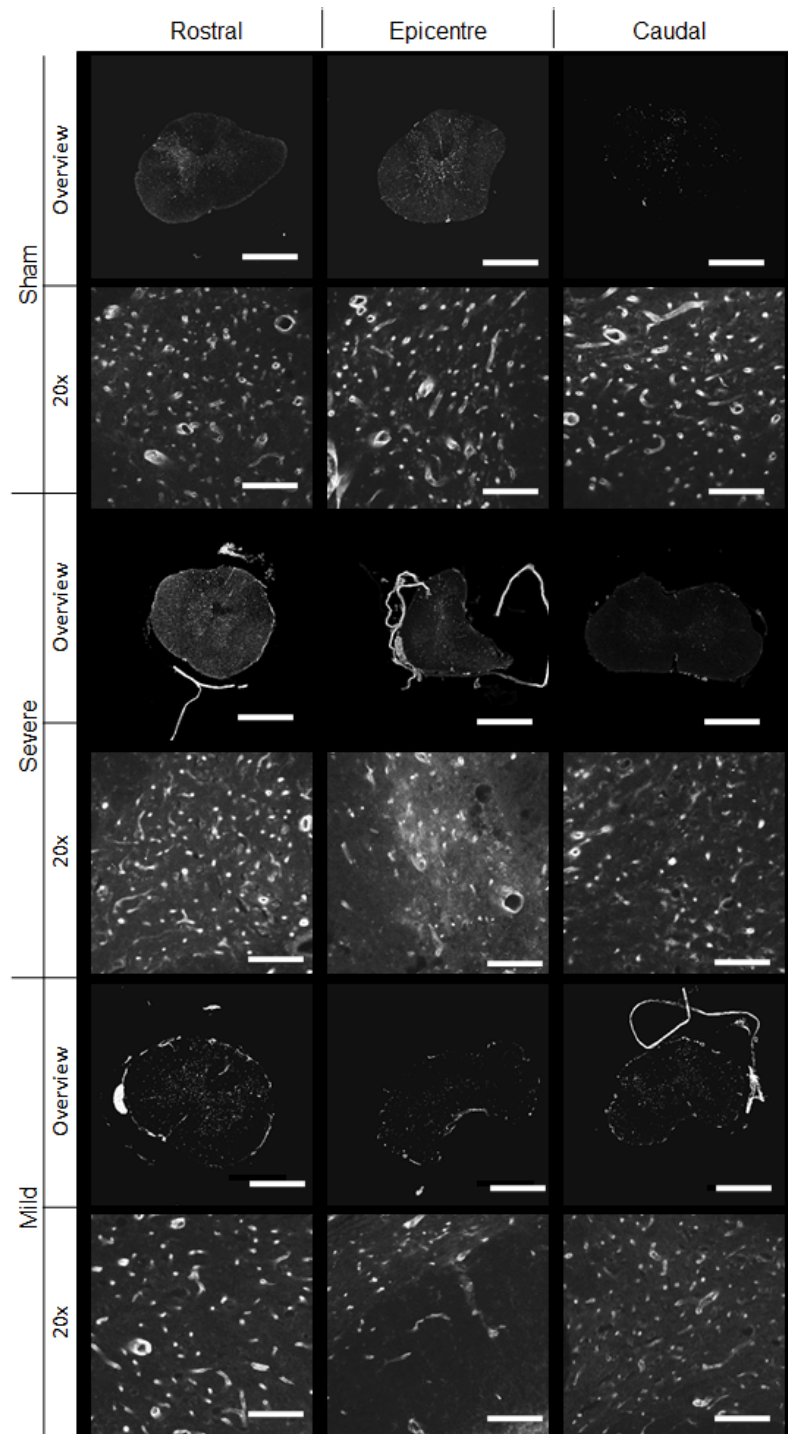
Figure 6.20: **Representative images of RECA-1 staining in ventral balloon catheter-induced NTSCI.** *Animals underwent a T10 laminectomy and balloon catheter inflation at T8/9 over 3 days. Animals were perfused two weeks after the maximal inflation. Animals were grouped based on the functional deficit obtained. In overview images, scale bar is 1 mm, in 20x images, scale bar is 100 μm*

6.5 Discussion

The aims of this chapter were to evaluate behavioural and histological outcomes in a newly developed rat model of NTSCI; in order to better understand NTSCI pathology. The key factors were to produce an injury which increased over a duration of days, as measured by an increasing functional deficit. The histopathological findings of the injury should have been distinct from TSCI, showing no haemorrhage or cystic cavity, but instead compression of the cord.

Surgery was undertaken on a total of 10 female Wistar rats. Each underwent a partial laminectomy at T10, and ventro-lateral 2F balloon catheter implantation with the balloon component being at T8 spinal cord level. The catheter was attached to an injection port, which was positioned trans-cutaneously at the shoulder blades. For sham animals this was implanted subcutaneously. In injury animals, the injection port was used to add a volume of 7.5 μL to the balloon on day 1, day 2, and day 3 after surgery. This was determined in the previous chapter to have an overall balloon diameter matched 15 μL standard inflation. Functional outcomes were measured using the BBB open field locomotor score. Two weeks after the initial surgery, animals were perfused and spinal cords dissected for histological analysis. Injured animals were subsequently grouped into mild and severe injury groups based on behavioural outcomes.

Based on previous *in-vitro* experiments, the first inflation of 7.5 μL theoretically corresponded with a balloon cross-sectional area of 2.5 mm^2; the second 4.6 mm^2 and the third 5.2 mm^2. This final cross-sectional area matched that of a 15 μL volume in a simple one inflation study, and spinal canal stenosis of between 70 and 75%.

6.5.1 Outcomes from injured animal groups

The experiment aimed to understand whether a functional deficit could be attained using a balloon catheter-injection port model of NTSCI; so motor function was scored using the BBB scale. Further, histology of the spinal cords gave insights into overall

histoarchitecture, and changes to both astrocytes and vasculature.

6.5.1.1 Lesion location and extension

The position of the balloon catheter insertion could be determined by evaluating the histology of serial transverse spinal cord sections. In sham, mild, and severe injury groups the balloon was predominantly ventral or ventrolateral (right hand side) at the site of insertion. At the injury epicentre, the balloon was lateral to the spinal cord on the right hand side. The rostral tip of the catheter was lateral or dorsolateral. None of the animals showed a dorsal lesion. The method therefore shows potential in inducing a ventral injury.

6.5.1.2 Functional deficits and histological damage

Functional deficits and histological damage were different in the mild and severe groups. In both groups, locomotor recovery occurred. Spontaneous recovery of locomotor function after spinal cord injury has been observed frequently in rodent models and is thought to be due to axonal sprouting (Ballermann and Fouad, 2006; Kjell et al., 2013; Hilton et al., 2016; May et al., 2017).

In the severe group motor function declined over the first three days, whilst the balloon was being inflated. With each inflation there would have been increasing compression of the spinal cord, resulting in an increasing functional deficit. The greatest change in deficit came with the third inflation where the animals were paralysed in their hindlimbs. This recovered over the course of the subsequent two weeks, but only to weight supported stepping, no co-ordination was observed. In future studies, it would be of interest to have animals which are perfused at various timepoints to evaluate lesions in the spinal cord with each inflation, and how these develop over time.

It is not possible to determine which tracts were damaged in order to cause the functional deficits obtained in each group, since the compression affected all areas of the spinal cord at the epicentre as opposed to a local injury. Further, the position of the balloon was lateral at the epicentre, more ventral caudal to the epicentre, and dorsal at the laminectomy site. Therefore at different spinal cord levels, different tracts were damaged.

This latter point is true for mild and sham injury groups as well as the severe group.

In this severe injury group, there was no consistent difference observed between left and right hindlimbs, indicating that both the left and right hemisections of the cord had been damaged equally. This finding was supported by lesion histology, where, at the lesion epicentre, there was observable damage in the left and right hemisections of the spinal cord, with observable loss of grey and white matter.

The maximum deficit observed in the mild injury group of co-ordinated stepping with paw dragging and external rotation was less marked than that of the severe group (no co-ordination), but greater than the sham group (trunk instability only). This occurred two days later than the minimum function observed in the sham group (day 3 compared to day 1), indicating that this was not due to the surgery alone and was in part due to balloon inflation. Histologically, this group had a C shaped lesion with damage to the right lateral white matter. This right-sided pathology resulted in a consistent functional difference, with the right hindlimb performing worse than the left. There was a concurrent reduction in cross-sectional area of approximately 30% at the lesion epicentre. In spite of the significant deformation of the shape of the spinal cord in this mild injury group, the functional deficits were not severe.

At the epicentre, the difference in cross-sectional area between the mild and severe injury groups was just 12%. Both groups showed significant spinal cord compression. It is of interest that the mild injury group did not gain a substantial hindlimb dysfunction, whereas the severe group did. Clinically, significant stenosis can be observed without functional deficit (Watanabe and Parke, 1986; Boden et al., 1990a; Steurer et al., 2011; Weber et al., 2016). The findings of this study suggest that there is a threshold value over which damage to the histoarchitecture of the spinal cord results in more marked functional deficits.

Correlating the minimum cross-sectional area of the spinal cord with the minimum BBB score gave a Spearman correlation coefficient of 0.63 ($p = 0.05$), indicating moderate to good correlation. This confirms that there is an association between decreasing cross-

sectional area and minimum BBB score, as observed in the results. The Spearman correlation is most suitable for this type of data since the BBB scale is non-linear (i.e. the difference between each score in the scale is not proportional (Fouad et al., 2013)), and the data has an non-linear distribution (i.e. is non-parametric), with a small sample size in each group. Plotting the minimum cross-sectional area with the minimum BBB score suggests a non-linear trend with threshold value in cross-sectional area (i.e. spinal cord compression), below which results in significant deficits (Figure 6.11 in section 6.4.3).

Comparing functional outcomes of NTSCI herein with TSCI lesions in other studies allows greater insight into the pathological mechanism. In a traumatic dorsal balloon lesion studies with a volume of 15 µL, hindlimb paralysis was observed with motor recovery over two weeks (Vanicky et al., 2001; Urdzikova et al., 2006; Sedy et al., 2007). In these TSCI studies at two weeks post-injury, extensive movements of all three joints of the hindlimb were observed, but no sweeping or stepping. The severe NTSCI lesion group in this research therefore had greater motor recovery than a similar TSCI lesion, despite matching the spinal cord compression extent (Vanicky et al., 2001; Urdzikova et al., 2006; Sedy et al., 2007). The reason for this may be inherent to the slow velocity of increasing compression in NTSCI, allowing adaptation and plasticity in the spinal cord. Clinically, neural remodelling in the sensori-motor network has been observed in patients with NTSCI at the cervical levels (Karadimas et al., 2015; Zhou et al., 2015; Bernabeu-Sanz et al., 2019). The increased speed of TSCI means that such plasticity and adaptive changes intrinsically cannot take place.

6.5.1.3   Lesion histopathology

GFAP expression and astrogliosis

Immunohistochemistry markers used herein (GFAP, MBP, CS-56, RECA-1) can help elucidate mechanisms of injury in the balloon-catheter induced NTSCI. It is worth noting that although trends were observed, particularly in the severe injury group, none were statistically significant due to the low N number (N=2) and, as such, high variation.

Therefore, all discussion and potential mechanisms of injury described below require further study with an increased number of animals.

In this study, there was an observed increased in the proportion of tissue stained with GFAP at the epicentre of severe injuries compared to all locations in sham and mild injured animals. The reasons for this may be two fold: either due to threshold-driven astrogliosis at the injury epicentre, with the threshold explaining why differences were observed in severe groups but not mild groups; or due to the lack of grey matter in the severe injury group epicentre region, thereby resulting in an altered ratio of grey and white matter, and a difference in GFAP labelling.

Few studies have evaluated GFAP labelling and astrogliosis after NTSCI. In TSCI, astrogliosis occurs immediately after the primary injury and is core to glial scar formation (Cullen et al., 2007; Kawano et al., 2012; Wanner et al., 2013; Weightman et al., 2014). In NTSCI, primary and secondary injury are not easily distinguished due to the ongoing quasi-static compression of the spinal cord. In rabbit models of disc herniation leading to lumbar stenosis, two studies described an increase in GFAP levels compared to controls (Klironomos et al., 2011; Shunmugavel et al., 2013); however this is not quantified and the representative images used do not show such a clear trend. The experiments undertaken herein had insufficient N numbers to show significant differences, but can act as an important pilot study to guide further research. The research herein suggests that when NTSCI is induced to compress the spinal cord to such an extent that grey matter parenchyma is disrupted, astrogliosis of the remaining astrocytes results. The reasons for this and long term outcomes require further research, i.e. using more animals for a greater statistically powered study or lower the variance observed, and longer timepoints.

Chondroitin sulphate expression, perineuronal nets and plasticity

In the intact spinal cord, CSPGs are one component of perineuronal nets, which surround neurones (Kwok et al., 2011; Burnside and Bradbury, 2014; Haggerty et al., 2017; Irvine and Kwok, 2018). The chondroitin sulphate components can be sulphated in various

patterns, and the CS-56 antibody predominantly labels 6-sulphated chondroitin sulphate (C6S) (Miyata et al., 2012).

Perineuronal nets have a role in modulating neural plasticity (Sorg et al., 2016), which is a key distinguishing factor of NTSCI to TSCI (Karadimas et al., 2015; Zhou et al., 2015; Bernabeu-Sanz et al., 2019). As such, it could be hypothesised that a change would be observed in CSPG expression in NTSCI, to modulate plasticity. There have been no studies evaluating CSPGs or perineuronal nets after NTSCI. In this study, there were no observable differences in CS-56 labelling in any group. In all cases, less than 9% of the spinal cord was stained with CS-56. In the cortex, one study in mice identified a reduction in C6S with age (Miyata and Kitagawa, 2016), and suggested that this corresponded with a reduction in plasticity; i.e. that an increase in C6S is associated with increase plasticity. The research herein was the first to evaluate the expression of C6S in NTSCI, and found no observable difference compared to contorls. However, the expression was only evaluated from low magnification images, using the whole transverse cross-section of the spinal cord. Greater differences may have been observed if the grey matter alone was assessed at high magnifications; since the grey matter is where the perineuronal nets are established (Irvine and Kwok, 2018). Further, it is possible that in NTSCI there are other mechanisms involved in neural plasticity, beyond a difference in C6S, which is why no changes in C6S were observed herein. Other markers of perineuronal nets molecules, such as Wisteria floribunda agglutinin (WFA) or aggrecan, could be used. The mechanisms of plasticity in NTSCI and changes to perineuronal nets require further study.

MBP staining and demyelination

Reviews of the pathology of chronic spinal cord compression frequently discuss ischaemia and subsequent demyelination as mechanisms of injury (Baptiste and Fehlings, 2006; Dolan et al., 2016). This is supported by experimental studies. For example, Shunmugavel et al. (2013) induced lumbar stenosis in rats by inserting a silicone block at L4 and L6, and identified demyelination at the injury site as measured by fast blue

intensity. Other models of NTSCI using a line surrounding the spinal cord and a thoracic screw method have also observed demyelination (Kubota et al., 2011; Sun et al., 2016). Similarly, in human studies of chronic compression of the spinal cord, apoptosis of oligodendrocytes was observed using various immunohistochemical markers (Yamaura et al., 2002; Newcombe et al., 2015).

The results of the study herein identified a slight reduction in the proportion of tissue stained with MBP for mild injured animals at the epicentre, and a greater reduction in severe injured animals. These differences were not statistically significant due to the low N number. In spite of this, they correspond to the wider literature of NTSCI, supporting the role of demyelination in pathogenesis.

RECA-1 and changes to the vasculature

In NTSCI, compression of the spinal cord is hypothesised to lead to compression of the vasculature, resulting in ischaemic damage to cells. For example, Xu et al. (2017) implanted a water-absorbent polymer at C6, and evaluated changes to the neurovascular unit, including endothelial cells, using electron microscopy. The results, including increased vacuoles in endothelial cells, small gaps in tight junctions, and neuronal degeneration, indicated that chronic compression in NTSCI results in significant damage to the neurovascular unit. This reduction in the local vascular supply is core to the pathology of NTSCI (Karadimas et al., 2013; Long et al., 2014).

Alongside narrowing of the vasculature due to compression, further changes hypothesised to be involved in NTSCI are an increase in permeability of the blood spinal cord barrier (Karadimas et al., 2013, 2015). (Karadimas et al., 2013) implanted a water-absorbing polymer at C6 in to induce NTSCI in a rat model. At 10 weeks after implantation, injections with Evans Blue were carried out to assess blood spinal cord barrier permeability, followed by histological assessment for various markers. The key findings of the study were an increase in blood spinal cord barrier permeability (i.e. a loss of barrier integrity), a reduction in the number of RECA-1 stained endothelial

cells, and, in a subsequent paper, a reduction in laminin staining (Karadimas et al., 2015). This indicated that at 10 weeks post-injury, there were fewer intact endothelial cell-lined vessels, and vessles were more permeable.

Kurokawa et al. (2011) carried out an experiment using a water-absorbing polymer model of NTSCI, evaluating ischaemia by injecting fluorescent microspheres into the bloodstream and subsequently evaluating the fluorescence per gram of tissue at the injured spinal cord level (12 weeks post injury). There was 20% less fluorescence in compressed spinal cord compared to healthy control specimens, indicating circulatory disturbance and ischaemia. The Kurokawa study did not assess the number or size of blood vessels.

In this study, a difference in the number of objects stained with RECA-1 (normalised to area) was not observed. Instead, a reduction in the average size of objects stained with RECA-1 was observed, at the epicentre for the severe injury only. This corresponds to a reduction in diameter, i.e. narrowing, of the vessels at the severe injury epicentre. As with the other immuno-stains used herein, this difference was observed but not statistically significant due to the low N number. The biological significance is supported by the other studies of NTSCI.

Across the wider literature and the research herein, chronic spinal cord compression in NTSCI results in clear effects to the spinal cord vasculature. Together, the studies suggest that in the short term after NTSCI there are the same number of vessels which become narrow, and then by latter time points this results in vascular remodelling, a reduction in number of vessels, and increased vascular permeability.

NTSCI Functional Threshold

In the severely injured animals, localised regions of necrosis and cellular infiltration were observed, along with white matter vacuoles extending beyond the lesion itself. In terms of immunohistochemistry, a reduction in MBP staining and an increase in GFAP staining was also observed in the severe group. These findings were not observed in mild or sham groups. Such pathological findings have only been reported in one other NTSCI study,

which used a flat screw to compress the spinal cord (Sun et al., 2016). In the Sun study, once the cord was compressed by over 40%, reactive gliosis, white matter demyelination and missing tissue were observed at the injury epicentre. In more mild injuries, where the spinal cord was compressed by less than 40%, observations were compression/flattening of the cord with white matter vacuoles observed in some studies but not others (Kim et al., 2004; Kubota et al., 2011; Lee et al., 2012; Long et al., 2013; Sun et al., 2016). This finding of a threshold value was also reflected in the functional data described above. Once the spinal cord is compressed to above this threshold value, as occurred in the severe but not mild injury groups, the normal histoarchitecture of the cord is lost and functional deficit becomes significantly more severe. The difference in cross-sectional area between mild and severe groups was just 12%. The results from this study indicate that in this model, the threshold lies within the range of these two groups, between 32% and 44% spinal cord compression. This value is in keeping with previous clinical studies, where the threshold for symptoms is between 25 and 50%, with variation between populations and vertebral levels (Penning et al., 1986; Matsunaga et al., 2008; Steurer et al., 2011; Iwahashi et al., 2016; Weber et al., 2016; Kadanka et al., 2017; Lim et al., 2017; Martin et al., 2018; Witiw et al., 2018).

6.5.2   Outcomes from sham surgery

A functional deficit was observed in sham animals at day 1 post-surgery, but this recovered by day 7. The only maintained functional abnormality was postural instability. There was no consistent difference between left and right hindlimbs. These findings indicate minimal damage to the spinal cord through implanting the balloon system, which was corroborated by histological analysis. The postural instability observed may have been due to damage to the lateral white matter on the right hand side of the spinal cord due to the balloon at the epicentre, due to damage caused caudally to the epicentre during balloon insertion, or as a result of musculoskeletal disruption during the partial laminectomy at T10. It is not possible to fully understand this based on the histology and behavioural

assays undertaken. Future studies should include a laminectomy only group to further evaluate this finding.

6.5.3   Limitations of outcome measures

At termination in this study, only one balloon system could be extracted intact. This balloon had deflated due to loss of pressure within the system. The decompression of the spinal cord due to deflation or damage to the balloon-port system may have facilitated the functional recovery observed in mild and severe injury groups. In spite of this, a lasting functional deficit occurred, indicating an injury to the spinal cord.

The functional deficit obtained was only measured using the open field BBB scoring system. This has disadvantages in user bias, a lack of quantitative data, and the non-linear nature of the scale (Martinez et al., 2009; Fouad et al., 2013; Sharif-Alhoseini and Rahimi-Movaghar, 2014). Further studies should fully characterise the functional deficit obtained through the use of kinematic analysis. Other measurements such as sensory function using the von Frey filament test would add further information about the injury modality. These tests should be undertaken at least once prior to surgery to evaluate the motor deficit caused by surgery itself.

The BBB scale cannot distinguish NTSCI from TSCI, nor dorsal from ventral lesions, due to its broad nature and the overlap in function between spinal cord tracts. It can only determine if the animal is injured, and some element of injury severity although this latter point is subject to bias by human scorers (Molina et al., 2015). The histology could determine NTSCI/TSCI and ventral/dorsal. In these preliminary tests, the BBB scale was used as a crude measure of function after inflation to check if the animal was injured. More thorough evaluation of the sensori-motor function of the animals would be required for future studies.

6.5.4 Technical Challenges

6.5.4.1 Variation in inflation volume

In spite of using the method and technique, animals in the mild and severe injury groups had different functional and histological outcomes. The reasons for this may be in variation in the surgical method: insertion technique or balloon inflations.

The 2F Fogarty catheter was manufactured for laparoscopic embolectomy surgery, and as such contains a radio-opaque wire to evaluate position and location of the device. This has been made use of in a previous rat spinal cord injury study using the apparatus, where the position of the catheter was confirmed using a microCT scan (Su et al., 2015). This could be carried out in future studies to ensure the correct spinal level and improve reproducibility of the study. Additionally, inflation of the balloon with a radio-opaque agent instead of water would allow the entire balloon to be visible with imaging. The agent used would need to be non-toxic, so that if the animal destroys their injection port either ingestion or expulsion of the agent within the body would not cause negative outcomes.

Alternatively, the rate of balloon filling and volume used could be measured more precisely. A volume of 7.5 µL was attempted to be added to the balloon each day, manually using a very fine syringe. This could have lead to human error due to the very small volume required, and backflow from the balloon into the syringe could have occurred. Similarly, the rate of injection of volume was not highly controlled. A microprocessor controlled injector such as a Nanolitre device, or a sampling device as used in the previous Vanicky et al. (2001) study could be used to add volume into the balloon more precisely.

The rate of balloon inflation in SCI was shown to be important in study undertaken by Sedy et al. (2009). These authors used a dorsal balloon catheter lesion and inflated the balloon with a total of 15 µL, but used various timesteps: immediate 15 µL (total

time 2 seconds), 3 x5 µL (total time 30 seconds), or 3 µL followed by 6 x 2 µL (total time 3 minutes). Heart rate and lung function were evaluated, as well as pulmonary oedema. With faster balloon inflations, heart rate dropped significantly and the rate of pulmonary complications increased, due to insufficient time to adapt the sympathetic tone (eg changes in blood pressure and blood volume distribution). This may explain the differences observed in this study. Herein, the rate of inflation was not controlled, and therefore may have been substantially quicker in the first group than the second. This could explain the change in breathing pattern observed in animals with a severe injury. The Sedy study did not assess the histological or behavioural outcomes of the different injury groups.

6.5.4.2 Port system

The use of a trans-cutaneous injection port allowed inflation of the balloon over various timepoints, to model NTSCI. All of the animals showed irritation around the sites of their injection port, which occurred up to one week after surgery for mild injured animals, and once some motor function was restored for severely injured animals. Ultimately, the majority of the animals destroyed their injection ports themselves or they had to be manually removed due to risk of infection, thereby deflating the balloon due to loss of fluid.

In future studies, the port itself could be placed subcutaneously for injury animals as well as control animals. Other studies have used subcutaneously implanted injection ports, with injection through the skin and port at each timepoint (de Wit et al., 2001; Fiebig et al., 2013; Figueiredo et al., 2015; Gossman et al., 2017). An alternative could be to implant the port subcutaneously with one or two sutures in the skin. When injection is required, a single suture could be cut to reveal the port for injection; then the suture could be replaced. Subcutaneous port implantation would reduce skin irritation which will be particularly important in control animals, allow longer study periods, allow housing in pairs and preclude the need for large cages which take up more space and are more costly.

It would also allow for improved evaluation of the system after perfusion, since the system should remain intact. This method was not chosen for the study herein since the repeated opening of the wound and subsequent suturing could have lead to infection or damage to the skin.

6.5.5 Conclusion

Referring back to the three characteristics of NTSCI distinguishing it from TSCI, as described by Karadimas et al. (2015) of no acute mechanical insult, absence of gross haemorrhagic necrosis, and chronic nature: this model fulfils each three of these objectives. The injury was induced slowly over the course of three days with continuing balloon inflation, and the histology revealed minimum parenchyma disruption or necrosis, even in the severe injury group.

The results described in this chapter (summarised in Table 6.1) act as a pilot study to exemplify that the method developed does induce a measurable NTSCI. There are limitations to the study, including the low N number and variation seen between injury groups, which require further assessment.

The variation between groups led to injured animals being split into mild and severe groups. The work shows that histologically, a greater lesion was observed with the mild than sham group; but no significant differences were observed in functional outcomes. Conversely, even greater damage and functional deficit in the severe group. Therefore, the results suggest a threshold value in spinal cord compression after which non-recoverable damage is observed. This should be further investigated. Overall:

Volume injected $\not\propto$ Balloon inflation $\propto$ Behavioural and histological outcomes

The method developed and used herein resulting in an NTSCI lesion with a functional deficit and histological differences to sham controls, with a reduced invasiveness compared to screw or line NTSCI methods. Now that the model has been developed using these measures, more refined evaluation of the pathology can be undertaken in future studies.

Table 6.1: **Conclusions of Chapter 6: Outcomes of NTSCI in-vivo Studies**

Aim	Objective	Result and Implications
Histological and functional outcomes which occur after long term spinal cord compression	Implant balloon catheter port system into rats, inflate balloon over 3 days and monitor animals.	Surgery was undertaken in 10 animals, all survived the surgery and subsequent balloon inflations.
		Animals lost between 5 to 10% of their body weight in the first week after surgery, but this recovered to pre-injury levels by day 9 to 10.
		Irritation was observed around the injection port between one and two weeks post-surgery, meaning they had to be removed at this point.
	Characterise functional deficits using BBB scale.	Injured animals were categorised based on their minimum BBB score; where severely injured animals had a minimum BBB of less than 2
		In mild and severe groups, motor function was at its minimum on day 3, and recovered significantly to day 9.
		In the mild injury group, there was a trend for the right hindlimb to have an increased functional deficit to the left hindlimb, but variation was high.
		The functional deficit observed in the severe group recovered more than a concurrent TSCI study using the same balloon diameter.
	Shape and area of tissue at the lesion site	An obvious reduction in cross-sectional area was observed at the injury epicentre, with significant differences between injury groups.
		Cross-sectional area and minimum BBB score had a moderate to good correlation, with data suggesting a threshold value for compression and severe deficits.
	Changes to the spinal cord parenchyma	Global compression of the spinal cord was observed in mild and severe injury groups, with loss of grey matter, inflammatory cell infiltrate, and white matter vacuolisation in the severe group only.
	Immuno-staining of lesions	Due to low N numbers and high variation, none of the changes observed in IHC were statistically significant.
	Glial scar evaluation using GFAP & CSPG	A trend of increased GFAP staining at the epicentre for severe lesions only. No changes for CSPG labelling, i.e. no astrogliosis.
	Myelin staining using MBP	A trend of demyelination at the epicentre of severe lesions only.
	Vasculature changes using RECA1	A trend of more narrow vessels at the epicentre for severe lesions only, no changes to the number of vessels.

Chapter 7

Discussion

Slow velocity, chronic compression of the spinal cord results in NTSCI. The underlying cause of the compression can vary, with metastases and degenerative bone spurs causing over 50% of cases (New et al., 2014). The prevalence of NTSCI is estimated to be greater than or equal to that of traumatic injuries, and the incidence is predicted to increase with an ageing population (Razdan et al., 1994; Noonan et al., 2012; Lee et al., 2014). Further, in patients with NTSCI, treatment is limited and involves surgical interventions of decompression and fixation (NHS, 2010; NICE, 2015, 2016).

Slow and progressive occlusion of the spinal cord in NTSCI does not result in gross haemorrhage or parenchyma disruption (which are seen in traumatic injuries), instead post-mortem observations include demyelination, changes to the vasculature and change in spinal cord shape (Someya et al., 2011; Karadimas et al., 2013). The pathways involved and contribution of each cell type are not understood. In patients, it is impossible to decouple the mechanical injury from other factors, such as compression of the vasculature and ischaemia. Therefore, there is a need to develop experimental models of NTSCI, in order to further understand the pathological mechanisms, and evaluate specific parameters in detail.

It was hypothesised that the mechanisms of NTSCI could be elucidated by the development of *in-vitro* and *in-vivo* models. For the *in-vitro* model, this study built on the

work of previous studies and aimed to utilise collagen hydrogels seeded with neural cells and compressed at various velocities in a BOSE 5110 Electroforce. The cells of choice were astrocytes, since they are core to the TSCI cascade but their role in NTSCI was unknown. For the *in-vivo* model, this aimed to use a balloon catheter method (previously used in a TSCI context) to induce a ventral NTSCI lesion in a rat. The outcome measure for this is would be a functional deficit, and pathology different to that observed in TSCI.

7.1 General discussion: outcomes in NTSCI and TSCI

7.1.1 *In-vitro* models

Compared with *in-vivo* models and clinical scenarios, *in-vitro* models allow greater control of conditions, including the matrix environment, cell populations, and environmental factors. Each of these can be manipulated and the effects observed. Collagen hydrogels retain cell adhesion motifs and provide a 3D environment, supporting cells and facilitating interactions with the matrix, ultimately resulting in a better representation of physiological conditions (Caliari and Burdick, 2016). Furthermore, collagen hydrogels have been used to assess neural cell responses in a 3D environment, including after impaction in a TSCI context (East et al., 2010, 2012; Bar-Kochba et al., 2016; Smith, 2016; Kirk, 2018). As such, these hydrogels were the basis of the *in-vitro* model developed herein.

7.1.1.1 Development of *in-vitro* model

The research carried out in this thesis builds on two previous studies at the University of Leeds (Smith, 2016; Kirk, 2018). The first of these studies (Smith, 2016) used the Infinite Horizon impactor to apply load-controlled local insults to astrocyte-seeded collagen hydrogels. Future work identified in the Smith study was to investigate the use of other impactors. The second of these studies (Kirk, 2018) used a BOSE 5110 Electroforce to apply velocity and displacement-controlled local insults to the same type of gels, seeded

with astrocytes or microglia. The future work described in the Kirk study was to optimise and validate the cell populations, and fully characterise the BOSE apparatus in terms of inputs and outputs, different mechanisms of injury and platen fixtures.

The work described in chapter 3 of this thesis built on these two studies and fully characterised the capacity of the BOSE 5110 Electroforce instrument to apply mechanical insults at various velocities with new platen fixtures; as well as characterising the astrocyte population. Findings from this chapter validated the cell population in terms of response to TGF-beta treatment as a positive control for astrogliosis. Furthermore, the use of new platens in the impactor device had no impact on the maximum output velocity. The maximum velocity of the device obtained herein was 1000 mm.s^{-1}, in contrast to previous research which stated a velocity of 3000 mm.s^{-1} was used (Kirk, 2018). Greater evaluation of the capacity of the impactor device was undertaken, and it was observed that a maximum velocity of 100 mm.s^{-1} should be used for the optimum accuracy. This was significantly less than clinically observed velocities in TSCI (Wilcox et al., 2003), and this was a limitation of the research herein.

Further, chapter 3 characterised astrocytes isolated from mixed glial populations, in 2D and in 3D, under both physiological and pathological conditions. In 2D, approximately 90% of cells expressed GFAP, and therefore the cells could be identified as astrocytes (East et al., 2009; Kerstetter and Miller, 2012; Smith, 2016). Further, the astrocytes remained viable and non-reactive over two weeks in collagen hydrogels, as demonstrated by no significant differences in the proportion of cells labelled with ethidium homodimer, nor changes in the area stained with GFAP. Conversely, TGF-beta treatment (10 ng.mL^{-1}) of the astrocyte-seeded hydrogels, resulted in increased astrocyte reactivity: an increase in area stained with GFAP of 227% between days 1 and 14. These findings reflect an astrogliotic response, and were in keeping with the wider literature (Logan et al., 1994; Cullen et al., 2007; East et al., 2009; Kimura-Kuroda et al., 2010; Vogelaar et al., 2015; Smith, 2016).

The chapter also evaluated wider experimental parameters, such as the optimal gel

volume and imaging protocols for the cells. The implications of this chapter were that the BOSE 5110 Electroforce was suitable for applying controlled mechanical insults at various velocities to collagen hydrogels, and that astrocytes behaved as expected in the same collagen hydrogels. Therefore, a model for *in-vitro* NTSCI had been established, and could be used to evaluate pathological mechanisms.

7.1.2   Evaluation of astrocyte outcomes after TSCI and NTSCI *in-vitro*

In chapter 4, astrocyte-seeded hydrogels were compressed at various velocities, and cellular outcomes were established.

After high velocity compression (100 mm.s^{-1}) astrocytes had a significantly reduced circularity from day 11 (i.e. were more ramified), a significantly greater area stained with GFAP per cell from day 11, and expressed a significantly greater quantity of IL-6 compared to negative controls on day 14 (p $<$0.05). In spite of the previously described mismatch between clinical velocity and velocities used *in-vitro*, the phenotype observed in astrocytes when compressed at 100 mm.s^{-1} showed signs of astrogliosis and inflammation, which are both markers of secondary injury observed in TSCI clinically and in *in-vivo* studies of TSCI (Norenberg et al., 2004; Hu et al., 2010; Sofroniew and Vinters, 2010; Wanner et al., 2013; Ahadi et al., 2015; Anwar et al., 2016; Morin, 2018).

No previous studies have characterised mechanical impacts *in-vitro* in the context of NTSCI. In lower velocity impacts, the findings of astrogliosis and inflammation were not replicated, with no significant differences in any assay with a velocity of 10 mm.s^{-1} or lower. In NTSCI, the pathological cascade is poorly understood, and therefore the markers used were exploratory, and based on expected findings from TSCI lesions. Few *in-vivo* models of NTSCI report GFAP expression, and those which did report contrasting findings (Shunmugavel et al., 2013; Cho et al., 2015). The research herein suggests that astrocyte reactivity was not induced by direct mechanical compression of astrocytes alone in low velocity NTSCI contexts, but was induced in high velocity TSCI. In NTSCI,

compression of the vasculature is hypothesised to result in ischaemia (Karadimas et al., 2013). Therefore, the pathology may be linked to ischaemia or changes to the neuro-vascular unit. Further, the responses of other cell types to low velocity NTSCI insults are yet to be established. Based on the findings of the *in-vivo* studies described in chapter 5 and 6, the model can be tailored to elucidate further mechanisms (see section 7.1.4).

The findings of this chapter elucidate the mechanical origins of TSCI. At 10 mm.s^{-1}, the load imparted and transferred onto the hydrogels was the same as at 100 mm.s^{-1} but outcomes were different. Previous studies have a lack of coherence on the predominant injury mechanics important in determining TSCI outcomes (Kearney et al., 1988; Kwo et al., 1989; Jakeman et al., 2000; Seki et al., 2002; Kim et al., 2009; Lam et al., 2014). Based on the differences in mechanics and cellular outcomes between impact velocities, this study found that neither load nor the displacement extent were not the predominant factor affecting cellular outcomes. The remaining factors therefore were work done, or velocity. These two factors were interlinked due to the viscoelastic nature of the collagen hydrogel material: for a given displacement changing strain rate affected stiffness and therefore load and energy (Dogliotti and Yelland, 1964; Hussein, 2018). Therefore in this hydrogel system, the effects of load, work done, and velocity could not be uncoupled.

There were limitations to the assays used, including a lack of resources leading to not all timepoints or experimental conditions being tested using the IL-6 and IL-10 ELISA. Further, the lack of evaluation of cell viability in the study, which would be of interest in future studies. The lack of control of environmental conditions such as temperature, atmospheric gas levels meant long-term culture under compression more relevant to NTSCI could not be undertaken.

Overall, this chapter confirmed that the BOSE 5110 Electroforce instrument could induce TSCI and NTSCI-like velocities onto astrocyte-seeded collagen hydrogels. Clear differences in physiological responses were observed with different velocities. No significant changes were observed in low velocity insults, whereas astrocytes became reactive with an inflammatory phenotype at the highest velocity. This was characterised

by an increase in IL-6 production, an increase in the size of cells (hypertrophy), and a reduction in their circularity (ramification) at days 11 and 14 post-injury. Astrocyte reactivity as a result of mechanical compression was not core to the NTSCI cascade.

7.1.3 *In-vivo* models

In-vivo models are more complex than *in-vitro* models, incorporating tissue architecture, multiple cell types, surrounding tissues and biological systems *in-situ*. There are various considerations in developing a new *in-vivo* model, including the species: ease of husbandry, ethical requirements, and physiological and pathological similarities to humans (Hassannejad et al., 2016). In this study, rats were chosen as the animal model, since they are widely used in TSCI research, are relatively low cost, and of sufficient size to undertake spinal cord surgery (Talac et al., 2004; Zhang et al., 2014; Kjell and Olson, 2016). Chapters 5 and 6 described the development and outcomes of a novel *in-vivo* model of NTSCI.

7.1.3.1 Development of an *in-vivo* model of NTSCI

In the wider scientific literature of *in-vivo* models of spinal cord injuries, no models of NTSCI could be modified to induce an injury from the ventral approach in a suitable timescale without a highly invasive approach (Kim et al., 2004; Kubota et al., 2011; Kurokawa et al., 2011; Lee et al., 2012; Sun et al., 2016). The ventral directionality of NTSCI is important, since the spinal cord is asymmetrical ventrally/dorsally, and most clinical injuries occur from the ventral aspect (Watson et al., 2009; Ferrara, 2012; Tetreault et al., 2015; Martin et al., 2018). One method which had the potential to induce a ventral NTSCI was a balloon catheter method (Martin et al., 1992; Vanicky et al., 2001), although this had not been previously attempted. A further important factor in developing a model of NTSCI was control over canal stenosis. Clinically, there are three stages to stenosis and symptoms: a latent phase without symptoms, symptom onset, and symptom deterioration (Karadimas et al., 2012, 2013). However, the degree of stenosis required to initiate each

phase are poorly characterised (Penning et al., 1986; Steurer et al., 2011; Iwahashi et al., 2016; Weber et al., 2016; Kadanka et al., 2017; Martin et al., 2018; Witiw et al., 2018). Chapter 5 aimed to address these gaps in the literature and develop a clinically-relevant model of NTSCI with increasing stenosis over a time frame of days, using a ventral lesion.

The first aim of the chapter was to evaluate the histology of a ventral balloon catheter spinal cord lesion, using a traumatic injury. TSCI in rats has been modelled using a 2F balloon catheter in various studies (Martin et al., 1992; Vanicky et al., 2001; Lonjon et al., 2010; Chung et al., 2013). By using a slightly different technique to insert the balloon laterally and subsequently ventrally to the spinal cord, it was hypothesised a similar lesion could be established. A total of 4 animals were operated upon, where a balloon catheter was inserted into the vertebral canal at the T10 vertebra, and subsequently positioned and inflated at T7/8 spinal cord level. The volume used was 12.5 µL for 2 animals, and 15 µL for the other 2 animals. One week after this, spinal cords were excised and histology was performed. The spinal cord of one of the animals injured with a volume of 12.5 µL was damaged during tissue processing, and could not be assessed, leaving an N of 1 for this group.

Histological outcomes after TSCI *in-vivo* via balloon catheter

With both volumes, there was clear disruption to the tissue parenchyma at the injury epicentre. This damage extended rostrally and caudally, beyond the length of the inserted catheter itself. The length of the lesion and degree of damage observed was greater in the 15 µL group based on analysis of the histological images. It could not be determined whether the injury was ventral or dorsal, due to the extent of tissue damage at the injury epicentre. At the injury epicentre, conserved white matter remained in the penumbra only, and the central region was filled with a cystic cavity, loose debris, and macrophage infiltration. Parenchyma disruption, white matter vacuoles, and lesion extension have been observed widely in other TSCI balloon models (Martin et al., 1992; Vanicky et al., 2001; Lonjon et al., 2010; Chung et al., 2013).

Upon evaluation with immunohistochemistry, across all animals, a significantly greater proportion of tissue was stained with GFAP and CS56 at the injury epicentre compared to the nearest intact rostral and caudal regions ($p < 0.05$). This was indicative of reactive astrogliosis, and, again, similar findings have been established in dorsal TSCI balloon catheter model (Martin et al., 1992; Chung et al., 2013). Reactive gliosis is a hallmark of TSCI pathology and increased GFAP and CSPG expression have been observed widely in animal models and clinically (Norenberg et al., 2004; Sofroniew and Vinters, 2010; Wanner et al., 2013; Hol and Pekny, 2015; Tachi et al., 2015; Sofroniew, 2018). This gives confidence that the balloon catheter model can induce a TSCI similar to that of the wider literature using a modified insertion approach. In future studies, the diameter of the 15 µL balloon will be matched for cohesion with previous TSCI studies.

Vertebral column anatomy and geometry

The subsequent unknown was how to control the extent of stenosis in NTSCI. This involved two critical elements: the dimensions of the vertebral canal, and dimensions of the balloon catheter system. This would facilitate understanding of the degree of vertebral canal stenosis which could be applied with varying balloon volumes. Therefore, the second aim of this chapter was to characterise the dimensions of the rat spinal canal/vertebral foramen in the thoraco-lumbar region. The geometry of the spinal canal has not been widely established in the literature but was important to understand for NTSCI. A CT scan was undertaken of one rat post-mortem. The maximum cross-sectional area was observed at vertebral level T7/8 (spinal cord level T8/9), with a value of 8.9 mm^2. At the lumbar levels, the differences between cross-sectional area at various vertebrae were in keeping with a previous study (Jaumard et al., 2015). Due to the lack of wider data, and the use of only one animal (to comply with the 3Rs), the exact dimensions of the spinal canal could not be fully elucidated taking into account variation between animals. However, this experiment was useful to provide an approximation, and could be validated in the NTSCI studies themselves.

Characterising 2F balloon catheter inflation

The other factor in determining spinal canal stenosis in the *in-vivo* model of NTSCI was the balloon catheter dimensions. Various studies used a 2F balloon catheter with a volume of 15 μL, but no previous studies had quantified the dimensions of the balloon with this volume, or how the balloon dimensions changed with inflation. The third aim of this study was to characterise how balloon volume affected diameter. The results of this section were that the maximum diameter of the balloon was 4 mm. At 15 μL, the diameter of the balloon was 2.8 mm. This equated to a cross-sectional area at the widest point of 6.165 mm^2. One previous study using the same system stated with a volume of 15 μL a diameter of 2.5 mm, but did not determine how it was measured (Lonjon et al., 2010). A different study included a photograph of the balloon inflated with 15 μL, and the balloon appeared to have a diameter of 3 mm (Figure 2 in Vanicky et al. (2001)). Therefore the finding of this study was in keeping with other research.

The final aim of this chapter was to modify the balloon catheter system to facilitate induction of NTSCI, i.e. inflation over the course of a period of days. The first method attempted was to use an osmotic pump to inflate the balloon, however this did not provide sufficient pressure to inflate the balloon. So, an injection port was subsequently developed. Injection ports have been used in previous studies for venous injection studies over an extended timeframe (Fiebig et al., 2013; Figueiredo et al., 2015). Using this port affixed to the balloon catheter, a series of volumes were tested using multiple injections. The overall aim was to achieve a diameter of 2.8 mm (matched to a volume of 15 μL in the previous experiment) over 3 volume injections (i.e. 3 days *in-vivo* for future experiments). Due to loss of volume and pressure upon needle insertion for each injection, this was achieved using 3 x 7.5 μL injections (a total volume of 22.5 μL rather than 15 μL to compensate). The estimated proportion of canal stenosis with each inflation was 8% stenosis with no inflation; 28% stenosis with 1 inflation; 53% stenosis with 2 inflations; 73% stenosis with 3 inflations (matching a diameter of 2.8 mm).

Previous TSCI studies which have used a balloon volume of 15 μL resulted in a

significant functional deficit (Lonjon et al., 2010; Vanicky et al., 2001). As such, the maximum inflation used herein should also have resulted in a significant functional deficit, since the balloon dimensions were matched. The degree of canal stenosis which would initiate symptoms is not well understood. Clinical studies have identified that most patients with symptoms have between 25% and 50% canal stenosis (Penning et al., 1986; Steurer et al., 2011; Iwahashi et al., 2016; Weber et al., 2016; Kadanka et al., 2017; Martin et al., 2018; Witiw et al., 2018). Conversely, a rat study undertaken by Kim et al. (2004) found that 48% occlusion of the spinal canal did not induce functional deficits, but this used implantation of an expanding material at the cervical level and therefore results may be different using a balloon at T7/8. At 25% spinal canal stenosis, this may begin to impinge on the spinal cord, however, the diameter of the spinal cord relative to the spinal canal at T7/8 in a rat has not been established. It was of interest in subsequent *in-vivo* studies to identify at which point functional deficits were observed.

Overall, this chapter developed a system for inducing NTSCI. Each component of the system was evaluated separately: ventral balloon lesion; vertebral column geometry; evaluation of the balloon catheter; and development of the injection port system for NTSCI. The findings of this chapter were all limited by the fact they were carried out on the bench, as opposed to *in-vivo*. The following chapter built upon this, and evaluated the effects and success of the entire system *in-vivo*.

7.1.3.2 Outcomes of the NTSCI *in-vivo* model

In chapter 6, the model developed in chapter 5 was tested *in-vivo*, on a total of 10 animals. This study was important to validate the model. Functional and histological changes were evaluated in order to understand the injury induced, and determine whether it was distinct from a traumatic lesion characterised earlier in the research. Of the 10 animals, 3 were shams, where the balloon system was implanted but not inflated. Theoretically, the remaining 7 animals should have had the same functional and histological outcomes. The primary aims of the chapter were to evaluate the histology/morphology of the lesion

compared to TSCI lesions characterised in the model development phase of the study; and to assess basic functional outcomes using the open field locomotor scale.

Animal weights and functional outcomes

All of the animals survived the surgery with minimal complications. However, the same outcomes were not observed in all of the injury animals. For example, some of the injured animals required manual bladder expression for up to 10 days after maximal balloon inflation, whereas others did not. Based on this, and functional deficits, the animals were split into severe and mild injury groups to evaluate histological outcomes relating to motor deficit.

The open field locomotor score in all animals (sham and both injury groups) reduced immediately after surgery, from a score of 21 to 19, and did not change after one inflation in the injury groups. This may have been due to damage caused during the laminectomy, or due to catheter insertion. A limitation of the study was that it did not contain a 'laminectomy only' group, so this cannot be further elucidated. Since functional deficit remained the same immediately after surgery and after one inflation in the injury groups (from 0.38 to 2.38 mm^2, approximate canal stenosis from 8% to 28%), the impingement of the spinal cord at these timepoints was minimal.

With subsequent balloon inflations, the deficit in the severe injury group increased, with a reduction in BBB score to 14 after 2 inflations; and to complete paralysis (score of 0) after 3 inflations. In the sham group, this was not reproduced and instead the open field score improved to 21 by day 11. In the severe injury group, motor function subsequently recovered up to a score of 11 to 12 (indicating weight supported plantar stepping with minimal co-ordination). Using this information and the results of the model development research, it could be concluded that after 2 inflations (approximately 50% spinal canal stenosis), spinal cord impingement was achieved. This impingement increased after the 3rd inflation, when function further deteriorated.

The marked locomotor recovery observed in the severe injury group, was in keeping

with wider studies of spinal cord injury in rats (Ballermann and Fouad, 2006; Kjell et al., 2013; Hilton et al., 2016; May et al., 2017). In various TSCI dorsal balloon catheter studies at the same spinal level, with a matched maximum balloon diameter to that used in the present study, a finding of complete paralysis was observed immediately after surgery (Vanicky et al., 2001; Urdzikova et al., 2006; Sedy et al., 2007). However, in these studies, the recovery was more limited. At two weeks post injury, no sweeping or stepping was observed in the TSCI studies, but this was observed in the study herein. This difference in NTSCI and TSCI functional outcomes is noteworthy, and is discussed below in combination with differences in histological outcomes.

In the mild injury group, the functional deficits observed in the severe group were not reproduced, in spite of having subsequent inflations and intact catheter systems. Instead, a moderate decline to a BBB score of 16 was observed after 3 inflations. This recovered to a score of 20 or 21 by day 16. It was observed *in-vitro* that there was a loss of volume in the balloon-port system each time the injection port was punctured. Although this was overcome by using a greater total volume to achieve the same final diameter (22.5 μL rather than 15 μL), the control of the volume of water injected in the animal study was achieved by eye using a low volume Hamilton syringe, which offered less precise control of volume. A difference in inflation volume between mild and severe groups would also explain the difference in spinal cord compression (transverse cross-sectional area) between groups. This lack of precise control of the balloon volume was a limitation of this study.

NTSCI lesion histology

In terms of lesion histology, there was a reduction in transverse cross-sectional area of the spinal cord in all three groups, with the greatest effect being observed in the severe injury group. The shape of the spinal cord at the epicentre and damage to the parenchyma differed between groups. In all groups, the predominant region of damage was the right lateral funiculus. In the sham group, this funiculus was no longer observable. In the

mild group the epicentre had a C shape lesion around the lateral funiculus (where the catheter was present), but the white and grey matter of the cord were still present and distinguishable. Conversely, in the severe group the lesion site was semicircular, and the right hand side of the spinal cord was no longer apparent, instead it had been flattened. Further, there was observable local disruption of the grey matter. Similar observations of compression of the cord as opposed to parenchyma disruption have been identified in other models of NTSCI (Kubota et al., 2011; Long et al., 2013; Sun et al., 2016). These findings are in contrast to those of the traumatic study in the model development chapter (see section 7.1.3.1), wherein the round shape of the spinal cord was retained, but the only the tissue penumbra remained intact and the centre became a cystic cavity.

A previous study evaluated a traumatic balloon catheter lesion at one week post-injury (Martin et al., 1992). The epicentre was inhabited by lipid laden 'foamy' astrocytes, and subsequently a fibrogliotic (GFAP positive) scar tissue formed. This is in keeping with reviews of spinal cord injury pathology and further animal models which identify that the primary damage causes haemorrhage and gross tissue loss, then between two days and two weeks post-injury macrophage infiltration, initiation of glial scar formation, and oligodendrocyte apoptosis are observed (Kim et al., 2004; Rowland et al., 2008; Almad et al., 2011; Kubota et al., 2011; Lee et al., 2012; Long et al., 2013; Wanner et al., 2013; Anwar et al., 2016; Kjell and Olson, 2016; Alizadeh et al., 2019). In the NTSCI balloon catheter study described herein, these findings were not replicated. A greater proportion of spinal cord parenchyma was retained in this model of NTSCI than comparative TSCI lesions in the model developmement chapter. Overall, this indicates that the lesion induced by the injection port/balloon catheter system is distinct from TSCI, and instead represented an NTSCI phenotype.

The shape of the spinal cord allowed elucidation of the direction of the injury. In spite of attempting to induce a ventral lesion, the injury epicentre itself appeared to have a lateral lesion. This was a limitation of the method, since ventral lesions are more clinically relevant in NTSCI (Watson et al., 2009; Ferrara, 2012; Tetreault et al., 2015; Martin et al.,

2018). However, there is a balance to be made between how invasive the method is, relative to the directionality. This balloon catheter method, although it did not induce a fully ventral lesion, was minimally invasive and required only a partial laminectomy at T10, leaving the injury region closed (vertebral level T7/8).

Mechanical injury mechanics affect outcomes in TSCI and NTSCI

These differences between TSCI and NTSCI functional and pathological outcomes were likely to be due to the differences in injury velocity and timeframes. The spinal cord is viscoelastic; therefore the load exerted onto the cord and cells within are dependent on strain rate (Dogliotti and Yelland, 1964; Hussein, 2018). For example, using a porcine spinal cord in transverse compression, an increase in strain rate from 0.5 s^{-1} to 50 s^{-1} resulted in an increase in elastic modulus of 170%, reflecting the viscoelastic nature of the spinal cord (Fradet et al., 2016). In adult rat samples *ex-vivo*, under uniaxial tension, for any given strain, the stress was greater at higher strain rates (Clarke et al., 2009). Therefore, at low strain rates in NTSCI, the spinal cord is more easily deformed, and less load is imparted onto the system and cells within. Histologically this meant in NTSCI the spinal cord appears deformed and compressed with a changed shape, as opposed to gross tissue damage in TSCI (section 7.1.3.1). The resulting lower stress on the cells meant neurones and tracts remained intact, allowing functional recovery. The paralysis observed at 3 days post NTSCI therefore was likely to be due to other factors, such as vascular ischaemia, as opposed to direct neuronal damage due to compression.

Immunohistochemistry after NTSCI

Immunohistochemical staining for RECA-1 allowed assessment of the vasculature after NTSCI. At the severe injury epicentre, it was observed that the mean area of each blood vessel was less than in intact regions and other injury groups. This indicated a narrowing of vessels; which was hypothesised to be core to the pathology of NTSCI (Karadimas et al., 2013; Long et al., 2014). For example, in a study using an expanding polymer to model NTSCI, ischaemia was identified at the injury epicentre through a

reduction in fluorescence, via injection of fluorescent microspheres into the bloodstream before perfusion (Kurokawa et al., 2011). The findings of this chapter, alongside the wider research, therefore suggest ischaemia and vessel narrowing is important in the pathogenesis of NTSCI.

There are few studies which have undertaken immunohistochemistry after NTSCI to elucidate injury mechanisms. This study aimed to assess changes to GFAP (astrocytes) and MBP (myelin) expression. There was a moderate increase in GFAP expression at the epicentre of severe lesions, compared to intact rostral and caudal regions and mild and sham injury groups. This finding was not statistically significant due to the low number of repeats in the severe injury group, but warrants further investigation. Increased GFAP expression, astrogliosis, and subsequent glial scar formation are the established pathology of TSCI, but minimal studies have evaluated these outcomes in NTSCI (Cullen et al., 2007; Klironomos et al., 2011; Kawano et al., 2012; Shunmugavel et al., 2013; Wanner et al., 2013; Weightman et al., 2014). This finding was also observed where the balloon catheter lesion was used in a TSCI context (Chapter 5, *in-vivo* model development). For *in-vitro* studies, using a simplified reductionist approach to evaluate the effects of mechanical impacts on astrocytes alone, an increase in GFAP staining was observed at high velocity but not low velocity impacts. From these chapters, pathological mechanisms in NTSCI can be elucidated. In TSCI, GFAP reactivity is stimulated, in part, by direct compression of the astrocytes at high velocity. However, in NTSCI, this is not the case. The moderate astrogliotic response observed *in-vivo* was therefore likely to be due to the presence of other factors and systems. Together, the *in-vitro* and *in-vivo* results added strength to the hypothesis that local changes to the vasculature, and concurrent ischaemia, are important in the pathology of NTSCI.

There were no observable differences in myelin expression (MBP staining) in the sham group at epicentre, rostral and caudal regions. In the mild group there was a slight reduction in staining at the injury epicentre, and this effect was greater in the severe group. It is worth noting that this difference was normalised to the overall tissue area

and hence does not represent a loss of white matter tissue. Demyelination is frequently reported in studies of NTSCI, whether the injury is caused by implanting an expanding material, using a line to compress the spinal cord, or using a screw method (Baptiste and Fehlings, 2006; Kubota et al., 2011; Shunmugavel et al., 2013; Dolan et al., 2016; Sun et al., 2016). In clinical cases, apoptosis of oligodendrocytes has been observed (Yamaura et al., 2002; Newcombe et al., 2015). A mouse model of chronic cervical spondylosis, through ossification of the posterior longitudinal ligament, identified a correlation between oligodendrocyte apoptosis and the magnitude of cord compression, as seen in this research (Uchida et al., 2002). Oligodendrocytes are the myelinating cells within the CNS, and their apoptosis results in demyelination. This demyelination impacts neuronal electrical transmission and signalling, and therefore functional and sensory disturbances. It is yet to be established whether this is due to direct mechanical compression of the oligodendrocytes; or due to ischaemia in NTSCI.

7.1.4 Study limitations and future work

Overall, *in-vitro* and *in-vivo* models of NTSCI have been developed. The major limitation of the *in-vivo* study was the low N numbers in each group, which meant statistical significance was not obtained. In spite of this, the model of NTSCI was validated in chapter 6: outcomes of NTSCI *in-vivo*. An observable functional and histological deficit was achieved, with the lesion histopathology being distinct from that of TSCI in the *in-vivo* NTSCI model development chapter (chapter 5). The findings of chapter 6, together with chapter 4 (responses of neural cells to varying mechanical inputs) provide an understanding of the cell types involved in the pathology of NTSCI. This is important to direct future work in these experimental models, in order to better understand the whole pathological cascade in NTSCI.

In both *in-vitro* and *in-vivo* studies, physiological changes observed in NTSCI were distinct from those in TSCI. For NTSCI, the differences observed *in-vitro* were minimal, whereas those *in-vivo* were more marked and diverse. The outcomes of the *in-vivo* model

may provide direction for future work *in-vitro*.

As previously described, the main limitations of the *in-vivo* study described herein were the low N number, and variation observed between groups. Therefore, the primary focus of future work *in-vivo* should be to increase the number of animals, and develop a system to better control or characterise inflation. This should be undertaken in injury and sham groups, and also additional laminectomy only and healthy intact controls. This would allow greater understanding of the damage induced by insertion of the catheter, compared to the laminectomy itself, and therefore increased understanding of the injury paradigm. It would also be of interest to incoporate further timepoints into future studies, for example terminating animals immediately after each inflation to characterise the effects of each inflation itself on spinal cord histopathology, as well as the overall injury and recovery.

One potential reason for the difference between mild and severe injury groups, as previously described, was a lack of precision in injecting injury volume. To better control or characterise inflation, injection systems could be used including microprocessor controlled injectors such as a Nanolitre device, or a sampling device such as used by Vanicky et al. (2001). Further, use of devices such as these should prevent backflow into the device, and therefore minimise the loss of volume and pressure observed for each injection. This should be characterised *in-vitro* before use *in-vivo*. Evaluation of the balloon *in-situ* within the vertebral column could be carried out by inflating the balloon with a radio-opaque agent and undergoing imaging experiments at various timepoints. This would allow assessment of balloon inflation during the experiment.

Once the findings of the model *in-vivo* are well established, these can be used to direct the *in-vitro* model, and understand the contribution of specific cell populations and input factors (e.g. mechanical compression or ischaemia). For example, if the demyelination observed herein is reproduced on a larger scale and number of animals, oligodendrocytes should be evaluated in the *in-vitro* model. The benefits of *in-vitro* modelling are the direct control of cellular and environmental factors. This means

individual cell populations can be evaluated in isolation, and the effects of ischaemia (low oxygen, high carbon dioxide) and mechanical compression compared both in combination and separately

Further, *in-vitro* models can elucidate the mechanisms of injury in terms of the neurovascular unit. Tissue engineered neurovascular units are currently under development, with 3D models created using a combination of biomaterials, bioprinting and microfluidic channels (Kim et al., 2015; Uwamori et al., 2017; Potjewyd et al., 2018). It remains to be determined if mechanical insults could be applied using the BOSE 5110 Electroforce or other devices.

There are, of course, a wide range of other markers which could be evaluated in the *in-vivo* model: including electrophysiology to assess specific tracts, (Lee et al., 2012; Sun et al., 2016), sensory methods such as the von Frey filament test (Kubota et al., 2011; Sun et al., 2016), and other motor tests such as inclined plane (Martin et al., 1992; Lee et al., 2012). In terms of histological markers, this could incorporate neuronal cell changes using NeuN staining or Nissl (Kim et al., 2004; Lee et al., 2012), along with markers for apoptosis to evaluate specific cell populations (Newcombe et al., 2015).

7.2   Conclusion

Experimental models of NTSCI *in-vitro* and *in-vivo* have been developed:

- *In-vitro* the model comprised a rat astrocyte-seeded collagen I hydrogel, compressed at various velocities in the BOSE 5110 Electroforce apparatus

- *In-vivo*, the model consisted of a 2F Fogarty balloon catheter, which was adapted to connect to an injection port. This was implanted into a rat, with the balloon positioned within the vertebral canal at vertebral level T7/8 (spinal cord level T8/9).

Physiological changes were observed in these models, which differed in TSCI and NTSCI:

- *In-vitro* and *in-vivo*, high velocity TSCI resulted in reactive astrogliosis (increased GFAP expression). *In-vitro*, this was accompanied with inflammation (IL-6 release), and *in-vivo*, this was accompanied with increased CSPG expression. These results are indicative of secondary injury cascades described in the wider literature.

- *In-vitro*, low velocity insults to astrocytes in isolation did not result in any significant changes to reactivity or cytokine release.

- *In-vivo*, the pathology of NTSCI comprised demyelination and narrowing of vessels. Statistical significance was not established due to the low N Numbers

- Further work should be undertaken to evaluate these phenomena in greater detail, as well as develop further complexities within the models to evaluate the pathology of NTSCI.

Appendices

A Consumable materials

Materials used herein are described below (Table 1).

*Table 1: **Consumable materials including plasticware used in this research***

Material	Cat No.	Supplier
Autoclave tape	GS849	Appleton Woods, UK
Balloon catheter, 2F	120602F	Edwards Lifesciences, UK
Bijou 5 mL	SLS7522	Scientific Laboratory Supplies Ltd, UK
Blue 25cm barrel roll, 2ply	12754296	Thermo-Fisher Scientific, UK
Bone wax	1130563	Henry Schein, UK
Cannula (Sentrawin 22G)	LOCAA/ 1103/ 22/P/50	VWR International, UK
Cell scraper (18mm length, 260mm handle)	11597692	Thermo-Fisher Scientific, UK
Cotton buds	-	Boots, UK
Coverslips - 22x22 mm	MIC3114	Scientific Laboratory Supplies Ltd, UK
Coverslips - 22x64 mm	MIC3228	Scientific Laboratory Supplies Ltd, UK
Cryomolds (extra large)	11356810	Thermo-Fisher Scientific, UK
Cryomolds (large)	12542696	Thermo-Fisher Scientific, UK
Cryomolds (medium)	12559036	Thermo-Fisher Scientific, UK
Cryovials 2 mL	72.380.992	Sarstedt, UK
Disposable plastic syringe 10mL	S5-10ES	Terumo, UK
Disposable plastic syringe 1mL	GS572	Appleton Woods, UK

Consumable materials including plasticware used in this research continued.

Material	Cat No.	Supplier
Disposable plastic syringe 2mL	SYR2	Greiner Bio-one Ltd
Disposable plastic syringe 5mL	SYR6204	Scientific Laboratory Supplies Ltd, UK
Disposable scalpel (21)	INS4765	Scientific Laboratory Supplies Ltd, UK
Eppendorfs 1.5 mL	72.690	Sarstedt, UK
Falcon tubes 15 mL	352095	Thermo-Fisher Scientific, UK
Falcon tubes 50 mL	14-959-49A	Thermo-Fisher Scientific, UK
Gauze (7.5 x 7.5 cm)	9003308	Henry Schein, UK
Glass Duran Bottle (500mL, 1L, 2L)	Various	Thermo-Fisher Scientific, UK
Incontinence pads	-	Amazon, UK
Isathal	Vm 24883/4003	Henry Schein, UK
Lubrithal	LELUB01	Henry Schein, UK
Masking tape	-	Wilko, UK
Microtome blades S35	3808310E	Leica Biosystems, Germany
Needles, 21G	SYR6108	Scientific Laboratory Supplies Ltd, UK
Needles, 23G	SYR6112	Scientific Laboratory Supplies Ltd, UK
Needles, 26G	SYR6250	Scientific Laboratory Supplies Ltd, UK
Needles, 30G	SYR6124	Scientific Laboratory Supplies Ltd, UK
Nitrile gloves	62 5122	Shield Scientific, UK
Optiplate ^{TM}	6005290	PerkinElmer, UK
Osmotic pump filling tubes	0007988	Charles River, UK
Osmotic pumps (Alzet)	1002	Charles River, UK
Parafilm	SEL-400-030P	Scientific Laboratory Supplies Ltd, UK
Pasteur pipette	612-1681	VWR International, UK
Petri dishes, 60mm diameter	CLS430166	Sigma-Aldrich, UK
Prolene suture	ETW8710	Henry Schein, UK
Silicone 3140 (Dow Corning)	2399677	RS Components Ltd, UK
Silicone tubing	007750	Charles River, UK
Slides - Themofrost Plus	10149870	Thermo-Fisher Scientific, UK
Spongostan	JJ-005	Henry Schein, UK
Standard pipette tips (20, 200, 1000 microlitres)	Various	Starlab, UK

Consumable materials including plasticware used in this research continued.

Material	Cat No.	Supplier
Sterile pot (60mL, 150mL, 250mL)	Various	Scientific Laboratory Supplies Ltd, UK
Surgical drapes (60 x 90 cm)	WDDRA60	Henry Schein, UK
Surgical masks	9882161	Henry Schein, UK
Sylgard 170	2785010	Onecall Farnell, UK
Syringe filter (0.22 micrometre pore size)	10268401	Merck Millipore, UK
Syringes (various sizes)	Various	Greiner Bio-one, UK
Tissue culture dish (60 x 10 mm)	CLS430166	Sigma-Aldrich, UK
Tissue culture flask 75 mL (T75)	TKT-130-210-T	Thermo-Fisher Scientific, UK
Universal tubes 30 mL	CON9000	Scientific Laboratory Supplies Ltd, UK
Universal tubes 30 mL	ARVET69	Henry Schein, UK
Vetcal	MPCAL01	Henry Schein, UK
Vicryl suture (resorbable)	ETW9105	Henry Schein, UK
Weighing boat	Various	Scientific Laboratory Supplies Ltd, UK
Well plate, 24 well, Nunclon delta coated	150628	Thermo-Fisher Scientific, UK
Well plate, 48 well, Nunclon delta coated	150687	Thermo-Fisher Scientific, UK
Well plate, 96 well, Nunclon delta coated	161093	Thermo-Fisher Scientific, UK
Wide-bore pipette tips (1000 microlitres)	Z709999-960EA	Scientific Laboratory Supplies Ltd, UK

B   Equipment

Equipment used in this research are listed below (Table 2).

*Table 2: **Equipment used in this research***

Equipment	Model/Product No.	Supplier
Animal transport boxes	-	University of Leeds, UK
Autoclave	-	Priorclave, UK
Automatic pipettes	Various (2, 20, 200, 1000 μL	Scientific Laboratory Supplies Ltd, UK
Automatic plate washer	Wellwash	Thermo-Fisher Scientific, UK
Balances	GR200 GX2000	A&D, Jensons PLC, UK
BOSE Biodynamic	Electroforce 5110	TA Instruments, USA
Centrifuge	Harrier 15/80	Sanyo Biomedical, Japan
Chameleon plate reader	-	Hidex, Finland
Class II Laminar Flow Cabinet	HERA safe	Thermo-Fisher Scientific, UK
Confocal microscope	LSM880 Axio Imager Z2	Carl Zeiss AG, UK
Cryostat	CM1850	Leica Biosystems, UK
Dissection microscope	47 50 52	Carl Zeiss AG, UK
Eppendorf Centrifuge	5415R	Hyland Scientific, USA
Excel software	2013	Microsoft, UK
Fiji Is Just Image J (FIJI) software	-	Open source (online)
Forceps, Addisons	11028-15	Interfocus, UK, UK
Forceps, locking	12010	Interfocus, UK, UK
Forceps, Rat tooth	12710926	Thermo-Fisher Scientific, UK
Freezer (-20 ºC)	-	Jencons Plc, UK
Freezer (-80 ºC)	-	Sanyo Biomedical, Japan
Fridge (+4 ºC)	-	Jencons Plc, UK
Fume cupboard	-	Whiteley fume extraction solutions, UK
Glass beaker	Various	Thermo-Fisher Scientific, UK
Graticule	01B21202	Pyser Optics, UK
Haemocytometer Neubauer	717805	Sigma-Aldrich, UK
Haemostat	14109	VWR International, UK
Hamilton Syringe (10 μL)	20976	VWR International, UK
Hamilton Syringe (50 μL)	80920	VWR International, UK

Equipment used in this research

Material	Model/Product No.	Manufacturer
Hollow punch set	TL17196	Onecall Farnell, UK
Image J software	-	ImageJ (online)
Incubator	inCu safe	Sanyo Biomedical, Japan
Light microscope	CK40-SLP	Olympus, UK
Light microscope	Axio Imager M2	Carl Zeiss AG, UK
Light source	CLD-01	Optika, Italy
Liquid Nitrogen Dewar	BIO65	Jencons Plc, UK
Magnetic Stirrer	GyroStir 280H	SciQuip, UK
Magnetic Stirrer Bar	Various	Scientific Laboratory Supplies Ltd, UK
Nail brush	-	Wilko, UK
Orbital Shaker	PSU 10i	Grant-bio, UK
Peristaltic pump (Masterflex)	WZ-77921-75	Cole-Parmer Instrument Co Ltd, UK
Permanent marker	-	Wilko, UK
pH meter	Jenway 3510	VWR International, UK
Pipette boy	Integra acu	Integra Bioscience, UK
Plate reader	Multiskan Go	Thermo-Fisher Scientific, UK
Razor blades; single edge	233-0156	VWR International, UK
Retractor	17003-03	Interfocus, UK
Rongeur clippers	16121-14	Interfocus, UK
Scissors, Curved Dissecting, 10 cm	14394	World Precision Instruments, UK
Scissors, Curved Iris 4.5 inches	501759	World Precision Instruments, UK
Scissors, Curved Spring, 10.5 cm	14127	World Precision Instruments, UK
Scissors, straight, blunt 14 cm	501219	World Precision Instruments, UK
Scissors, straight, blunt 16 cm	501224	World Precision Instruments, UK
Scissors, straight, sharp 7.5 cm	503669	World Precision Instruments, UK
Scissors, straight, sharp 9 cm	14070-09	Interfocus, UK
Spatula	231-1059	VWR International, UK
Stainless steel bowls	Various	Wilko, UK
Tea towel	-	Wilko, UK
Test tube rack	-	Scientific Laboratory Supplies Ltd, UK
Tweezers, extra fine point	T147	TAAB, UK

Equipment used in this research

Material	Model/Product No.	Manufacturer
Watchmaker forceps, 4	232-0202	VWR International, UK
Watchmaker forceps, 55	14099	World Precision Instruments, UK
Water Bath	JBA5	Grant Instruments Ltd, UK
Xtreme CT	-	ScanCo Medical, Switzerland

C Reagents

Chemical reagents used are listed below (Table 3).

*Table 3: **Chemical Reagents, Storage Conditions and Suppliers***

Chemical/Reagent	Storage (°C)	Cat No.	Supplier
10X Minimum Essential Media	4	60-91-810	First Link, UK
Acetone	Room temperature	LS8/1970/G	Genta Medical, UK
ATPlite 1000 assay kit	4	6016941	Perkin-Elmer, UK
Baytril	Room temperature	BABAY49	Henry Schein, UK
Bovine serum albumin (BSA)	4	A7030	Sigma-Aldrich, UK
Chondroitin sulfate proteoglycan Antibody (CS-56)	-20	C8035	Sigma-Aldrich, UK
Deoxyribonuclease (Dnase)	-20	D5025	Sigma-Aldrich, UK
Dimethyl sulfoxide	Room temperature	D26650	Sigma-Aldrich, UK
DPX mountant	Room temperature	RRSP29	Atom Scientific, UK
Dulbecco's modified Eagle's medium (DMEM)	4	11594416	Lonza Biological, UK
Endothelial Cells Antibody (RECA-1)	4	MA140240	Thermo-Fisher Scientific, UK
Eosin	Room temperature	1.09844.1000	Merck Millipore, UK
Ethanol (100% v/v)	Room temperature	E/055DF/25	Thermo-Fisher Scientific, UK
Foetal bovine serum (FBS)	-20	E/0650DF/25	Thermo-Fisher Scientific, UK
GFAP primary antibody	4	Z0334	DAKO, UK
Goat anti-mouse IgG Alexa Fluor 647	4	A21236	Thermo-Fisher Scientific, UK
Goat anti-mouse IgM Alexa Fluor 568	-20	A21043	Thermo-Fisher Scientific, UK
Goat anti-rabbit IgG Dylight 488	4	DI-1488	Vector Laboratories, UK

Chemical Reagents, Storage Conditions and Suppliers continued.

Chemical/Reagent	Storage (°C)	Cat No.	Supplier
Haematoxylin (Mayer's)	Room temperature	RRSP60	Atom Scientific, UK
Ham's F-12	4	N4888	Sigma-Aldrich, UK
Hanks Balanced Salt Solution (HBSS)	Room temperature	H9269	Sigma-Aldrich, UK
Hanks Balanced Salt Solution (without Calcium or Magnesium; HBSS modified)	Room temperature	H9394	Sigma-Aldrich, UK
HEPES buffer	Room temperature	LZBE17-737E	Scientific Laboratory Supplies Ltd, UK
Hoechst 33258	-20	16756	Cambridge Bioscience, UK
Horse serum	-20	H1270	Sigma-Aldrich, UK
Hydrochloric acid (6M)	Room temperature	2611.5	VWR International, UK
Isoflurane	Room temperature	1182097	Henry Schein, UK
L-glutamine	-20	G7513	Sigma-Aldrich, UK
LIVE/DEAD Viability/Cytotoxicity Kit, for mammalian cells	-20	L3224	Thermo-Fisher Scientific, UK
Marvel milk powder	Room temperature	-	Premier Foods, UK
Methanol	Room temperature	428	Genta Medical, UK
Myelin Basic Protein Antibody (MBP)	4	ab40390	Abcam, UK
Neutralising solution	4	A-0054	Tap Biosystems (now Sartorium Stedim Biotech), UK
Normal goat serum	4	OASB01365	Generon, UK
Optimum cutting temperature (OCT)	Room temperature	361063E	VWR International, UK
Paraformaldehyde (PFA) powder	Room temperature	P6148	Sigma-Aldrich, UK
Paraformaldehyde (PFA) solution	-20	AR1068	Insight biotechnology, UK
Penicillin/streptomycin	-20	P4458	Sigma-Aldrich, UK

Chemical Reagents, Storage Conditions and Suppliers continued.

Chemical/Reagent	Storage (°C)	Cat No.	Supplier
Pentoject (pentobarbitone 200 mg.mL^{-1})	Room temperature		Henry Schein, UK
Phosphate buffered saline (PBS) tablets	Room temperature	10209252	Thermo-Fisher Scientific, UK
Phosphate buffered saline (PBS) without calcium and magnesium	Room temperature	D8537	Sigma-Aldrich, UK
Poly-D-Lysine	-20	P7886	Sigma-Aldrich, UK
Rat IL-10 ELISA Kit	4	CRE0007-096	Generon, UK
Rat IL-6 ELISA Kit	4	CRE0005-096	Generon, UK
Rat tail collagen	4	60-30-810	First Link, UK
Saline	Room temperature	VDAQU02	Aqupharm, UK
Scott's tap water substitute 10X	Room temperature	RRSP190	Atom Scientific, UK
Sodium azide	Room temperature	786-299	VWR International, UK
Sodium chloride	Room temperature	42429-5000	Thermo-Fisher Scientific, UK
Sodium phosphate monobasic	Room temperature	10667823	Thermo-Fisher Scientific, UK
Soybean trypsin inhibitor (SBTI)	4	T6522	Sigma-Aldrich, UK
Sucrose	Room temperature	S9378	Sigma-Aldrich, UK
TGF-beta 1	-20	GFH39-5	Cell Guidance Systems, UK
Trigene	Room temperature	TRI1322	Scientific Laboratory Supplies Ltd, UK
Tris	Room temperature	B2005	Sigma-Aldrich, UK
Triton X-100	Room temperature	X100	Sigma-Aldrich, UK
Trizma base	Room temperature	T-1503	Sigma-Aldrich, UK
Trypan blue	Room temperature	T8154	Sigma-Aldrich, UK
Trypsin	4	T0303	Sigma-Aldrich, UK
Trypsin/EDTA	-20	T3924	Sigma-Aldrich, UK

Chemical Reagents, Storage Conditions and Suppliers continued.

Chemical/Reagent	Storage (ºC)	Cat No.	Supplier
Tween 20	Room temperature	P1379	Sigma-Aldrich, UK
Vetergesic	Room temperature	VDVET02	Henry Schein, UK
Veterinary iodine solution	Room temperature	IodineV	Hyperdrug.co.uk
Virkon	Room temperature	148-0202	VWR International, UK
Water (sterile)	Room temperature	31-58-589	Leeds Teaching Hospitals, UK
Xylene	Room temperature	GPS1001-G	Atom Scientific, UK

D   FIJI Image Analysis Macros

The general outline of all the FIJI Macros used is import, followed by set scale/threshold/analyse, followed by export. The set scale/threshold/analyse macros used were bespoke for each image type and can be found in the subsections below. The import and export macros were as follows:

IMPORT:

```
dir1 = getDirectory("Choose Source Directory ");
format = getFormat();
dir2 = getDirectory("Choose Destination Directory ");
list = getFileList(dir1);
setBatchMode(true);
for (i=0; i<list.length; i++) {
showProgress(i+1, list.length);
open(dir1+list[i]);
```

EXPORT:

```
if (format=="8-bit TIFF" || format=="GIF")
convertTo8Bit(); saveAs(format, dir2+list[i]);
close(); }

function getFormat() {
formats = newArray("TIFF", "8-bit TIFF", "JPEG",
"GIF", "PNG",
"PGM", "BMP", "FITS", "Text Image", "ZIP", "Raw");
Dialog.create("Batch Convert");
Dialog.addChoice("Convert to: ", formats, "TIFF");
Dialog.show();
return Dialog.getChoice(); }

function convertTo8Bit() {
if (bitDepth==24) run("8-bit Color", "number=256");
else run("8-bit");}}
```

D.1 Macro for GFAP image analysis

The macro below was modified from Smith (2016) and the methods herein. It was used to analyse the total area, count and average size of GFAP-labelled astrocytes in hydrogels.

```
//MACRO written by K Timms 16th December 2016,
automatic GFAP analysis
run("8-bit"); title=getTitle(); run("Set Scale...",
"distance=1.48 known=1 pixel=1 unit=um global");
run("Set Measurements...", "area mean min
shape redirect=None decimal=3");

if (matches(title, ".*Ch1.*")){
run("Auto Local Threshold", "method=Phansalkar
radius=10 parameter_1=0 parameter_2=0 white");
run("Watershed Irregular Features", "erosion=1
convexity_threshold=0 separator_size=7-Infinity");
run("Despeckle"); run("Fill Holes");

run("Select All"); run("Measure");
run("Analyze Particles...", "size=10-infinity
circularity=0.00-1.00 show=Masks display
exclude clear include summarize in_situ");
```

D.2 Transverse Spinal Cord Sections Area

Spinal cords were sectioned in the transverse plane at 40 μm thickness. These were stained with H&E and imaged using brightfield microscopy. The area of tissue on each image was determined using the macro below (adapted from Fedorova and Pavel (2019)):

```
//MACRO written by K Timms April 2019, analyse
cross-sectional area spinal cord tissue after H&E.
run("Set Scale...", "distance=736 known=1 pixel=1
unit=mm global"); run("Despeckle"); run("8-bit");
title=getTitle(); run("Auto Threshold", "method=Huang");

run("Set Measurements...", "area mean min
shape area_fraction limit display
redirect=None decimal=3"); run("Measure");
```

D.3 Image Analysis of Immunofluorescent-labelled Spinal Cord Sections

Spinal cords were sectioned in the transverse plane at 40 μm thickness. These were stained with various immuno-fluorescent markers, including GFAP (488) + CS-56 (568), and MBP (488) + RECA-1. The images were evaluated using the macro below:

```
//MACRO written by K Timms 10th Sept 2019, IHC analysis
sourcetitle=getTitle(); run("Duplicate...", " ");
copy = getImageID(); run("8-bit");
run("Set Scale...", "distance=603 known=1 pixel=1
unit=mm global");
run("Set Measurements...", "area mean min shape
redirect=["+sourcetitle+"] decimal=3");

// select 488, 568, 647 images
if (matches(sourcetitle, ".*568.*")
|| matches(sourcetitle, ".*488.*" )
|| matches(sourcetitle, ".*647.*" )) {

run("Auto Local Threshold", "method=Phansalkar
radius=10 parameter_1=0 parameter_2=0 white");
//reduce background
run("Despeckle"); run("Select All"); run("Measure");
run("Analyze Particles...", "size=0.000-0.001
circularity=0.00-1.00 exclude clear include summarize");
```

E BBB Scale, Open Field Locomotor Score

The scores and associated attributes, and definitions used therein, for the open field locomotor scale (BBB scale) from Basso et al. (1995) are listed below (Table 4).

Definitions:

- **Slight** partial joint movement through less than half the range of joint motion

- **Extensive** movement through more than half of the range of joint motion

- **Sweeping** rhythmic movement of HL in which all three joints are extended, then fully flex and extend again; animal is usually sidelying, the plantar surface of paw may or may not contact the ground; no weight support across the HL is evident

- **No weight support** no contraction of the extensor muscles of the HL during plantar placement of the paw; or no elevation of the hindquarters

- **Weight support** contraction of the extensor muscles of the HL during plantar placement of the paw, or elevation of the hindquarter

- **Plantar stepping** The paw is in *plantar* contact with weight support then the HL is advanced forward and *plantar* contact with weight support is reestablished

- **Dorsal stepping** weight is supported through the dorsal surface of the paw at some point in the step cycle

- **FL-HL coordination** for every FL step an HL step is taken and the HLs alternate

- **Occasional** less than or equal to half of the time; 0-50%

- **Frequent** more than half but not always; 51-94%

- **Consistent** nearly always or always; 95-100%

- **Trunk Instability** lateral weight shifts that cause waddling from side to side or a partial collapse of the trunk

*Table 4: **The 21-point Basso, Beattive, Bresnahan (BBB) locomotor rating scale and operational definitions of categories and attributes.** Details from Basso et al. (1995)*

	Score	Attributes
Hindlimb movement extent and frequency	0	No observable hindlimb (HL) movement
	1	Slight movement of one **or** two joints, usually the hip and/or knee
	2	Extensive movement of one joint **or** extensive movement of one joint *and* slight movement of one other joint
	3	Extensive movement of two joints
	4	Slight movement of all three joints of the HL
	5	Slight movement of two joints *and* extensive movement of the third
	6	Extensive movement of two joints *and* slight movement of the third
	7	Extensive movement of all three joints of the HL
Weight support and co-ordination	8	Sweeping with no weight support **or** plantar placement of the paw with no weight support
	9	Plantar placement of the paw with weight support in stance only (i.e. when stationaru) **or** occasional, frequency, **or** consistent weight supported dorsal stepping and no plantar stepping
	10	Occasional weight supported plantar steps, no forelimb (FL)-HL coordination
	11	Frequent to consistent weight supported plantar steps *and* no FL-HL coordination
	12	Frequent to consistent weight supported plantar steps *and* occasional FL-HL coordination
	13	Frequent to consistent weight supported plantar steps *and* frequent FL-HL coordination
Paw position and toe clearance	14	Consistent weight supported plantar steps, consistent FL-HL cordination; *and* predominant paw position during locomotion is rotated (internally **or** externally) when it makes *initial contact* with the surface as well as just before it is *lifted off* at the end of stance **or** frequent plantar stepping, consistent FL-HL coordination, and occasional dorsal stepping
	15	Consistent plantar stepping and consistent FL-HL coordination, *and* no toe clearance **or** occasional toe clearance during forward limb advancement; predominant paw position is parallel to the body at initial contact
	16	Consistent plantar stepping and consistent FL-HL coordination during gait *and* toe clearance occurs frequently during forward limb advancement; predominant paw position is parallel at initial contact and rotated at lift off

The 21-point Basso, Beattive, Bresnahan (BBB) locomotor rating scale continued.

	Score	Attributes
Paw position and toe clearance	17	Consistent plantar stepping and consistent FL-HL coordination during gait *and* toe clearance occurs frequently during forward limb advancement; predominant paw position is parallel at initial contact *and* lift off
	18	Consistent plantar stepping and consistent FL-HL coordination during gait *and* toe clearance occurs consistently during forward limb advancement; predominant paw position is parallel at initial contact and rotated at lift off
Stability	19	Consistent plantar stepping and consistent FL-HL coordination during gait *and* toe clearance occurs frequently during forward limb advancement; predominant paw position is parallel at initial contact *and* lift off; and tail is down part **or** all of the time
	20	Consistent plantar stepping and consistent FL-HL coordination during gait *and* toe clearance occurs frequently during forward limb advancement; predominant paw position is parallel at initial contact *and* lift off; tail consistently up; trunk instability
	21	Consistent plantar stepping and consistent FL-HL coordination during gait *and* toe clearance occurs frequently during forward limb advancement; predominant paw position is parallel at initial contact *and* lift off; tail consistently up; consistent trunk stability

F Mechanics of Collagen Hydrogel Compression

The table below describes further detail of compression mechanics.

*Table 5: **Mechanical compression data from astrocyte-seeded hydrogel experiments.** Data shown are mean $\pm$ S.E.M., of at least 4 repeats per datapoint. Velocity data is the maximum velocity recorded.*

	Theoretical input velocity (mm.s^{-1})			
Mechanic	0.1	1	10	100
Experimental velocity (mm.s^{-1})	0.28 ± 0.02	1.31 ± 0.1	10.2 ± 0.01	112.11 ± 0.21
Theoretical velocity (mm.s^{-1})	$0.1 \pm 5.21 \times 10^{-4}$	$1.02 \pm 3.33 \times 10^{-4}$	$10.01 \pm 5.44 \times 10^{-3}$	$100.15 \pm 3.86 \times 10^{-3}$
% Difference	-169.01	-28.54	-1.9	-11.94
Displacement (mm)	1.88 ± 0.08	1.98 ± 0.08	1.95 ± 0.02	1.95 ± 0.01
Axial command (mm)	1.88 ± 0.08	1.98 ± 0.08	1.94 ± 0.02	1.95 ± 0.01
% Difference	-0.06	-0.11	-0.24	0.02
Load (N)	0.16 ± 0.02	0.65 ± 0.06	1.45 ± 0.03	1.51 ± 0.1
Work done (mJ)	0.05 ± 0.02	0.26 ± 0.03	0.78 ± 0.1	1.12 ± 0.13

Bibliography

Aarabi, B., Simard, J. M., Kufera, J. A., Alexander, M., Zacherl, K. M., Mirvis, S. E., Shanmuganathan, K., Schwartzbauer, G., Maulucci, C. M., Slavin, J., Ali, K., Massetti, J., and Eisenberg, H. M. (2012). Intramedullary lesion expansion on magnetic resonance imaging in patients with motor complete cervical spinal cord injury. *Journal of Neurosurgery Spine*, 17(3):243–250.

Abu-Rub, M., McMahon, S., Zeugolis, D. I., Windebank, A., and Pandit, A. (2010). Spinal cord injury in vitro: modelling axon growth inhibition. *Drug Discovery Today*, 15(11-12):436–43.

Agrawal, G., Kerr, C., Thakor, N. V., and All, A. H. (2010). Characterization of graded multicenter animal spinal cord injury study contusion spinal cord injury using somatosensory-evoked potentials. *Spine*, 35(11):1122–1127.

Ahadi, R., Khodagholi, F., Daneshi, A., Vafaei, A., Mafi, A. A., and Jorjani, M. (2015). Diagnostic value of serum levels of GFAP, pNF-H, and NSE compared with clinical findings in severy assessment of human traumatic spinal cord injury. *Spine*, 40(14):E823–830.

Ahearne, M., Wilson, S. L., Liu, K. K., Rauz, S., El Haj, A. J., and Yang, Y. (2010). Influence of cell and collagen concentration on the cell-matrix mechanical relationship in a corneal stroma wound healing model. *Experimental Eye Research*, 91(5):584–591.

Ahmed, E. M. (2015). Hydrogel: Preparation, characterization, and applications: A review. *Journal of Advanced Research*, 6(2):105–121.

Alafifi, T., Kern, R., and Fehlings, M. (2007). Clinical and MRI predictors of outcome after surgical intervention for cervical spondylotic myelopathy. *Journal of Neuroimaging*, 17(4):315–22.

Alizadeh, A., Dyck, S., and S., K.-A. (2019). Traumatic spinal cord injury: An overview of pathophysiology, models and acute injury mechanisms. *Frontiers in Neurology*, 10:282.

Almad, A., Sahinkaya, F. R., and McTigue, D. M. (2011). Oligodendrocyte fate after spinal cord injury. *Neurotherapeutics*, 8(2):262–73.

Anderson, M. A., Burda, J. E., Ren, Y., Ao, Y., O'Shea, T. M., Kawaguchi, R., Coppola, G., Khakh, B. S., Deming, T. J., and Sofroniew, M. V. (2016). Astrocyte scar formation aids central nervous system axon regeneration. *Nature*, 532(7598):195–200.

Anderson, T. E. (1982). A controlled pneumatic technique for experimental spinal cord contusion. *Journal of Neuroscience Methods*, 6(4):327 – 333.

Anderson, T. E. (1985). Spinal cord contusion injury: experimental dissociation of hemorrhagic necrosis and subacute loss of axonal conduction. *Journal of Neurosurgery.*, 62(1):115–119.

Andreollo, N. A., Santos, E. F., Araujo, M. R., and Lopes, L. R. (2012). Rat's age versus human's age: what is the relationship? *ABCD = Brazilian Archives of Digestive Surgery*, 25(1):49–51.

Andriakopoulou, C. (2016). *Preparation and Mechanical Characterisation of Self-Compressed Collagen Gels*. PhD thesis, Delft University of Technology.

Antoine, E. E., Vlachos, P. P., and Rylander, M. N. (2014). Review of collagen I hydrogels for bioengineered tissue microenvironments: characterization of mechanics, structure, and transport. *Tissue Engineering: Part B, Reviews*, 20(6):683–696.

Antoine, E. E., Vlachos, P. P., and Rylander, M. N. (2015). Tunable collagen I hydrogels for engineered physiological tissue micro-environments. *PLoS ONE*, 10(3):e0122500.

Anwar, M. A., Al Shehabi, T. S., and Eid, A. H. (2016). Inflammogenesis of secondary spinal cord injury. *Frontiers in Cellular Neuroscience*, 10:98.

Ataoglu, E., Tiftik, T., Kara, M., Tunc, H., Ersoz, M., and Akkus, S. (2013). Effects of chronic pain on quality of life and depression in patients with spinal cord injury. *Spinal Cord*, 51(1):23–6.

Avril, S., Badel, P., Gabr, M., Sutton, M. A., and Lessner, S. M. (2013). Biomechanics of porcine renal arteries and role of axial stretch. *Journal of Biomechanical Engineering*, 135(8):0810071–08100710.

Ballermann, M. and Fouad, K. (2006). Spontaneous locomotor recovery in spinal cord injured rats is accompanied by anatomical plasticity of reticulospinal fibers. *European Journal of Neuroscience*, 23(8):1988–1996.

Banerjee, P., Lenz, D., Robinson, J. P., Rickus, J. L., and Bhunia, A. K. (2008). A novel and simple cell-based detection system with a collagen-encapsulated B-lymphocyte cell line as a biosensor for rapid detection of pathogens and toxins. *Laboratory Investigations*, 88(2):196–206.

Banks, J. M., Mozdzen, L. C., Harley, B. A. C., and Bailey, R. C. (2014). The combined effects of matrix stiffness and growth factor immobilization on the bioactivity and differentiation capabilities of adipose-derived stem cells. *Biomaterials*, 35(32):8951–8959.

Baptiste, D. C. and Fehlings, M. G. (2006). Pathophysiology of cervical myelopathy. *The Spine Journal*, 6(6 Suppl):190S–197S.

Bar-Kochba, E., Scimone, M. T., Estrada, J. B., and Franck, C. (2016). Strain and rate-dependent neuronal injury in a 3D in vitro compression model of traumatic brain injury. *Scientific Reports*, 6:30550.

Barthelat, F., Zavattieri, P., Korach, C. S., Prorok, B., and Grande-Allen, K. (2014). *Mechanics of Biological Systems and Materials, Volume 4: Proceedings of the 2013 Annual Conference on Experimental and Applied Mechanics*. Springer International Publishing.

Bartlett, R. D., Choi, D., and Phillips, J. B. (2016a). Biomechanical properties of the spinal cord: implications for tissue engineering and clinical translation. *Regenerative Medicine*, 11(7):659–73.

Bartlett, R. D., Choi, D., and Phillips, J. B. (2016b). A novel protocol to characterise the mechanical properties of spinal cord tissue and benchmark candidate biomaterials for CNS tissue-engineering. *European Cells and Materials*, 31(1):8.

Baschek, G., Hartwig, G., and Zahradnik, F. (1999). Effect of water absorption in polymers at low and high temperatures. *Polymer*, 40(12):3433–3441.

Basso, D. M., Beattie, M. S., and Bresnahan, J. C. (1995). A sensitive and reliable locomotor rating scale for open field testing in rats. *Journal of Neurotrauma*, 12(1):1–21.

Basso, D. M., Beattie, M. S., and Bresnahan, J. C. (1996). Graded histological and locomotor outcomes after spinal cord contusion using the NYU weight-drop device versus transection. *Experimental Neurology*, 139(2):244–256.

Beattie, M. S. and Manley, G. T. (2011). Tight squeeze, slow burn: inflammation and the aetiology of cervical myelopathy. *Brain*, 132(Pt 5):1259–1261.

Behrmann, D. L., Bresnahan, J. C., Beattie, M. S., and Shah, B. R. (1992). Spinal cord injury produced by consistent mechanical displacement of the cord in rats: behavioral and histologic analysis. *Journal of Neurotrauma*, 9(3):197–217.

Bernabeu-Sanz, A., Molla-Torro, J. V., Lopez-Celada, S., Moreno Lopez, P., and Fernandez-Jover, E. (2019). MRI evidence of brain atrophy, white matter damage, and functional adaptive changes in patients with cervical spondylosis and prolonged spinal cord compression. *European Radiology*.

Bilston, L. E., Clarke, E. C., and Brown, J. (2011). Spinal injury in car crashes: crash factors and the effects of occupant age. *Injury Prevention*, 17(4):228–232.

Bilston, L. E. and Thibault, L. E. (1996). The mechanical properties of the human cervical spinal cord in vitro. *Annals of Biomedical Engineering*, 24(1):67–74.

Black, P., Markowitz, R. S., Damjanov, I., Finkelstein, S. D., Kushner, H., Gillespie, J., and Feldman, M. (1988). Models of spinal cord injury: Part 3. Dynamic load technique. *Neurosurgery*, 22(1 Pt 1):51–60.

Boden, S. D., Davis, D. O., Dina, T. S., Patronas, N. J., and Wiesel, S. W. (1990a). Abnormal magnetic-resonance scans of the lumbar spine in asymptomatic subjects. a prospective investigation. *Journal of Bone and Joint Surgery: American volume*, 72(3):403–8.

Boden, S. D., McCowin, P. R., Davis, D. O., Dina, T. S., Mark, A. S., and Wiesel, S. (1990b). Abnormal magnetic-resonance scans of the cervical spine in asymptomatic subjects. A prospective investigation. *Journal of Bone and Joint Surgery: American volume*, 72(8):1178–1184.

Bonnici, B. and Kapfhammer, J. P. (2008). Spontaneous regeneration of intrinsic spinal cord axons in a novel spinal cord slice culture model. *European Journal of Neuroscience*, 27(10):2483–2492.

BOSE (2014). BOSE electroforce biodynamic test instruments.

Bradbury, E. J., Moon, L. D., Popat, R. J., King, V. R., Bennett, G. S., Patel, P. N., Fawcett, J. W., and McMahon, S. B. (2002). Chondroitinase ABC promotes functional recovery after spinal cord injury. *Nature*, 416(6881):636–640.

Bradke, F., Fawcett, J. W., and Spira, M. E. (2012). Assembly of a new growth cone after axotomy: the precursor to axon regeneration. *Nature Reviews Neuroscience*, 13(3):183–193.

Bresnahan, J. C., Beattie, M. S., Stokes, B. T., and Conway, K. M. (1991). Three-dimensional computer-assisted analysis of graded contusion lesions in the spinal cord of the rat. *Journal of Neurotrauma*, 8(2):91–101.

Burke, N. N., Fan, C. Y., and Trang, T. (2016). Microglia in health and pain: impact of noxious early life events. *Experimental Physiology*, 101(8):1003–21.

Burmeister, A. R. and Marriott, I. (2018). The interleukin-10 family of cytokines and their role in the CNS. *Frontiers in Cellular Neuroscience*, 12:458.

Burnside, E. R. and Bradbury, E. J. (2014). Manipulating the extracellular matrix and its role in brain and spinal cord plasticity and repair. *Neuropathology and Applied Neurobiology*, 40(1):26–59.

Busby, G. A., Grant, M. H., Mackay, S. P., and Riches, P. E. (2013). Confined compression of collagen hydrogels. *J Biomech*, 46(4):837–840.

Buss, A., Pech, K., Kakulas, B. A., Martin, D., Schoenen, J., Noth, J., and Brook, G. A. (2009). NG2 and phosphacan are present in the astroglial scar after human traumatic spinal cord injury. *BMC Neurology*, 9:32.

Butler, D. L., Hunter, S. A., Chokalingam, K., Cordray, M. J., Shearn, J., Juncosa-Melvin, N., Nirmalanandhan, S., and Jain, A. (2009). Using functional tissue engineering and bioreactors to mechanically stimulate tissue-engineered constructs. *Tissue Engineering. Part A*, 15(4):741–749.

Cai, J., Sheng, K., Sheehan, J. P., Benedict, S. H., Larner, J. M., and Read, P. W. (2007). Evaluation of thoracic spinal cord motion using dynamic MRI. *Radiotherapy and Oncology*, 84(3):279–82.

Caliari, S. R. and Burdick, J. A. (2016). A practical guide to hydrogels for cell culture. *Nature Methods*, 13(5):405–414.

Cargill, R. S. and Thibault, L. E. (1996). Acute alterations in [Ca2+]i in NG108-15 cells subjected to high strain rate deformation and chemical hypoxia: an in vitro model for neural trauma. *Journal of Neurotrauma*, 13(7):395–407.

Carpanese, E., Moretto, P., Filpa, V., Marchet, S., Moro, E., Crema, F., Frigo, G., and Giaroni, C. (2014). Antagonism of ionotropic glutamate receptors attenuates chemical ischemia-induced injury in rat primary cultured myenteric ganglia. *PLoS One*, 9(11).

Chang, G. L., Hung, T. K., Bleyaert, A., and Jannetta, P. J. (1981). Stress-strain measurement of the spinal cord of puppies and their neurological evaluation. *The Journal of Trauma*, 21(9):807–810.

Chang, G. L., Hung, T. K., and Feng, W. W. (1988). An in-vivo measurement and analysis of viscoelastic properties of the spinal cord of cats. *Journal of Biomechanical Engineering*, 110(2):115–22.

Cho, H. K., Ahn, S. H., Kim, S. Y., Choi, M. J., Hwang, S. J., and Cho, Y. W. (2015). Changes in the expressions of Iba1 and Calcitonin Gene-Related Peptide in adjacent lumbar spinal segments after lumbar disc herniation in a rat model. *Journal of Korean Medical Science*, 30(12):1902–1910.

Chung, W.-H., Lee, J.-H., Chung, D.-J., Yang, W.-J., Lee, A. J., Choi, C.-B., Chang, H.-S., Kim, D.-H., Chung, H. J., Suh, H. J., Hwang, S.-H., Han, H., Do, S. H., and Kim, H.-Y. (2013). Improved rat spinal cord injury model using spinal cord compression by percutaneous method. *Journal of Veterinary Science*, 14(3):329–335.

Clarke, E. C. (2011). *Neural Tissue Biomechanics*. Springer-Verlag, Berlin.

Clarke, E. C., Cheng, S., and Bilston, L. E. (2009). The mechanical properties of neonatal rat spinal cord in vitro, and comparisons with adult. *Journal of Biomechanics*, 42(10):1397–1402.

Cohen, D. M., Patel, C. B., Ahobila-Vajjula, P., Sundberg, L. M., Chacko, T., Liu, S. J., and Narayana, P. A. (2009). Blood-spinal cord barrier permeability in experimental spinal cord injury: dynamic contrast-enhanced MRI. *NMR in Biomedicine*, 22(3):332–41.

Corning (2008). Surface areas and recommended medium volumes for corning cell culture vessels. Online. Available from: www.corning.com.

Coronado, R., Hudson, B., Sheets, C., Roman, M., Isaacs, R., Mathers, J., and Cook, C. (2009). Correlation of magnetic resonance imaging findings and reported symptoms in patients with chronic cervical dysfunction. *The Journal of Manual & Manipulative Therapy*, 17(3):148–153.

Cosar, S. N., Yemisci, O. U., Oztop, P., Cetin, N., Sarifakioglu, B., Yalbuzdag, S. A., Ustaomer, K., and Karatas, M. (2010). Demographic characteristics after traumatic and non-traumatic spinal cord injury: a retrospective comparison study. *Spinal Cord*, 48(12):862–6.

Crapo, P. M., Medberry, C. J., Reing, J. E., Tottey, S., van der Merwe, Y., Jones, K. E., and Badylak, S. F. (2012). Biologic scaffolds composed of central nervous system extracellular matrix. *Biomaterials*, 33(13):3539–47.

Cullen, D. K. and LaPlaca, M. C. (2006). Neuronal response to high rate shear deformation depends on heterogeneity of the local strain field. *Journal of Neurotrauma*, 23(9):1304–1319.

Cullen, D. K., Simon, C. M., and LaPlaca, M. C. (2007). Strain rate-dependent induction of reactive astrogliosis and cell death in three-dimensional neuronal-astrocytic co-cultures. *Brain Research*, 1158:103–115.

Cullen, D. K., Vernekar, V. N., and LaPlaca, M. C. (2011). Trauma-induced plasmalemma disruptions in three-dimensional neural cultures are dependent on strain modality and rate. *Journal of Neurotrauma*, 28(11):2219–2233.

David, S. and Kroner, A. (2011). Repertoire of microglial and macrophage responses after spinal cord injury. *Nature Reviews Neuroscience*, 12(7):388–399.

de Wit, M., Raabe, A., Tuinmann, G., and Hossfeld, D. (2001). Implantable device for intravenous drug delivery in the rat. *Laboratory Animals*, 35(4):321–234.

Demchenko, A. P. (2008). *Introduction to Fluorescence Sensing*. Springer, Switzerland.

Devlin, V. (2012). *Spine Secrets Plus (Second Edition)*. Elsevier Mosby, Missouri, USA.

Dimar, J. R., Glassman, S. D., Raque, G. H., Zhang, Y. P., and Shields, C. B. (1999). The influence of spinal canal narrowing and timing of decompression on neurologic recovery after spinal cord contusion in a rat model. *Spine (Phila Pa 1976)*, 24(16):1623–33.

Dogliotti, E. and Yelland, W. (1964). Effect of strain rate on the viscoelastic properties of high polymeric fibrous materials. *Journal of Applied Polymer Science*, 8:211–235.

Dohrmann, G. J. and Panjabi, M. M. (1976). Standardized spinal cord trauma: biomechanical parameters and lesion volume. *Surgical Neurology International*, 6(5):263–267.

Dolan, R. T., Butler, J. S., O'Byrne, J. M., and Poynton, A. R. (2016). Mechanical and cellular processes driving cervical myelopathy. *World Journal of Orthopedics*, 7(1):20–29.

Dong, H., Fazzaro, A., Xiang, C., Korsmeyer, S. J., Jacquin, M. F., and McDonald, J. W. (2003). Enhanced oligodendrocyte survival after spinal cord injury in bax-deficient mice and mice with delayed wallerian degeneration. *Journal of Neuroscience*, 23(25):8682–91.

Dong, Y. and Shannon, C. (2000). Heterogeneous immunosensing using antigen and antibody monolayers on gold surfaces with electrochemical and scanning probe detection. *Analytical Chemistry*, 72(11):2371–2376.

Donnay, M., Timoneda, M., and Angel, M. (2013). *Cellular behavior after mechanical stimulation on biofunctionalized polylactic acid nanofibers for tendon tissue engineering*. PhD thesis, Universitat Politecnica de Catalunya.

Donnelly, D. J. and Popovich, P. G. (2008). Inflammation and its role in neuroprotection, axonal regeneration and functional recovery after spinal cord injury. *Experimental Neurology*, 209(2):378–388.

Doppman, J. (1990). The mechanism of ischemia in anteroposterior compression of the spinal cord. *Investigative Radiology*, 25(4):444 – 52.

Du, S., Sun, Y., and Zhao, B. (2018). Interleukin-6 serum levels are elevated in individuals with degenerative cervical myelopathy and are corraleted with symptom severity. *Medical Science Monitor*, 24:7405–7413.

East, E., de Oliveira, D. B., Golding, J. P., and Phillips, J. B. (2010). Alignment of astrocytes increases neuronal growth in three-dimensional collagen gels and is maintained following plastic compression to form a spinal cord repair conduit. *Tissue Engineering. Part A*, 16(10):3173–3184.

East, E., Golding, J. P., and Phillips, J. B. (2009). A versatile 3D culture model facilitates monitoring of astrocytes undergoing reactive gliosis. *Journal of Tissue Engineering and Regenerative Medicine*, 3(8):634–46.

East, E., Golding, J. P., and Phillips, J. B. (2012). Engineering an integrated cellular interface in three-dimensional hydrogel cultures permits monitoring of reciprocal astrocyte and neuronal responses. *Tissue Engingeering. Part C, Methods*, 18(7):526–36.

East, E., Johns, N., Georgiou, M., Golding, J. P., Loughlin, A. J., Kingham, P. J., and Phillips, J. B. (2013). A 3D in vitro model reveals differences in the astrocyte response elicited by potential stem cell therapies for CNS injury. *Regenerative Medicine*, 8(6):10.2217/rme.13.61.

Esposito, E., Paterniti, I., Meli, R., Bramanti, P., and Cuzzocrea, S. (2012). GW0742, a high-affinity PPAR-I agonist, mediates protection in an organotypic model of spinal cord damage. *Spine*, 37(2):E73–78.

Estandarte, A. K. C. (2012). A review of the different staining techniques for human metaphase chromosomes. Master's thesis, University College London.

Fedorova, J. and Pavel, J. (2019). An accurate method for histological determination of neural tissue loss/sparing after compression-induced spinal cord injury with optimal reproducibility. *Journal of Neurotrauma*.

Feng, Y., Clayton, E. H., Chang, Y., Okamoto, R. J., and Bayly, P. V. (2013). Viscoelastic properties of the ferret brain measured in vivo at multiple frequencies by magnetic resonance elastography. *Journal of Biomechanics*, 46(5):863–70.

Fenwick, N., Griffin, G., and Gauthier, C. (2009). The welfare of animals used in science: how the "Three Rs" ethic guides improvements. *The Canadian Veterinary Journal*, 50(5):523–530.

Ferrara, L. A. (2012). The biomechanics of cervical spondylosis. *Advances in Orthopedics*, 2012.

Fettes, P. D., Leslie, K., McNabb, S., and Smith, P. J. (2006). Effect of spinal flexion on the conus medullaris: a case series using magnetic resonance imaging. *Anaesthesia*, 61(6):521–3.

Fiebig, T., Figueiredo, G., Boll, H., Kerl, H. U., Noelte, I. S., Forster, A., Groden, C., Kramer, M., and Brockmann, M. A. (2013). A low cost metal-free vascular access mini-port for artifact free imaging and repeated injections in mice. *PLoS ONE*, 8(6):e65939.

Fiford, R. J. and Bilston, L. E. (2005). The mechanical properties of rat spinal cord in vitro. *Journal of Biomechanics*, 38(7):1509–1515.

Figley, C. R. and Stroman, P. W. (2007). Investigation of human cervical and upper thoracic spinal cord motion: implications for imaging spinal cord structure and function. *Magnetic Resonance Medicine*, 58(1):185–9.

Figueiredo, G., Fiebig, T., Kirschner, S., Nikoubashman, O., Kabelitz, L., Othman, A., Nonn, A., Kramer, M., and Brockmann, M. A. (2015). Minimally invasive monitoring of chronic central venous catheter patency in mice using digital subtraction angiography (DSA). *PLoS ONE*, 10(6):e0130661.

Filli, L., Engmann, A. K., Zorner, B., Weinmann, O., Moraitis, T., Gullo, M., Kasper, H., Schneider, R., and Schwab, M. E. (2014). Bridging the gap: a reticulo-propriospinal detour bypassing an incomplete spinal cord injury. *Journal of Neuroscience*, 34(40):13399–13410.

Fonseca, A. F. D., Scheffer, J. P., Coelho, B. P., Aiello, G., Guimaraes, A. G., Gama, C. R., Vescovini, V., Cabral, P. G., and Oliveira, A. L. (2016). Technique of spinal cord compression induced by inflation of epidural balloon catheter in rabbits (oryctologus cuniculus): efficient and easy to use model. *Anais da Academia Brasileira de Ciencias*, 88:1511–1517.

Fouad, K., Hurd, C., and Magnuson, D. S. (2013). Functional testing in animal models of spinal cord injury: not as straight forward as one would think. *Frontiers in Integrative Neuroscience*, 7:85.

Fournier, A. J., Hogan, J. D., Rajbhandari, L., Shrestha, S., Venkatesan, A., and Ramesh, K. T. (2015). Changes in neurofilament and microtubule distribution following focal axon compression. *PLoS ONE*, 10(6):e0131617.

Fradet, L., Cliche, F., Petit, Y., Mac-Thiong, J. M., and Arnoux, P. J. (2016). Strain rate dependent behavior of the porcine spinal cord under transverse dynamic compression. *Proceedings of the Institution of Mechanical Engineers, Part H*, 230(9):858–860.

Fratini, M., Moraschi, M., Maraviglia, B., and Giove, F. (2014). On the impact of physiological noise in spinal cord functional MRI. *Journal of Magnetic Resonance Imaging*, 40(4):770–777.

Frieboes, L. R. and Gupta, R. (2009). An in-vitro traumatic model to evaluate the response of myelinated cultures to sustained hydrostatic compression injury. *Journal of Neurotrauma*, 26(12):2245–2256.

Fung, Y. (1993). *Biomechanics: Mechanical Properties of Living Tissues*. Springer-Verlag, New York, USA.

Funk, J. R., Cormier, J. M., and Manoogian, S. J. (2012). Comparison of risk factors for cervical spine, head, serious, and fatal injury in rollover crashes. *Accident Analysis and Prevention*, 45:67–74.

Garcia, E. and Stewart, C. M. (2016). Stress corrosion cracking in generic aluminum foil under 3.5% nacl solution. *Proceedings of the ASME 2016 International Mechanical Engineering Congress and Exposition IMECE2016.*

Garcia-Lopez, P., Garcia-Marin, V., and Freire, M. (2010). The histological slides and drawings of Cajal. *Frontiers in Neuroanatomy*, 4:9.

Garcia-Marin, V., Garcia-Lopez, P., Freire, M., and Ramon y Cajal, S. (2007). Cajal's contributions to glia research. *Trends in Neuroscience.*, 30(9):479–487.

Gelderd, J. B. and Chopin, S. F. (1977). The vertebral level of origin of spinal nerves in the rat. *The Anatomical Record.*, 188(1):45–47.

Gensel, J. C. and Zhang, B. (2015). Macrophage activation and its role in repair and pathology after spinal cord injury. *Brain Research*, 1619:1–11.

Gerbig, S. (2014). Polyamide moisture absorption — relative dimensional change of various nylon products. Online. Available from: www.knowledge.ulprospector.com.

Goodfellow (2017). Polymer physical properties. Online. Available from: www.goodfellow.com.

Goossens, D., Dousse, M., Ventura, M., and Fattal, C. (2009). Chronic neuropathic pain in spinal cord injury patients: What is the impact of social and environmental factors on care management? *Annals of Physical and Rehabilitation Medicine*, 52(2):173–179.

Gossman, M. S., Zheng, H., Evans, J. G., Li, J., and Ng, C. K. (2017). Assessment of radiopharmaceutical retention for vascular access ports using positron emission tomography imaging. *ournal of Applied Clinical Medical Physics*, 18(6):244–249.

Gray, H. (1918). *Anatomy of the Human Body*. Lea & Febiger, Philadelphia.

Greenberg, S. A. (2003). The history of dermatome mapping. *Archives of Neurology*, 60(1):126–131.

Grill, R., Murai, K., Blesch, A., Gage, F. H., and Tuszynski, M. H. (1997). Cellular delivery of neurotrophin-3 promotes corticospinal axonal growth and partial functional recovery after spinal cord injury. *Journal of Neuroscience*, 17(14):5560–5572.

Guilcher, S. J., Munce, S. E., Couris, C. M., Fung, K., Craven, B. C., Verrier, M., and Jaglal, S. B. (2010). Health care utilization in non-traumatic and traumatic spinal cord injury: a population-based study. *Spinal Cord*, 48(1):45–50.

Gupta, A., Taly, A. B., Srivastava, A., and Murali, T. (2009). Non-traumatic spinal cord lesions: epidemiology, complications, neurological and functional outcome of rehabilitation. *Spinal Cord*, 47(4):307–11.

Haggerty, A. E., Marlow, M. M., and Oudega, M. (2017). Extracellular matrix components as therapeutics for spinal cord injury. *Neuroscience Letters*, 652:50–55.

Hamimi, A., Kassab, F., and Kazkaz, G. (2015). Osteoporotic or malignant vertebral fracture? this is the question. what can we do about it? *The Egyptian Journal of Radiology and Nuclear Medicine*, 46(1):97–103.

Harms, J. and Tabasso, G. (1999). *Principles of Instrumented Spinal Surgery*. Thieme Publishing Group, Stuttgart, Germany.

Harrison, D. E., Cailliet, R., Harrison, D. D., Troyanovich, S. J., and Harrison, S. O. (1999a). A review of biomechanics of the central nervous system–part II: spinal cord strains from postural loads. *Journal of Manipulative and Physiological Therapeutics*, 22(5):322–32.

Harrison, D. E., Cailliet, R., Harrison, D. D., Troyanovich, S. J., and Harrison, S. O. (1999b). A review of biomechanics of the central nervous system—part I: Spinal canal deformations resulting from changes in posture. *Journal of Manipulative and Physiological Therapeutics*, 22(4):227–234.

Hassannejad, Z., Sharif-Alhoseini, M., Shakouri-Motlagh, A., Vahedi, F., Zadegan, S. A., Mokhatab, M., Rezvan, M., Saadat, S., Shokraneh, F., and Rahimi-Movaghar, V. (2016). Potential variables affecting the quality of animal studies regarding pathophysiology of traumatic spinal cord injuries. *Spinal Cord*, 54(8):579–83.

Hebel, R. and Stromberg, M. (1976). *Anatomy of the Laboratory Rat*. The Williams and Wilkins Company, Maryland, USA.

Heidemann, M., Streit, J., and Tscherter, A. (2015). Investigating functional regeneration in organotypic spinal cord co-cultures grown on multi-electrode arrays. *Journal of Visualized Experiments*, (103).

Heintz, N. (2017). Gene expression nervous system atlas. Online. Available from: www.gensat.org.

Hilton, B. J., Anenberg, E., Harrison, T. C., Boyd, J. D., Murphy, T. H., and Tetzlaff, W. (2016). Re-establishment of cortical motor output maps and spontaneous functional recovery via spared dorsolaterally projecting corticospinal neurons after dorsal column spinal cord injury in adult mice. *Journal of Neuroscience*, 36(14):4080–4092.

Hojjat, S. P., Foltz, W., Wise-Milestone, L., and Whyne, C. M. (2012). Multimodal muct/mumr based semiautomated segmentation of rat vertebrae affected by mixed osteolytic/osteoblastic metastases. *Med Phys*, 39(5):2848–53.

Hol, E. M. and Pekny, M. (2015). Glial fibrillary acidic protein (GFAP) and the astrocyte intermediate filament system in diseases of the central nervous system. *Current Opinion in Cell Biology*, 32:121–130.

Hopkins, A. M., DeSimone, E., Chwalek, K., and Kaplan, D. L. (2015). 3D in vitro modeling of the central nervous system. *Progress in Neurobiology*, 0:1–25.

Hosmane, S., Fournier, A., Wright, R., Rajbhandari, L., Siddique, R., Yang, I. H., Ramesh, K. T., Venkatesan, A., and Thakor, N. (2011). Valve-based microfluidic compression platform: single axon injury and regrowth. *Lab Chip*, 11(22):3888–95.

Howat, W. J. and Wilson, B. A. (2014). Tissue fixation and the effect of molecular fixatives on downstream staining procedures. *Methods*, 70(1):12–19.

Hu, R., Zhou, J., Luo, C., Lin, J., Wang, X., Li, X., Bian, X., Li, Y., Wan, Q., Yu, Y., and Feng, H. (2010). Glial scar and neuroregeneration: histological, functional, and magnetic resonance imaging analysis in chronic spinal cord injury. *Journal of Neurosurgery: Spine*, 13(2):169–180.

Hu, Y., Wen, C. Y., Li, T. H., Cheung, M. M., Wu, E. X., and Luk, K. D. (2011). Somatosensory-evoked potentials as an indicator for the extent of ultrastructural damage of the spinal cord after chronic compressive injuries in a rat model. *Clinical Neurophysiology*, 122(7):1440–7.

Hussein, M. (2018). Effects of strain rate and temperature on the mechanical behavior of carbon black reinforced elastomers based on butyl rubber and high molecular weight polyethylene. *Results in Physics*, 9:511–514.

Ichihara, K., Taguchi, T., Sakuramoto, I., Kawano, S., and Kawai, S. (2003). Mechanism of the spinal cord injury and the cervical spondylotic myelopathy: new approach based on the mechanical features of the spinal cord white and gray matter. *Journal of Neurosurgery*, 99(3 Suppl):278–85.

Ichihara, K., Taguchi, T., Shimada, Y., Sakuramoto, I., Kawano, S., and Kawai, S. (2001). Gray matter of the bovine cervical spinal cord is mechanically more rigid and fragile than the white matter. *Journal of Neurotrauma*, 18(3):361–7.

ImageJ (2012). Imagej user guide. online. available from imagej.nih.gov.

Irvine, S. F. and Kwok, J. C. F. (2018). Perineuronal nets in spinal motoneurones: chondroitin sulphate proteoglycan around alpha motoneurones. *International Journal of Molecular Sciences*, 19(4).

Ishii, H., Tanabe, S., Ueno, M., Kubo, T., Kayama, H., Serada, S., Fujimoto, M., Takeda, K., Naka, T., and Yamashita, T. (2013). ifn-Y-dependent secretion of IL-10 from Th1 cells and microglia/macrophages contributes to functional recovery after spinal cord injury. *Cell Death and Disease*, 4:e710.

Ito, T., Ohtori, S., Hata, K., Inoue, G., Moriya, H., Takahashi, K., and Yamashita, T. (2007). Rho kinase inhibitor improves motor dysfunction and hypoalgesia in a rat model of lumbar spinal canal stenosis. *Spine (Phila Pa 1976)*, 32(19):2070–5.

Iwahashi, H., Yoshimura, N., Hashizume, H., Yamada, H., Oka, H., Matsudaira, K., Shinto, K., Ishimoto, Y., Nagata, K., Teraguchi, M., Kagotani, R., Muraki, S., Akune, T., Tanaka, S., Kawaguchi, H., Nakamura, K., Minamide, A., Nakagawa, Y., and Yoshida, M. (2016). The association between the cross-sectional area of the dural sac and low back pain in a large population: The Wakayama spine study. *PLoS ONE*, 11(8):e0160002.

Iwamoto, H., Kuwahara, H., Matsuda, H., Noriage, A., and Yamano, Y. (1995). Production of chronic compression of the cauda equina in rats for use in studies of lumbar spinal canal stenosis. *Spine (Phila Pa 1976)*, 20(24):2750–7.

Jakeman, L. B., Guan, Z., Wei, P., Ponnappan, R., Dzwonczyk, R., Popovich, P. G., and Stokes, B. T. (2000). Traumatic spinal cord injury produced by controlled contusion in mouse. *Journal of Neurotrauma*, 17(4):299–319.

Jang, E., Kim, J. H., Lee, S., Kim, J. H., Seo, J. W., Jin, M., Lee, M. G., Jang, I. S., Lee, W. H., and Suk, K. (2013a). Phenotypic polarization of activated astrocytes: the critical role of lipocalin-2 in the classical inflammatory activation of astrocytes. *Journal of Immunology*, 191(10):5204–5219.

Jang, E., Lee, S., Kim, J. H., Kim, J. H., Seo, J. W., Lee, W. H., Mori, K., Nakao, K., and Suk, K. (2013b). Secreted protein lipocalin-2 promotes microglial M1 polarization. *The FASEB Journal*, 27(3):1176–1190.

Jaumard, N. V., Leung, J., Gokhale, A. J., Guarino, B. B., Welch, W. C., and Winkelstein, B. A. (2015). Relevant anatomic and morphological measurements of the rat spine: Considerations for rodent models of human spine trauma. *Spine (Phila Pa 1976)*, 40(20):E1084–92.

Jayaraj, R. L., Azimullah, S., Beiram, R., Jalal, F. Y., and Rosenberg, G. A. (2019). Neuroinflammation: friend and foe for ischemic stroke. *Journal of Neuroinflammation*, 16(1):142.

Jiang, X., Chen, D., Lou, Y., and Li, Z. (2016). Kinematic analysis of cervical spine canal diameter and its association with grade of degeneration. *European Spine Journal*, 25(7):2166–72.

Kadanka, Z., Adamova, B., Kerkovsky, M., Kadanka, Z., Dusek, L., Jurova, B., Vlckova, E., and Bednarik, J. (2017). Predictors of symptomatic myelopathy in degenerative cervical spinal cord compression. *Brain and Behavior*, 7(9):e00797.

Kalsi-Ryan, S., Karadimas, S. K., and Fehlings, M. G. (2013). Cervical spondylotic myelopathy: the clinical phenomenon and the current pathobiology of an increasingly prevalent and devastating disorder. *Neuroscientist*, 19(4):409–21.

Kameyama, T. and Hashizume, Y. (2003). Clinicopathology of cervical spondylotic myelopathy. *No no Kagaku (Japan)*, 25:767–75.

Karadimas, S. K., Gatzounis, G., and Fehlings, M. (2015). Pathobiology of cervical spondylotic myelopathy. *European Spine Journal*, 24(Supplement 2):132–138.

Karadimas, S. K., Moon, E. S., Yu, W. R., Satkunendrarajah, K., Kallitsis, J. K., Gatzounis, G., and Fehlings, M. G. (2013). A novel experimental model of cervical spondylotic myelopathy (csm) to facilitate translational research. *Neurobiology of Disease*, 54:43–58.

Karadimas, S. K., Yu, W. R., and Fehlings, M. (2012). Compromise of spinal cord microvasculature in cervical spondylotic myelopathy. *Society for Neuroscience*.

Karimi, A., Shojaei, A., and Tehrani, P. (2017). Mechanical properties of the human spinal cord under the compressive loading. *Journal of Chemical Neuroanatomy*, 86:15–18.

Kaur, J., Flores Gutierrez, J., and Nistri, A. (2016). Neuroprotective effect of propofol against excitotoxic injury to locomotor networks of the rat spinal cord in vitro. *European Journal of Neuroscience*.

Kawano, H., Kimura-Kuroda, J., Komuta, Y., Yoshioka, N., Li, H. P., Kawamura, K., Li, Y., and Raisman, G. (2012). Role of the lesion scar in the response to damage and repair of the central nervous system. *Cell and Tissue Research*, 349(1):169–180.

Kearney, P. A., Ridella, S. A., Viano, D. C., and Anderson, T. E. (1988). Interaction of contact velocity and cord compression in determining the severity of spinal cord injury. *Journal of Neurotrauma*, 5(3):187–208.

Kerstetter, A. E. and Miller, R. H. (2012). Isolation and culture of spinal cord astrocytes. *Methods in Molecular Biology*, 814:93–104.

Khakh, B. S. and Sofroniew, M. V. (2015). Diversity of astrocyte functions and phenotypes in neural circuits. *Nature Neuroscience*, 18(7):942–952.

Khan, S., Plummer, M., Martinez-Arizala, A., and Banovac, K. (2007). Hypothermia in patients with chronic spinal cord injury. *Journal of Spinal Cord Medicine*, 30(1):27–30.

Kim, J. A., Kim, H. N., Im, S. K., Chung, S., Kang, J. Y., and Choi, N. (2015). Collagen-based brain microvasculature model in vitro using three-dimensional printed template. *Biomicrofluidics*, 9(2):024115.

Kim, J. H., Tu, T. W., Bayly, P. V., and Song, S. K. (2009). Impact speed does not determine severity of spinal cord injury in mice with fixed impact displacement. *Journal of Neurotrauma*, 26(8):1395–1404.

Kim, P., Haisa, T., Kawamoto, T., Kirino, T., and Wakai, S. (2004). Delayed myelopathy induced by chronic compression in the rat spinal cord. *Annals of Neurology*, 55(4):503–511.

Kimura-Kuroda, J., Teng, X., Komuta, Y., Yoshioka, N., Sango, K., Kawamura, K., Raisman, G., and Kawano, H. (2010). An in vitro model of the inhibition of axon growth in the lesion scar formed after central nervous system injury. *Mol. Cell. Neurosci.*, 43(2):177–187.

Kirk, J. (2018). *Development of a 3D in vitro spinal cord injury model to investigate how the mechanical properties of the matrix affeect CNS cell behaviour*. PhD thesis, University of Leeds.

Kirshblum, S. C., Burns, S. P., Biering-Sorensen, F., Donovan, W., Graves, D. E., Jha, A., Johansen, M., Jones, L., Krassioukov, A., Mulcahey, M. J., Schmidt-Read, M., and Waring, W. (2011). International standards for neurological classification of spinal cord injury (revised 2011). *Journal of Spinal Cord Medicine*, 34(6):535–546.

Kjell, J. and Olson, L. (2016). Rat models of spinal cord injury: from pathology to potential therapies. *Disease Models & Mechanisms*, 9(10):1125–1137.

Kjell, J., Sandor, K., Josephson, A., Svensson, C. I., and Abrams, M. B. (2013). Rat substrains differ in the magnitude of spontaneous locomotor recovery and in the development of mechanical hypersensitivity after experimental spinal cord injury. *Journal of Neurotrauma*, 30(21):1805–1811.

Klimo, P. and Schmidt, M. H. (2004). Surgical management of spinal metastases. *The Oncologist*, 9(2):188–196.

Klironomos, G., Karadimas, S., Mavrakis, A., Mirilas, P., Savvas, I., Papadaki, E., Papachristou, D. J., and Gatzounis, G. (2011). New experimental rabbit animal model for cervical spondylotic myelopathy. *Spinal Cord*, 49(11):1097–1102.

Koivisto, J., Joki, T., Parraga, J., Paakkonen, R., Yla-Outinen, L., Salonen, L., Jonkkari, I., Peltola, M., Ihalainen, T., Narkilahti, S., and Kellomaki, M. (2017). Bioamine-crosslinked gellan gum hydrogel for neural tissue engieering. *Biomedical Materials*, 12(2).

Koschorek, F., Jensen, H. P., and Terwey, B. (1986). Dynamic studies of cervical spinal canal and spinal cord by magnetic resonance imaging. *Acta Radioligica Supplementum*, 369:727–9.

Krassioukov, A. V., Ackery, A., Schwartz, G., Adamchik, Y., Liu, Y., and Fehlings, M. G. (2002). An in vitro model of neurotrauma in organotypic spinal cord cultures from adult mice. *Brain Research: Brain Research Protocols*, 10(2):60–68.

Kubota, M., Kobayashi, S., Nonoyama, T., Shimada, S., Takeno, K., Miyazaki, T., Guerrero, A. R., Iwamoto, H., and Baba, H. (2011). Development of a chronic cervical cord compression model in rat: changes in the neurological behaviors and radiological and pathological findings. *Journal of Neurotrauma*, 28(3):459–67.

Kurokawa, R., Murata, H., Ogino, M., Ueki, K., and Kim, P. (2011). Altered blood flow distribution in the rat spinal cord under chronic compression. *Spine (Phila Pa 1976)*, 36(13):1006–9.

Kuwazawa, Y., Pope, M. H., Bashir, W., Takahashi, K., and Smith, F. W. (2006). The length of the cervical cord: effects of postural changes in healthy volunteers using positional magnetic resonance imaging. *Spine (Phila Pa 1976)*, 31(17):E579–83.

Kwo, S., Young, W., and Decrescito, V. (1989). Spinal cord sodium, potassium, calcium, and water concentration changes in rats after graded contusion injury. *Journal of Neurotrauma*, 6(1):13–24.

Kwok, J. C., Dick, G., Wang, D., and Fawcett, J. W. (2011). Extracellular matrix and perineuronal nets in CNS repair. *Developmental Neurobiology*, 71(11):1073–89.

Kwon, B. K., Oxland, T. R., and Tetzlaff, W. (2002). Animal models used in spinal cord regeneration research. *Spine (Phila Pa 1976)*, 27(14):1504–10.

Labno, C. (N/A). Two ways to count cells with imagej. Online. Available from: www.unige.ch. Technical report.

Lam, C. J. (2013). *The Effects of Impact Depth and Velocity of Spinal Cord Injury Severity*. PhD thesis, The University of British Columbia.

Lam, C. J., Assinck, P., Liu, J., Tetzlaff, W., and Oxland, T. R. (2014). Impact depth and the interaction with impact speed affect the severity of contusion spinal cord injury in rats. *Journal of Neurotrauma*, 31(24):1985–1997.

Langer, T., Zanella, A., and Caironi, P. (2016). Understanding the role of the cerebrospinal fluid in acid-base disorders. *Intensive Care Medicine*, 42(3):436–9.

LaPlaca, M. C., Lee, V. M., and Thibault, L. E. (1997). An in vitro model of traumatic neuronal injury: loading rate-dependent changes in acute cytosolic calcium and lactate dehydrogenase release. *Journal of Neurotrauma*, 14(6):355–368.

LaPlaca, M. C., Simon, C. M., Prado, G. R., and Cullen, D. K. (2007). CNS injury biomechanics and experimental models. *Progress in Brain Research*, 161:13–26.

LaPlaca, M. C. and Thibault, L. E. (1998). Dynamic mechanical deformation of neurons triggers an acute calcium response and cell injury involving the N-methyl-D-aspartate glutamate receptor. *Journal of Neuroscience Research*, 52(2):220–229.

Lee, B. B., Cripps, R. A., Fitzharris, M., and Wing, P. C. (2014). The global map for traumatic spinal cord injury epidemiology: update 2011, global incidence rate. *Spinal Cord*, 52(2):110–116.

Lee, D. G. (2015). Biomechanics of the thorax: Research evidence and clinical expertise. *The Journal of Manual & Manipulative Therapy*, 23(3):128–138.

Lee, J., Satkunendrarajah, K., and Fehlings, M. G. (2012). Development and characterization of a novel rat model of cervical spondylotic myelopathy: the impact of chronic cord compression on clinical, neuroanatomical, and neurophysiological outcomes. *Journal of Neurotrauma*, 29(5):1012–27.

Lee, M. W., McPhee, R. W., and Stringer, M. D. (2008). An evidence-based approach to human dermatomes. *Clinical Anatomy*, 21(5):363–73.

Li, X., Jiang, L., Liu, Z., Liu, X., Zhang, H., Zhou, H., Wei, F., Yu, M., and Wu, F. (2015). Different approaches for treating multilevel cervical spondylotic myelopathy: A retrospective study of 153 cases from a single spinal center. *PLoS ONE*, 10(10):e0140031.

Liddelow, S. A. and Barres, B. A. (2017). Reactive astrocytes: production, function, and therapeutic potential. *Immunity*, 46(6):957–967.

Lifesciences, E. (2019). Vascular clot management. Online. Available from: /www.edwards.com/gb.

Lim, Y. S., Mun, J. U., Seo, M. S., Sang, B. H., Bang, Y. S., Kang, K. N., Koh, J. W., and Kim, Y. U. (2017). Dural sac area is a more sensitive parameter for evaluating lumbar spinal stenosis than spinal canal area: A retrospective study. *Medicine (Baltimore)*, 96(49):e9087.

Lingford-Hughes, A. and Kalk, N. (2012). *Core Psychiatry (Third Edition)*. Saunders Elsevier, London.

Logan, A., Berry, M., Gonzalez, A. M., Frautschy, S. A., Sporn, M. B., and Baird, A. (1994). Effects of transforming growth factor beta 1 on scar production in the injured central nervous system of the rat. *European Journal of Neuroscience*, 6(3):355–363.

Long, H.-Q., Li, G.-S., Lin, E.-J., Xie, W.-H., Chen, W.-L., Luk, K. D.-K., and Hu, Y. (2013). Is the speed of chronic compression an important factor for chronic spinal cord injury rat model? *Neuroscience Letters*, 545:75–80.

Long, H. Q., Xie, W. H., Chen, W. L., Xie, W. L., Xu, J. H., and Hu, Y. (2014). Value of micro-CT for monitoring spinal microvascular changes after chronic spinal cord compression. *International Journal of Molecular Science*, 15(7):12061–73.

Lonjon, N., Kouyoumdjian, P., Prieto, M., Bauchet, L., Haton, H., Gaviria, M., Privat, A., and Perrin, F. E. (2010). Early functional outcomes and histological analysis after spinal cord compression injury in rats. *Journal of Neurosurgery Spine*, 12(1):106–113.

Lopez-Garcia, M. D., Beebe, D. J., and Crone, W. C. (2010). Young's modulus of collagen at slow displacement rates. *Biomedical Materials Engineering*, 20(6):361–369.

Loy, D. N., Talbott, J. F., Onifer, S. M., Mills, M. D., Burke, D. A., Dennison, J. B., Fajardo, L. C., Magnuson, D. S., and Whittemore, S. R. (2002). Both dorsal and ventral spinal cord pathways contribute to overground locomotion in the adult rat. *Experimental Neurology*, 177(2):575–580.

Macaya, D. and Spector, M. (2012). Injectable hydrogel materials for spinal cord regeneration: a review. *Biomedical Materials*, 7(1):012001.

Maier, I. C., Ichiyama, R. M., Courtine, G., Schnell, L., Lavrov, I., Edgerton, V. R., and Schwab, M. E. (2009). Differential effects of anti-Nogo-A antibody treatment and treadmill training in rats with incomplete spinal cord injury. *Brain*, 132(Pt 6):1426–40.

Maikos, J. T., Qian, Z., Metaxas, D., and Shreiber, D. I. (2008). Finite element analysis of spinal cord injury in the rat. *Journal of Neurotrauma*, 25(7):795–816.

Maneshi, M. M., Maki, B., Gnanasambandam, R., Belin, S., Popescu, G. K., Sachs, F., and Hua, S. Z. (2017). Mechanical stress activates NMDA receptors in the absence of agonists. *Scientific Reports*, 7:39610.

Maneshi, M. M., Sachs, F., and Hua, S. Z. (2015). A threshold shear force for calcium influx in an astrocyte model of traumatic brain injury. *Journal of Neurotrauma*, 32(13):1020–1029.

Maneshi, M. M., Sachs, F., and Hua, S. Z. (2018). Heterogeneous Cytoskeletal Force Distribution Delineates the Onset Ca2+ Influx Under Fluid Shear Stress in Astrocytes. *Frontiers in Cellular Neuroscience*, 12:69.

Mao, Y., Mathews, K., and Gorrie, C. A. (2016). Temporal Response of Endogenous Neural Progenitor Cells Following Injury to the Adult Rat Spinal Cord. *Frontiers of Cellular Neuroscience*, 10:58.

Marinho, A. R., Flett, H. M., Craven, C., Ottensmeyer, C. A., Parsons, D., and Verrier, M. C. (2012). Walking-related outcomes for individuals with traumatic and non-traumatic spinal cord injury inform physical therapy practice. *Journal of Spinal Cord Medicine*, 35(5):371–81.

Martin, A. R., De Leener, B., Cohen-Adad, J., Cadotte, D. W., Nouri, A., Wilson, J. R., Tetreault, L., Crawley, A. P., Mikulis, D. J., Ginsberg, H., and Fehlings, M. G. (2018). Can microstructural MRI detect subclinical tissue injury in subjects with asymptomatic cervical spinal cord compression? A prospective cohort study. *BMJ Open*, 8(4).

Martin, D., Schoenen, J., Delree, P., Gilson, V., Rogister, B., Leprince, P., Stevenaert, A., and Moonen, G. (1992). Experimental acute traumatic injury of the adult rat spinal cord by a subdural inflatable balloon: methodology, behavioral analysis, and histopathology. *Journal of Neuroscience Research*, 32(4):539–550.

Martinez, M., Brezun, J. M., Bonnier, L., and Xerri, C. (2009). A new rating scale for open-field evaluation of behavioral recovery after cervical spinal cord injury in rats. *Journal of Neurotrauma*, 26(7):1043–53.

Martini, F., Ober, W., and Nath, J. (2011). *Visual Anatomy and Physiology (International Edition)*. Benjamin Cummings, San Francisco.

Matsumoto, M., Fujimura, Y., Suzuki, N., Nishi, Y., Nakamura, M., Yabe, Y., and Shiga, H. (1998). MRI of cervical intervertebral discs in asymptomatic subjects. *The Journal of Bone and Joint Surgery: British Volume*, 80(1):19–24.

Matsumoto, M., Okada, E., Toyama, Y., Fujiwara, H., Momoshima, S., and Takahata, T. (2013). Tandem age-related lumbar and cervical intervertebral disc changes in asymptomatic subjects. *European Spine Journal*, 22(4):708–713.

Matsunaga, S., Nakamura, K., Seichi, A., Yokoyama, T., Toh, S., Ichimura, S., Satomi, K., Endo, K., Yamamoto, K., Kato, Y., Ito, T., Tokuhashi, Y., Uchida, K., Baba, H., Kawahara, N., Tomita, K., Matsuyama, Y., Ishiguro, N., Iwasaki, M., Yoshikawa, H., Yonenobu, K., Kawakami, M., Yoshida, M., Inoue, S., Tani, T., Kaneko, K., Taguchi, T., Imakiire, T., and Komiya, S. (2008). Radiographic predictors for the development of myelopathy in patients with ossification of the posterior longitudinal ligament: a multicenter cohort study. *Spine*, 33(24):2648–2650.

Matthews, J. B., Mitchell, W., Stone, M., Fisher, J., and Ingham, E. (2001). A novel three-dimensional tissue equivalent model to study the combined effects of cyclic mechanical strain and wear particles on the osteolytic potential of primary human macrophages in vitro. *Proceedings of the Institution of Mechanical Engineers, Part H*, 215(5):479–486.

May, Z., Fenrich, K. K., Dahlby, J., Batty, N. J., Torres-Espin, A., and Fouad, K. (2017). Following Spinal Cord Injury Transected Reticulospinal Tract Axons Develop New Collateral Inputs to Spinal Interneurons in Parallel with Locomotor Recovery. *Neural Plasticity*, 2017:1932875.

Mazuchowski, E. and Thibault, L. (2003). Biomechanical properties of the human spinal cord and pia mater. *Summer Bioengineering Conference, Sonesta, FL, USA*.

McConnell, H. L., Kersch, C. N., Woltjer, R. L., and Neuwelt, E. A. (2017). The translational significance of the neurovascular unit. *Journal of Biological Chemistry*, 292(3):762–770.

McKinley, W. O., Seel, R. T., and Hardman, J. T. (1999). Nontraumatic spinal cord injury: Incidence, epidemiology, and functional outcome. *Archives of Physical Medicine and Rehabilitation*, 80(6):619–623.

Mecha, M., Inigo, P. M., Mestre, L., Hernangomez, M., Borrell, J., and Guaza, C. (2011). An easy and fast way to obtain a high number of glial cells from rat cerebral tissue: A beginners approach. *Protocol Exchange*.

Metz, G. A., Merkler, D., Dietz, V., Schwab, M. E., and Fouad, K. (2000). Efficient testing of motor function in spinal cord injured rats. *Brain Research*, 883(2):165–177.

Michalopoulos, E., Knight, R. L., Korossis, S., Kearney, J. N., Fisher, J., and Ingham, E. (2012). Development of methods for studying the differentiation of human mesenchymal stem cells under cyclic compressive strain. *Tissue Engineering, Part C Methods*, 18(4):252–262.

Middeldorp, J. and Hol, E. M. (2011). GFAP in health and disease. *Progress in Neurobiology*, 93(3):421–443.

Mishra, A. (2017). Binaural blood flow control by astrocytes: listening to synapses and the vasculature. *Journal of Physiology*, 595(6):1885–1902.

Mitchell, E. J., McCallum, S., Dewar, D., and Maxwell, D. J. (2016). Corticospinal and Reticulospinal Contacts on Cervical Commissural and Long Descending Propriospinal Neurons in the Adult Rat Spinal Cord; Evidence for Powerful Reticulospinal Connections. *PLoS ONE*, 11(3):e0152094.

Miyata, S. and Kitagawa, H. (2016). Chondroitin 6-sulfation regulates perineuronal net formation by controlling the stability of aggrecan. *Neural Plasticity*, 2016:1305801.

Miyata, S., Komatsu, Y., Yoshimura, Y., Taya, C., and Kitagawa, H. (2012). Persistent cortical plasticity by upregulation of chondroitin 6-sulfation. *Nature Neuroscience*, 15(3):414–422.

Molina, A. E., Cristante, A. F., de Barros, T. E., Molina, M. S., and Molina, T. P. (2015). A computerized system for the application of Basso, Beattie and Bresnahan scale in Wistar rats. *Acta Ortopedica Brasileria*, 23(4):179–183.

Morin, D. (2018). Spinal cord trauma: An overview of normal structure and function, primary and secondary mechanisms of injury, and emerging treatment modalities. Master's thesis, Liberty University.

Morris, R. and Whishaw, I. Q. (2016). A proposal for a rat model of spinal cord injury featuring the rubrospinal tract and its contributions to locomotion and skilled hand movement. *Frontiers in Neuroscience*, 10:5.

Muir, E., De Winter, F., Verhaagen, J., and Fawcett, J. (2019). Recent advances in the therapeutic uses of chondroitinase ABC. *Experimental Neurology*, 321:113032.

Nakashima, H., Yukawa, Y., Suda, K., Yamagata, M., Ueta, T., and Kato, F. (2016). Narrow cervical canal in 1211 asymptomatic healthy subjects: the relationship with spinal cord compression on MRI. *Eurropean Spine Journal*, 25(7):2149–54.

Nathan, P. W. (1994). Effects on movement of surgical incisions into the human spinal cord. *Brain*, 117 (Pt 2):337–346.

Navarro-Orozco, D. and Bollu, P. (2018). *Neuroanatomy, Medical Lemniscus*. StatPearls Publishing, Florida, USA.

Nawashiro, H., Brenner, M., Fukui, S., Shima, K., and Hallenbeck, J. M. (2000). High susceptibility to cerebral ischemia in GFAP-null mice. *Journal of Cerebral Blood Flow Metabolism*, 20(7):1040–4.

Nawashiro, H., Messing, A., Azzam, N., and Brenner, M. (1998). Mice lacking GFAP are hypersensitive to traumatic cerebrospinal injury. *Neuroreport*, 9(8):1691–6.

New, P. W., Cripps, R. A., and Bonne Lee, B. (2014). Global maps of non-traumatic spinal cord injury epidemiology: towards a living data repository. *Spinal Cord*, 52(2):97–109.

New, P. W. and Jackson, T. (2010). The costs and adverse events associated with hospitalization of patients with spinal cord injury in Victoria, Australia. *Spine (Phila Pa 1976)*, 35(7):796–802.

New, P. W. and Marshall, R. (2014). International spinal cord injury data sets for non-traumatic spinal cord injury. *Spinal Cord*, 52(2):123–32.

New, P. W., Simmonds, F., and Stevermuer, T. (2011). A population-based study comparing traumatic spinal cord injury and non-traumatic spinal cord injury using a national rehabilitation database. *Spinal Cord*, 49(3):397–403.

Newcombe, R. E., Finnie, J. W., Leonard, A. V., Manavis, J., Reilly, P. L., Vink, R., and Blumbergs, P. C. (2015). Apoptosis in human compressive myelopathy due to metastatic neoplasia. *Spine (Phila Pa 1976)*, 40(8):E450–7.

NHS (2010). Guidelines for analgesic treatment of chronic pain. Online. Available from: www.southworcsccg.nhs.uk.

NICE (2015). Neck pain - cervical radiculopathy - clinical knowledge summary. Online. Available from: www.nice.org.uk.

NICE (2016). Managing low back pain and sciatica - nice pathway.

Nicholson, C. and Sykova, E. (1998). Extracellular space structure revealed by diffusion analysis. *Trends in Neuroscience*, 21(5):207–215.

Noonan, V. K., Fingas, M., Farry, A., Baxter, D., Singh, A., Fehlings, M. G., and Dvorak, M. F. (2012). Incidence and prevalence of spinal cord injury in canada: a national perspective. *Neuroepidemiology*, 38(4):219–26.

Norenberg, M. D., Smith, J., and Marcillo, A. (2004). The pathology of human spinal cord injury: defining the problems. *Journal of Neurotrauma*, 21(4):429–440.

Noyes, D. H. (1987). Correlation between parameters of spinal cord impact and resultant injury. *Experimental Neurology*, 95(3):535 – 547.

Okada, S. (2016). The pathophysiological role of acute inflammation after spinal cord injury. *Inflammation and Regeneration*, 36:20.

Okada, S., Nakamura, M., Mikami, Y., Shimazaki, T., Mihara, M., Ohsugi, Y., Iwamoto, Y., Yoshizaki, K., Kishimoto, T., Toyama, Y., and Okano, H. (2004). Blockade of interleukin-6 receptor suppresses reactive astrogliosis and ameliorates functional recovery in experimental spinal cord injury. *Journal of Neuroscience Research*, 76(2):265–276.

Oliveira, K. M., Lavor, M. S., Silva, C. M., Fukushima, F. B., Rosado, I. R., Silva, J. F., Martins, B. C., Guimaraes, L. B., Gomez, M. V., Melo, M. M., and Melo, E. G. (2014). Omega-conotoxin MVIIC attenuates neuronal apoptosis in vitro and improves significant recovery after spinal cord injury in vivo in rats. *International Journal of Clinical and Experimental Pathology*, 7(7):3524–36.

Pandamooz, S., Salehi, M. S., Zibaii, M. I., Safari, A., Nabiuni, M., Ahmadiani, A., and Dargahi, L. (2019). Modeling traumatic injury in organotypic spinal cord slice culture obtained from adult rat. *Tissue and Cell*, 56:90–97.

Panjabi, M. M., Duranceau, J., Goel, V., Oxland, T., and Takata, K. (1991). Cervical human vertebrae. quantitative three-dimensional anatomy of the middle and lower regions. *Spine (Phila Pa 1976)*, 16(8):861–9.

Panjabi, M. M., Goel, V., Oxland, T., Takata, K., Duranceau, J., Krag, M., and Price, M. (1992). Human lumbar vertebrae. quantitative three-dimensional anatomy. *Spine (Phila Pa 1976)*, 17(3):299–306.

Park, D. K., An, H. S., Lurie, J. D., Zhao, W., Tosteson, A., Tosteson, T. D., Herkowitz, H., Errico, T., and Weinstein, J. N. (2010). Does multilevel lumbar stenosis lead to poorer outcomes?: a subanalysis of the Spine Patient Outcomes Research Trial (SPORT) lumbar stenosis study. *Spine*, 35(4):439–446.

Paterniti, I., Esposito, E., and S., C. (2015). *Recovery of Motor Function Following Spinal Cord Injury*. IntechOpen, Online.

Pearse, D. D., Lo, T. P., Cho, K. S., Lynch, M. P., Garg, M. S., Marcillo, A. E., Sanchez, A. R., Cruz, Y., and Dietrich, W. D. (2005). Histopathological and behavioral characterization of a novel cervical spinal cord displacement contusion injury in the rat. *Journal of Neurotrauma*, 22(6):680–702.

Pedram, M. S., Dehghan, M. M., Soleimani, M., Sharifi, D., Marjanmehr, S. H., and Nasiri, Z. (2010). Transplantation of a combination of autologous neural differentiated and undifferentiated mesenchymal stem cells into injured spinal cord of rats. *Spinal Cord*, 48(6):457–463.

Penning, L., Wilmink, J. T., van Woerden, H. H., and Knol, E. (1986). CT myelographic findings in degenerative disorders of the cervical spine: clinical significance. *American Journal of Roentgenology*, 146(4):793–801.

Petersen, T. H., Willerslev-Olsen, M., Conway, B. A., and Nielsen, J. B. (2012). The motor cortex drives the muscles during walking in human subjects. *Journal of Physiology (London)*, 590(10):2443–2452.

Phillips, J. B. (2014a). Building stable anisotropic tissues using cellular collagen gels. *Organogenesis*, 10(1):6–8.

Phillips, J. B. (2014b). Monitoring neuron and astrocyte interactions with a 3D cell culture system. *Methods in Molecular Biology*, 1162:113–24.

Potjewyd, G., Moxon, S., Wang, T., Domingos, M., and Hooper, N. M. (2018). Tissue engineering 3D neurovascular units: A biomaterials and bioprinting perspective. *Trends in Biotechnology.*, 36(4):457–472.

Presysin (2019). Precision systems and instrumentation, llc: A contusion deice specifically designed for medical research using rats and mice. ih-0400.

Quinn, R. (2005). Comparing rat's to human's age: how old is my rat in people years? *Nutrition*, 21(6):775–777.

Raiszadeh, K. and Spivak, J. (1999). *Orthopaedics: A study guide*. McGraw-Hill, New York, USA.

Ramo, N. L., Shetye, S. S., Streijger, F., Lee, J. H. T., Troyer, K. L., Kwon, B. K., Cripton, P., and Puttlitz, C. M. (2018). Comparison of in vivo and ex vivo viscoelastic behavior of the spinal cord. *Acta Biomaterialia*, 68:78–89.

Razdan, S., Kaul, R. L., Motta, A., Kaul, S., and Bhatt, R. K. (1994). Prevalence and pattern of major neurological disorders in rural Kashmir (India) in 1986. *Neuroepidemiology*, 13(3):113–9.

Ren, H., Chen, X., Tian, M., Zhou, J., Ouyang, H., and Zhang, Z. (2018). Regulation of inflammatory cytokines for spinal cord injury repair through local delivery of therapeutic agents. *Advanced Science*, 5(11):1800529.

Roeder, B. A., Kokini, K., Sturgis, J. E., Robinson, J. P., and Voytik-Harbin, S. L. (2002). Tensile mechanical properties of three-dimensional type I collagen extracellular matrices with varied microstructure. *Journal of Biomechanical Engineering*, 124(2):214–222.

Roughley, P. J., Melching, L. I., Heathfield, T. F., Pearce, R. H., and Mort, J. S. (2006). The structure and degradation of aggrecan in human intervertebral disc. *European Spine Journal*, 15(Suppl 3):326–332.

Rowland, J. W., Hawryluk, G. W., Kwon, B., and Fehlings, M. G. (2008). Current status of acute spinal cord injury pathophysiology and emerging therapies: promise on the horizon. *Neurosurgery Focus*, 25(5):E2.

Russell, W. and Burch, R. (1992). *Principles of humane experimental technique*. Methuen, Online.

Russi, A. E. and Brown, M. A. (2015). The meninges: New therapeutic targets for multiple sclerosis. *Translational Research : The Journal of :aboratory and Clinical Medicine*, 165(2):255–269.

Ruzicka, J., Romanyuk, N., Jirakova, K., Hejcl, A., Janouskova, O., Machova, L. U., Bochin, M., Pradny, M., Vargova, L., and Jendelova, P. (2019). The effect of iPS-derived neural progenitors seeded on laminin-coated pHEMA-MOETACl hydrogel with dual porosity in a rat model of chronic spinal cord injury. *Cell Transplant*, page 963689718823705.

Ruzicka, J., Urdzikova, L. M., Kloudova, A., Amin, A. G., Vallova, J., Kubinova, S., Schmidt, M. H., Jhanwar-Uniyal, M., and Jendelova, P. (2018). Anti-inflammatory compound curcumin and mesenchymal stem cells in the treatment of spinal cord injury in rats. *Acta Neurobiologiae Experimentalis Journal (Warsaw)*, 78(4):358–374.

Salegio, E. A., Bresnahan, J. C., Sparrey, C. J., Camisa, W., Fischer, J., Leasure, J., Buckley, J., Nout-Lomas, Y. S., Rosenzweig, E. S., Moseanko, R., Strand, S., Hawbecker, S., Lemoy, M. J., Haefeli, J., Ma, X., Nielson, J. L., Edgerton, V. R., Ferguson, A. R., Tuszynski, M. H., and Beattie, M. S. (2016). A unilateral cervical spinal cord contusion injury model in non-human primates (macaca mulatta). *Journal of Neurotrauma*, 33(5):439–459.

Samano, C., Kaur, J., and Nistri, A. (2016). A study of methylprednisolone neuroprotection against acute injury to the rat spinal cord in vitro. *Neuroscience*, 315:136–49.

Sayıt, E., Aghdasi, B., Daubs, M. D., and Wang, J. C. (2015). The occupancy of the components in the cervical spine and their changes with extension and flexion. *Global Spine Journal*, 5(5):396–405.

Schaub, N. J., Johnson, C. D., Cooper, B., and Gilbert, R. J. (2016). Electrospun fibers for spinal cord injury research and regeneration. *Journal of Neurotrauma*, 33(15):1405–15.

Scheff, S. W., Rabchevsky, A. G., Fugaccia, I., Main, J. A., and Lumpp, J. E. (2003). Experimental modeling of spinal cord injury: characterization of a force-defined injury device. *Journal of Neurotrauma*, 20(2):179–193.

Schitine, C., Nogaroli, L., Costa, M. R., and Hedin-Pereira, C. (2015). Astrocyte heterogeneity in the brain: from development to disease. *Front Cell Neurosci*, 9:76.

Schucht, P., Raineteau, O., Schwab, M. E., and Fouad, K. (2002). Anatomical correlates of locomotor recovery following dorsal and ventral lesions of the rat spinal cord. *Experimental Neurology*, 176(1):143–153.

Sedy, J., Urdzikova, L., Jendelova, P., and Sykova, E. (2008). Methods for behavioral testing of spinal cord injured rats. *Neuroscience & Biobehavioral Reviews*, 32(3):550–580.

Sedy, J., Urdzikova, L., Likavcanova, K., Hejcl, A., Burian, M., Jendelova, P., Zicha, J., Kunes, J., and Sykova, E. (2007). Low concentration of isoflurane promotes the development of neurogenic pulmonary edema in spinal cord injured rats. *Journal of Neurotrauma*, 24(9):1487–1501.

Sedy, J., Zicha, J., Kunes, J., Jendelova, P., and Sykova, E. (2009). Rapid but not slow spinal cord compression elicits neurogenic pulmonary edema in the rat. *Physiological Research*, 58(2):269–277.

Sekhon, L. H. and Fehlings, M. G. (2001). Epidemiology, demographics, and pathophysiology of acute spinal cord injury. *Spine*, 26(24 Suppl):2–12.

Seki, T., Hida, K., Tada, M., Koyanagi, I., and Iwasaki, Y. (2002). Graded contusion model of the mouse spinal cord using a pneumatic impact device. *Neurosurgery*, 50(5):1075–1081.

Sekiguchi, M., Kikuchi, S., and Myers, R. R. (2004). Experimental spinal stenosis: relationship between degree of cauda equina compression, neuropathology, and pain. *Spine (Phila Pa 1976)*, 29(10):1105–11.

Sengul, G. and Watson, C. (2015). *The Rat Nervous System, Fourth Edition*. Academic Press, Massachusetts, USA.

Sengupta, P. (2011). A scientific review of age determination for a laboratory rat: How old is it in comparison with human age? *Biomedicine International Journals*, 2(2).

Shabbir, A., Bianchetti, E., Cargonja, R., Petrovic, A., Mladinic, M., Pilipović, K., and Nistri, A. (2015a). Role of HSP70 in motoneuron survival after excitotoxic stress in a rat spinal cord injury model in vitro. *European Journal of Neuroscience*, 42(12):3054–3065.

Shabbir, A., Bianchetti, E., and Nistri, A. (2015b). The volatile anesthetic methoxyflurane protects motoneurons against excitotoxicity in an in vitro model of rat spinal cord injury. *Neuroscience*, 285:269–80.

Sharif-Alhoseini, M. and Rahimi-Movaghar, V. (2014). Animal models in traumatic spinal cord injury, topics in paraplegia.

Shingu, H., Kimura, I., Nasu, Y., Shiotani, A., Oh-hama, M., Hijioka, A., and Tanaka, J. (1989). Microangiographic study of spinal cord injury and myelopathy. *Paraplegia*, 27(3):182–189.

Shinozaki, Y., Shibata, K., Yoshida, K., Shigetomi, E., Gachet, C., Ikenaka, K., Tanaka, K. F., and Koizumi, S. (2017). Transformation of astrocytes to a neuroprotective phenotype by microglia via P2Y1 receptor downregulation. *Cell Reports*, 19(6):1151–1164.

Shunmugavel, A., Martin, M. M., Khan, M., Copay, A. G., Subach, B. R., Schuler, T. C., and Singh, I. (2013). Simvastatin ameliorates cauda equina compression injury in a rat model of lumbar spinal stenosis. *Journal of Neuroimmune Pharmacology*, 8(1):274–286.

Silva, N. A., Sousa, N., Reis, R. L., and Salgado, A. J. (2014). From basics to clinical: A comprehensive review on spinal cord injury. *Progress in Neurobiology*, 114:25–57.

Smith, J. (2016). *A 3D Culture Model to Investigate Cellular Responses to Mechanical Loading in Spinal Cord Injury*. PhD thesis, University of Leeds.

Smith, J. A., Siegel, J. H., and Siddiqi, S. Q. (2005). Spine and spinal cord injury in motor vehicle crashes: a function of change in velocity and energy dissipation on impact with respect to the direction of crash. *Journal of Trauma*, 59(1):117–131.

Sobel, R. A. (1998). The extracellular matrix in multiple sclerosis lesions. *Journal of Neuropathology and Experimental Neurology*, 57(3):205–17.

Sofroniew, M. V. (2005). Reactive astrocytes in neural repair and protection. *Neuroscientist*, 11(5):400–7.

Sofroniew, M. V. (2018). Dissecting spinal cord regeneration. *Nature*, 557(7705):343–350.

Sofroniew, M. V. and Vinters, H. V. (2010). Astrocytes: biology and pathology. *Acta Neuropathologica*, 119(1):7–35.

Someya, Y., Koda, M., Hashimoto, M., Okawa, A., Masaki, Y., and Yamazaki, M. (2011). Postmortem findings in a woman with history of laminoplasty for severe cervical spondylotic myelopathy. *Journal of Spinal Cord Medicine*, 34(5):523–526.

Sorg, B. A., Berretta, S., Blacktop, J. M., Fawcett, J. W., Kitagawa, H., Kwok, J. C., and Miquel, M. (2016). Casting a wide net: Role of perineuronal nets in neural plasticity. *Journal of Neuroscience*, 36(45):11459–11468.

Sparrey, C. J., Choo, A. M., Liu, J., Tetzlaff, W., and Oxland, T. R. (2008). The distribution of tissue damage in the spinal cord is influenced by the contusion velocity. *Spine*, 33(22):E812–819.

Sparrey, C. J. and Keaveny, T. M. (2011). Compression behavior of porcine spinal cord white matter. *Journal of Biomechanics*, 44(6):1078–1082.

Sparrey, C. J., Salegio, E. A., Camisa, W., Tam, H., Beattie, M. S., and Bresnahan, J. C. (2016). Mechanical design and analysis of a unilateral cervical spinal cord contusion injury model in non-human primates. *Journal of Neurotrauma*, 33(12):1136–1149.

Steurer, J., Roner, S., Gnannt, R., and Holder, J. (2011). Quantitative radiologic criteria for the diagnosis of lumbar spinal stenosis: A systematic literature review. *BMC Musculoskeletal Disorders*, 12:175.

Stokes, B. T. (1992). Experimental spinal cord injury: a dynamic and verifiable injury device. *Journal of Neurotrauma*, 9(2):129–131.

Strbian, D., Durukan, A., Pitkonen, M., Marinkovic, I., Tatlisumak, E., Pedrono, E., Abo-Ramadan, U., and Tatlisumak, T. (2008). The blood-brain barrier is continuously open for several weeks following transient focal cerebral ischemia. *Neuroscience*, 153(1):175–81.

Sturdivant, N. M., Smith, S. G., Ali, S. F., Wolchok, J. C., and Balachandran, K. (2016). Acetazolamide mitigates astrocyte cellular edema following mild traumatic brain injury. *Scientific Reports*, 6:33330.

Su, Y. F., Lin, C. L., Lee, K. S., Tsai, T. H., Wu, S. C., Hwang, S. L., Chen, S. C., and Kwan, A. L. (2015). A modified compression model of spinal cord injury in rats: functional assessment and the expression of nitric oxide synthases. *Spinal Cord*, 53(6):432–5.

Sun, Y., Zhang, L. H., Fu, Y. M., Li, Z. R., Liu, J. H., Peng, J., Liu, B., and Tang, P. F. (2016). Establishment of a rat model of chronic thoracolumbar cord compression with a flat plastic screw. *Neural Regeneration Research*, 11(6):963–70.

Sutherland, T. C., Mathews, K. J., Mao, Y., Nguyen, T., and Gorrie, C. A. (2016). Differences in the Cellular Response to Acute Spinal Cord Injury between Developing and Mature Rats Highlights the Potential Significance of the Inflammatory Response. *Frontiers in Cellular Neuroscience*, 10:310.

Sypecka, J., Koniusz, S., Kawalec, M., and Sarnowska, A. (2015). The organotypic longitudinal spinal cord slice culture for stem cell study. *Stem Cells International*, 2015:471216.

Tachi, Y., Okuda, T., Kawahara, N., Kato, N., Ishigaki, Y., and Matsumoto, T. (2015). Expression of hyaluronidase-4 in a rat spinal cord hemisection model. *Asian Spine Journal*, 9(1):7–13.

TAInstruments (2016). Biodynamic 5110. Online. Available from: www.tainstruments.com.

Takano, M., Kawabata, S., Komaki, Y., Shibata, S., Hikishima, K., Toyama, Y., Okano, H., and Nakamura, M. (2014). Inflammatory cascades mediate synapse elimination in spinal cord compression. *J Neuroinflammation*, 11:40.

Talac, R., Friedman, J. A., Moore, M. J., Lu, L., Jabbari, E., Windebank, A. J., Currier, B. L., and Yaszemski, M. J. (2004). Animal models of spinal cord injury for evaluation of tissue engineering treatment strategies. *Biomaterials*, 25(9):1505–10.

Tan, Y., Uchida, K., Nakajima, H., Guerrero, A. R., Watanabe, S., Hirai, T., Takeura, N., Liu, S. Y., Johnson, W. E., and Baba, H. (2013). Blockade of interleukin 6 signaling improves the survival rate of transplanted bone marrow stromal cells and increases locomotor function in mice with spinal cord injury. *Journal of Neuropathology and Experimental Neurology*, 72(10):980–993.

Tani, S., Yamada, S., Fuse, T., and Nakamura, N. (1991). Changes in lumbosacral canal length during flexion and extension–dynamic effect on the elongated spinal cord in the tethered spinal cord. *No To Shinkei*, 43(12):1121–1125.

Taylor, Z. A., Comas, O., Cheng, M., Passenger, J., Hawkes, D. J., Atkinson, D., and Ourselin, S. (2009). On modelling of anisotropic viscoelasticity for soft tissue simulation: numerical solution and GPU execution. *Medical Image Analysis*, 13(2):234–244.

Teresi, L. M., Lufkin, R. B., Reicher, M. A., Moffit, B. J., Vinuela, F. V., Wilson, G. M., Bentson, J. R., and Hanafee, W. N. (1987). Asymptomatic degenerative disk disease and spondylosis of the cervical spine: MR imaging. *Radiology*, 164(1):83–8.

Tetreault, L., Goldstein, C. L., Arnold, P., Harrop, J., Hilibrand, A., Nouri, A., and Fehlings, M. G. (2015). Degenerative cervical myelopathy: A spectrum of related disorders affecting the aging spine. *Neurosurgery*, 77 Suppl 4:S51–67.

Tschirhart, C. E., Nagpurkar, A., and Whyne, C. M. (2004). Effects of tumor location, shape and surface serration on burst fracture risk in the metastatic spine. *J Biomech*, 37(5):653–660.

Tveten, L. (1976). Spinal cord vascularity. iv. the spinal cord arteries in the rat. *Acta Radiol Diagn (Stockh)*, 17(4):385–98.

Uchida, K., Baba, H., Maezawa, Y., and Kubota, C. (2002). Progressive changes in neurofilament proteins and growth-associated protein-43 immunoreactivities at the site of cervical spinal cord compression in spinal hyperostotic mice. *Spine (Phila Pa 1976)*, 27(5):480–6.

Urdzikova, L., Jendelova, P., Glogarova, K., Burian, M., Hajek, M., and Sykova, E. (2006). Transplantation of bone marrow stem cells as well as mobilization by granulocyte-colony stimulating factor promotes recovery after spinal cord injury in rats. *Journal of Neurotrauma*, 23(9):1379–1391.

Urdzikova, L. and Kwok, J. (2019). Email and conversation with katie timms: Ventral traumatic spinal cord injury model in rats using 2f balloon catheter. *Unpublished.*

Uwamori, H., Higuchi, T., Arai, K., and Sudo, R. (2017). Integration of neurogenesis and angiogenesis models for constructing a neurovascular tissue. *Scientific Reports*, 7(1):17349.

Valero, C., Amaveda, H., Mora, M., and Garcia-Aznar, J. M. (2018). Combined experimental and computational characterization of crosslinked collagen-based hydrogels. *PLoS ONE*, 13(4):e0195820.

van den Berg, M. E., Castellote, J. M., de Pedro-Cuesta, J., and Mahillo-Fernandez, I. (2010). Survival after spinal cord injury: A systematic review. *Journal of Neurotrauma*, 27(8):1517–28.

Vanicky, I., Urdzikova, L., Saganova, K., Cizkova, D., and Galik, J. (2001). A simple and reproducible model of spinal cord injury induced by epidural balloon inflation in the rat. *Journal of Neurotrauma*, 18(12):1399–407.

Vogelaar, C. F., Konig, B., Krafft, S., Estrada, V., Brazda, N., Ziegler, B., Faissner, A., and Muller, H. W. (2015). Pharmacological suppression of CNS scarring by deferoxamine reduces lesion volume and increases regeneration in an in vitro model for astroglial-fibrotic scarring and in rat spinal cord injury in vivo. *PLoS ONE*, 10(7):e0134371.

Wanner, I. B., Anderson, M. A., Song, B., Levine, J., Fernandez, A., Gray-Thompson, Z., Ao, Y., and Sofroniew, M. V. (2013). Glial scar borders are formed by newly proliferated, elongated astrocytes that interact to corral inflammatory and fibrotic cells via STAT3-dependent mechanisms after spinal cord injury. *Journal of Neuroscience*, 33(31):12870–86.

Watanabe, R. and Parke, W. W. (1986). Vascular and neural pathology of lumbosacral spinal stenosis. *Journal of Neurosurgery*, 64(1):64–70.

Watson, C., Paxinos, G., and Kayalioglu, G. (2009). *The Spinal Cord: A Christoper and Dana Reeve Foundation Text and Atlas*. Elsevier, China.

Weber, C., Giannadakis, C., Rao, V., Jakola, A. S., Nerland, U., Nygaard, . P., Solberg, T. K., Gulati, S., and Solheim, O. (2016). Is there an association between radiological severity of lumbar spinal stenosis and disability, pain or sugical outcomes?: A multicenter observational study. *Spine*, 41(2):78–83.

Weightman, A. P., Pickard, M. R., Yang, Y., and Chari, D. M. (2014). An in vitro spinal cord injury model to screen neuroregenerative materials. *Biomaterials*, 35(12):3756–65.

Welniarz, Q., Dusart, I., and Roze, E. (2017). The corticospinal tract: Evolution, development, and human disorders. *Developmental Neurobiology*, 77(7):810–829.

Werndle, M. C., Saadoun, S., Phang, I., Czosnyka, M., Varsos, G. V., Czosnyka, Z. H., Smielewski, P., Jamous, A., Bell, B. A., Zoumprouli, A., and Papadopoulos, M. C. (2014). Monitoring of spinal cord perfusion pressure in acute spinal cord injury: initial findings of the injured spinal cord pressure evaluation study. *Critical Care Medicine*, 42(3):646–55.

White, A. and Panjabi, M. M. (1990). *Clinical Biomechanics of the Spine*. Lippincott Williams & Wilkins, Philadelphia, PA.

Whyne, C. M., Hu, S. S., and Lotz, J. C. (2003). Burst fracture in the metastatically involved spine: development, validation, and parametric analysis of a three-dimensional poroelastic finite-element model. *Spine (Phila Pa 1976)*, 28(7):652–60.

Wilcox, R. K., Boerger, T. O., Allen, D. J., Barton, D. C., Limb, D., Dickson, R. A., and Hall, R. M. (2003). A dynamic study of thoracolumbar burst fractures. *Journal of Bone and Joint Surgery American volume*, 85(11):2184–2189.

Winklhofer, S., Schoth, F., Stolzmann, P., Krings, T., Mull, M., Wiesmann, M., and Stracke, C. P. (2014). Spinal cord motion: influence of respiration and cardiac cycle. *Rofo*, 186(11):1016–21.

Witiw, C. D., Mathieu, F., Nouri, A., and Fehlings, M. G. (2018). Clinico-radiographic discordance: An evidence-based commentary on the management of degenerative cervical spinal cord compression in the absence of symptoms or with only mild symptoms of myelopathy. *Global Spine Journal*, 8(5):527–534.

World Health Organisation (2016). Spinal cord injury. Online. Available from: www.who.int.

Wu, H., Yu, W. D., Jiang, R., and Gao, Z. L. (2013). Treatment of multilevel degenerative lumbar spinal stenosis with spondylolisthesis using a combination of microendoscopic discectomy and minimally invasive transforaminal lumbar interbody fusion. *Experimental and Therapeutic Medicine*, 5(2):567–571.

Xu, J., Long, H., Chen, W., Cheng, X., Yu, H., Huang, Y., Wang, X., and Li, F. (2017). Ultrastructural features of neurovascular units in a rat model of chronic compressive spinal cord injury. *Frontiers in Neuroanatomy*, 11:136.

Xu, P., Gong, W. M., Li, Y., Zhang, T., Zhang, K., Yin, D. Z., and Jia, T. H. (2008). Destructive pathological changes in the rat spinal cord due to chronic mechanical compression. laboratory investigation. *Journal of Neurosurgery Spine*, 8(3):279–85.

Yamaura, I., Yone, K., Nakahara, S., Nagamine, T., Baba, H., Uchida, K., and Komiya, S. (2002). Mechanism of destructive pathologic changes in the spinal cord under chronic mechanical compression. *Spine*, 27(1):21–26.

Yang, T., Wu, L., Wang, H., Fang, J., Yao, N., and Xu, Y. (2015). Inflammation level after decompression surgery for a rat model of chronic severe spinal cord compression and effects on ischemia-reperfusion injury. *Neurologica Medico-Chirurgica (Tokyo)*, 55(7):578–86.

Yang, Y. L., Motte, S., and Kaufman, L. J. (2010). Pore size variable type I collagen gels and their interaction with glioma cells. *Biomaterials*, 31(21):5678–5688.

Yoon, H., Walters, G., Paulsen, A. R., and Scarisbrick, I. A. (2017). Astrocyte heterogeneity across the brain and spinal cord occurs developmentally, in adulthood and in response to demyelination. *PLoS ONE*, 12(7):e0180697.

Yu, W. R., Liu, T., Kiehl, T. R., and Fehlings, M. G. (2011). Human neuropathological and animal model evidence supporting a role for fas-mediated apoptosis and inflammation in cervical spondylotic myelopathy. *Brain*, 134(5):1277–92.

Yuan, Q., Dougherty, L., and Margulies, S. S. (1998). In vivo human cervical spinal cord deformation and displacement in flexion. *Spine (Phila Pa 1976)*, 23(15):1677–83.

Zhang, S., Cao, X., Stablow, A. M., Shenoy, V. B., and Winkelstein, B. A. (2016). Tissue strain reorganizes collagen with a switchlike response that regulates neuronal extracellular signal-regulated kinase phosphortylation in vitro: Implications for ligamentious injury and mechanotransduction. *Journal of Biomechanical Engineering*, 138(2):021013.

Zhang, Y. and Barres, B. A. (2010). Astrocyte heterogeneity: an underappreciated topic in neurobiology. *Current Opinion in Neurobiology*, 20(5):588–594.

Zhang, Z., Zhang, Y. P., Shields, L. B. E., and Shields, C. B. (2014). Technical comments on rodent spinal cord injuries models. *Neural Regeneration Research*, 9(5):453–5.

Zhou, F. Q., Tan, Y. M., Wu, L., Zhuang, Y., He, L. C., and Gong, H. H. (2015). Intrinsic functional plasticity of the sensory-motor network in patients with cervical spondylotic myelopathy. *Scientific Reports*, 5:9975.

Zhou, X., He, X., and Ren, Y. (2014). Function of microglia and macrophages in secondary damage after spinal cord injury. *Neural Regeneration Research*, 9(20):1787–1795.

Zibly, Z., Schlaff, C. D., Gordon, I., Munasinghe, J., and Camphausen, K. A. (2012). A novel rodent model of spinal metastasis and spinal cord compression. *BMC Neuroscience*, 13(1):137.